IOWA STATE UNIVERSITY
Digital Repository

Retrospective Theses and Dissertations

Iowa State University Capstones, Theses and Dissertations

1971

Diffraction of piezoelectric surface waves

LeRoy Paul Venteicher
Iowa State University

Follow this and additional works at: https://lib.dr.iastate.edu/rtd

Part of the Electrical and Electronics Commons

Recommended Citation
Venteicher, LeRoy Paul, "Diffraction of piezoelectric surface waves " (1971). *Retrospective Theses and Dissertations*. 4596.
https://lib.dr.iastate.edu/rtd/4596

This Dissertation is brought to you for free and open access by the Iowa State University Capstones, Theses and Dissertations at Iowa State University Digital Repository. It has been accepted for inclusion in Retrospective Theses and Dissertations by an authorized administrator of Iowa State University Digital Repository. For more information, please contact digirep@iastate.edu.

المنارة للاستشارات

www.manaraa.com

72-12,607

VENTEICHER, LeRoy Paul, 1938-
DIFFRACTION OF PIEZOELECTRIC SURFACE WAVES.

Iowa State University, Ph.D., 1971
Engineering, electrical

University Microfilms, A XEROX Company, Ann Arbor, Michigan

THIS DISSERTATION HAS BEEN MICROFILMED EXACTLY AS RECEIVED

Diffraction of piezoelectric surface waves

by

LeRoy Paul Venteicher

A Dissertation Submitted to the

Graduate Faculty in Partial Fulfillment of

The Requirements for the Degree of

DOCTOR OF PHILOSOPHY

Major Subject: Electrical Engineering

Approved:

Signature was redacted for privacy.

In Charge of Major Work

Signature was redacted for privacy.

For the Major Department

Signature was redacted for privacy.

For the Graduate College

Iowa State University
Ames, Iowa

1971

PLEASE NOTE:

Some Pages have indistinct print. Filmed as received.

UNIVERSITY MICROFILMS

TABLE OF CONTENTS

		Page
I.	INTRODUCTION	1
	A. Background	1
	1. Uniform surface waves	4
	2. Uniform Rayleigh waves on the basal plane of hexagonal crystals	7
	3. Energy flow	10
	4. Nonuniform surface waves	11
	B. Diffraction Methods	12
	1. Scalar diffraction theory	12
	2. Experimental methods	14
II.	DIFFRACTION OF TRANSVERSELY ISOTROPIC SUBSTRATES	16
	A. Formulation	16
	B. Initial Condition	22
	C. Evaluation of the Integrals	25
	D. Electrostatic Potential and Electric Field Intensity	29
	E. Poynting Vector	30
	F. Series Validity and Convergence	32
III.	NUMERICAL COMPUTATION	33
IV.	CALCULATED RESULTS	35
V.	CONCLUSIONS	40a
VI.	LITERATURE CITED	41
VII.	ACKNOWLEDGEMENTS	45
VIII.	APPENDIX A	46
IX.	APPENDIX B	48
X.	APPENDIX C	51
XI.	APPENDIX D	78

I. INTRODUCTION

During the past decade there has been a marked growth of interest in the use of piezoelectric surface waves for microwave signal processing. There has been a consequent growth of research activity concerned with a wide range of piezoelectric surface wave phenomena (1, 2, 3). One facet of this activity involves the diffraction of piezoelectric surface waves by transducers and apertures. The work presented here uses an angular spectrum of uniform Rayleigh-mode piezoelectric surface waves, which satisfy the stress equations of motion and Maxwell's equations on a stress-free piezoelectric surface, to investigate these diffractive phenomena. This approach allows the calculation of the three components of particle displacement, the three electric field intensity components, the electrostatic potential, and the Poynting vector at all points around a diffracting object. The next two sections present a background of descriptive physics and a survey of the methods used by others in treating surface wave diffraction.

A. Background

Newton's Second Law of Motion requires elastic wave propagation to obey the stress equation of motion given by

$$\rho \frac{\partial^2 u_i}{\partial t^2} = \frac{\partial T_{ij}}{\partial x_j} \tag{1}$$

where ρ is the density of the crystal,

u_j is the particle displacement in the Cartesian coordinates x_i, and

T_{ij} is the stress tensor.

For piezoelectric crystals Hooke's law is

$$T_{ij} = C_{ijk\ell} S_{k\ell} - e_{pij} E_p \tag{2}$$

where $S_{k\ell}$ is the strain tensor,

$C_{ijk\ell}$ is a constant entropy fourth rank tensor of elastic rigidity,

e_{pij} is a third rank piezoelectric tensor, and

E_p is the electric field intensity.

The strain tensor is related to the displacements by

$$S_{k\ell} = \frac{1}{2}\left(\frac{\partial u_k}{\partial x_\ell} + \frac{\partial u_\ell}{\partial x_k} \right). \tag{3}$$

Acoustic wave propagation on piezoelectric crystals is complicated by the presence of electromagnetic field quantities that must satisfy Maxwell's equations for a magnetically isotropic dielectric

$$\frac{\partial D_i}{\partial x_i} = 0 \tag{4a}$$

$$D_i = e_{ik\ell} S_{k\ell} + \epsilon_{ip} E_p \tag{4b}$$

$$\frac{\partial H_i}{\partial x_j} = 0 \tag{4c}$$

$$\epsilon_{ijk} \frac{\partial H_k}{\partial x_j} = \frac{\partial D_i}{\partial t} \tag{4d}$$

$$\epsilon_{ijk} \frac{\partial E_k}{\partial x_j} = - \mu_o \frac{\partial H_i}{\partial t} \tag{4e}$$

where D_i is the electric flux density,

H_i is the magnetic field intensity,

μ_o is the permeability of free space,

ϵ_{ijk} is the rotation tensor, and

ϵ_{ip} is the dielectric permittivity at constant strain.

Equations 4d, 4e, 4b, and 3 can be combined to eliminate the magnetic field intensity, strain, and electric flux density to yield

$$\frac{\partial^2 E_j}{\partial x_i \partial x_j} - \frac{\partial^2 E_i}{\partial x_j \partial x_j} = -\frac{1}{2}\mu_o e_{ik\ell}\frac{\partial^2}{\partial t^2}\left(\frac{\partial u_k}{\partial x_\ell} + \frac{\partial u_\ell}{\partial x_k}\right) - \mu_o \epsilon_{ip}\frac{\partial^2 E_p}{\partial t^2} \quad . \tag{5}$$

The stress equations of motion can be expressed in terms of the displacement and the electric field intensity by combining Equations 1, 2, and 3; this yields

$$\rho\frac{\partial^2 u_i}{\partial t^2} = \frac{1}{2} C_{ijk\ell}\frac{\partial}{\partial x_j}\left(\frac{\partial u_k}{\partial x_\ell} + \frac{\partial u_\ell}{\partial x_k}\right) - e_{pij}\frac{\partial E_p}{\partial x_j} \quad . \tag{6}$$

For piezoelectric crystals, elastic wave propagation can be described by the simultaneous solution of Equations 5 and 6 subject to the boundary conditions: (1) continuity of the stress vector at the surface, (2) continuity of the tangential component of the electric field intensity at the surface, and (3) continuity of the normal component of the electric flux density on a charge free surface. For nonpiezoelectric materials, solutions need only satisfy Equation 6 with $e_{pij} = 0$ and continuity of the stress vector at surfaces.

1. Uniform surface waves

When a disturbance described by Equations 5 and 6 propagates so that most of its energy is near an interface between the material and free space, it is referred to as a surface wave. The particle displacements and electric field components will decay with distance from the surface. If these components are independent of a coordinate lying in the plane of the surface and normal to the direction of propagation, the disturbance is considered to be a uniform surface wave.

A coordinate system is chosen with x_k parallel to the surface and in the direction of propagation, x_n perpendicular to the surface and to the direction of propagation while x_t is measured parallel to the surface and perpendicular to the direction of propagation. The $x_n - x_k$ plane is called the sagittal plane. A disturbance is considered to be a uniform surface wave if it is independent of the x_t coordinate and therefore uniform in a direction perpendicular to the sagittal plane. Any field or displacement component can be represented by

$$f_p = C_p \exp\left[\beta k x_n + jkx_k - j\omega t\right] \tag{7}$$

or a superposition of functions of this form. The uniform surface solutions of Equations 5 and 6 have been studied extensively (4, 5, 6, 7) since they are tractable and provide much insight into the behavior of surface waves of finite width.

In general a uniform piezoelectric surface wave has three components of particle displacement $\vec{U}(U_k, U_n, U_t)$ and three components of electric field intensity $\vec{E}(E_k, E_n, E_t)$ when expressed in Cartesian coordinates

(x_k, x_n, x_t). In many cases, this general form of uniform surface waves decomposes into simpler modes.

The various components of particle displacement and electric field intensity of uniform waves couple together in several different ways depending on the symmetries associated with the sagittal plane (8, 9, 10). Mathematically, this decomposition occurs when Equations 5 and 6 can be separated into independent sets of equations. The solutions to each subset of Equations 5 and 6 must satisfy the boundary conditions if that particular mode is to propagate. Therefore the boundary conditions may forbid the existence of certain mode groups or they may introduce coupling between mode groups that are not coupled together through the lattice dynamics described by Equations 5 and 6. The various types of uniform surface waves that are known to propagate on free surfaces can be clearly described as follows (9, 10, 11, 12):

General Piezoelectric Surface Wave

$$\vec{E}(E_k, E_n, E_t) + \vec{U}(U_k, U_n, U_t)$$

Elastic Rayleigh Surface Wave

$$\vec{E}(0, 0, E_t) + \vec{U}(U_k, U_n, 0)$$

SH-mode Piezoelectric Surface Wave (Bleustein Wave)

$$\vec{E}(E_k, E_n, 0) + \vec{U}(0, 0, U_t)$$

Rayleigh-mode Piezoelectric Surface Wave

$$\vec{E}(E_k, E_n, 0) + \vec{U}(U_k, U_n, 0)$$

where E_t is included for the elastic Rayleigh surface wave but is very small in magnitude. Tseng (10) has shown that two of these modes can

exist at the same time with different velocities on certain orientations of cubic crystals.

Lim and Farnell (13, 14) investigated certain highly anisotropic nonpiezoelectric and weakly piezoelectric cases numerically and found that there is no reason to consider the propagation of uniform surface waves as fortuitous. Their search did not reveal any forbidden directions in that there always appears to be a uniform surface wave solution which satisfies the free-surface boundary conditions and is unattenuated in the direction of propagation. However, near certain specific directions, the penetration of this wave below the surface becomes very deep. In addition, for certain ranges of direction they found second or pseudo-surface-wave solutions which radiate into the bulk of the material, while normal uniform elastic Rayleigh waves do not radiate into the bulk of the material.

In anisotropic media, piezoelectric and nonpiezoelectric, generally the direction of energy flow of uniform bulk waves and uniform surface waves will not be parallel to the propagation vector (15, 16). This phenomena is often referred to a beam steering since it has the effect of directing the energy in a direction different than that of the propagation vector. Farnell (4) and Musgrave (7) summarize the results of many techniques used to calculate the energy flow direction for uniform surface waves on more complex anisotropic solids. For isotropic and nearly isotropic materials, and for isotropic planes imposed by crystal symmetry such as on the basal plane of 4mm and 6mm crystals, all uniform surface waves are pure mode, that is, power flow is parallel

to the propagation vector regardless of the direction of propagation.

2. Uniform Rayleigh waves on the basal plane of hexagonal crystals

Koerber (8) has demonstrated that a plane of symmetry parallel to the sagittal plane of an uniform surface wave is sufficient to decouple the wave equations and the boundary condition equations into the mode groups (u_t E_t) and (u_k u_n E_k E_n). He also notes that these same mode groups exist for a uniform disturbance upon the basal planes of crystals having 4mm or 6mm symmetry regardless of the orientation of the plane of symmetry relative to the sagittal plane. Tseng and White (11) have analyzed surface wave propagation on the basal plane of a number of hexagonal crystals and have found that the Rayleigh-mode piezoelectric surface wave, (u_k u_n E_k E_n), can propagate on a free surface while the transverse mode, (u_t E_t), can not propagate on a free surface (12). Therefore, on the basal plane of these 6mm crystals, only one mode can propagate in any particular direction.

Tseng and White (11) derive a determinantal characteristic equation appropriate to the Rayleigh-mode piezoelectric surface wave inside the crystal from Equations 5 and 6, and the pertinent characteristic equation outside the crystal from Equation 5 where $e_{ik\ell} = 0$. The roots of these characteristic equations suggest that each field and displacement component will be a superposition of three solutions in the form of Equation 7. Thus the form of the particle displacement and the electric field intensity is

$$u_k = A_1[a_{11}\exp(\Omega_1 kx_n)+a_{21}\exp(\Omega_2 kx_n)+a_{31}\exp(\Omega_3 kx_n)]\exp[j(kx_k-\omega t)]$$

$$u_n = A_1 p_1[p_{11}\exp(\Omega_1 kx_n)+p_{21}\exp(\Omega_2 kx_n)+p_{31}\exp(\Omega_3 kx_n)]\exp[j(kx_k-\omega t)]$$

$$E_k = kq_1 A_1[q_{11}\exp(\Omega_1 kx_n)+q_{21}\exp(\Omega_2 kx_n)+q_{31}\exp(\Omega_3 kx_n)]\exp[j(kx_k-\omega t)]$$

$$E_n = kr_1 A_1[r_{11}\exp(\Omega_1 kx_n)+r_{21}\exp(\Omega_2 kx_n)+r_{31}\exp(\Omega_3 kx_n)]\exp[j(kx_k-\omega t)]$$

$$E_t = u_t = 0 \quad , \; k = \text{propagation constant} \; , \; x_n \leq 0 \; . \tag{8}$$

The boundary conditions at the free surface are used to form a second determinantal equation. Each of these determinantal equations relates the phase velocity and the decay constants; in principle these equations could be used to find the phase velocity by eliminating the decay constants in a simultaneous solution. Due to the algebraic intricacy, this problem can only be solved numerically by assigning a velocity to the characteristic equation and then solving it for the decay constants. These decay constants along with the assumed velocity must satisfy the boundary condition determinant. This procedure must be repeated until one obtains a solution. Equations 8 and the constants calculated by Tseng and White (11) for CdS are used for the quantitative diffraction work done in this thesis. The constants are listed in Table 1. These constants are independent of the direction of propagation on the basal plane of CdS. In Table 1, the units on q_1 and r_1 are volts/meter, while the rest are dimensionless constants. When the values are used to evaluate Equations 8, the same system of units must be used for u_k, u_n, A_1, $1/k$, and x_n.

Table 1. Velocity, decay constants and amplitude constants of surface waves on the basal plane of CdS

$v_s = 1.7306 \times 10^3$ m/sec		
$\Omega_1 = 1.6550$	$\Omega_2 = 0.1940$	$\Omega_3 = 0.7474$
$p_1 = -j\ 0.3794$	$a_{21} = -0.5015$	$a_{31} = 0.5230$
$q_1 = -0.8516 \times 10^{10}$	$p_{21} = -7.6450$	$p_{31} = 1.6401$
$r_1 = j\ 1.409 \times 10^{10}$	$q_{21} = 1.0731$	$q_{31} = -1.6530$
$a_{11} = q_{11} = r_{11} = p_{11} = 1$	$r_{21} = 0.1256$	$r_{31} = -0.7465$

An approximate electrostatic potential can be obtained from Equation 8 since

$$\phi \cong -\int \bar{E} \cdot \overline{d\ell} \tag{9}$$

Therefore,

$$\phi(x_k) = -\int E_k dx_k = -\int k q_1 A_1 \sum_i q_{i1} \exp(\Omega_i k x_n) \exp[j(kx_k - \omega t)] dx_k$$

$$= -q_1 A_1 \sum_i q_{i1} \exp(\Omega_i k x_n) \exp[j(kx_k - \omega t)] + \text{constant} \tag{10}$$

or

$$\phi(x_n) = -\int E_n dx_n = -\int k r_1 A_1 \sum_i r_{i1} \exp(\Omega_i k x_n) \exp[j(kx_k - \omega t)] dx_n$$

$$= r_1 A_1 \sum_i \frac{r_{i1}}{\Omega_i} \exp(\Omega_i k x_n) \exp[j(kx_k - \omega t)] + \text{constant} . \tag{11}$$

A check of these constants in Table 1 shows that

$$- j\, q_1\, q_{i1} = \frac{r_1 r_{i1}}{\Omega_i}\,, \quad i = 1, 2, 3 \tag{12}$$

so these two expressions are equivalent and either one provides the electrostatic potential at all points in the crystal.

3. Energy flow

The time-average transport of energy by mechanical waves with a sinusoidal time dependence can be specified by a vector whose components are (4)

$$P_i = -\frac{1}{2}\,\mathrm{Re}\,\{T_{ij}\,\dot{u}_j^*\} \tag{13}$$

where T_{ij} is the stress tensor, and
$\dot{u}_j^*$ is the conjugate of the derivative with respect to time of the particle displacement.

This is analogous to the "time-averaged Poynting vector" of electromagnetic theory and is referred to simply as the "Poynting vector". This Poynting vector gives the time-average energy flow per unit area across a surface normal to this vector. In terms of the elastic tensor this Poynting vector is (7)

$$P_i = -\frac{1}{4}\,C_{ijk\ell}\,[u_{k,\ell}\dot{u}_j^* + u_{k,\ell}^*\dot{u}_j] \tag{14}$$

where $C_{ijk\ell}$ is the elastic tensor, and

$u_{k,\ell}$ is the derivative of the particle displacement u_k with respect to the position coordinate x_ℓ.

It is not necessary to consider the electrical Poynting vector, $\bar{E} \times \bar{H}$, for piezoelectric disturbances. Even in strongly piezoelectric materials the acoustic wave velocity is small compared to the speed of light and the magnetic field intensity is so small that the electrical Poynting vector contributes little to the transport of energy (16).

4. Nonuniform surface waves

Acoustic waves on piezoelectric delay lines and other microsound devices are nonuniform perpendicular to the sagittal plane because the interdigital transducers used to excite these surface waves are of finite width. A large number of recent publications have been concerned with various aspects of nonuniform surface wave propagation (17-27). Two phenomena which have a large influence on the behavior of nonuniform surface waves are (1) beam steering, and (2) diffraction. Diffractive phenomena become more important the narrower the nonuniform surface wave. Diffraction pertains to the behavior of a wave when it encounters an obstacle which is capable of "interacting" with the wave; reflection and refraction phenomena are not included in this classification. The main effect of diffraction is to spread the nonuniform surface as the wave propagates away from the diffracting object; it can also cause interference and therefore large variations in intensity along the path of the wave. In highly anisotropic crystals, beam steering can either increase or decrease the diffractive spreading of a nonuniform surface wave (18, 20).

Weglein, Pedinoff, and Winston (20) report measurements, on y-cut $LiNbO_3$, of far-field diffraction spreading of surface acoustic waves which were generated by 10 wavelength wide interdigital transducers. These measurements were made along the z-axis and at an angle of $\pm 21.9^{\circ}$ from the z-axis because propagation is pure mode in these directions. They found the acoustic beam's half-power points to spread at an angle of 0.327° along the z-axis, an angle of 4.53° along the axis at 21.9° from z, as compared to a predicted angle of 2.56° for the isotropic case. Their measured beam-spread angles are approximately 30% larger than those predicted by a theory based on the Rayleigh-Sommerfeld diffraction integral (33). Slobodnik (23) found the far-field of a 75 wavelength wide interdigital transducer to exhibit wide variations in intensity. He suggests that imperfections in the crystal or transducer are responsible for this distortion, since a transducer this wide will introduce little diffractive distortion.

B. Diffraction Methods

The "angular spectrum of plane waves" representation has been used extensively to investigate electromagnetic wave propagation and diffraction (28-32), and recently to investigate acoustic wave diffraction (21, 22, 33).

1. Scalar diffraction theory

Kharusi and Farnell (21) introduce the angular spectrum, Fourier transform and "scalar diffraction theory" concepts (28) to the analysis

of acoustic surface wave diffraction and beam steering on highly anisotropic piezoelectric substrates. On the basis of the agreement obtained between experimental and calculated diffraction patterns over a frequency range extending from 107-905 Mhz for propagation directions having a very high phase-velocity anisotropy, they conclude that an angular spectrum of uniform surface waves offers a valid means of solving surface wave diffraction problems.

Scalar diffraction theory requires the definition of some scalar function $f(x,y,z)$, which is a solution of the Helmholtz equation

$$\nabla^2 f + k^2 f = 0 \tag{15}$$

where the time dependence has been suppressed to ease analysis. Kharusi and Farnell (21, 22) define $f(x,y,z)$ such that the intensity of the acoustic wave is the square of the scalar function $f(x,y,z)$. In other situations one could define $f(x,y,z)$ to represent the particle displacement in the direction of propagation. The choice depends on the aspect of diffraction under investigation.

Kharusi and Farnell (21) consider a surface wave propagating on the x-z plane, where the aperture is located at $z = 0$ and transmitting acoustic energy into the region for $z > 0$. In terms of the Fourier transform the solution for $f(x,z)$ is given by

$$f(x,z) = \int_{-\infty}^{+\infty} F(k_1) \exp\left[j(k_1 x + k_3 z)\right] dk_1 \tag{16}$$

given that

$$[k_3(k_1)]^2 = [k(\hat{k})]^2 - k_1^2 \tag{17a}$$

and

$$k(\hat{k}) = {}^{2\pi\nu}/v(\hat{k}) \tag{17b}$$

where ν is frequency, and

$v(\hat{k})$ is the phase velocity in the wave vector direction $\hat{k}$.

One can see that

$$F(k_1) = \int_{-\infty}^{+\infty} f(x,0) \exp[-jk_1x]dx \tag{18}$$

where $f(x,0)$ is the distribution at the aperture of the function represented by $f(x,z)$. In order to calculate $F(k_1)$, they assume a distribution which is constant for $-R/2 \leq x \leq R/2$ and zero for all other x at $z = 0$. They use numerical integration techniques to solve Equation 16 using several different phase-velocity functions, $v(\hat{k})$. The main thrust of their work was to obtain calculated diffraction patterns for propagation on or near pure mode axis of highly anisotropic crystals and compare these to previously published experimental results.

2. Experimental methods

Several techniques have proven useful in obtaining information concerning the spatial distribution of the acoustic surface wave particle displacement amplitudes and their phase velocity. These include (a) detection of the electric field intensity associated with the piezoelectric elastic wave using interdigital transducers (15),

(b) detection of the electrostatic potential with wire probes (20, 24), and (c) detection of surface corrugations by Brillouin scattering of a laser beam (23, 25, 26, 27). The last two processes are most suitable for careful examination because they are able to trace the topographic profile of certain surface wave parameters. Each of these methods responds to a surface wave parameter whose value is a function of the magnitude and relative phase of the modes which compose a particular surface wave. If the amplitude ratios and relative phase were to change from position to position, these measurement techniques may not indicate the true energy flux distribution.

These measurement techniques have shown spreading of the main lobe, and they have shown that energy is lost to side lobes (24, 25) in quantitative agreement with the work of Kharusi and Farnell (21). Cambon, Rouzeyre, and Simon (25) report "near field" measurements on the free surface of a y-cut quartz crystal; there have been no reports of theoretical calculations in this range. The angular variation of the phase velocity on this cut of quartz is very small.

II. DIFFRACTION OF TRANSVERSELY ISOTROPIC SUBSTRATES

Piezoelectric surface waves propagating upon the basal planes of crystals having 6mm or 4mm symmetry have certain features that make it algebraically feasible to formulate diffraction integrals in terms of specific displacement and field components. These features were discussed in detail in the previous section. Of particular importance, one finds that only piezoelectric Rayleigh-mode surface waves can propagate on the free surface of the basal plane. Their phase velocity and decay constants are independent of direction.

This formulation is capable of providing much detailed information concerning the particle displacement and electric field intensity components. This in turn allows the calculation of the Poynting vector and thus provides information concerning the energy flux distribution.

A. Formulation

Consider an angular spectrum of uniform Rayleigh-mode piezoelectric surface waves whose sagittal planes contain the x_3 axis and whose components of particle displacement and electric field intensity decay in the negative x_3 direction. The crystal is located in the region $x_3 \leq 0$ and the plane, $x_3 = 0$, coincides with the crystal surface. The propagation constant of each component wave in this spectrum will have a positive component in the x_2 direction.

The particle displacement component in the x_3 direction of a wave propagating at an angle θ with the x-axis, as indicated in Figure 1, can be expressed as

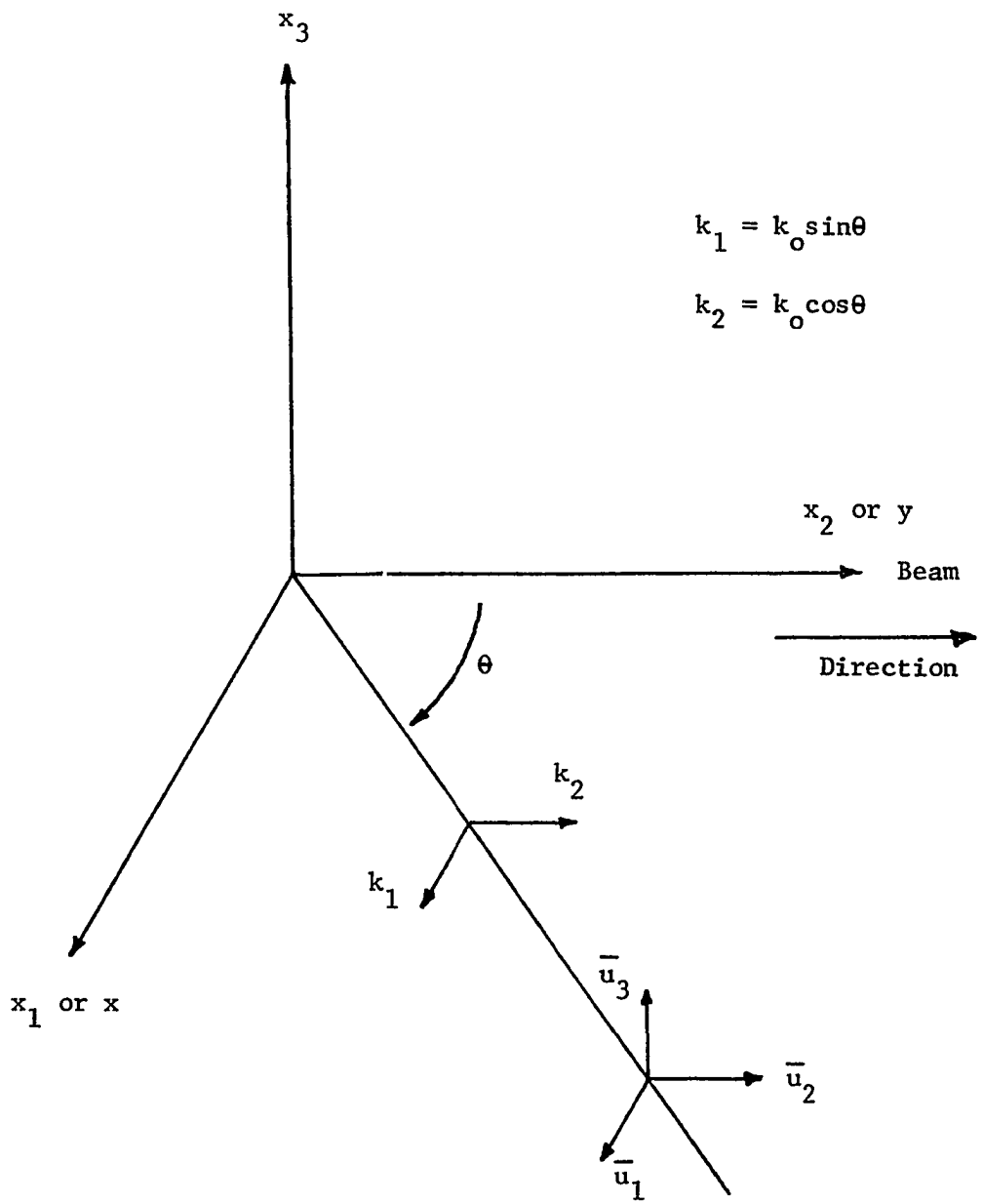

Figure 1. Coordinate Systems

$$\bar{u}_3(x_1,x_2,x_3,t) = \hat{u}_3(x_3)\exp[j(k_1x_1+k_2x_2)]\exp[-j\omega t] \tag{19}$$

by analogy to Equations 8 where $\hat{u}_3(x_3)$ represents the functional behavior in the sagittal plane perpendicular to the direction of propagation,

$$k_o^2 = \omega^2/v^2 = k_1^2 + k_2^2, \quad \text{and} \quad \tan\theta = k_2/k_1 \ .$$

An arbitrary initial condition at $x_2 = 0$ can be specified by a linear combination of solutions by the integral equation

$$U_3(x_1,x_2,x_3,t) = \int_{-\infty}^{+\infty} A(k_1)\bar{u}_3(x_1,x_2,x_3,t)dk_1 \ . \tag{20}$$

This integral is a solution regardless of the path of integration and value of $A(k_1)$ if each wave in this angular spectrum satisfies the system's equations. Substituting Equation 19 into Equation 20 yields

$$U_3(x_1,x_2,x_3,t) = \int_{-\infty}^{+\infty} \hat{u}_3(x_3)A(k_1)\exp[+j(k_1x_1+k_2x_2-\omega t)]dk_1 \ . \tag{21}$$

Equation 21 gives the value of U_3 as a sum of the $\bar{u}_3$ components of each wave in the angular spectrum. The direction of propagation of a particular component is determined by the factor $\exp[j(k_1x_1+k_2x_2)]$. Since $\hat{u}_3(x_3)\exp[-j\omega t]$ is not a function of the direction of propagation, Equation 21 can be written

$$U_3(x_1,x_2,x_3) = \hat{u}_3(x_3)\int_{-\infty}^{+\infty} A(k_1)\exp[j(k_1x_1+k_2x_2)]dk_1 \tag{22}$$

where the time dependence has been suppressed for convenience. At the aperture, $x_2 = 0$ and Equation 22 becomes

$$U_3(x_1,0,x_3) = \hat{u}_3(x_3) \int_{-\infty}^{\infty} A(k_1)\exp[+jk_1x_1]dk_1 \tag{23}$$

hence via Fourier transform concepts, one can write

$$A(k_1) = \frac{1}{2\pi} \int_{-\infty}^{\infty} \frac{U_3(x_1,0,x_3)}{\hat{u}_3(x_3)} \exp[-jk_1x_1]dx_1 \ . \tag{24}$$

Thus $A(k_1)$ is the Fourier transform of the U_3 component of the non-uniform wave at $x_2 = 0$ with the time and x_3 dependence suppressed. For conditions on the existence of the Fourier transform and its inverse see Bracewell (34) or Titchmarsh (35).

The displacement component in the direction of propagation of each wave in the angular spectrum will contribute to both U_1 and U_2 of the acoustic beam, therefore

$$\bar{u}_1 = \hat{u}_2(x_3) \left(\frac{k_1}{k_o}\right) \exp[j(k_1x_1+k_2x_2)] \tag{25}$$

and

$$\bar{u}_2 = \hat{u}_2(x_3) \left(\frac{k_2}{k_o}\right) \exp[j(k_1x_1+k_2x_2)] \tag{26}$$

by analogy to Equations 8 and 19. The integral equation for the non-uniform surface wave's component of displacement in the x_1 direction will be

$$U_1(x_1,x_2,x_3) = \frac{\hat{u}_2(x_3)}{k_o} \{ \int_{-k_o}^{+k_o} A(k_1)k_1 \exp[j(k_1x_1+k_2x_2)]dk_1$$

$$+\int_{-\infty}^{-k_o} A(k_1)\exp[j(k_1x_1+k_2x_2)]dk_1 + \int_{+k_o}^{\infty} A(k_1)\exp[j(k_1x_1+k_2x_2)]dk_1 \} \tag{27}$$

and for the displacement component in the x_2 direction

$$U_2(x_1,x_2,x_3) = \frac{\hat{u}_2(x_3)}{k_o} \{ \int_{-\infty}^{-k_o} 0 \, dk_1$$

$$+ \int_{-k_o}^{+k_o} A(k_1)k_2 \exp[j(k_1x_1+k_2x_2)]dk_1 + \int_{+k_o}^{\infty} 0 \, dk_1 \} \tag{28}$$

by analogy to Equation 21.

Since the integral Equations 22, 27, and 28 are inverse Fourier transforms, they should extend from $-\infty$ to $+\infty$; however, when $k_1 > k_o$ or when $k_1 < -k_o$, k_2 is complex. For this range of k_1, the waves which compose the angular spectrum are not uniform. These evanescent (inhomogeneous) waves are propagating along the x_1 axis with a velocity greater than k_o, and for $x_2 > 0$, they decay in magnitude with distance from the $x_2 = 0$ plane. They will contribute very little to the U_1, U_2, and U_3 displacement components of the nonuniform wave at large distances in the x_2 direction. In fact while evanescent wave solutions do satisfy Helmholtz's equation (22), it has never been demonstrated that evanescent Rayleigh-mode piezoelectric surface waves satisfy the system of equations used to describe elastic surface wave propagation. Note that the

homogeneous waves, $-k_o \leq k_1 \leq k_o$, have a propagation constant of k_o and therefore satisfy the system's equations.

In summary, for a nonuniform acoustic beam propagating on the basal plane of 4mm or 6mm crystals, the integral expressions for the displacement components in terms of an angular spectrum of uniform Rayleigh-mode piezoelectric surface waves can be written

$$U_1(x_1,x_2,x_3) = \frac{\hat{u}_2(x_3)}{k_o} \int_{k_1=-k_o}^{+k_o} A(k_1)k_1 \exp[j(k_1x_1+k_2x_2)]dk_1 \tag{29}$$

$$U_2(x_1,x_2,x_3) = \frac{\hat{u}_2(x_3)}{k_o} \int_{k_1=-k_o}^{+k_o} A(k_1)k_2 \exp[j(k_1x_1+k_2x_2)]dk_1 \tag{30}$$

$$U_3(x_1,x_2,x_3) = \hat{u}_3(x_3) \int_{k_1=-k_o}^{+k_o} A(k_1) \exp[j(k_1x_1+k_2x_2)]dk_1 \tag{31}$$

where

$$A(k_1) = \frac{1}{2\pi} \int_{x_1=-\infty}^{+\infty} [U_3(x_1,0,x_3)/\hat{u}_3(x_3)] \exp[-jk_1x_1]dx_1 \ . \tag{32}$$

Equations 29, 30, and 31 are approximate within a few wavelengths of the aperture where the evanescent waves will contribute to the total displacements of the nonuniform acoustic beam.

B. Initial Condition

For propagation on the basal plane of piezoelectric crystals with 4mm or 6mm symmetry, the x_3 dependence of particle displacement is separable as indicated by Equations 8, so $U_3(x_1,0,x_3) = \hat{u}_3(x_3)a(x_1)$ and

$$A(k_1) = \frac{1}{2\pi}\int_{-\infty}^{+\infty} a(x_1)\exp[-jk_1x_1]dx_1 \ . \tag{33}$$

Note that specifying this boundary condition on $U_3(x_1,0,x_3)$ also sets the values of $U_1(x_1,0,x_3)$ and $U_2(x_1,0,x_3)$.

Assume a functional form of $a(x_1)$ as indicated in Figure 2. For this $a(x_1)$ Equation 33 evaluates to

$$A(k_1) = \frac{M}{\pi}\ \frac{\sin k_1L}{k_1} \ . \tag{34a}$$

Figure 3 shows the approximate shape of $A(k_1)$ emphasizing the maximum values and zeros. By evaluating Equations 29, 30, and 31 for $-k_o \le k_1 \le k_o$, one includes only a finite number of the "peaks" of this function. As an example if $L = 10\ \lambda_o$, then $k_1 = k_o$ when $k_1 = \frac{20\pi}{L}$ and this evaluation includes 20 "cycles" of $A(k_1)$. Where $\lambda_o = \frac{2\pi}{k_o}$ is the wavelength of the surface wave. Doubling the transducer width, doubles the number of "peaks" included in the evaluation of Equations 29, 30, and 31; therefore, these equations will most accurately reproduce $U_3(x_1,0,x_3)$, $U_2(x_1,0,x_3)$, and $U_1(x_1,0,x_3)$ when L is large.

To estimate the effect of neglecting the evanescent waves, note that when $L = 10\ \lambda_o$, the magnitude of the first peak in the region $k_1 > k_o$ has an approximate value equal to $\frac{A(0)}{20.5\ \pi}$.

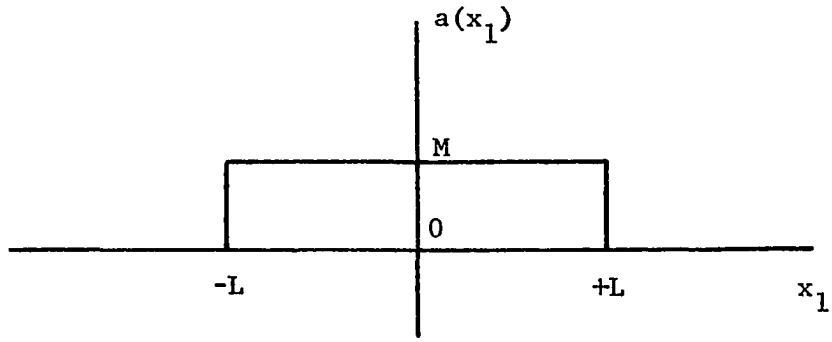

Figure 2. $a(x_1)$ at $x_2 = 0$

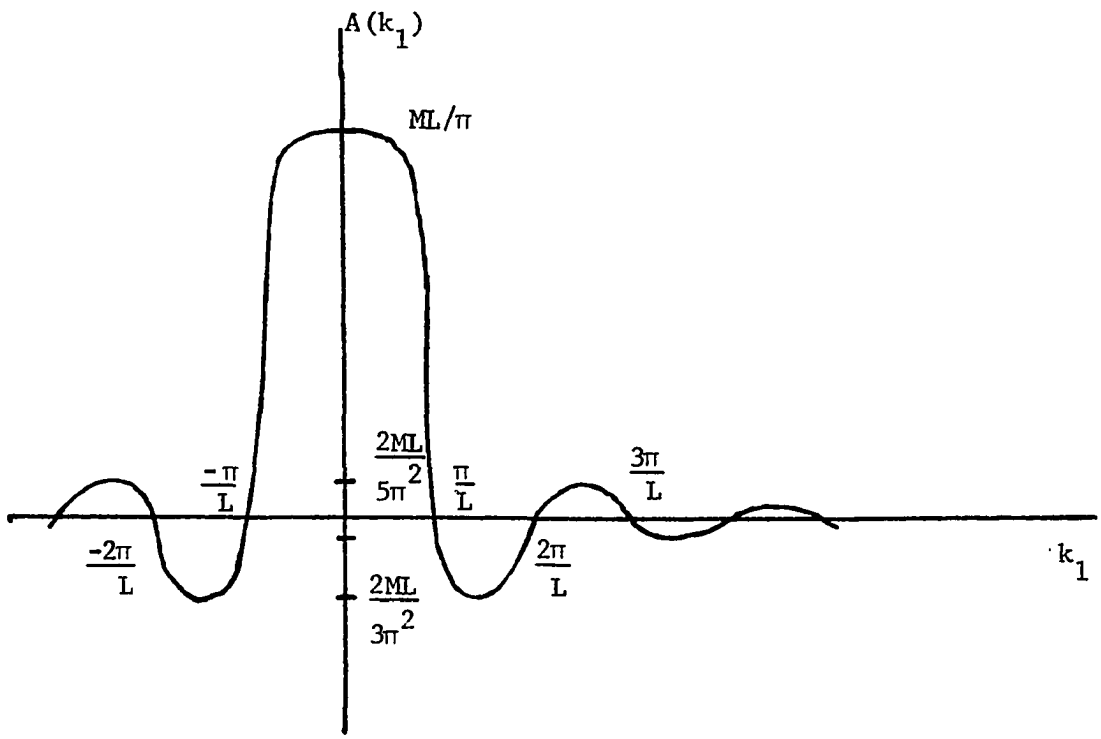

Figure 3. $A(k_1)$ for $a(x_1)$ of Figure 2

In this region the peak values of $A(k_1)$ vary as the reciprocal of k_1, so for $k_1 > k_o$, the peak values do not decrease as rapidly as in the range $0 < k_1 < k_o$. The magnitude of these evanescent waves decays in the x_2 direction since for $k_1 > k_o$, $k_2 = j\sqrt{k_1^2 - k_o^2}$. In the range $k_o < k_1 < 2k_o$, $0 < \sqrt{k_1^2 - k_o^2} < \sqrt{3}\, k_o$, hence for $k_1 > 2k_o$, the decay constant of the waves in the x_2 direction is less than $\lambda_o/2\sqrt{3}\pi < 0.1\lambda_o$. While it is tempting to conclude that the evanescent waves will have little effect on the values of the particle displacements when $x_2 > 10\,\lambda_o$; an exact evaluation is needed to prove this conclusion.

An alternate approach is to consider the distribution of the particle displacement, $U_3(x_1,0,x_3)$ to be defined by $b(x_1)$ in place of $a(x_1)$ when

$$b(x_1) = \int_{-k_o}^{+k_o} A(k_1)\exp[jk_1x_1]dk_1 \tag{34b}$$

where $A(k_1)$ is defined by Equation 34a. This integral is difficult to evaluate and in general the solution would be a function of L; when L is large, $b(x_1) \simeq a(x_1)$. From this point of view, one can say that the diffraction Equations 29, 30, and 31 provide exact solutions for a distribution $b(x_1)$; however, $b(x_1)$ appears to be a less accurate description of the beam emitted by a real transducer or aperture. Neither of the initial conditions $a(x_1)$ or $b(x_1)$ represent a "rigorous" solution to the boundary value problem. As demonstrated by Kharusi and Farnell (21), $a(x_1)$ does provide an acceptable solution when the transducer is wide.

C. Evaluation of the Integrals

The integral Equations 29, 30, and 31, are very difficult to solve. Saddle point and stationary phase methods have been successfully used to obtain approximate solutions for some equations of this type (28). These solutions are restricted to a narrow range of the variables x_1 and x_2. Kharusi and Farnell (22) used numerical integration techniques to solve an equation similar to these. The method used here involves the use of several series expansions. A change of variables illustrated in Figure 1, was made in order to facilitate the evaluation of these equations. For Equation 29, this substitution yields

$$U_1(x_1,x_2,x_3) = \hat{u}_2(x_3)\int_{\theta=-\pi/2}^{+\pi/2} k_o A(k_o \sin\theta)\cos\theta \sin\theta \exp[jk_o(x_1\sin\theta + x_2\cos\theta)]\,d\theta \ . \tag{35}$$

It is now expedient to change from the Cartesian variables to the cylindrical variables illustrated in Figure 4. For Equation 35, one obtains

$$U_1(r,\phi,x_3) = k_o\hat{u}_2(x_3)\int_{\theta=-\pi/2}^{+\pi/2} A(k_o\sin\theta)\sin\theta\cos\theta \exp[jk_o r(\cos\phi\sin\theta + \sin\phi\cos\theta)]\,d\theta \tag{36}$$

a trigonometric identity simplifies Equation 36 to yield

$$U_1(r,\phi,x_3) = k_o\hat{u}_2(x_3)\int_{\theta=-\pi/2}^{+\pi/2} A(k_o\sin\theta)\sin\theta\cos\theta \exp[jk_o r \sin(\theta+\phi)]\,d\theta \ . \tag{37}$$

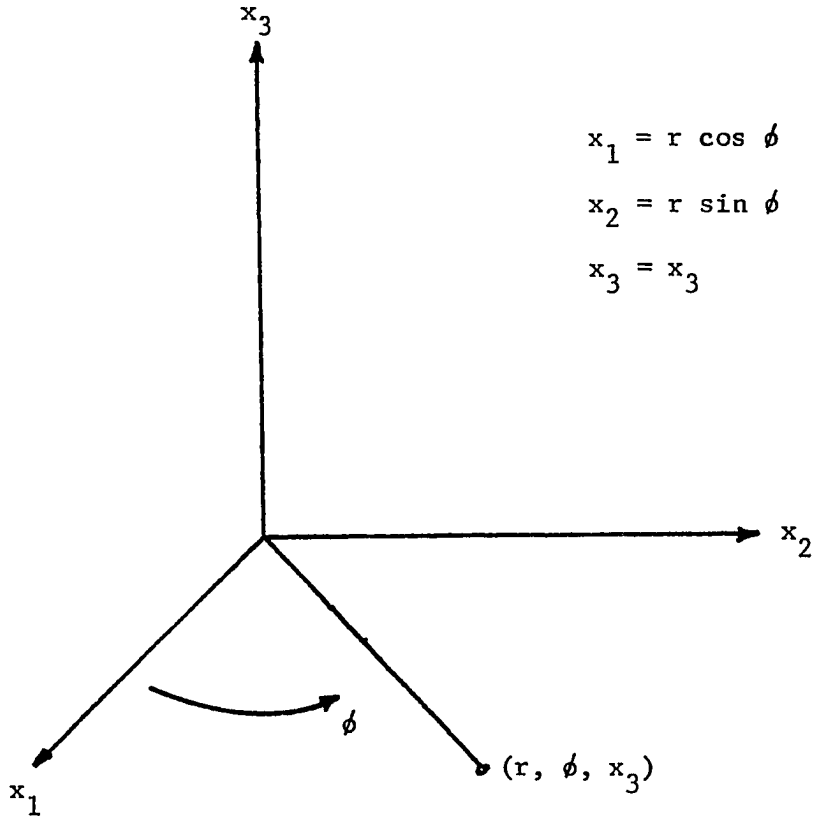

Figure 4. The cylindrical coordinate system

Now following the same procedure which was illustrated on the equation for U_1, one obtains for U_2

$$U_2(r,\phi,x_3) = k_o\hat{u}_2(x_3)\int_{\theta=-\pi/2}^{+\pi/2} A(k_o\sin\theta)\cos^2\theta \exp[jk_o r \sin(\theta+\phi)]d\theta \tag{38}$$

and for U_3

$$U_3(r,\phi,x_3) = k_o\hat{u}_3(x_3)\int_{\theta=-\pi/2}^{+\pi/2} A(k_o\sin\theta)\cos\theta \exp[jk_o r \sin(\theta+\phi)]d\theta \ . \tag{39}$$

The equations for U_1, U_2, and U_3 represent the Cartesian components of the particle displacements as a function of cylindrical variables.

Before proceeding with evaluation of Equations 37, 38, and 39, the exponential in these equations and the expression for $A(k_1)$ must be expanded as infinite series. Equation 34a for $A(k_1)$ can be expressed in terms of θ by the substitution $k_1 = k_o\sin\theta$ to yield

$$A(\theta) = \frac{M}{\pi k_o} \frac{\sin(k_o L \sin\theta)}{\sin\theta} \tag{40}$$

which in turn can be expressed as a series of Bessel functions of the first kind by using the series (36)

$$\sin(z \sin x) = 2 \sum_{k=0}^{\infty} J_{2k+1}(z)\sin[(2k+1)x] \ . \tag{41}$$

The substitution of Equation 41 into Equation 40 yields

$$A(\theta) = \frac{2M}{\pi k_o} \left(\frac{1}{\sin\theta} \sum_{k=0}^{\infty} J_{2k+1}(k_o L)\sin[(2k+1)\theta] \right) . \tag{42}$$

Another useful form of $A(\theta)$ can be obtained by realizing that

$$\sin n\theta/\sin\theta = 1 + 2 \sum_{m=1}^{m = \frac{(n-1)}{2}} \cos 2m\theta . \tag{43}$$

This result is proven in Appendix A. The substitution of Equation 43 into Equation 42 yields

$$A(\theta) = \frac{M}{\pi k_o} \{2 \sum_{m=0}^{\infty} J_{2m+1}(k_o L) + 4 \sum_{n=1}^{\infty} [\cos 2n\theta \sum_{m=n}^{\infty} J_{2m+1}(k_o L)] \} . \tag{44}$$

The exponential expression $\exp[jk_o r \sin(\theta+\phi)]$ can be represented by a series of products of Bessel functions of the first kind and trigonometric functions by using Euler's equation

$$\exp[jk_o r \sin(\theta+\phi)] = \cos[k_o r \sin(\theta+\phi)] + j \sin[k_o r \sin(\theta+\phi)] \tag{45}$$

and items 818.1, and 818.2 from Dwight (37), which are reproduced here for convenience

$$\cos[k_o r \sin(\theta+\phi)] = J_o(k_o r) + 2 \sum_{n=1}^{\infty} J_{2n}(k_o r)\cos 2n(\theta+\phi) \tag{46}$$

$$\sin[k_o r \sin(\theta+\phi)] = 2 \sum_{n=0}^{\infty} J_{2n+1}(k_o r)\sin(2n+1)(\theta+\phi) . \tag{47}$$

One can obtain series expressions for the integrands of the integral equations representing U_1, U_2, and U_3 by successively substituting Equations 45, 46, 47, and 42 or 44 into Equations 37, 38, and 39. The sequence of operations and substitutions described above produces a set of integral equations which can be evaluated, but the procedure is quite lengthy and will not be presented here. The resulting diffraction equations are quite cumbersome and are listed in Appendix B.

D. Electrostatic Potential and Electric Field Intensity

The integral equations for the electric field intensity and the electrostatic potential are similar to those obtained for the particle displacements since a uniform Rayleigh-mode piezoelectric surface wave has electric field intensity components in the same directions as its particle displacement components. The electrostatic potential is a scalar summation of the potential from each wave in the angular spectrum.

The $E_1(x_1,x_2,x_3)$ component of the field will involve the same integral as $U_1(x_1,x_2,x_3)$, $E_2(x_1,x_2,x_3)$ will involve the same integral as $U_2(x_1,x_2,x_3)$, and $E_3(x_1,x_2,x_3)$ will involve the same integral as $U_3(x_1,x_2,x_3)$ since only the x_3 functional dependence of each of these integrals will be different. The electrostatic potential will involve the same integral as $U_3(x_1,x_2,x_3)$ except for the x_3 dependence which again does not effect the integration. The following equations will help clarify this situation:

$$E_1(x_1,x_2,x_3) = \frac{U_1(x_1,x_2,x_3)}{\hat{u}_2(x_2)} \quad \hat{U}(x_3) \tag{48}$$

and

$$\phi(x_1,x_2,x_3) = \frac{U_3(x_1,x_2,x_3)}{\hat{u}_3(x_3)} \hat{\phi}(x_3) \tag{49}$$

where from Equations 8

$$\hat{u}_2(x_3) = A_1 \sum_j a_{j1} \exp(\Omega_j k_o x_3) \tag{50}$$

$$\hat{u}_3(x_3) = A_1 P_1 \sum_j P_{j1} \exp(\Omega_j k_o x_3) \tag{51}$$

$$\hat{e}_2(x_3) = k q_1 A_1 \sum_j q_{j1} \exp(\Omega_j k_o x_3) \tag{52}$$

and from Equation 11

$$\hat{\phi}(x_3) = r_1 A_1 \sum_j \frac{r_{j1}}{\Omega_j} \exp(\Omega_j k_o x_3) \ , \ j = 1, 2, 3 \ . \tag{53}$$

E. Poynting Vector

On the basal plane of a hexagonal piezoelectric crystal, Equation 14 can be used to calculate the energy flow. The component of the Poynting vector in the x_1 direction, perpendicular to the propagation direction and the sagittal plane of the acoustic beam, will involve the elastic constants: C_{1111}, C_{1122}, C_{1133}, C_{1313}, C_{1331}, C_{1212}, and C_{1221}. The component in the x_2 direction, along the direction of propagation in the sagittal plane, will involve the elastic constants: C_{2222}, C_{2211}, C_{2233}, C_{2323}, C_{2332}, C_{2112}, and C_{2121}. The component along the x_3 direction will depend on the elastic constants: C_{3333}, C_{3311}, C_{3322},

C_{3223}, C_{3232}, C_{3131}, and C_{3113}. The Poynting vector calculations also require the various derivatives of U_1, U_2, and U_3 with respect to x_1, x_2, x_3, and t. The U_1, U_2, and U_3 particle displacements, listed in Appendix B, were obtained by evaluating Equations 37, 38, and 39, respectively. These series expressions are a function of r, ϕ, and x_3; the cylindrical variables defined in Figure 4. The following expression

$$U_{1,1} = \frac{\partial U_1}{\partial x_1} = \frac{\partial U_1}{\partial r}\frac{\partial r}{\partial x_1} + \frac{\partial U_1}{\partial \phi}\frac{\partial \phi}{\partial x_1} = \cos\phi\,\frac{\partial U_1}{\partial r} + \frac{\sin\phi}{r}\frac{\partial U_1}{\partial \phi} \tag{54}$$

illustrates the procedure used to calculate the various derivatives from these series expressions. The series expressions for the particle displacements and their derivatives were numerically evaluated with a Fortran computer program and then used to evaluate the Poynting vector.

Equation 14 gives the time-averaged energy flow per unit area in the x_1, x_2, and x_3 directions as a function of the depth, x_3. The integral

$$W_i = \int_{x_3=-\infty}^{0} P_i dx_3 \tag{55}$$

was used to obtain expressions for the time-averaged energy flow per unit width in the x_1 and x_2 directions. Since the expressions for U_1, U_2, and U_3 are separable, this was easily performed. Each of the seven components which compose the Poynting vector in a particular direction, will differ by a constant multiplier depending on whether one is calculating W_i or P_i at the surface. In general, the net value of W_i and P_i will not have the same functional dependence.

F. Series Validity and Convergence

The derivation of the relations listed in Appendix B for the particle displacements U_1, U_2, and U_3 required the product of two infinite series and the interchange of the summation of an infinite series with an integration of the terms in that series. According to Taylor (38) and Widder (39) these operations are valid if these series are uniformly convergent. According to the Weierstrass's M-test, these two series are uniformly convergent.

Evaluation of the Poynting vector, requires differentiating the infinite series for the particle displacements with respect to x_1, x_2, and x_3. In order for the derivative of an infinite series to be valid, the original series as well as that of the derivative must be uniformly convergent (39). Again all the derivatives are uniformly convergent.

III. NUMERICAL COMPUTATION

The Fortran computer programs used to evaluate the infinite series of the previous sections are listed in Appendix C. These computer programs were designed to perform the calculations in two different coordinate systems. One of the programs was designed to calculate the various particle displacements and their derivatives as well as the Poynting vector at distances far from the transducer along a path of constant radius as measured from the transducer. The other program was designed to perform these calculations along a straight line which could be in any direction on the surface of the crystal. Two programs were written because calculation of the Bessel functions of large arguments for many orders is the most time consuming and expensive part of the program. The "straight line" program was necessary for useful calculations near the transducer, but it requires a new set of Bessel function calculations at each point. The "constant radius" program requires only one set of Bessel function calculations for each value of the radius; this program yields useful information at large distances from the transducer.

Bessel functions of the first kind of integral order $J_n(x)$ have both positive and negative values when $n < x$, but for $n > x$ the values are all positive with magnitudes that decrease monotonically to zero as $n \to \infty$ for a fixed argument, x. According to Watson (40), when $n > 1.4\ x$

$$J_n(x) \sim \left(\frac{x}{2n} \right)^n n^{-\frac{1}{2}} \exp(n) \ . \tag{56}$$

This is the reason that the series expressions for U_1, U_2, and U_3 are convergent. This also means that the number of terms required to accurately evaluate the series for a particular particle displacement or its derivative depends on the location of the points, i.e., the magnitude of the argument, x.

Since we are evaluating an infinite series for the particle displacements and their derivatives, we must be concerned with the rapidity of convergence of these series. We need good accuracy and a minimum use of computer time. The series can be factored so that all terms which are a function of the transducer width and not a function of the field point's distance from the transducer can be evaluated and placed in storage for use as long as the transducer width remains fixed. If m is the number of terms included in the partial sum of a series, L the transducer width, and r the field point location, when $m \geq (3/2)k_oL$ and $k_oL \leq k_or$, the m+1 term of the series is less than 10^{-5} of the partial sum for those series which are alternating and less than 10^{-20} for those that do not alternate. The $J_m(k_oL)$ functions in the series are responsible for this convergence. When $k_or < k_oL$, the Bessel functions $J_m(k_or)$ influence the convergence. In this range, when $m \geq k_or + 30$, the m+1 term of the series is less than 10^{-10} of the partial sum. The Bessel functions used in these evaluations were calculated by recurrence techniques (41, 42).

IV. CALCULATED RESULTS

The series expressions for the particle displacements U_1, U_2, and U_3, and the various derivatives of these displacements $U_{1,1}$, $U_{1,2}$, ... were evaluated at various points and used to calculate the Poynting vector at these points. Plots of these quantities, Figures 5-119, see Appendix D, illustrate the important features of a nonuniform acoustic wave on the surface of a piezoelectric crystal that is transversely isotropic. The total transducer width is 20 λ_o($L = 10\ \lambda_o$) and the angular frequency is 6.2×10^7 rad./sec. for all plots. These figures are plots of the various quantities obtained from both the "straight line" and "polar" computer programs listed in Appendix C.

The straight line plots have the dimensionless variables $k_o x$ and $k_o y$ as their axes. The y coordinate is equivalent to x_2 and the x coordinate is equivalent to x_1 as indicated in Figure 1. Each "polar" plot was made at a fixed distance r from the transducer and calculated in terms of the dimensionless parameter $k_o r$. The transverse distance on these plots is a dimensionless variable which is a product of k_o and the distance from the x_2 axis along a path of constant radius. The magnitude is arbitrary on all these plots. Since each of the particle displacements, etc., is symmetrical with respect to the y axis, only half of each is plotted on these figures.

Figures 17-27 are straight line plots, parallel to the y axis, of U_1 with $k_o x$ equal to 1.0 and 50.0 respectively, and $k_o y$ ranging from 0 to 100.0. Figures 20-24 are straight line plots of U_1, parallel to the

x axis, with $k_o y$ equal to 1.0, 50.0, and 160.0 respectively, and $k_o x$ ranging from 0.0 to 100.0. Figures 24-27 are polar plots of U_1 with $k_o r$ equal to 400.0, 900.0, 2500.0, and 20,000.0 respectively, with the transverse variable ranging from 0.0 to 2000.0. These plots show that U_1 is small in comparison with U_2 and U_3. The particle displacement U_1 exhibits the largest values near the outer edge of the transducer. The magnitude of U_1 oscillates very rapidly near the aperture (near field region). This indicates a large amount of destructive interference. At large distances from the aperture (far field region), the various components of the angular spectrum interfere constructively and U_1 exhibits the same number of lobes as U_2 and U_3. In the far field all the lobes of U_1 appear to have nearly equal magnitudes. In the near field, the peak values of these lobes exhibit a large range of magnitudes.

Figures 5-16 are straight line and polar plots of the magnitude of the U_2 and U_3 particle displacement phasors. These plots are of the same type and cover the same ranges as those for U_1. Figure 5 reveals a large peak in U_2 and U_3 located at $k_o y$ approximately equal to seven transducer widths. Figure 14 indicates that this is a "narrow" peak; the width of the peak intensity region is less than half of the transducer width. Figures 5, 14, 15, and 16 show that U_2 and U_3 decrease as an inverse function of $(k_o r)^{\frac{1}{2}}$ in the far field region (beyond the peak) and that the side lobes are small in magnitude compared to the main lobe. Figures 6-14 indicate that the high intensity region, of the particle displacements U_2 and U_3, spreads little in the near field region (in front of the peak). This near field behavior is a result of destructive

interference due to phase differences between the components of the angular spectrum.

Figures 28-35 are straight line and polar plots of the phase of U_1, U_2, and U_3 versus the transverse distance from the y axis. Although no data is presented here, it was found that the phase decreases linearly with $k_o y$ for U_2 and U_3 in the main beam. As might be anticipated, the rate of decrease was 2π radians for each wavelength. This is true in both the near and far field regions. However, outside the main beam in the near field region, the phase retardation was nonlinear with $k_o y$ and not at the normal rate. The displacement U_1 exhibited no large regions of linear phase behavior at the normal rate. These phase plots show that U_2 and U_3 are in phase everywhere in the acoustic beam. In the near field region, these phase plots show that the phase varies rapidly with transverse position. This explains the large amount of constructive and destructive interference observed there. In the far field, one can recognize the phase shifts which are inherent in these lobe patterns. Figure 31 is a straight line phase plot. Figure 32 is a polar phase plot. Because of this they appear to exhibit a different functional behavior.

Figures 36-47 are straight line and polar plots of the absolute value of the y component of the integrated Poynting vector with arbitrary scaling. Figures 62-73 are plots of the absolute values of the various terms which compose this component of the integrated Poynting vector with arbitrary scaling. These plots demonstrate that the energy flux distribution is very complex. Figures 36, 44, 45, and 46 show that near

the transducer this component of the Poynting vector is negative. The negative regions are indicated by arrows directed downward adjacent to the curve. This component is positive in a narrow region less than one wavelength wide at the center of the beam. One must remember that the neglected evanescent waves will have their largest effect, if any, in this region of the beam. Also note that the side lobes carry a small percentage of the beam's energy, even in the far field. Figures 62-73 show that this component of energy flux is dominated by the C_{2332} term with the C_{2323}, C_{2222}, and C_{2233} terms making smaller but important contributions. The rest of the terms are insignificant everywhere.

Figures 44-55 are straight line and polar plots of the absolute value of the x component of the integrated Poynting vector with arbitrary scaling. Figures 74-85 are plots of the absolute value of the significant terms of this component of the integrated Poynting vector with arbitrary scaling. The negative regions are indicated by arrows directed downward. The only points where the x component of the energy flux density is larger than the y component occur in the near field region. This occurs at the edges of the region where the y component is negative. Note that the x component is zero along the y axis and a maximum at points where the derivatives of the particle displacements with respect to x are maximum. Figures 86-116 are plots of the magnitude and phase of these derivatives. Figures 74-85 show that the x component of energy flux is dominated by the C_{1331} term, with the C_{1122} and C_{1313} terms making a small contribution.

Figures 56-61 are straight line and polar plots of the x_3 component of the surface energy density with arbitrary scaling. Figures 117-119

are straight plots of this surface energy flux component in the y direction near the aperture. Figures 57-59 and 61 also include the y component of the surface energy density for reference. This x_3 component of energy flux is small compared to the other energy flux densities and is the most complex. Note that for a uniform Rayleigh wave, this component of energy flux is zero. While it is positive everywhere in the far field, it is negative at many points in the near field. Again the negative regions are indicated by arrows directed downward on the plots.

The plots of the y component of the integrated Poynting vector in the far field show that the 1/2 power points of the beam spread at an angle of 2.56° and show that the edge of the main lobe spreads at an angle of 5.72°, see Table 2. In the near field, the energy flux distribution is complex but shows little apparent spreading. The data in Table 2 also shows that the peak energy density in the main lobe and the first lobe is decreasing with distance from the transducer.

Table 2. Data from the polar plots of the y component of the integrated energy flux density

$k_o r$	value of main lobe maximum	value of first lobe maximum	location of min. between main and first lobe	location of first lobe maximum
20,000.0	$.189 \times 10^{20}$	$.889 \times 10^{18}$	1000.0	1500.0
15,000.0	$.252 \times 10^{20}$	---	750.0	---
5,000.0	$.746 \times 10^{20}$	$.375 \times 10^{19}$	250.0	355.0
2,500.0	$.140 \times 10^{21}$	$.890 \times 10^{19}$	125.0	175.0
900.0	$.270 \times 10^{21}$	$.127 \times 10^{20}$	90.0	107.5
650.0	$.245 \times 10^{21}$	$.286 \times 10^{20}$	65.0	75.0

V. CONCLUSIONS

The analysis presented here leads to a diffraction field in which the particle displacement has a major maximum about 150 acoustic wavelengths from a 20 wavelength wide transducer. This maximum distinguishes the far field region from the near field region. In the far field along the center of the main beam, the amplitude of the particle displacement varies inversely with distance from the transducer. The main lobe half-power points diverge at an angle of approximately 2.56°. The particle displacement in the first secondary lobe is less by approximately a factor of 4 and the energy density is more than an order of magnitude less than in the main lobe. The ratio of the displacement components U_2/U_3 is constant, and U_1 is small everywhere in the far field. The value of the Poynting vector is dominated by the C_{44} elastic component, and its direction and magnitude is consistent with the displacement lobe patterns described previously.

In the near field, close to the transducer, the ratio U_2/U_3 ceases to be constant, and U_1 is fairly large near the transducer edges. The behavior of the Poynting vector is quite complicated in this region, and there are, in fact, sub-regions where the time average energy flow is toward the transducer rather than away from it.

The radiation field described above is qualitatively consistent with the measurements of Cambon, Rouzeyre, and Simon (25) on a quartz substrate. The laser beam Brillouin diffraction technique used by them, measures the total particle displacement on the surface. Their measurements were performed on the surface of a quartz crystal which has a

small angular variation of the wave velocity. Their transducer was 15.6 acoustic wavelengths wide. The total displacement which they report appears to be consistent with those calculated here. Their peak appears to be located 171 wavelengths from the transducer.

As long as the amplitude ratios and phase differences between the major particle displacements for a surface acoustic wave remain fixed, detection schemes using lasers, electric field intensity or the electrostatic potential will yield useful information concerning the beam's energy distribution. Under these same conditions one can probably choose a meaningful parameter to use in scalar diffraction theories of the type developed by Kharusi and Farnell (22) even though the system's equations, Equations 5 and 6, are complex and these scalar theories ignore the coupling which exists between the various components of particle displacement.

VI. LITERATURE CITED

1. Stern, E. Microsound components, circuits and applications. Institute of Electrical and Electronics Engineers Transactions on Microwave Theory and Techniques MTT-17: 835-845. 1969.

2. Luukkala, M. and Kino, G. S. Convolution and time inversion using parametric interactions of acoustic surface waves. Applied Physics Letters 18: 393-394. 1971.

3. Wang, W. C. Singal generation via nonlinear interaction of oppositely directed sonic waves in piezoelectric semiconductors. Applied Physics Letters 18: 337-338. 1971.

4. Farnell, G. W. Properties of elastic surface waves. In Mason, W. P. and Thurston, R. N., eds. Physical Acoustics. Vol. 6. Pp. 109-166. New York, New York, Academic Press, Inc. 1970.

5. Campbell, J. J. and Jones, W. R. A method for estimating optimal crystal cuts and propagation directions for excitation of piezoelectric surface waves. Institute of Electrical and Electronics Engineers Transactions on Sonics and Ultrasonics SU-15: 209-217. 1968.

6. Bleustein, J. L. A new surface wave in piezoelectric materials. Applied Physics Letters 13: 412-413. 1968.

7. Musgrave, M. J. P. Crystal Acoustics. San Francisco, California, Holden-Day, Incorporated. 1970.

8. Koerber, G. Uncoupled piezoelectric surface-wave modes. Institute of Electrical and Electronics Engineers Transactions on Sonics and Ultrasonics SU-18: 73-78. 1971.

9. Tseng, C.-C. Piezoelectric surface waves in cubic orthorhombic crystals. Applied Physics Letters 16: 253-255. 1970.

10. Tseng, C.-C. Piezoelectric surface waves in cubic crystals. Journal of Applied Physics 41: 2270-2276. 1970.

11. Tseng, C.-C. and White, R. M. Propagation of piezoelectric and elastic surface waves on the basal plane of hexagonal piezoelectric crystals. Journal of Applied Physics 38: 4274-4280. 1967.

12. Tseng, C.-C. Propagation and amplification of surface elastic waves on hexagonal piezoelectric crystals. Ph.D. dissertation. Berkeley, California, Library, University of California-Berkeley. 1966.

13. Lim, T. C. and Farnell, G. W. Search for forbidden directions of elastic surface-wave propagation in anisotropic crystals. Journal of Applied Physics 39: 4319-4325. 1968.

14. Lim, T. C. and Farnell, G. W. Character of pseudo surface waves on anisotropic crystals. Journal of the Acoustical Society of America 45: 845-851. 1969.

15. Dransfeld, K. and Salzmann, E. Excitation, detection, and attenuation of high-frequency elastic surface waves. In Mason, W. P. and Thurston, R. N., eds. Physical Acoustics. Vol. 7. Pp. 219-272. New York, New York, Academic Press, Inc. 1970.

16. Havlice, J. F. Bond, W. L., and Wigton, L. B. "Elastic" Poynting vector in a piezoelectric medium. Institute of Electrical and Electronics Engineers Transactions on Sonics and Ultrasonics SU-17: 246-249. 1970.

17. Slobodnik, A. J., Jr., Carr, P. H., and Budreau, A. J. Microwave frequency acoustic surface-wave loss mechanism on $LiNbO_3$. Journal of Applied Physics 41: 4380-4387. 1970.

18. Reeder, T. M., Westbrook, E. M., and Winslow, P. K. Visualisation of surface acoustic waves. Electronics Letters 6: 30-32. 1970.

19. Cho, F. Y., Lawson, R. L., and Hunsinger, B. J. A note on the determination of the diffraction pattern of interdigital surface-wave devices. Institute of Electrical and Electronic Engineers Transactions of Sonics and Ultrasonics SU-17: 199-200. 1970.

20. Weglein, R. D., Pedinoff, M. E., and Winston, H. Diffraction spreading of surface waves on $LiNbO_3$. Electronics Letters 6: 654-656. 1970.

21. Kharusi, M. S., and Farnell, G. W. Diffraction and beam steering for surface-wave comb structures on anisotropic substrates. Institute of Electrical and Electronic Engineers Transactions on Sonics and Ultrasonics SU-18: 35-42. 1971.

22. Kharusi, M. S., and Farnell, G. W. Plane ultrasonic transducer diffraction fields in highly anisotropic crystals. Journal of the Acoustical Society of America 48: 665-670. 1970.

23. Slobodnik, A. J., Jr. Microwave acoustic surface wave investigations using laser light deflection. Proceedings of Institute of Electrical and Electronic Engineers 58: 488-490. 1970

24. Richardson, B. A., and Kino, G. S. Probing of elastic surface waves in piezoelectric media. Applied Physics Letters 16: 82-84. 1970.

25. Cambon, G., Rouzeyre, M., and Simon, G. Optical probing of surface Rayleigh waves. Applied Physics Letters 18: 295-298. 1971.

26. Hallermeier, R. J., and Walter, G. M. Scattering of a Gaussian light beam by reflection from attenuated surface waves. Institute of Electrical and Electronic Engineers Transactions on Sonics and Ultrasonics SU-18: 176-180. 1971.

27. Salzmann, E., and Weismann, D. Optical detection of Rayleigh waves. Journal of Applied Physics 40: 3408-3409. 1969.

28. Born, M., and Wolf, E. Principles of Optics. 4th ed. New York, New York, Pergamon Press. 1970.

29. Goodman, J. W. Introduction to Fourier Optics. New York, New York, McGraw-Hill Book Company. 1968.

30. Whittaker, E. T., and Watson, G. N. A Course of Modern Analysis. 4th ed. Cambridge, England, Cambridge University Press. 1927.

31. Lalor, E. Conditions for the validity of the angular spectrum of plane waves. Journal of the Optical Society of America 58: 1235-1237. 1968.

32. Stratton, J. A. Electromagnetic Theory. New York, New York, McGraw-Hill Book Company, Inc. 1941.

33. Cohen, M. G. Optical study of ultrasonic diffraction and focusing in anisotropic media. Journal of Applied Physics 38: 3821-3828. 1967.

34. Bracewell, R. M. The Fourier Transform and Its Applications. New York, New York, McGraw-Hill Book Company, Inc. 1965.

35. Titchmarsh, E. C. Introduction to the Theory of Fourier Integrals. Oxford, England, Clarendon Press. 1937.

36. Olver, F. W. J. Bessel functions of integer order. In Abramowitz, M. and Stegun, I. A., eds. Handbook of Mathematical Functions with Formulas, Graphs, and Mathematical Tables. Pp. 355-433. Washington, D. C., U. S. Government Printing Office. 1964.

37. Dwight, H. B. Tables of Integrals and Other Mathematical Data. 4th ed. New York, New York, The Macmillan Company. 1961.

38. Taylor, A. E. Advanced Calculus. New York, New York, Ginn and Company. 1955.

39. Widder, D. V. Advanced Calculus. 2nd ed. Englewood Cliffs, New Jersey, Prentice-Hall, Inc. 1961.

40. Watson, G. N. A Treatise on the Theory of Bessel Functions. 2nd ed. Cambridge, England, University Press. 1952.

41. Goldstein, M., and Thaler, R. M. Recurrence techniques for the calculations of Bessel functions. Mathematical Tables and Aids to Computation 13: 102-108. 1959.

42. Stegun, I. A., and Abramowitz, M. Generation of Bessel functions on high speed computers. Mathematical Tables and Aids to Computation 11: 255-257. 1957.

VII. ACKNOWLEDGEMENTS

The author wishes to express his appreciation to Dr. G. G. Koerber for his suggestion of this topic and for his help and guidance throughout this research.

VIII. APPENDIX A

This is an inductive proof that

$$\frac{\sin n\theta}{\sin \theta} = 1 + 2 \sum_{m=1}^{m = \frac{(n-1)}{2}} \cos 2m\theta \ , \tag{A-1}$$

for odd integers n where $n \geq 3$. When $n = 3$, several trigonometric identities from Dwight (37), can be used to reduce Equation A-1 to

$$\frac{\sin 3\theta}{\sin \theta} = 1 + 2 \cos 2\theta \ ,$$

when $n = 5$, one can obtain

$$\frac{\sin 5\theta}{\sin \theta} = 1 + 2 \cos 2\theta + 2 \cos 4\theta \ .$$

So Equation A-1 holds for $n = 3$ and 5. Suppose Equation A-1 holds for any odd positive integer k, so that

$$\frac{\sin k\theta}{\sin \theta} = 1 + 2 \cos 2\theta + \cdots + 2 \cos (k-5)\theta + 2 \cos (k-3)\theta + 2 \cos (k-1)\theta \ . \tag{A-2}$$

Then Equation A-1 also holds for $n = k + 2$, since

$$\frac{\sin(k+2)\theta}{\sin \theta} = 1 + 2 \cos 2\theta + \cdots + 2 \cos (k-3)\theta + 2 \cos (k-1)\theta + 2 \cos (k+1)\theta \ . \tag{A-3}$$

Now using Equation A-2, Equation A-3 can be written

$$\frac{\sin(k+2)\theta}{\sin\theta} = \frac{\sin k\theta}{\sin\theta} + 2\cos(k+1)\theta \ . \tag{A-4}$$

Equation A-4 can be rearranged as follows

$$\sin(k+2)\theta - \sin k\theta = 2\sin\theta \ \cos(k+1)\theta \ . \tag{A-5}$$

Two trigonometric identities can be used to write

$$\sin(k+2)\theta = \sin k\theta \ \cos 2\theta + \cos k\theta \ \sin 2\theta$$

and

$$\cos(k+1)\theta = \cos k\theta \ \cos\theta - \sin k\theta \ \sin\theta \ .$$

If one substitutes these equations into Equation A-5, some rearrangement yields

$$(\cos 2\theta - 1)\sin k\theta + \cos k\theta \ \sin 2\theta = 2\cos k\theta \ \cos\theta \ \sin\theta$$
$$- 2\sin k\theta \ \sin^2\theta \ . \tag{A-6}$$

The trigonometric identities $\cos 2\theta - 1 = -2\sin^2\theta$ and $2\cos\theta\sin\theta = \sin 2\theta$ can be used to reduce Equation A-6 to an identity. Therefore, Equation A-1 holds for all odd integers when n is greater than 3.

IX. APPENDIX B

This Appendix lists the infinite series expressions which were derived for the particle displacement phasors.

$$U_1 = \frac{M\,\hat{u}_2(x_3)\exp[-j\omega t]}{\pi}\,(U\,1\,RE + j\,U\,1\,IM)$$

where

$$U\,1\,RE = \sum_{n=1}^{\infty} G_1(n,k_oL)J_{2n}(k_or)\sin 2n\phi$$

$$U\,1\,IM = \sum_{n=0}^{\infty} (-1)^n F_1(n,k_oL)J_{2n+1}(k_or)\cos(2n+1)\phi$$

$$G_1(n,k_oL) = -\pi\,[J_{2n-1}(k_oL) + J_{2n+1}(k_oL)]$$

$$F_1(n,k_oL) = -8\sum_{m=0}^{\infty} \frac{(-1)^m[(2n+1)^2 + 4m(m+1)]}{[(2n+1)^2 - 4m^2][(2n+1)^2 - 4(m+1)^2]} J_{2m+1}(k_oL)$$

$$U_2 = \frac{M\,\hat{u}_2(x_3)\exp[-j\omega t]}{\pi}\,(U\,2\,RE + j\,U\,2\,IM)$$

where

$$U\,2\,RE = D_2(k_oL)J_o(k_or) + \sum_{n=1}^{\infty} G_2(n,k_oL)J_{2n}(k_or)\cos 2n\phi$$

$$U\,2\,IM = \sum_{n=0}^{\infty} (-1)^{n+1} F_2(n,k_oL)J_{2n+1}(k_or)\sin(2n+1)\phi$$

$$D_2(k_oL) = \pi \left[\sum_{m=0}^{\infty} J_{2m+1}(k_oL) + \sum_{m=1}^{\infty} J_{2m+1}(k_oL) \right]$$

$$G_2(n,k_oL) = \pi \left[J_{2n-1}(k_oL) + 3J_{2n+1}(k_oL) + 4 \sum_{m=n}^{\infty} J_{2m+3}(k_oL) \right]$$

$$F_2(n,k_oL) = \frac{16}{(2n+1)[(2n+1)^2-4]} \sum_{\ell=0}^{\infty} J_{2\ell+1}(k_oL)$$

$$- \sum_{m=1}^{\infty} \left(\frac{(-1)^{m+1}\, 32(2n+1)\, [(2n+1)^2+4(3m^2-1)]}{[(2n+1)^2-4(m-1)^2][(2n+1)^2-4m^2][(2n+1)^2-4(m+1)^2]} \right.$$

$$\left. \cdot \sum_{\ell=m}^{\infty} J_{2\ell+1}(k_oL) \right)$$

$$U_3 = \frac{M\, \hat{u}_3(x_3)\exp[-j\omega t]}{\pi} (U3RE + j\,U3IM)$$

$$U3RE = D_3(k_oL)J_o(k_or) + \sum_{n=1}^{\infty} (-1)^n F_3(n,k_oL)J_{2n}(k_or)\cos 2n\phi$$

$$U3IM = \sum_{n=0}^{\infty} G_3(n,k_oL)J_{2n+1}(k_or)\sin(2n+1)\phi$$

$$D_3(k_oL) = 4 \sum_{\ell=0}^{\infty} J_{2\ell+1}(k_oL) + \sum_{m=1}^{\infty} \left(\frac{8(-1)^{m+1}}{(2m+1)(2m-1)} \sum_{\ell=m}^{\infty} J_{2\ell+1}(k_oL) \right)$$

$$G_3(n,k_oL) = 2\pi\left[\sum_{\ell=n}^{\infty} J_{2\ell+1}(k_oL) + \sum_{\ell=n+1}^{\infty} J_{2\ell+1}(k_oL)\right]$$

$$F_3(n,k_oL) = \frac{-8}{(4n^2-1)} \sum_{\ell=0}^{\infty} J_{2\ell+1}(k_oL) + 16 \sum_{m=1}^{\infty} \left(\frac{(-1)^{m+1}[4n^2+4m^2-1]}{[4n^2-(2m-1)^2][4n^2-(2m+1)^2]} \cdot \sum_{\ell=m}^{\infty} J_{2\ell+1}(k_oL) \right)$$

X. APPENDIX C

The first eight pages contain the main program for the "straight line" calculations and several subroutines which are called only by this program. The next seven pages contain the main program for the polar calculations and several of the subroutines which are called only by this program. The last ten pages contain subroutines which are called by both main programs.

The subroutine SERSUM (MAB, ATHETA, BKR) performs a double precision evaluation of the series for the particle displacements U_1, U_2, U_3 and the derivatives $U_{1,1}$, $U_{1,2}$, ... at a particular point described by ATHETA and BKR. It uses these values to calculate the Poynting vector at this same point. All the data is transmitted into and out of this subroutine through common blocks. MAB is the number of terms included in the series summation.

The subroutine COEFF (BL, MAC, MAL) calculates the values of the coefficients in the infinite series whose value depends on the transducer width. This information is provided to SERSUM by the common block S. The subroutine DOEF (BL, MAC) can be used to read this information into the common block S from cards.

The subroutine RECFP (X,N) generates the Bessel functions used by COEFF and SERSUM through the common block V.

The subroutine ELACNT (WOM) provides the material constants needed for the Poynting vector calculations. The PHASE subroutine calculates the phase angle of the phasors generated by SERSUM.

The subroutine RANG (BNX, BNY, BKR, MAF) of the straight line program calculates the cylindrical coordinates of the point under investigation and determines the number of terms to be included in the series summation. The subroutine ITRPZW (XA, XB, KXA, KXB, E) performs a trapezoidal integration of the energy density. The subroutines TAWR (MB, MC, MAF, SCA, BMP) and EVAL (BKR, N) choose the points to be investigated, form the arrays, perform the write statements, and calculate the magnitude and angles of the various phasors.

The subroutine RANG1 (BNX, BNY, BMD, MAF) of the polar program calculates the cylindrical coordinates of the points to be investigated and determines the number of terms to be included in the summation. The subroutine EVAL2 (MB) performs the same duties as TWAR and EVAL of the straight line program.

```
0001          DIMENSION X(200),XL(5),YL(5),GL(5),DATL(5)
0002          COMMON/W/U1MG(200),V1MG(200),U1AN(200),V1AN(200),U2MG(200),V2MG(20
             10),U2AN(200),V2AN(200),U3MG(200),V3MG(200),U3AN(200),V3AN(200),DM1
             21(200),VM11(200),DA11(200),VA11(200),DM12(200),VM12(200),DA12(200)
             3,VA12(200),DM21(200),VM21(200),DA21(200),VA21(200),DM22(200),VM22(
             4200),DA22(200),VA22(200),DM31(200),VM31(200),DA31(200),VA31(200),
             5DM32(200),VM32(200),DA32(200),VA32(200)
0003          COMMON/AB/P1(200),V1(200),P2(200),V2(200),P3(200),V3(200),W1(200),
             1Y1(200),W2(200),Y2(200),W3(200),Y3(200)
0004          COMMON/AD/SP1(200,7,2),SP2(200,7,2),D8(200),D9(200),D10(200),
             1 D11(200),D12(200),D13(200),D14(200),TW1(200,7),D1(200),D2(200),
             2 D3(200),D4(200),D5(200),D6(200),D7(200),TW2(200,7)
0005          WOM=6.2E07
0006          CALL ELACNT(WOM)
0007          MAF=170
0008          CALL DOEF(BL,MAF)
0009          CALL TAWR(MB,MC,MAF,SCA,BMP)
0010          DO 50 I=MB,MC
0011          X(I)=I*SCA+BMP
0012       50 CONTINUE
0013          NAN=MC
0014          READ(5,100) XL,YL,GL,DATL
0015          CALL GRAPH(NAN,X,  W1,3,  7,5.5,-7.,0.,0.,0.,0.,XL,YL,GL,DATL)
0016          READ(5,100) XL,YL,GL,DATL
0017          CALL GRAPH(NAN,X,  W2,3,  7,5.5,-7.,0.,0.,0.,0.,XL,YL,GL,DATL)
0018          READ(5,100) XL,YL,GL,DATL
0019          CALL GRAPH(NAN,X,  P3,3,  7,5.5,-7.,0.,0.,0.,0.,XL,YL,GL,DATL)
0020          READ(5,100) DATL
0021          CALL GRAPH(NAN,X,  P2,4,107,0.0,0.0,0.,0.,0.,0.,0.,0.,DATL)
0022          READ(5,100) XL,YL,GL,DATL
0023          CALL GRAPH(NAN,X,U1AN,3,  7,5.5, 7.,0.,0.,0.,0.,XL,YL,GL,DATL)
0024          READ(5,100) DATL
0025          CALL GRAPH(NAN,X,U2AN,4,107,0.,0.,0.,0.,0.,0.,0.,0.,0.,DATL)
```

```
0026          READ(5,100) DATL
0027          CALL GRAPH(NAN,X,U3AN,7,107,0.,0.,0.,0.,0.,0.,0.,0.,0.,DATL)
0028          READ(5,100) XL,YL,GL,DATL
0029          CALL GRAPH(NAN,X,U1MG,3,  7,5.5, 7.,0.,0.,0.,0.,XL,YL,GL,DATL)
0030          READ(5,100) XL,YL,GL,DATL
0031          CALL GRAPH(NAN,X,U2MG,3,  7,5.5, 7.,0.,0.,0.,0.,XL,YL,GL,DATL)
0032          READ(5,100) DATL
0033          CALL GRAPH(NAN,X,U3MG,4,107,0.,0.,0.,0.,0.,0.,0.,0.,0.,DATL)
0034          READ(5,100) XL,YL,GL,DATL
0035          CALL GRAPH(NAN,X,DM22,3,  7,5.5, 7.,0.,0.,0.,0.,XL,YL,GL,DATL)
0036          READ(5,100) DATL
0037          CALL GRAPH(NAN,X,DM32,9,107,0.,0.,0.,0.,0.,0.,0.,0.,0.,DATL)
0038          READ(5,100) XL,YL,GL,DATL
0039          CALL GRAPH(NAN,X,DM12,3,  7,5.5, 7.,0.,0.,0.,0.,XL,YL,GL,DATL)
0040          READ(5,100) DATL
0041          CALL GRAPH(NAN,X,DM11,9,107,0.,0.,0.,0.,0.,0.,0.,0.,0.,DATL)
0042          READ(5,100) XL,YL,GL,DATL
0043          CALL GRAPH(NAN,X,DM21,3,  7,5.5, 7.,0.,0.,0.,0.,XL,YL,GL,DATL)
0044          READ(5,100) DATL
0045          CALL GRAPH(NAN,X,DM31,5,107,0.,0.,0.,0.,0.,0.,0.,0.,0.,DATL)
0046          READ(5,100) XL,YL,GL,DATL
0047          CALL GRAPH(NAN,X,DA11,3,  7,5.5, 7.,0.,0.,0.,0.,XL,YL,GL,DATL)
0048          READ(5,100) DATL
0049          CALL GRAPH(NAN,X,DA22,4,107,0.0,0.0,0.,0.,0.,0.,0.,0.,0.,DATL)
0050          READ(5,100) XL,YL,GL,DATL
0051          CALL GRAPH(NAN,X,  Y1,3,  7,5.5,-7.,0.,0.,0.,0.,XL,YL,GL,DATL)
0052          READ(5,100) DATL
0053          CALL GRAPH(NAN,X,  Y2,9,107,0.0,0.0,0.,0.,0.,0.,0.,0.,0.,DATL)
0054          READ(5,100) XL,YL,GL,DATL
0055          CALL GRAPH(NAN,X,  V3,3,  7,5.5,-7.,0.,0.,0.,0.,XL,YL,GL,DATL)
0056          READ(5,100) XL,YL,GL,DATL
0057          CALL GRAPH(NAN,X,V1MG,3,  7,5.5, 7.,0.,0.,0.,0.,XL,YL,GL,DATL)
0058          READ(5,100) XL,YL,GL,DATL
0059          CALL GRAPH(NAN,X,V2MG,3,  7,5.5, 7.,0.,0.,0.,0.,XL,YL,GL,DATL)
0060          READ(5,100) DATL
0061          CALL GRAPH(NAN,X,V3MG,4,107,0.,0.,0.,0.,0.,0.,0.,0.,0.,DATL)
```

```
0062          100 FORMAT(20A4)
0063              STOP
0064              END
```

```
      SUBROUTINE TAWR(MB,MC,MAF,SCA,BMP)
      COMMON/W/U1MG(200,2),U1AN(200,2),U2MG(200 ,2),U2AN(200,2),U3MG(
     1 200,2),U3AN(200,2),DM11(200,2),DA11(200,2),DM12(200,2),DA12(200,
     2 2),DM21(200,2),DA21(200,2),DM22(200,2),DA22(200,2),DM31(200,2),
     3 DA31(200,2),DM32(200,2),DA32(200,2)
      COMMON/AB/P1(200,2),P2(200,2),P3(200,2),W1(200,2),W2(200,2),
     2 W3(200,2)
     3 /AD/SP1(200,7,2),SP2(200,7,2),TW1(200,7,2),TW2(200,7,2)
      READ(5,10) MB,MC,BNY,BMP,SCA
   10 FORMAT(2(6X,I4)/3(4X,E16.8))
      WRITE(6,15) MB,MC,BMP,SCA
   15 FORMAT(11X,3HMB=I3/11X,3HMC=I3/11X,4HBMP=E16.8/11X,4HSCA=E16.8)
      DO 100 NX=MB,MC
      BNX=NX*SCA
      BNX = BNX + BMP
      CALL RANG(BNX,BNY,BKR,MAF)
      WRITE(6,136) BKR,BNX,BNY
  136 FORMAT(///7X,3HBKR,15X,3HBNX,15X,3HBNY//3E18.8/)
      CALL EVAL(BKR,NX)
  100 CONTINUE
      WRITE(6,85) ((NA,NB,U1MG(NA,NB),U1AN(NA,NB),U2MG(NA,NB),U2AN(NA,
     1 NB),U3MG(NA,NB),U3AN(NA,NB),NA=MB,MC),NB=1,2)
      WRITE(6,88) ((NA,NB,DM11(NA,NB),DA11(NA,NB),DM12(NA,NB),DA12(NA,NB
     1 ),DM21(NA,NB),DA21(NA,NB),NA=MB,MC),NB=1,2)
      WRITE(6,90) ((NA,NB,DM22(NA,NB),DA22(NA,NB),DM31(NA,NB),DA31(NA,NB
     1 ),DM32(NA,NB),DA32(NA,NB),NA=MB,MC),NB=1,2)
      WRITE(6,20) ((NA,NB,P1(NA,NB),W1(NA,NB),P2(NA,NB),W2(NA,NB),
     1 P3(NA,NB),W3(NA,NB),NA=MB,MC),NB=1,2)
      WRITE(6,30) (((NA,NB,NC,SP1(NA,NB,NC),TW1(NA,NB,NC),SP2(NA,NB,NC),
     1TW2(NA,NB,NC),NA=MB,MC),NB=1,7),NC=1,2)
   85 FORMAT(1H1,4X,2HNA,4X,2HNB,5X,11HU1MG(NA,NB),6X,11HU1AN(NA,NB),
     1 6X,11HU2MG(NA,NB),6X,11HU2AN(NA,NB),6X,11HU3MG(NA,NB),5X,12H U3AN
     2(NA,NB)//(1H ,2I6,6E17.7))
   88 FORMAT(1H1,4X,2HNA,4X,2HNB,5X,11HDM11(NA,NB),6X,11HDA11(NA,NB),
     1 6X,11HDM12(NA,NB),6X,11HDA12(NA,NB),6X,11HDM21(NA,NB),5X,12H DA21
     2(NA,NB)//(1H ,2I6,6E17.7))
```

```
90 FORMAT(1H1,4X,2HNA,4X,2HNB,5X,11HDM22(NA,NB),6X,11HDA22(NA,NB),
  1 6X,11HDM31(NA,NB),6X,11HDA31(NA,NB),6X,11HDM32(NA,NB),5X,12H DA32
  2(NA,NB)//(1H ,2I6,6E17.7))
20 FORMAT(1H1,4X,2HNA,4X,2HNB,6X,9HP1(NA,NB),8X,9HW1(NA,NB),8X,9HP2(N
  1A,NB),8X,9HW2(NA,NB),8X,9HP3(NA,NB),8X,9HW3(NA,NB)//(1H ,2I6,
  2 6E17.7))
30 FORMAT(1H1,4X,2HNA,4X,2HNB,4X,2HNC,2X,13HSP1(NA,NB,NC),4X,13HTW1(N
  1A,NB,NC),4X,13HSP2(NA,NB,NC),4X,13HTW2(NA,NB,NC)//(1H ,3I6,4E17.7)
  2)
   RI=MB*SCA
   RX=MC*SCA
   CALL ITRPZW(RI,RX,MB,MC,W21)
   WRITE(6,40) W21
40 FORMAT(1H1/////1H ,4HW21= E17.7)
   NC=1
   DO 50 NA=MB,MC
   DO 50 NB=1,7
   TW1(NA,NB,NC)=ALOG10(ABS(TW1(NA,NB,NC)))
   TW2(NA,NB,NC)=ALOG10(ABS(TW2(NA,NB,NC)))
50 CONTINUE
   DO 60 NA=MB,MC
   DO 60 NB=1,2
   W1(NA,NB)=ALOG10(ABS(W1(NA,NB)))
   W2(NA,NB)=ALOG10(ABS(W2(NA,NB)))
   P3(NA,NB)=ALOG10(ABS(P3(NA,NB)))
60 CONTINUE
   RETURN
   END
```

```
      SUBROUTINE EVAL(BKR,N)
      COMMON/W/U1MG(200,2),U1AN(200,2),U2MG(200 ,2),U2AN(200,2),U3MG(
     1 200,2),U3AN(200,2),DM11(200,2),DA11(200,2),DM12(200,2),DA12(200,
     2 2),DM21(200,2),DA21(200,2),DM22(200,2),DA22(200,2),DM31(200,2),
     3 DA31(200,2),DM32(200,2),DA32(200,2)
      COMMON/AB/P1(200,2),P2(200,2),P3(200,2),W1(200,2),W2(200,2),
     2 W3(200,2)
     3 /AD/SP1(200,7,2),SP2(200,7,2),TW1(200,7,2),TW2(200,7,2)
      COMMON/U/ANG(2),MAE,MAB
      COMMON/R/TEMP,TEMB,TEMC,TEMD,TEME,TEMF,TR11,TI11,TR12,TI12,TR21,
     2 TI21,TR22,TI22,TR31,TI31,TR32,TI32,F1,F2,CJ(14),DJ(14),D1,D2,
     3 F3,D3
      MAC=MAB+2
      CALL RECFP(BKR,MAC)
      DO 50 M=1,MAE
      CALL SERSUM(MAB,ANG(M),BKR)
      U1MG(N,M)=SQRT(TEMP**2+TEMB**2)
      U2MG(N,M)=SQRT(TEMC**2+TEMD**2)
      U3MG(N,M)=SQRT(TEME**2+TEMF**2)
      DM11(N,M)=SQRT(TR11**2+TI11**2)
      DM12(N,M)=SQRT(TR12**2+TI12**2)
      DM21(N,M)=SQRT(TR21**2+TI21**2)
      DM22(N,M)=SQRT(TR22**2+TI22**2)
      DM31(N,M)=SQRT(TR31**2+TI31**2)
      DM32(N,M)=SQRT(TR32**2+TI32**2)
      CALL PHASE(TEMP,TEMB,AP,U1AN(N,M))
      CALL PHASE(TEMC,TEMD,AP,U2AN(N,M))
      CALL PHASE(TEME,TEMF,AP,U3AN(N,M))
      CALL PHASE(TR11,TI11,AP,DA11(N,M))
      CALL PHASE(TR12,TI12,AP,DA12(N,M))
      CALL PHASE(TR21,TI21,AP,DA21(N,M))
      CALL PHASE(TR22,TI22,AP,DA22(N,M))
```

```
      CALL PHASE(TR31,TI31,AP,DA31(N,M))
      CALL PHASE(TR32,TI32,AP,DA32(N,M))
      P1(N,M)=F1
      P2(N,M)=F2
      P3(N,M)=F3
      W1(N,M)=D1
      W2(N,M)=D2
      W3(N,M)=D3
      DO 50 I=1,7
      KI=I+7
      SP1(N,I,M)=-CJ(KI)
      SP2(N,I,M)=-CJ(I)
      TW1(N,I,M)=-DJ(KI)
      TW2(N,I,M)=-DJ(I)
   50 CONTINUE
      RETURN
      END
```

```
      SUBROUTINE ITRPZW(XA,XB,KXA,KXB,E)
C     SUBROUTINE FOR TRAPEZOIDAL INTERGRATION
      COMMON/AB/Z(1600),Y(200),X(600)
      ITER=KXB-KXA
      HITER=ITER
      DX=(XB-XA)/HITER
      E=9.*Y(KXA)+28.*Y(KXA+1)+23.*Y(KXA+2)
      MITER=ITER-3
      DO 100 I=3,MITER
      KI=KXA+I
  100 E=E+Y(KI)
      E=(E+9.*Y(KXB)+28.*Y(KXB-1)+23.*Y(KXB-2))*DX/24.
      RETURN
      END
```

```
      SUBROUTINE RANG(BNX,BNY,BKR,MAF)
      COMMON/U/ANG(2),MD,MAD
      MD=2
      BKR=SQRT(BNX**2+BNY**2)
      BK=BKR+35.
      BL1=MAF-4
      MAD=MIN1(BL1,BK)
      IF(BNX) 5,5,8
    5 ANG(1)=1.570796
      ANG(2)=1.0E-6
      GO TO 9
    8 ANG(1)=ATAN(BNY/BNX)
      ANG(2)=1.5707963-ANG(1)
    9 RETURN
      END
```

```
0001          DIMENSION X(300),XL(5),YL(5),GL(5),DATL(5)
0002          COMMON/AB/DM11(300),DA11(300),DM12(300),DA12(300),DM21(300),
             1 DA21(300),DM22(300),DA22(300),DM31(300),DA31(300),DM32(300),
             2 DA32(300),U3AN(300),U1MG(300),U2MG(300),U3MG(300),U1AN(300),
             3 U2AN(300)
0003          COMMON/T/P1(300),P2(300),W1(300),W2(300),P3(300),W3(300)
             2/V20/BKR,M,NAN,SCA
0004          COMMON
             1/TV/C1(300),C2(300),C3(300),C4(300),C5(300),C6(300),C7(300),
             2C8(300),C9(300),C10(300),C11(300),C12(300),C13(300),C14(300),
             3D1(300),D2(300),D3(300),D4(300),D5(300),D6(300),D7(300),
             4D8(300),D9(300),D10(300),D11(300),D12(300),D13(300),D14(300)
0005          WOM=6.2E07
0006          CALL ELACNT(WOM)
0007          MAF=182
0008          CALL DOEF(BL,MAF)
0009          WRITE(6,35) MAF,BL
0010       35 FORMAT(10X,4HMAF=,I4//10X,3HBL= E17.7)
0011          READ(5,40) BKR,BNX,BMD,SCA
0012       40 FORMAT(14X,E16.8)
0013          CALL RANG1(BNX,BNY,BMD,MAF)
0014          WRITE(6,15) BNY,BNX,BKR
0015       15 FORMAT(//23X,3HBNY,13X,3HBNX,13X,3HBKR//(10X,3E16.8))
0016          WRITE(6,75) NAN,SCA
0017       75 FORMAT(10X,4HNAN=I5/10X,4HSCA= E16.8)
0018          MB= 1
0019          CALL EVAL2(MB)
0020          DO 50 I=MB,NAN
0021          X(I)=(I-1)*SCA
0022       50 CONTINUE
0023          READ(5,100) XL,YL,GL,DATL
0024          CALL GRAPH(NAN,X,  W1,3,  7,5.5,-7.,0.,0.,0.,0.,XL,YL,GL,DATL)
0025          READ(5,100) XL,YL,GL,DATL
0026          CALL GRAPH(NAN,X,  W2,3,  7,5.5,-7.,0.,0.,0.,0.,XL,YL,GL,DATL)
```

```
      READ(5,100) XL,YL,GL,DATL
      CALL GRAPH(NAN,X,  P3,3,  7,5.5,-7.,0.,0.,0.,0.,XL,YL,GL,DATL)
      READ(5,100) XL,YL,GL,DATL
      CALL GRAPH(NAN,X,U1AN,3,  7,5.5, 7.,0.,0.,0.,0.,XL,YL,GL,DATL)
      READ(5,100) DATL
      CALL GRAPH(NAN,X,U2AN,4,107,0.,0.,0.,0.,0.,0.,0.,0.,0.,DATL)
      READ(5,100) DATL
      CALL GRAPH(NAN,X,U3AN,7,107,0.,0.,0.,0.,0.,0.,0.,0.,0.,DATL)
      READ(5,100) XL,YL,GL,DATL
      CALL GRAPH(NAN,X,U1MG,3,  7,5.5, 7.,0.,0.,0.,0.,XL,YL,GL,DATL)
      READ(5,100) XL,YL,GL,DATL
      CALL GRAPH(NAN,X,U2MG,3,  7,5.5, 7.,0.,0.,0.,0.,XL,YL,GL,DATL)
      READ(5,100) DATL
      CALL GRAPH(NAN,X,U3MG,4,107,0.,0.,0.,0.,0.,0.,0.,0.,0.,DATL)
      READ(5,100) XL,YL,GL,DATL
      CALL GRAPH(NAN,X,DM22,3,  7,5.5, 7.,0.,0.,0.,0.,XL,YL,GL,DATL)
      READ(5,100) DATL
      CALL GRAPH(NAN,X,DM32,9,107,0.,0.,0.,0.,0.,0.,0.,0.,0.,DATL)
      READ(5,100) XL,YL,GL,DATL
      CALL GRAPH(NAN,X,DM12,3,  7,5.5, 7.,0.,0.,0.,0.,XL,YL,GL,DATL)
      READ(5,100) DATL
      CALL GRAPH(NAN,X,DM11,9,107,0.,0.,0.,0.,0.,0.,0.,0.,0.,DATL)
      READ(5,100) XL,YL,GL,DATL
      CALL GRAPH(NAN,X,DM21,3,  7,5.5, 7.,0.,0.,0.,0.,XL,YL,GL,DATL)
      READ(5,100) DATL
      CALL GRAPH(NAN,X,DM31,5,107,0.,0.,0.,0.,0.,0.,0.,0.,0.,DATL)
      READ(5,100) XL,YL,GL,DATL
      CALL GRAPH(NAN,X,DA11,3,  7,5.5, 7.,0.,0.,0.,0.,XL,YL,GL,DATL)
      READ(5,100) DATL
      CALL GRAPH(NAN,X,DA22,4,107,0.0,0.0,0.,0.,0.,0.,0.,0.,0.,DATL)
      READ(5,100) XL,YL,GL,DATL
      CALL GRAPH(NAN,X,  D1,3,  7,5.5,-8.,0.,0.,0.,0.,XL,YL,GL,DATL)
      READ(5,100) DATL
      CALL GRAPH(NAN,X,  D2,4,107,0.0,0.0,0.,0.,0.,0.,0.,0.,0.,DATL)
      READ(5,100) DATL
      CALL GRAPH(NAN,X,  D3,5,107,0.0,0.0,0.,0.,0.,0.,0.,0.,0.,DATL)
```

```
      READ(5,100) XL,YL,GL,DATL
      CALL GRAPH(NAN,X,  D4,3,  7,5.5,-7.,0.,0.,0.,0.,XL,YL,GL,DATL)
      READ(5,100) DATL
      CALL GRAPH(NAN,X,  D5,4,107,0.0,0.0,0.,0.,0.,0.,0.,0.,0.,DATL)
      READ(5,100) DATL
      CALL GRAPH(NAN,X,  D7,5,107,0.0,0.0,0.,0.,0.,0.,0.,0.,0.,DATL)
      READ(5,100) XL,YL,GL,DATL
      CALL GRAPH(NAN,X,  D8,3,  7,5.5,-7.,0.,0.,0.,0.,XL,YL,GL,DATL)
      READ(5,100) DATL
      CALL GRAPH(NAN,X,  D9,4,107,0.0,0.0,0.,0.,0.,0.,0.,0.,0.,DATL)
      READ(5,100) DATL
      CALL GRAPH(NAN,X, D10,5,107,0.0,0.0,0.,0.,0.,0.,0.,0.,0.,DATL)
      READ(5,100) XL,YL,GL,DATL
      CALL GRAPH(NAN,X, D11,3,  7,5.5,-7.,0.,0.,0.,0.,XL,YL,GL,DATL)
      READ(5,100) DATL
      CALL GRAPH(NAN,X, D12,4,107,0.0,0.0,0.,0.,0.,0.,0.,0.,0.,DATL)
      READ(5,100) DATL
      CALL GRAPH(NAN,X, D14,5,107,0.0,0.0,0.,0.,0.,0.,0.,0.,0.,DATL)
  100 FORMAT(20A4)
      STOP
      END
```

```
      SUBROUTINE EVAL2(MB)
      COMMON/AB/DM11(300),DA11(300),DM12(300),DA12(300),DM21(300),
     1 DA21(300),DM22(300),DA22(300),DM31(300),DA31(300),DM32(300),
     2 DA32(300),U3AN(300),U1MG(300),U2MG(300),U3MG(300),U1AN(300),
     3 U2AN(300)
      DOUBLE PRECISION BJ
      COMMON /V/BJ(201)
      COMMON/R/TEMP,TEMB,TEMC,TEMD,TEME,TEMF,TR11,TI11,TR12,TI12,TR21,
     2 TI21,TR22,TI22,TR31,TI31,TR32,TI32,F1,F2,CJ(14),DJ(14),D1,D2,
     3F3,D3
      COMMON/T/P1(300),P2(300),W1(300),W2(300),P3(300),W3(300)
     2/TV/SP2(300,7),SP1(300,7),TW2(300,7),TW1(300,7)
      COMMON/V20/BKR,MAB,MAE,SCA/U/ANG(300)
      MAC=MAB+2
      CALL RECFP(BKR,MAC)
      WRITE(6,82)(BJ(I),I,I=1,MAC)
   82 FORMAT(37H1 VALUE OF BESSEL FCTNS,ORDER 0,1,...//6(1H ,E16.8,I3)/)
      DO 50 M=MB,MAE
      CALL SERSUM(MAB,ANG(M),BKR)
      U1MG(M)=SQRT(TEMP**2+TEMB**2)
      U2MG(M)=SQRT(TEMC**2+TEMD**2)
      U3MG(M)=SQRT(TEME**2+TEMF**2)
      DM11(M)=SQRT(TR11**2+TI11**2)
      DM12(M)=SQRT(TR12**2+TI12**2)
      DM21(M)=SQRT(TR21**2+TI21**2)
      DM22(M)=SQRT(TR22**2+TI22**2)
      DM31(M)=SQRT(TR31**2+TI31**2)
      DM32(M)=SQRT(TR32**2+TI32**2)
      CALL PHASE(TEMP,TEMB,AP,U1AN(M))
      CALL PHASE(TEMC,TEMD,AP,U2AN(M))
      CALL PHASE(TEME,TEMF,AP,U3AN(M))
      CALL PHASE(TR11,TI11,AP,DA11(M))
      CALL PHASE(TR12,TI12,AP,DA12(M))
      CALL PHASE(TR21,TI21,AP,DA21(M))
      CALL PHASE(TR22,TI22,AP,DA22(M))
      CALL PHASE(TR31,TI31,AP,DA31(M))
      CALL PHASE(TR32,TI32,AP,DA32(M))
```

```
      P1(M)=F1
      P2(M)=F2
      P3(M)=F3
      W1(M)=D1
      W2(M)=D2
      W3(M)=D3
      DO 50 I=1,7
      KI=I+7
      SP1(M,I)=-CJ(KI)
      TW1(M,I)=-DJ(KI)
      SP2(M,I)=-CJ(I)
      TW2(M,I)=-DJ(I)
   50 CONTINUE
      WRITE(6,60)(I,U1MG(I),U1AN(I),U2MG(I),U2AN(I),U3MG(I),U3AN(I),
     1 I=MB,MAE)
      WRITE(6,70)(I,DM11(I),DA11(I),DM12(I),DA12(I),DM21(I),DA21(I),
     1 I=MB,MAE)
      WRITE(6,80)(I,DM22(I),DA22(I),DM31(I),DA31(I),DM32(I),DA32(I),
     1 I=MB,MAE)
      WRITE(6,55) ((NA,NB,SP1(NA,NB),TW1(NA,NB),SP2(NA,NB),TW2(NA,NB),
     1 NA=MB,MAE),NB=1,7)
      WRITE(6,65) (I,P1(I),W1(I),P2(I),W2(I),P3(I),W3(I),I=MB,MAE)
      RI=SCA*MB
      RX=MAE*SCA
      CALL ITRPZW(RI,RX,MB,MAE,W21)
      WRITE(6,15) W21
   15 FORMAT(1H1////5H W21= E16.8)
      DO 20 NA=MB,MAE
      DO 20 NB=1,7
      TW1(NA,NB)=ALOG10(ABS(TW1(NA,NB)))
      TW2(NA,NB)=ALOG10(ABS(TW2(NA,NB)))
   20 CONTINUE
      DO 10 NA=MB,MAE
      W1(NA)=ALOG10(ABS(W1(NA)))
      W2(NA)=ALOG10(ABS(W2(NA)))
      P3(NA)=ALOG10(ABS(P3(NA)))
   10 CONTINUE
```

```
   60 FORMAT(1H1,5X,1HI,8X,7HU1MG(I),11X,7HU1AN(I),11X,7HU2MG(I),11X,
     1 7HU2AN(I),11X,7HU3MG(I),11X,7HU3AN(I)//(1H ,I6,6E18.7))
   70 FORMAT(1H1,5X,1HI,8X,7HDM11(I),11X,7HDA11(I),11X,7HDM12(I),11X,
     1 7HDA12(I),11X,7HDM21(I),11X,7HDA21(I)//(1H ,I6,6E18.7))
   80 FORMAT(1H1,5X,1HI,8X,7HDM22(I),11X,7HDA22(I),11X,7HDM31(I),11X,
     1 7HDA31(I),11X,7HDM32(I),11X,7HDA32(I)//(1H ,I6,6E18.7))
   55 FORMAT(1H1,4X,2HNA,4X,2HNB,5X,10HSP1(NA,NB),7X,10HTW1(NA,NB),
     1 7X,10HSP2(NA,NB),7X,10HTW2(NA,NB)//(1H ,2I6,4E17.7))
   65 FORMAT(1H1,4X,1HI,9X,5HP1(I),11X,5HW1(I),11X,5HP2(I),11X,5HW2(I),
     1 11X,5HP3(I),11X,5HW3(I)//(1H ,I5,4X,6E16.8))
      RETURN
      END
```

```
      SUBROUTINE ITRPZW(XA,XB,KXA,KXB,E)
      COMMON/T/W(900),Y(300),Z(600)
C     SUBROUTINE FOR TRAPEZOIDAL INTERGRATION
      ITER=KXB-KXA
      HITER=ITER
      DX=(XB-XA)/HITER
      E=9.*Y(KXA)+28.*Y(KXA+1)+23.*Y(KXA+2)
      MITER=ITER-3
      DO 100 I=3,MITER
      KI=KXA+I
  100 E=E+Y(KI)
      E=(E+9.*Y(KXB)+28.*Y(KXB-1)+23.*Y(KXB-2))*DX/24.
      RETURN
      END
```

```
      SUBROUTINE RANG1(BNX,BNY,BMD,MAF)
C  BNY MEASURED IN DIRECTION OF PROPAGATION
C BNX IS ONE HALF TOTAL WIDTH OF THE TRANSDUCER.
C SPECIFYBNX,BNY AT THE OUTER EDGE OF THE TRANSDUCER AT THE RADIUS WHERE
C ONE DESIRES TO MAKE THE EVALUATION
C  BKR IS RADIUS OF THE POINT (BNX,BNY) FROM THE ORGIN.
C  USE BKR GREATER THAN 1 FOR THIS SUBROUTINE TO WORK EFFICIENTLY
      COMMON/U/ANG(300)
     1/V20/BKR,MAD,MD,SCA
      BNY=SQRT(BKR**2-BNX**2)
      BL1=MAF-4
      BK=BKR+35.
      MAD=MIN1(BL1,BK)
      DD=ATAN(BNX/BNY)/BNX*SCA
      MD=BNX+BMD
      DO 40 N=1,MD
      ANG(N)=1.570795-DD*(N-1)
   40 CONTINUE
      RETURN
      END
```

```
      SUBROUTINE SERSUM(MAB,ATHETA,BKR)
      DIMENSION VIMD(21)
      DOUBLE PRECISION BJ,BNS1,BNS2,BNS3,CNS1,CNS2,CNS3,TEMP,TEMB,TEMC,
     1TEMD,TEME,TEMF,T1R11,T2R11,T1I11,T2I11,T1R21,T2R21,T1I21,T2I21,
     2T1R31,T2R31,T1I31,T2I31,CIP,SID,CID,SIP,DCOS,DSIN,THETA
      COMMON/R/REMP,REMB,REMC,REMD,REME,REMF,TR11,TI11,TR12,TI12,TR21,
     2 TI21,TR22,TI22,TR31,TI31,TR32,TI32,F1,F2,CJ(14),DJ(14),D1,D2,F3,
     3D3/Q/C(9),WKO/P/D(9)
      COMMON/S/BNS1,BNS2,BNS3,CNS1(200),CNS2(200),CNS3(200)
     1/V/BJ(201)
      TEMP=BNS1*BJ(1)
      TEMC=BNS2*BJ(1)
      TEME=BNS3*BJ(1)
      TEMB=0.
      TEMD=0.
      TEMF=0.
      T1R11=BNS1*BJ(2)*2.
      T1R21=-BNS2*BJ(2)*2.
      T1R31=-BNS3*BJ(2)*2.
      T2R11=0.
      T1I11=0.
      T2I11=0.
      T2R21=0.
      T1I21=0.
      T2I21=0.
      T2R31=0.
      T1I31=0.
      T2I31=0.
      THETA=ATHETA
      DO 35 N=2,MAB,2
      DN=N
      DN1=N-1
      CIP=DCOS(DN*THETA)
      SID=DSIN(DN*THETA)
      CID=DCOS(DN1*THETA)
      SIP=DSIN(DN1*THETA)
```

```
      BUL=(-1)**(N/2)
      TEMP=TEMP+CNS1(N)*BJ(N+1)*SID
      TEMB=TEMB+CNS1(N-1)*BJ(N)*CID*BUL
      TEMC=TEMC+CNS2(N)*BJ(N+1)*CIP
      TEMD=TEMD-CNS2(N-1)*BJ(N)*SIP*BUL
      TEME=TEME+CNS3(N)*BJ(N+1)*CIP*BUL
      TEMF=TEMF-CNS3(N-1)*BJ(N)*SIP
      T1R11=T1R11+CNS1(N)*SID*(BJ(N)-BJ(N+2))
      T2R11=T2R11-DN*BJ(N+1)*CNS1(N)*CIP
      T1I11=T1I11+BUL*CNS1(N-1)*CID*(BJ(N-1)-BJ(N+1))
      T2I11=T2I11+BUL*CNS1(N-1)*BJ(N)*DN1*SIP
      T1R21=T1R21+CNS2(N)*CIP*(BJ(N)-BJ(N+2))
      T2R21=T2R21+DN*SID*BJ(N+1)*CNS2(N)
      T1I21=T1I21-CNS2(N-1)*BUL*SIP*(BJ(N-1)-BJ(N+1))
      T2I21=T2I21+CNS2(N-1)*BUL*CID*BJ(N)*DN1
      T1R31=T1R31+BUL*CNS3(N)*CIP*(BJ(N)-BJ(N+2))
      T2R31=T2R31+DN*BUL*CNS3(N)*SID*BJ(N+1)
      T1I31=T1I31-CNS3(N-1)*SIP*(BJ(N-1)-BJ(N+1))
      T2I31=T2I31+DN1*BJ(N)*CID*CNS3(N-1)
   35 CONTINUE
      SIF=SIN(ATHETA)
      CIF=COS(ATHETA)
      TR11=WKO*T1R11*CIF/2.0-T2R11*SIF/BKR
      TI11=WKO*T1I11*CIF/2.0-T2I11*SIF/BKR
      TR12=WKO*T1R11*SIF/2.0-T2R11*CIF/BKR
      TI12=WKO*T1I11*SIF/2.0-T2I11*CIF/BKR
      TR21=WKO*T1R21*CIF/2.0-T2R21*SIF/BKR
      TI21=WKO*T1I21*CIF/2.0-T2I21*SIF/BKR
      TR22=WKO*T1R21*SIF/2.0-T2R21*CIF/BKR
      TI22=WKO*T1I21*SIF/2.0-T2I21*CIF/BKR
      TR31=WKO*T1R31*CIF/2.0-T2R31*SIF/BKR
      TI31=WKO*T1I31*CIF/2.0-T2I31*SIF/BKR
      TR32=WKO*T1R31*SIF/2.0-T2R31*CIF/BKR
      TI32=WKO*T1I31*SIF/2.0-T2I31*CIF/BKR
      REMP=TEMP
      REMB=TEMB
      REMC=TEMC
```

```
      REMD=TEMD
      REME=TEME
      REMF=TEMF
      VIMD(1)=REMD*TR22-REMC*TI22
      VIMD(2)=REMD*TR11-REMC*TI11
      VIMD(3)=REMD*REMF+REME*REMC
      VIMD(4)=REMC*REME+REMD*REMF
      VIMD(5)=REMF*TR32-REME*TI32
      VIMD(6)=REMB*TR12-REMP*TI12
      VIMD(7)=REMB*TR21-REMP*TI21
      VIMD(8)=TR11*REMB-REMP*TI11
      VIMD(9)=REMB*TR22-REMP*TI22
      VIMD(10)=REMB*REMF+REMP*REME
      VIMD(11)=REMP*REME+REMB*REMF
      VIMD(12)=REMF*TR31-REME*TI31
      VIMD(13)=REMD*TR12-REMC*TI12
      VIMD(14)=REMD*TR21-REMC*TI21
      VIMD(15)=0.0
      VIMD(16)=-REME*TR11-REMF*TI11
      VIMD(17)=-REME*TR22-REMF*TI22
      VIMD(18)=0.0
      VIMD(19)=REMD*TI32+REMC*TR32
      VIMD(20)=REMB*TI31+REMP*TR31
      VIMD(21)=0.0
C     CJ1-CJ7  SURFACE POWER DENSITY IN X-2 DIRECTION
C    CJ8-CJ14  SURFACE POWER DENSITY IN X-1 DIRECTION
C    DJ1-DJ7  TOTAL ENERGY IN X-2 DIRECTION
C    DJ8-DJ14  TOTAL ENERGY IN X-1 DIRECTION
      DO 20 I=1,7
      KI=I+7
      CJ(I)=VIMD(I)*C(I)
      DJ(I)=VIMD(I)*D(I)
      DJ(KI)=VIMD(KI)*D(I)
      CJ(KI)=VIMD(KI)*C(I)
   20 CONTINUE
      D1=0.
```

```
      D2=0.
      F1=0.
      F2=0.
      DO 10 I=1,7
      KI=I+7
      F1=F1-CJ(KI)
      F2=F2-CJ(I)
      D1=D1-DJ(KI)
      D2=D2-DJ(I)
   10 CONTINUE
      F3=-C(8)*(VIMD(16)+VIMD(17))-C(9)*(VIMD(19)+VIMD(20))
      D3=-D(8)*(VIMD(16)+VIMD(17))-D(9)*(VIMD(19)+VIMD(20))
      RETURN
      END
```

```
      SUBROUTINE RECFP(X,N)
C       THIS SUBROUTINE GENERATES BESSEL FUNCTIONS OF THE FIRST KIND OF
C  ORDER 0,1,2,3,4,...N.  IT RECCURS DOWN FROM BJ(KR) OF ORDER KR AND
C  KR-1 TO THE FUNCTIONS OF LOWER ORDER.
      DOUBLE PRECISION B,BX,BX1,BN,BN1,BO,Z,ALPHA,BN2,DSQRT,DFLOAT
      COMMON/V/BO,B(200)
      CN=0.17E-28
      CD=1.0E-31
      IF(X-30.) 10,10,20
   10 KR=57.0+1.35*X
      GO TO 30
   20 IF(X-90.) 40,40,70
   40 KR=65.0+1.30*X
      GO TO 30
   70 IF(X-200.)80,80,90
   80 KR=77.0+1.250*X
      GO TO 30
   90 IF(X-800.)230,230,240
  230 KR=135.0+1.120*X
      CN=0.185E-43
      CD=0.370E-46
      GO TO 30
  240 KR=240.0+1.040*X
      CN=0.4E-65
      CD=0.0
   30 CONTINUE
      BN=CN+CD*X
      BX=KR
      BX1=KR-1
      Z=X
      BN1=2.0*BN*BX1*(DSQRT(BX/BX1))*((BX/BX1)**KR)/(Z*2.718281828459D0)
      ALPHA=0.0
      IF(KR-(KR/2)*2) 120,110,120
  110 JT=-1
      GO TO 130
  120 JT=1
  130 KN=KR-N
```

```
      DO 160 K=1,KN
      KRK=KR-K
      BN2=2.*DFLOAT(KRK)*BN1/Z-BN
      JT=-JT
      S=1+JT
      BN=BN1
      BN1=BN2
  160 ALPHA=ALPHA+BN2*S
      B(N)=BN
      B(N-1)=BN1
      IA=N-2
      DO 60 L=1,IA
      NL=N-L
      B(NL-1)=2.*B(NL)*DFLOAT(NL)/Z-B(NL+1)
      JT=-JT
      S=1+JT
   60 ALPHA=ALPHA+B(NL-1)*S
      BO=2.*B(1)/Z-B(2)
      ALPHA=ALPHA+BO
      DO 55 L=1,N
      B(L)=B(L)/ALPHA
   55 CONTINUE
      BO=BO/ALPHA
      RETURN
      END


      SUBROUTINE DOEF(BL,MAC)
      DOUBLE PRECISION BNS1,BNS2,BNS3,CNS1,CNS2,CNS3,DBL
      COMMON/S/BNS1,BNS2,BNS3,CNS1(200),CNS2(200),CNS3(200)
      READ(5,186) (CNS1(N),CNS2(N),CNS3(N),N=1,MAC)
  186 FORMAT(2X,3D20.11)
      READ(5,192) BNS1,BNS2,BNS3,DBL
  192 FORMAT(3X,4D19.11)
      BL=DBL
      RETURN
      END
```

```
      SUBROUTINE ELACNT(WOM)
      COMMON
     1/Q/C1,C2,C3,C4,C5,C6,C7,C8,C9,WKO
     2/P/D1,D2,D3,D4,D5,D6,D7,D8,D9
C     C1111=9.07E10
      C2222=9.07E10
      C2211=5.81E10
C     C1122=5.81E10
      C2233=5.1E10
C     C1133=5.1E10
      C2112=1.63E10
C     C2121=1.63E10
C     C1212=1.63E10
C     C1221=1.63E10
      C2332=1.50E10
      C2323=1.50E10
C     C1331=1.50E10
C     C1313=1.50E10
      VEL=1730.6
      WKO=WOM/VEL
      C1=C2222*1.0215**2*WOM
      C2=C2211*1.0215**2*WOM
      C3=C2233*1.0215*0.53028*WOM*WKO
      C4=C2323*1.8989*1.9486*WOM*WKO
      C5=C2332*1.8989**2*WOM
      C6=C2112*1.0215**2*WOM
      C7=C6
      C8=-C2233*WOM*1.939684
      C9=-C2323*WOM*1.939684
C     C8=C1,C9=C2,C10=C3,C11=C4,C12=C5,C13=C6,C14=C6,D8=D1,ETC.
      D1=C2222*0.469024*VEL
      D2=C2211*0.469024*VEL
      D3=C2233*0.375009*WOM
      D4=C2323*2.3146937*WOM
      D5=C2332*17.15725*VEL
      D6=C2112*0.469024*VEL
```

```
      D7=D6
      D8=C2233*VEL*0.80845
      D9=C2323*VEL*0.80845
      RETURN
      END


C     SUBROUTINE FOR DETERMINING PHASE OF A COMPLEX NUMBER
      SUBROUTINE PHASE (VREAL,VIMAG,PHSR,PHSD)
C     DETERMINE QUADRANT OF COMPLEX NUMBER
      IF (VIMAG) 101,102,103
  101 IF (VREAL) 111,112,113
  102 IF (VREAL) 121,150,123
  103 IF (VREAL) 131,132,133
C     USE ARCTANGENT FUNCTION TO DETERMINE PHASE
  111 PHSR=-3.14159+ATAN(-VIMAG/(-VREAL))
      GO TO 140
  112 PHSR=-1.57078
      GO TO 140
  113 PHSR=-ATAN(-VIMAG/VREAL)
      GO TO 140
  121 PHSR=3.14159
      GO TO 140
  123 PHSR=0.
      GO TO 140
  131 PHSR=3.14159-ATAN(VIMAG/(-VREAL))
      GO TO 140
  132 PHSR=1.57078
      GO TO 140
  133 PHSR=ATAN(VIMAG/VREAL)
  140 PHSD=PHSR*57.2958
      RETURN
C     IF MAGNITUDE IS ZERO, PHASE IS INDETERMINATE
  150 PRINT 155
  155 FORMAT (1H0,35HMAGNITUDE ZERO, PHASE INDETERMINATE)
      RETURN
      END
```

```
      SUBROUTINE COEFF(BL,MAC,MAL)
C MAC MUST BE AT LEAST 30 GREATER THAN  BL
C MAL MUST BE ODD FOR PART OF THIS SUBROUTINE TO WORK PROPERLY, MAL
C SHOULD BE CHOSEN AT LEAST 10 GREATER THAN MAC FOR BEST RESULTS
      DOUBLE PRECISION BNS1,BNS2,BNS3,CNS1,CNS2,CNS3,CM,CMA,CMB,CMD,CNI,
     1CMC,SBLJ,BLJ1,BLJ,BL,CA,CN,CNA,CN1,CNA1,CNB
      DIMENSION CM(200),CMA(200),CMB(200),CMD(200),CNI(200),CMC(200)
     1,SBLJ(205)
      COMMON/S/BNS1,BNS2,BNS3,CNS1(200),CNS2(200),CNS3(200)
     1/V/BLJ1,BLJ(200)
      IO=MAL
      CALL RECFP(BL,IO)
      WRITE(6,56) (BLJ(LN),LN,LN=1,MAL,2)
   56 FORMAT(1H1,2(7X,7HBLJ(LN),13X,2HLN)//2(1H ,D19.11,6X,I4))
      SBLJ(MAL+2) = 0.0
      DO 58 I =1,MAL,2
      SBLJ(MAL+1-I) = BLJ(MAL+1-I) + SBLJ(MAL+3-I)
58    CONTINUE
      WRITE(6,62) (SBLJ(I),I,I = 1,MAL,2)
62    FORMAT(1H1,3(5X,7HSBLJ(I),14X,1HI,5X)//3(1H ,D19.11,6X,I3,5X))
      BNS1=0.0
      BNS2=3.1415926536D0*(BLJ(1) + 2.*SBLJ(3))
      BNS3=4.*SBLJ(1)
      DO 68 N=3,MAL,2
      CA=N
      BNS3=BNS3+SBLJ(N)*8.*((-1)**((N+1)/2))/(CA*(CA-2.))
  68  CONTINUE
      DO 64 M=3,MAL,2
      CM(M)=M
      CMA(M)=M**2
      CMB(M)=(M+1)**2
      CMC(M)=(M-1)**2
      CMD(M)=(M-3)*(M-3)
      CNI(M)=CMC(M)*(CMD(M)+CMB(M))/8.-CMB(M)*CMD(M)/4.
 64   CONTINUE
      DO 74 N=2,MAC,2
      N1=N - 1
```

```
      CNS1(N)=-(BLJ(N-1)+BLJ(N+1))*3.1415926536D0
      CNS2(N)=3.1415926536D0*(BLJ(N-1)+3.*BLJ(N+1)+4.*SBLJ(N+3))
      CNS3(N1)=-6.283185307 2D0*(BLJ(N-1)+2.*SBLJ(N+1))
      CN=N
      CNA=N**2
      CN1=N1
      CNA1=N1**2
      CNB=N1**3
      CNS1(N1 )= 8.*BLJ(1)/(CNA1-4.)
      CNS2(N1) =-16.*SBLJ(1)/(CNB-4.*CN1)
      CNS3(N)=-8.*SBLJ(1)/(CNA-1.)
      DO 72 M=3,MAL,2
      CNS1(N1)=CNS1(N1)+8.*((-1)**((M-1)/2))*(CNA1+CMA(M)-1.)*BLJ(M)/
     1((CNA1-CMC(M))*(CNA1-CMB(M)))
      CNS2(N1)=CNS2(N1)+32.*CN1*(CNA1+CNI(M))*SBLJ(M)*((-1)**((M+1)/2))/
     1((CNA1-CMD(M))*(CNA1-CMC(M))*(CNA1-CMB(M)))
      CNS3(N)=CNS3(N)+16.*SBLJ(M)*((-1)**((M+1)/2))*(CNA+CMA(M)-2.*
     1CM(M))/((CNA-(CM(M)-2.)**2)*(CNA-CMA(M)))
   72 CONTINUE
 74   CONTINUE
      WRITE(6,76) BNS1,BNS2,BNS3
   76 FORMAT(1H1,6X,4HBNS1,12X,4HBNS2,12X,4HBNS3//1H ,3D19.11)
      WRITE(6,78) (CNS1(N),CNS2(N),CNS3(N),N,N=1,MAC)
 78   FORMAT(1H1,2(5X,7HCNS1(N),10X,7HCNS2(N),9X,7HCNS3(N),8X,1HN)//
     12(1H ,3D19.11,I6))
      WRITE(7,186)(CNS1(N),CNS2(N),CNS3(N),N,N=1,MAC)
 186  FORMAT(2X,3D20.11,5X,I5)
      WRITE(7,192)BNS1,BNS2,BNS3,BL
 192  FORMAT(3X,4D19.11)
      RETURN
      END
                                DOUBLE PRECISION BL
                                BL=62.83185400
                                MAL=131
                                MAC=120
                                CALL COEFF(BL,MAC,MAL)
                                STOP
                                END
```

XI. APPENDIX D

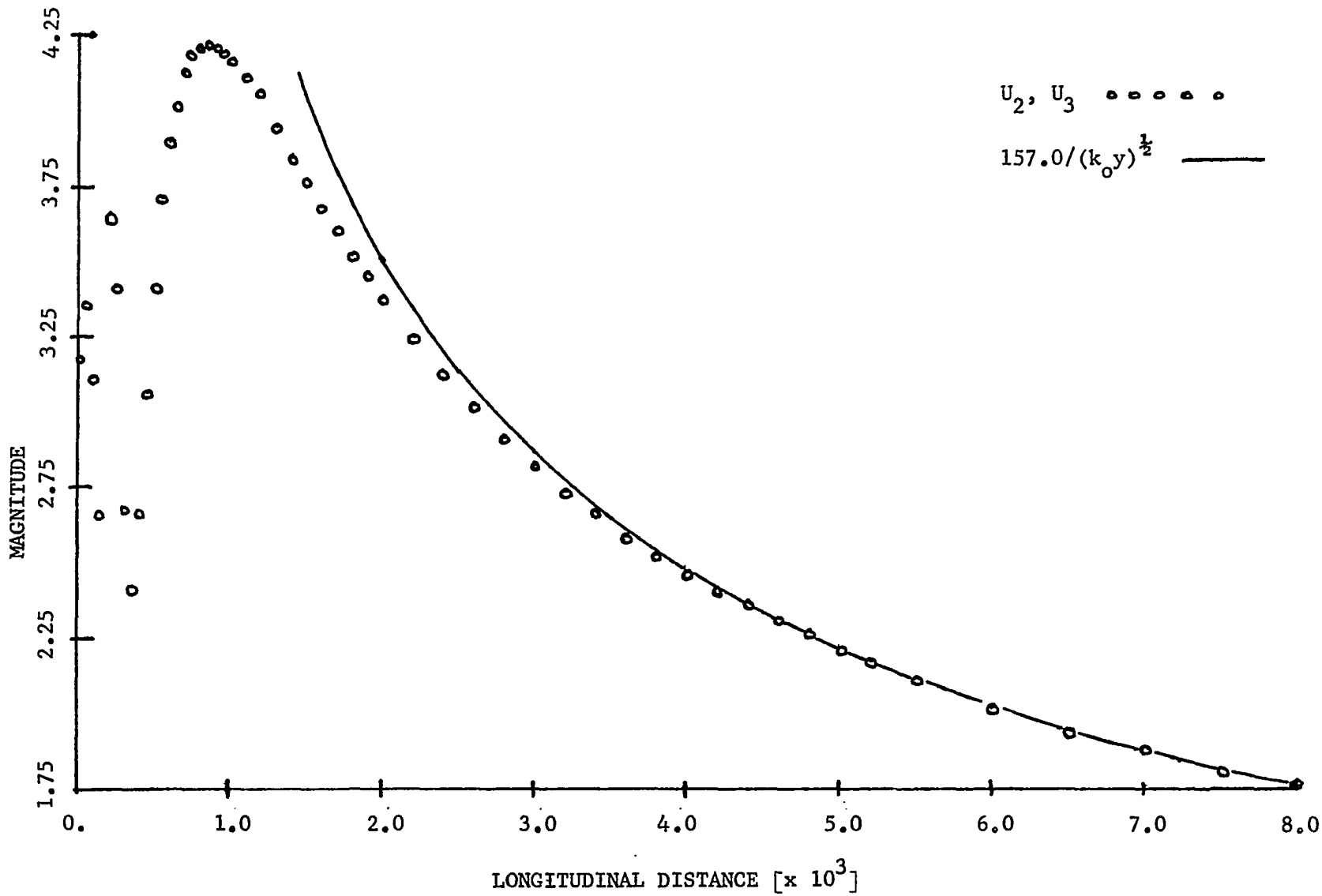

Figure 5. Particle displacement vs. longitudinal distance along $k_o y$ axis at $x = 0$

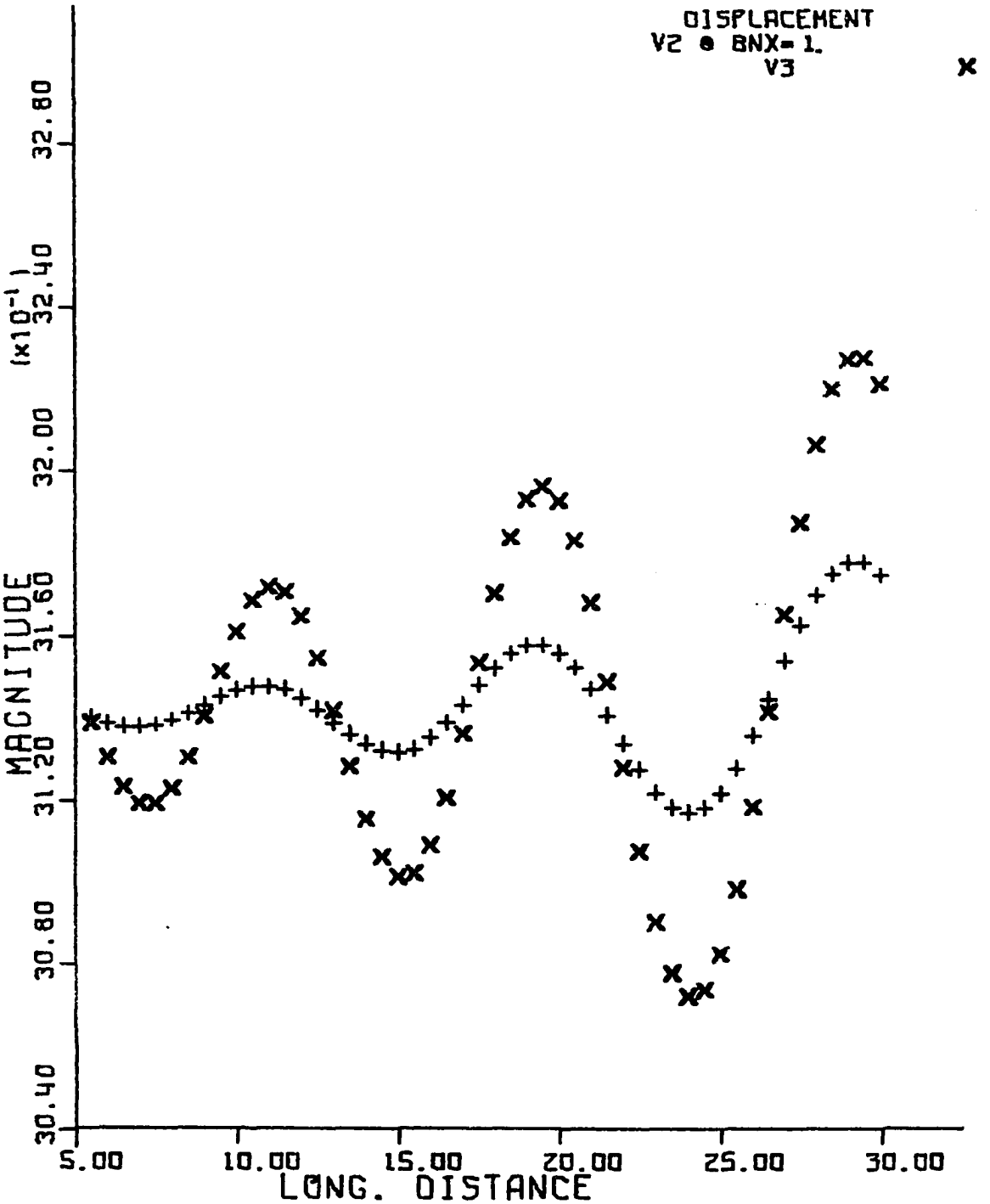

Figure 6. The magnitude of the U_2 and U_3 particle displacement vs. $k_o y$ at $k_o x = 1.0$

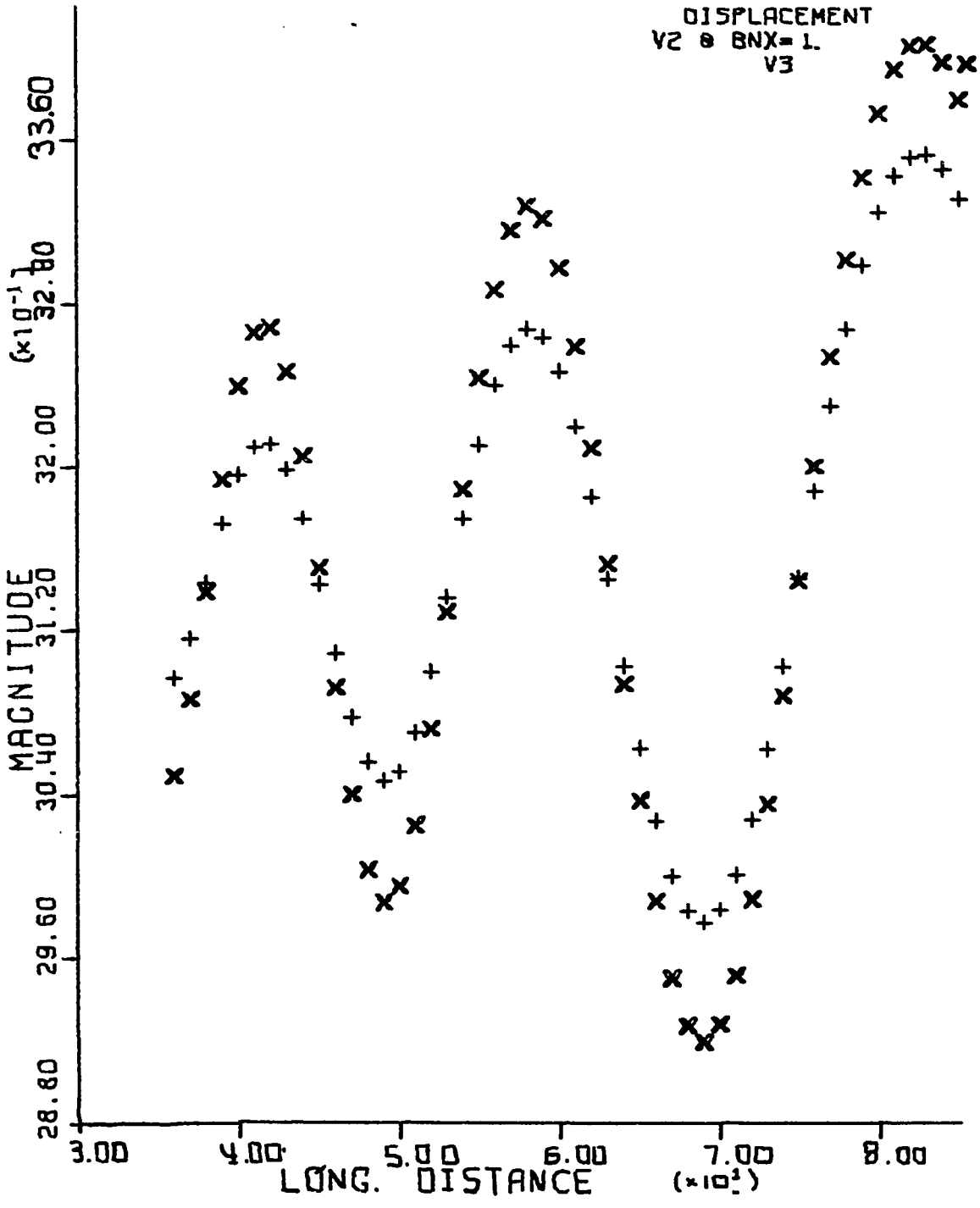

Figure 7. The magnitude of the U_2 and U_3 particle displacements vs. $k_o y$ at $k_o x = 1.0$

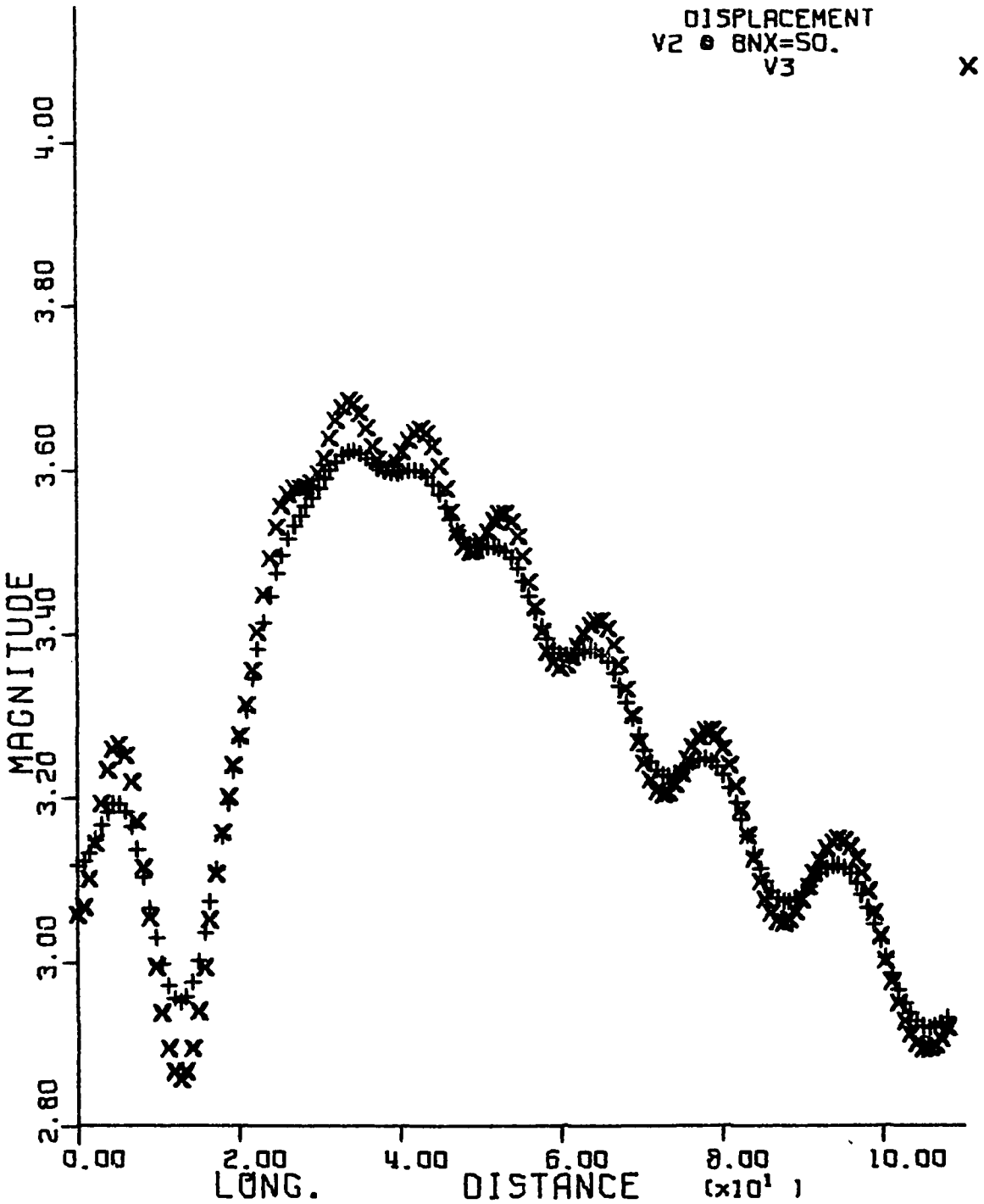

Figure 8. The magnitude of the U_2 and U_3 particle displacements vs. $k_o y$ at $k_o x = 50.0$

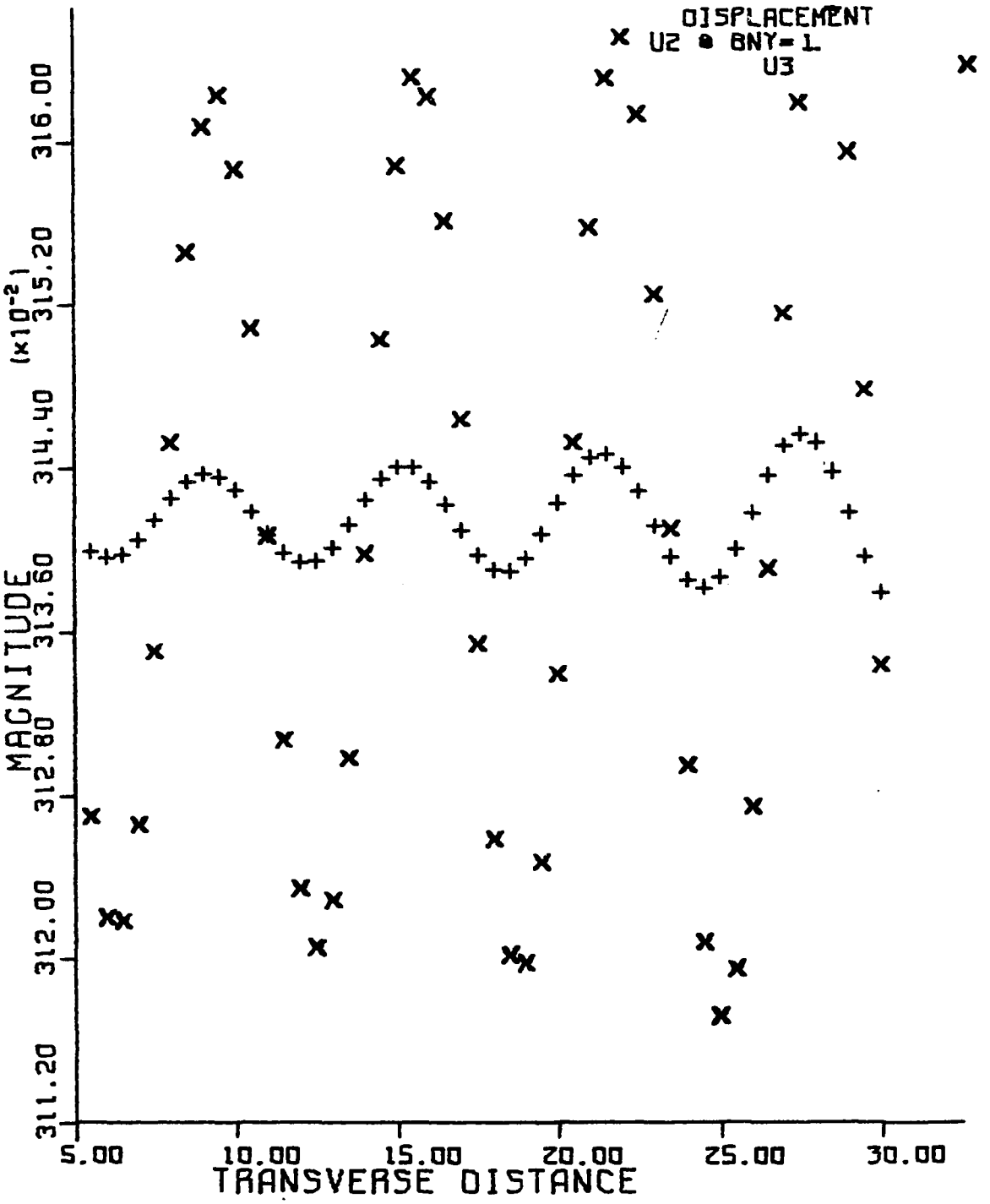

Figure 9. The magnitude of the U_2 and U_3 particle displacements vs. $k_o x$ at $k_o y = 1.0$

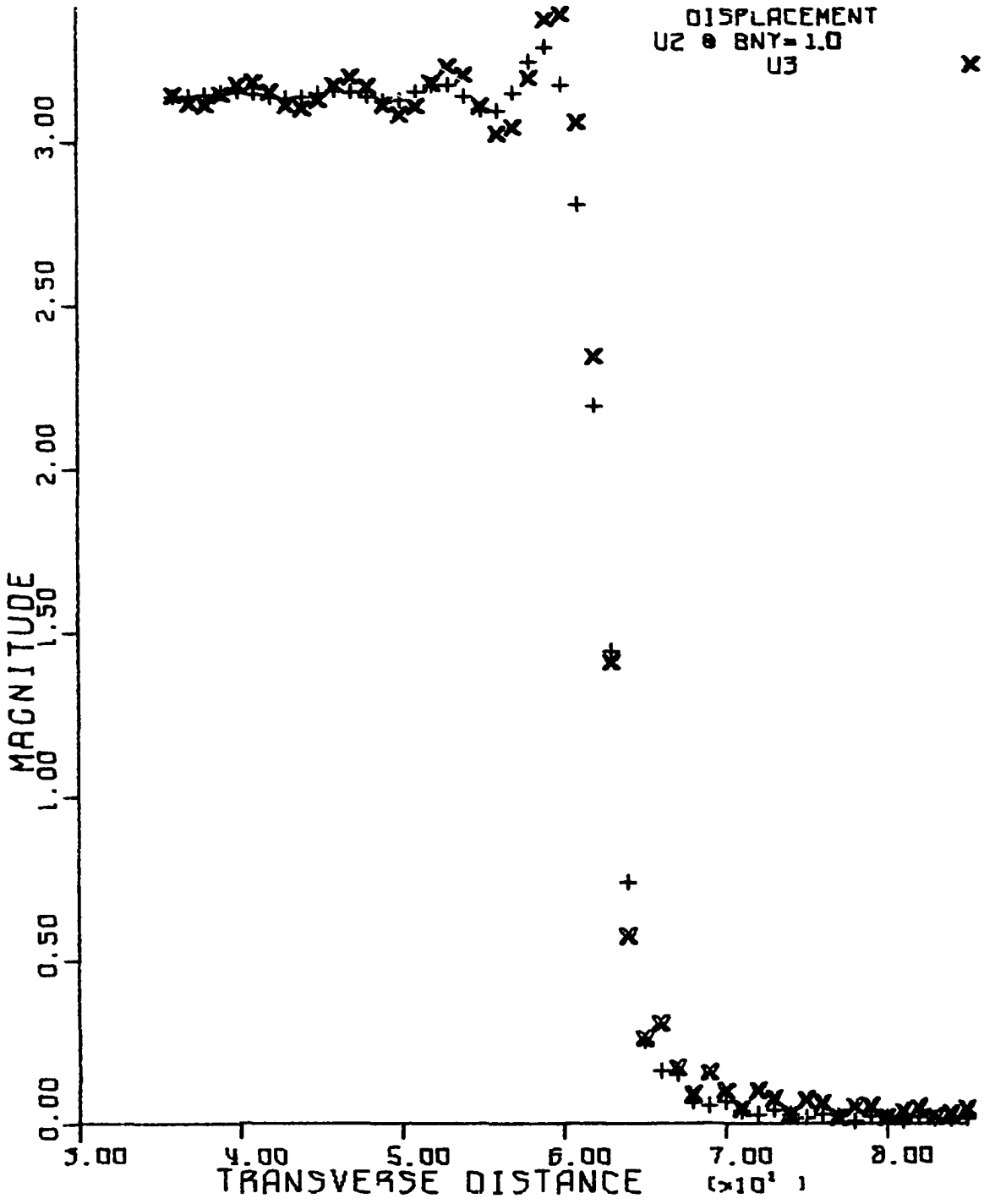

Figure 10. The magnitude of the U_2 and U_3 particle displacements vs. $k_o x$ at $k_o y = 1.0$

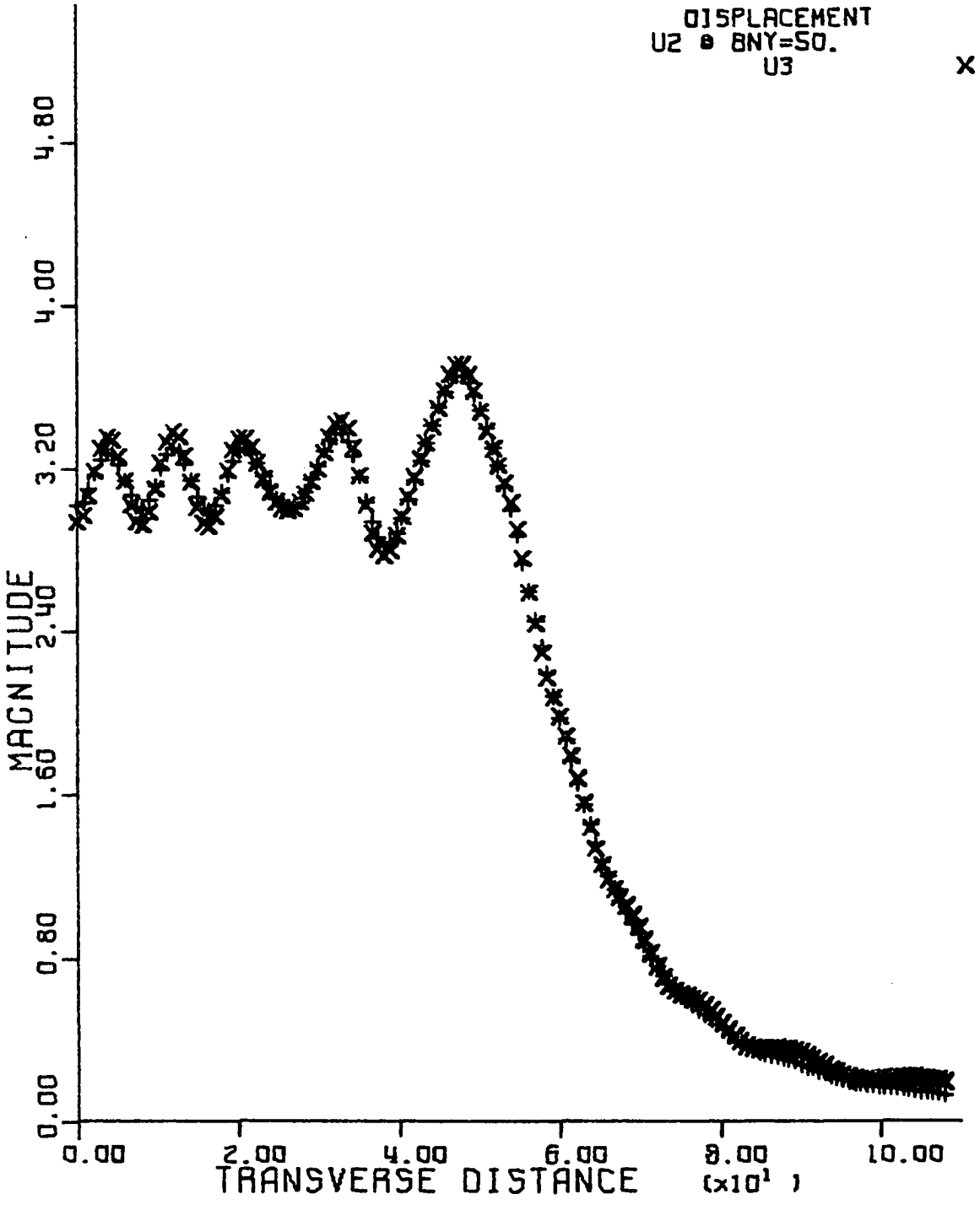

Figure 11. The magnitude of the U_2 and U_3 particle displacements vs. $k_o x$ at $k_o y = 50.0$

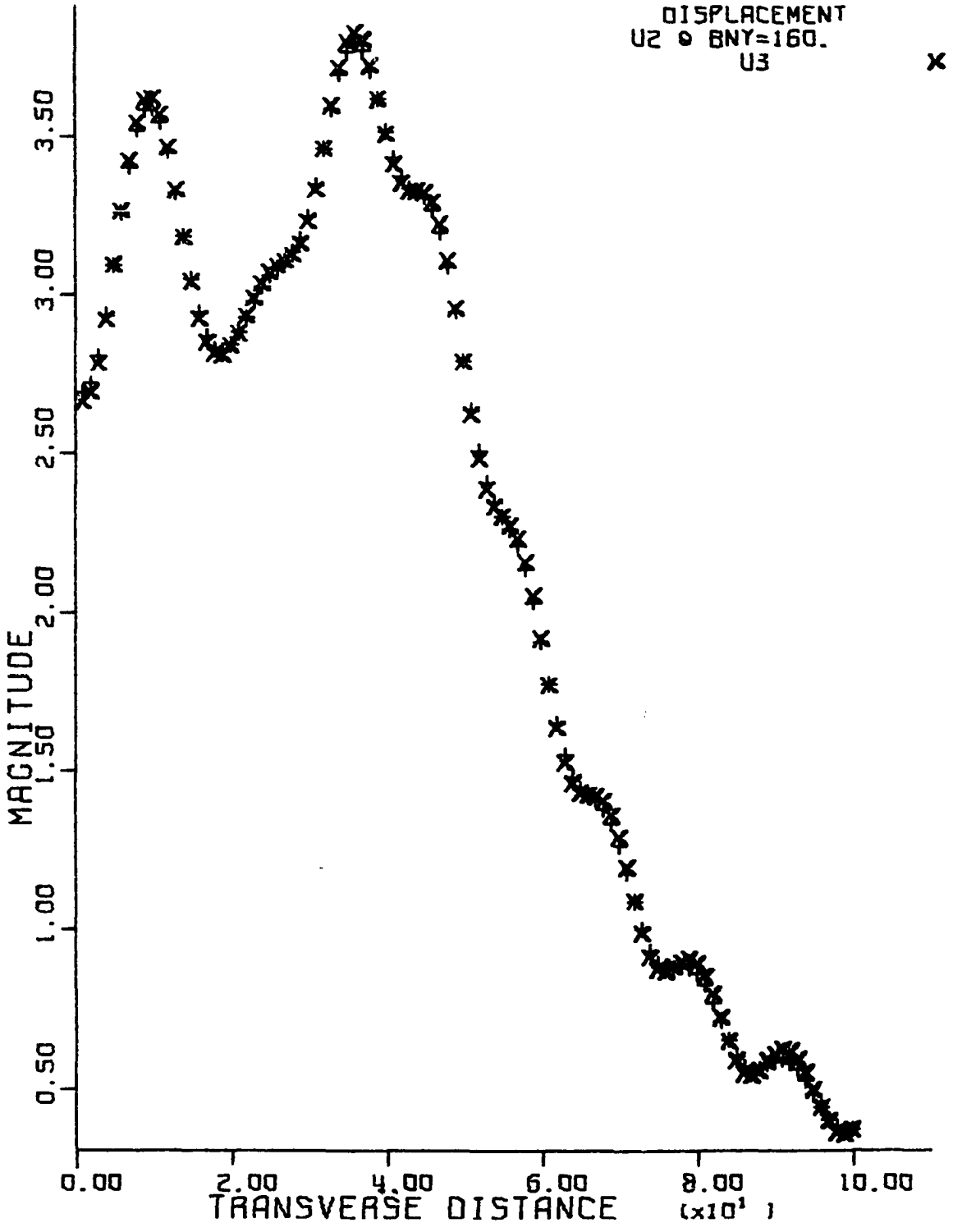

Figure 12. The magnitude of the U_2 and U_3 particle displacements vs. $k_o x$ at $k_o y = 160.0$

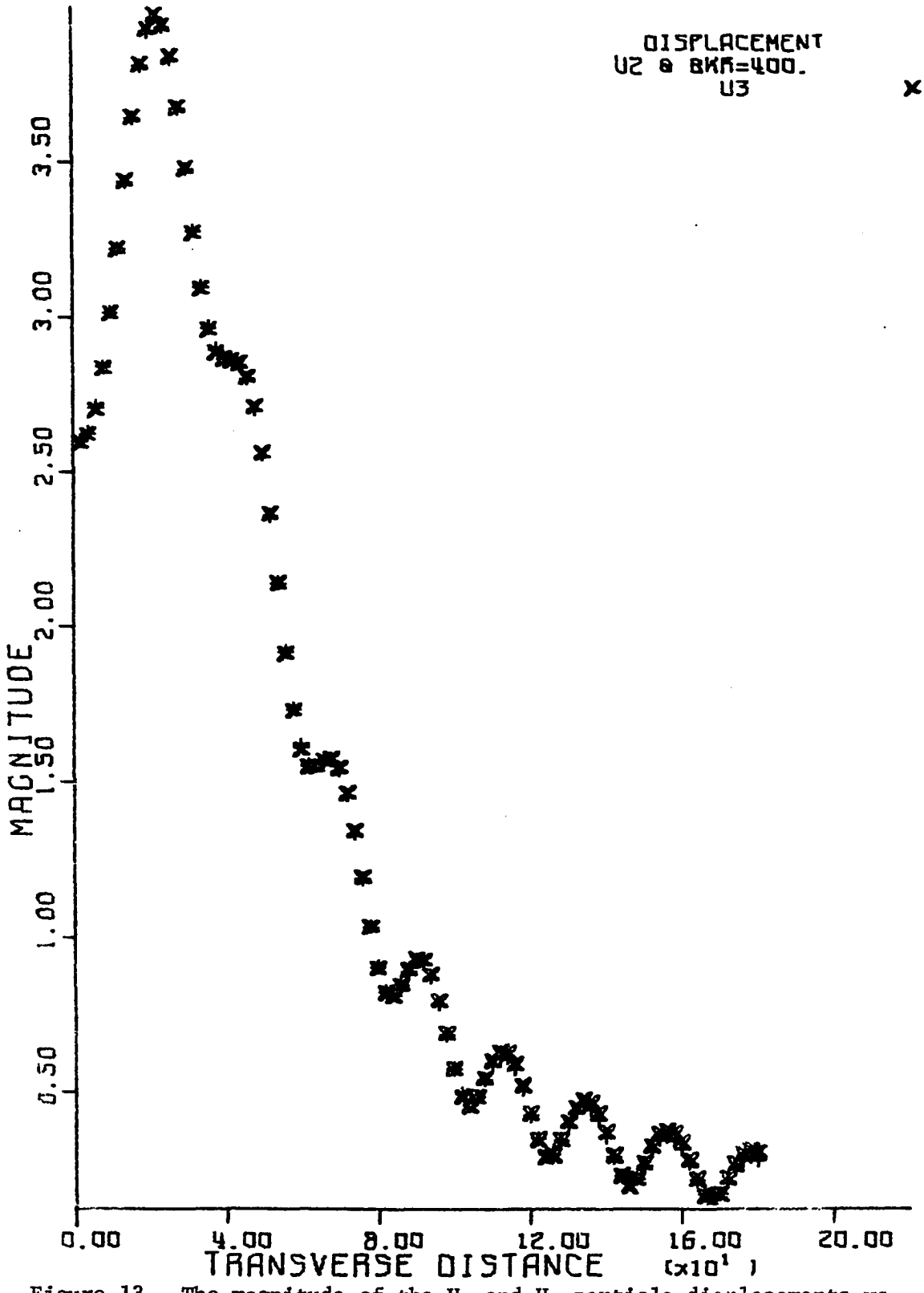

Figure 13. The magnitude of the U_o and U_3 particle displacements vs. $k_o x_t$ at $k_o r = 400.0$

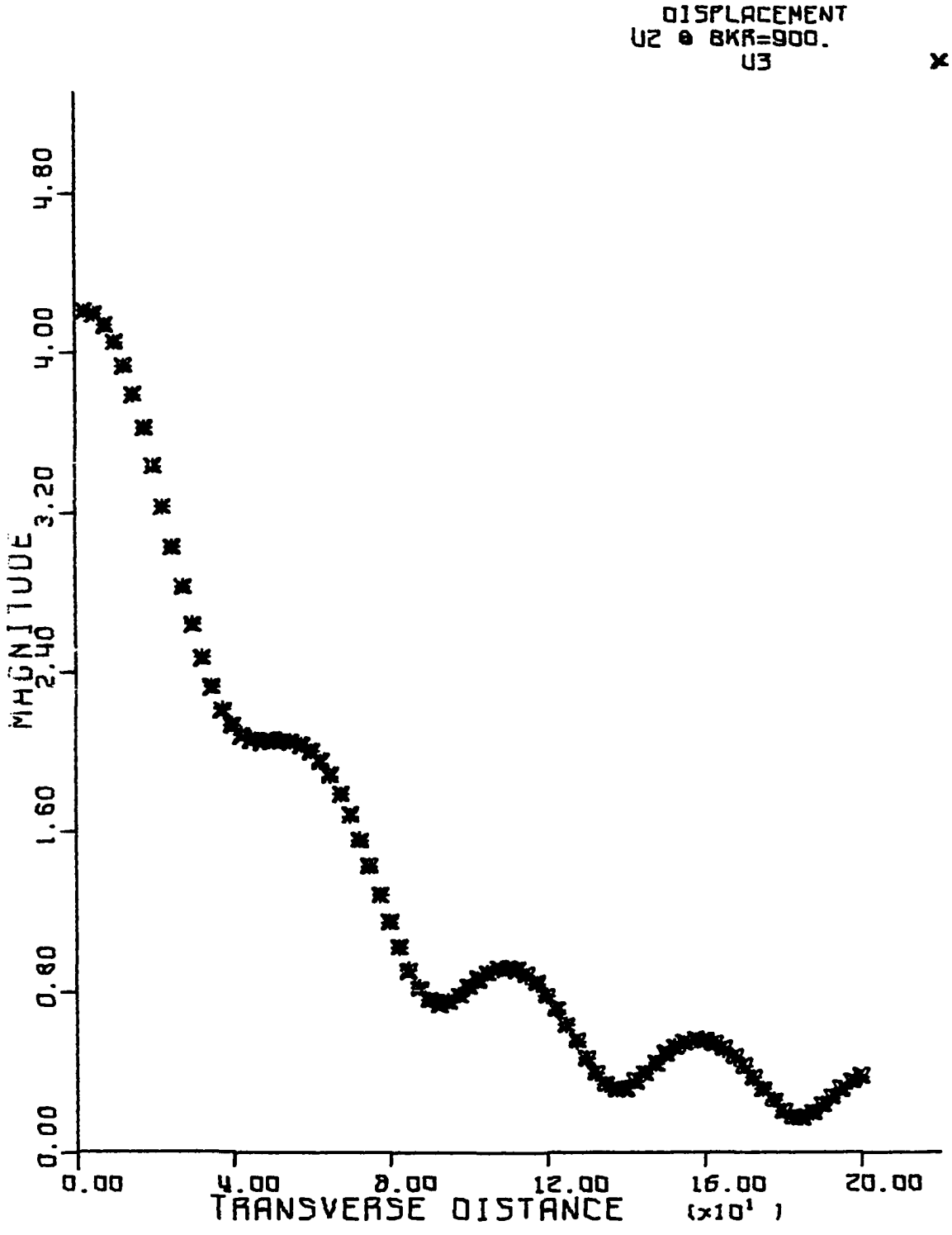

Figure 14. The magnitude of the U_2 and U_3 particle displacements vs. $k_o x_t$ at $k_o r = 900.0$

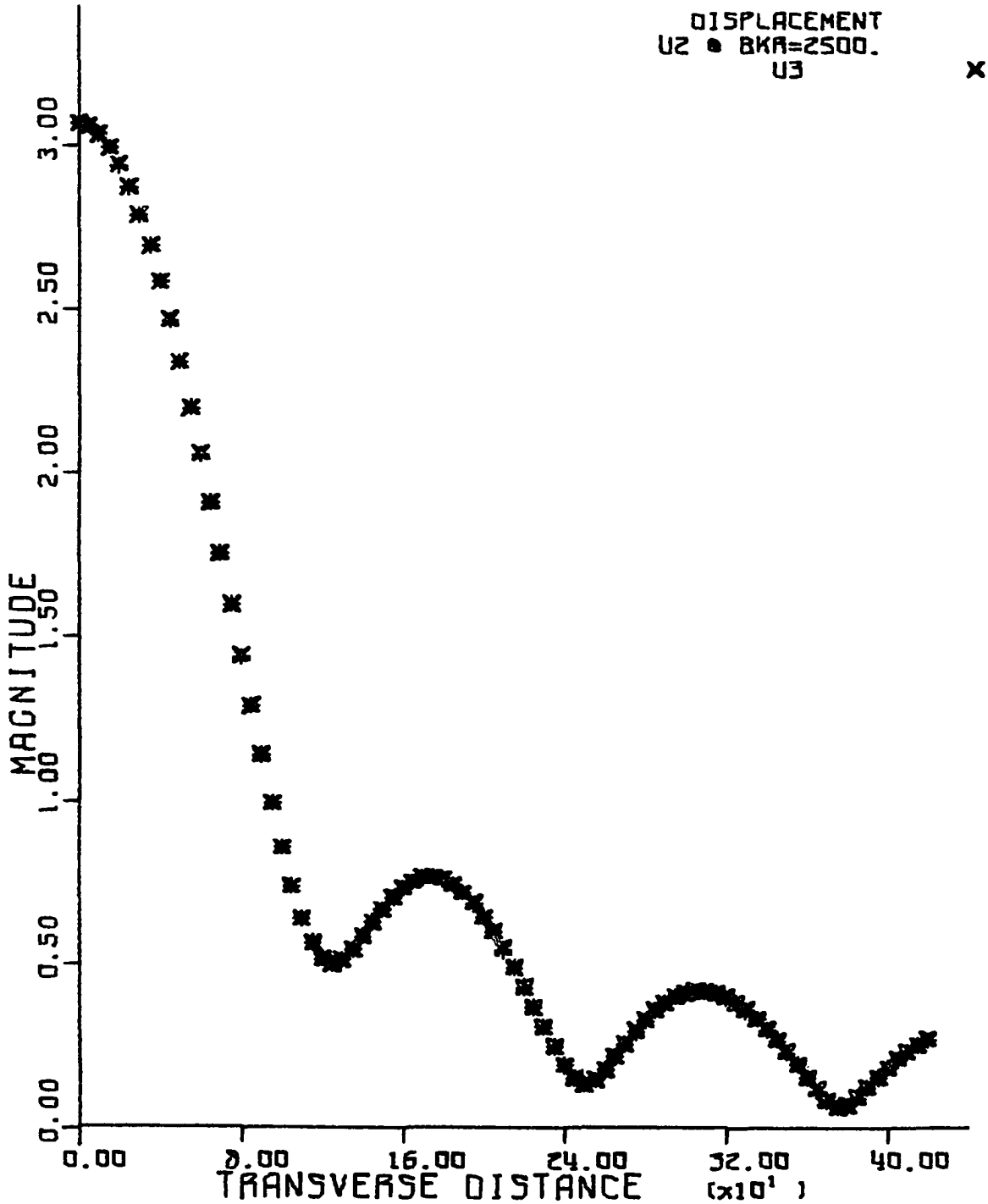

Figure 15. The magnitude of the U_2 and U_3 particle displacements vs. $k_o x_t$ at $k_o r = 2500.0$

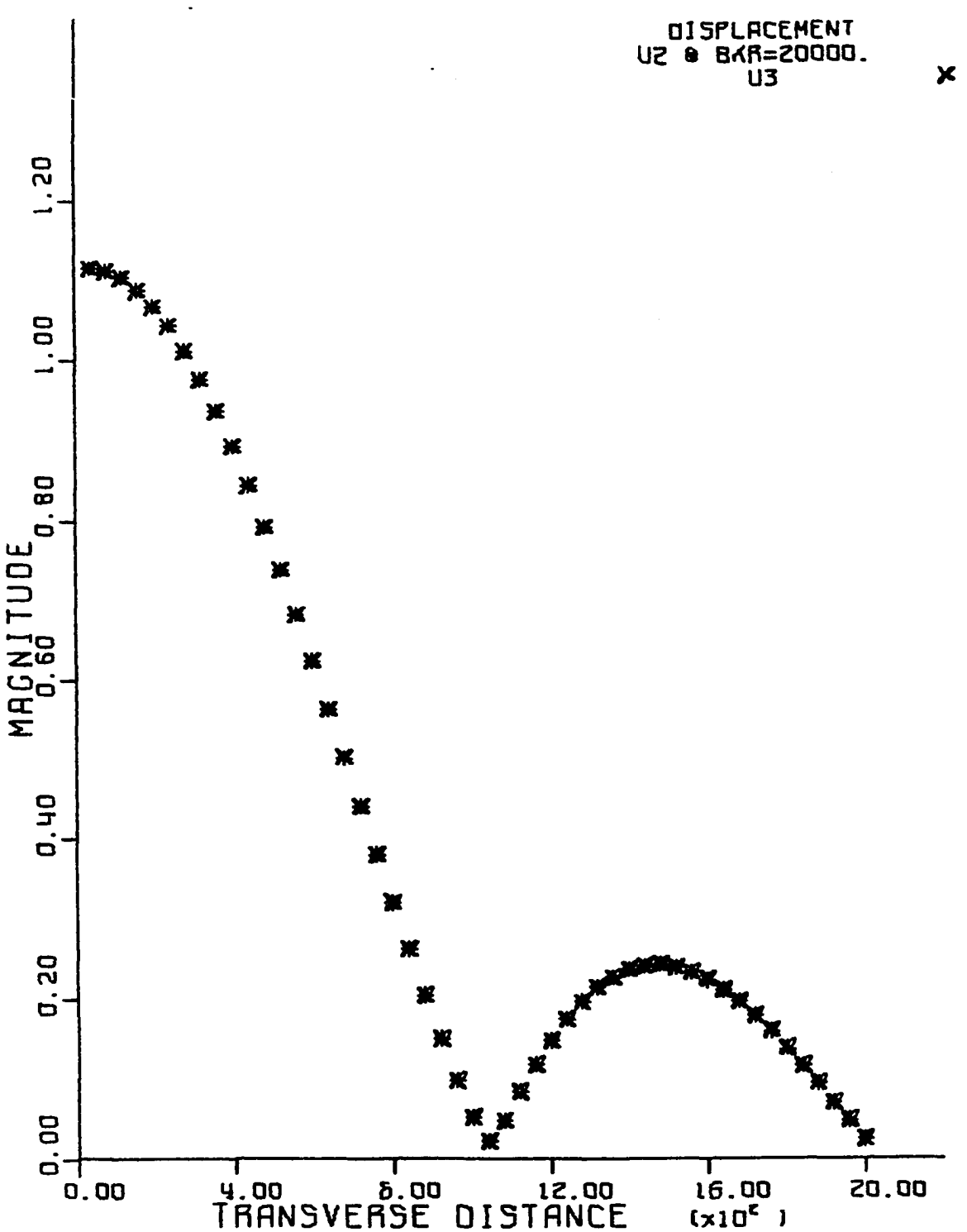

Figure 16. The magnitude of the U_2 and U_3 particle displacements vs. $k_o x_t$ at $k_o r$ = 20,000.0

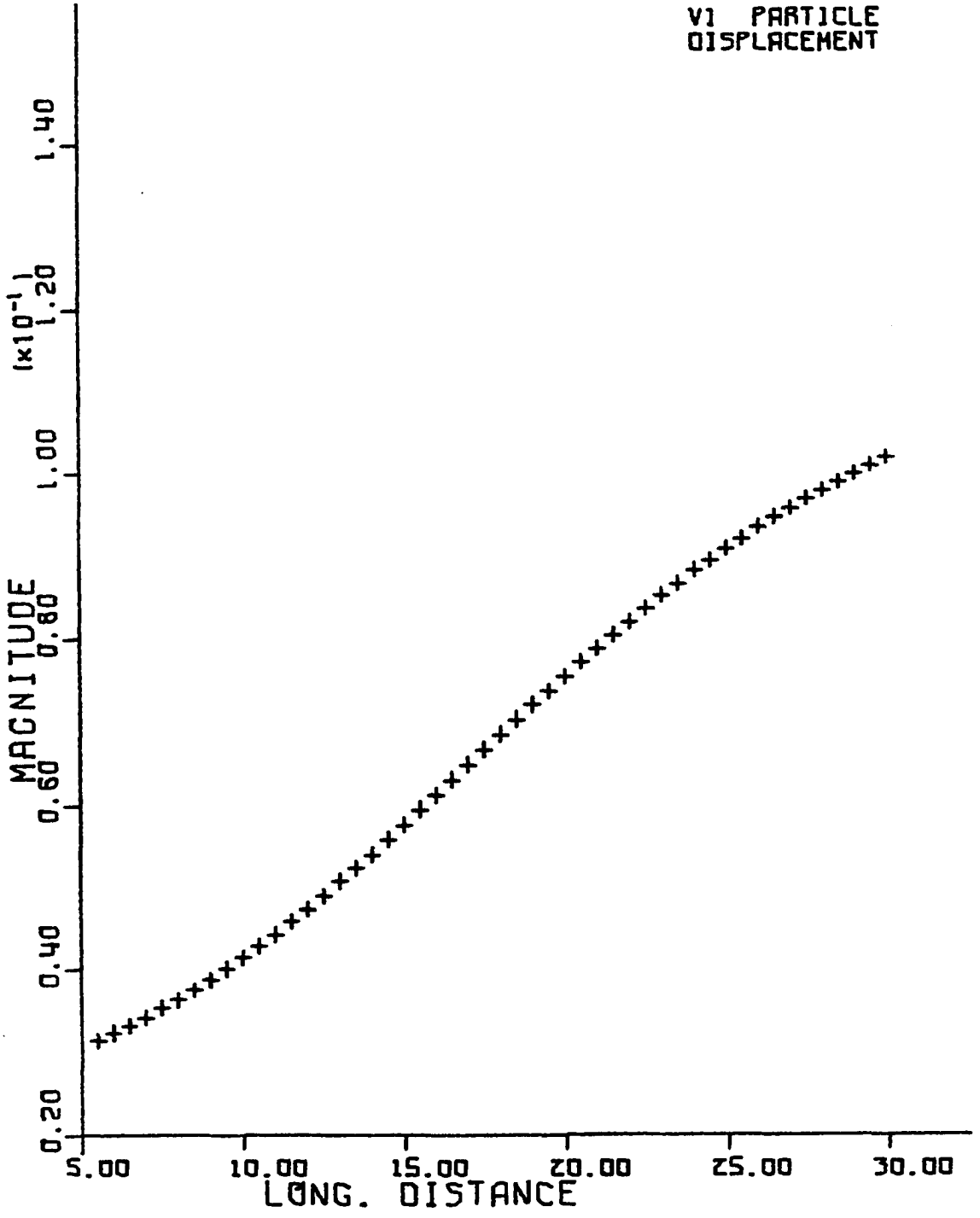

Figure 17. The magnitude of the U_1 particle displacement phasor vs. $k_o y$ at $k_o x = 1.0$

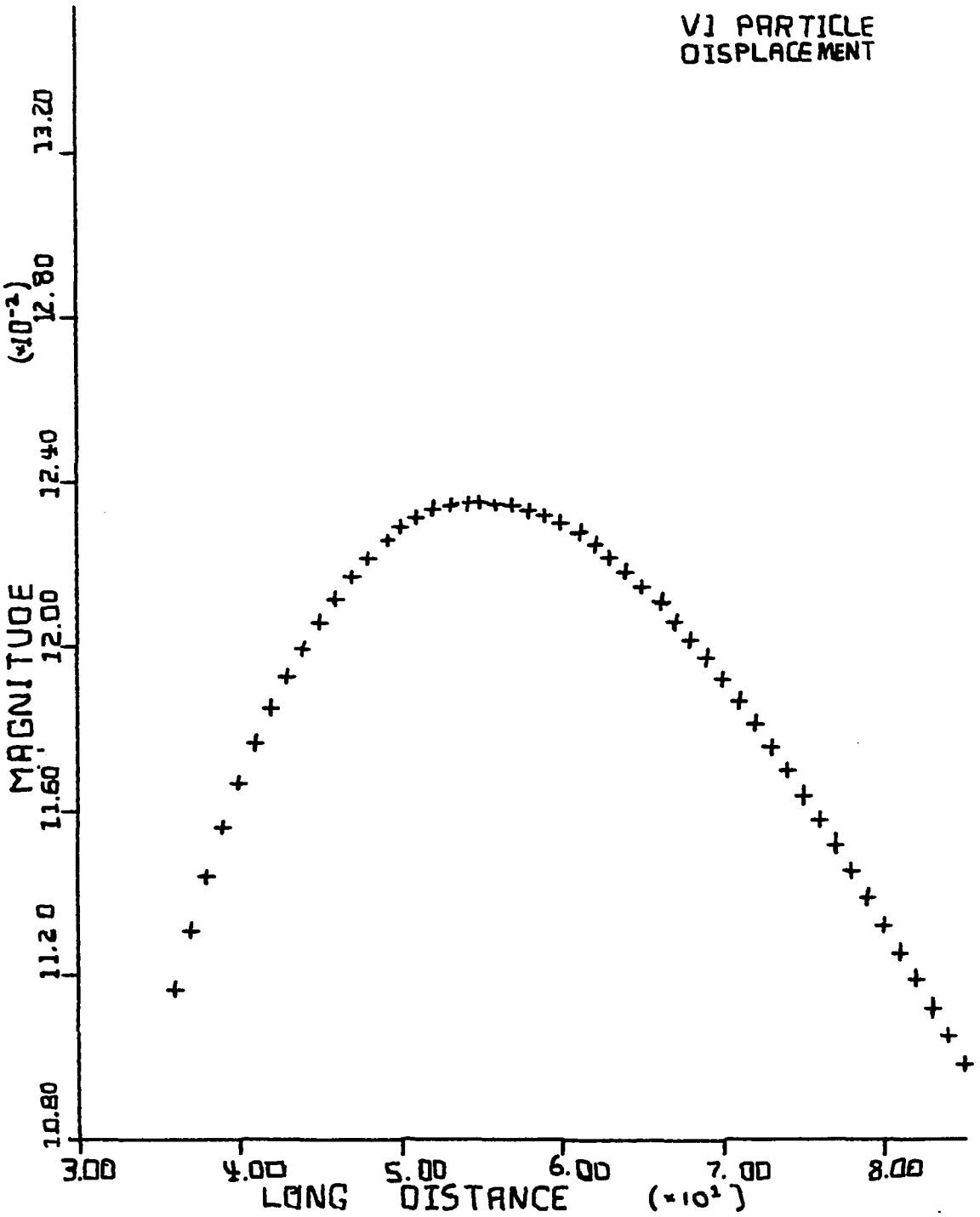

Figure 18. The magnitude of the U_1 particle displacement phasor vs. $k_o y$ at $k_o x = 1.0$

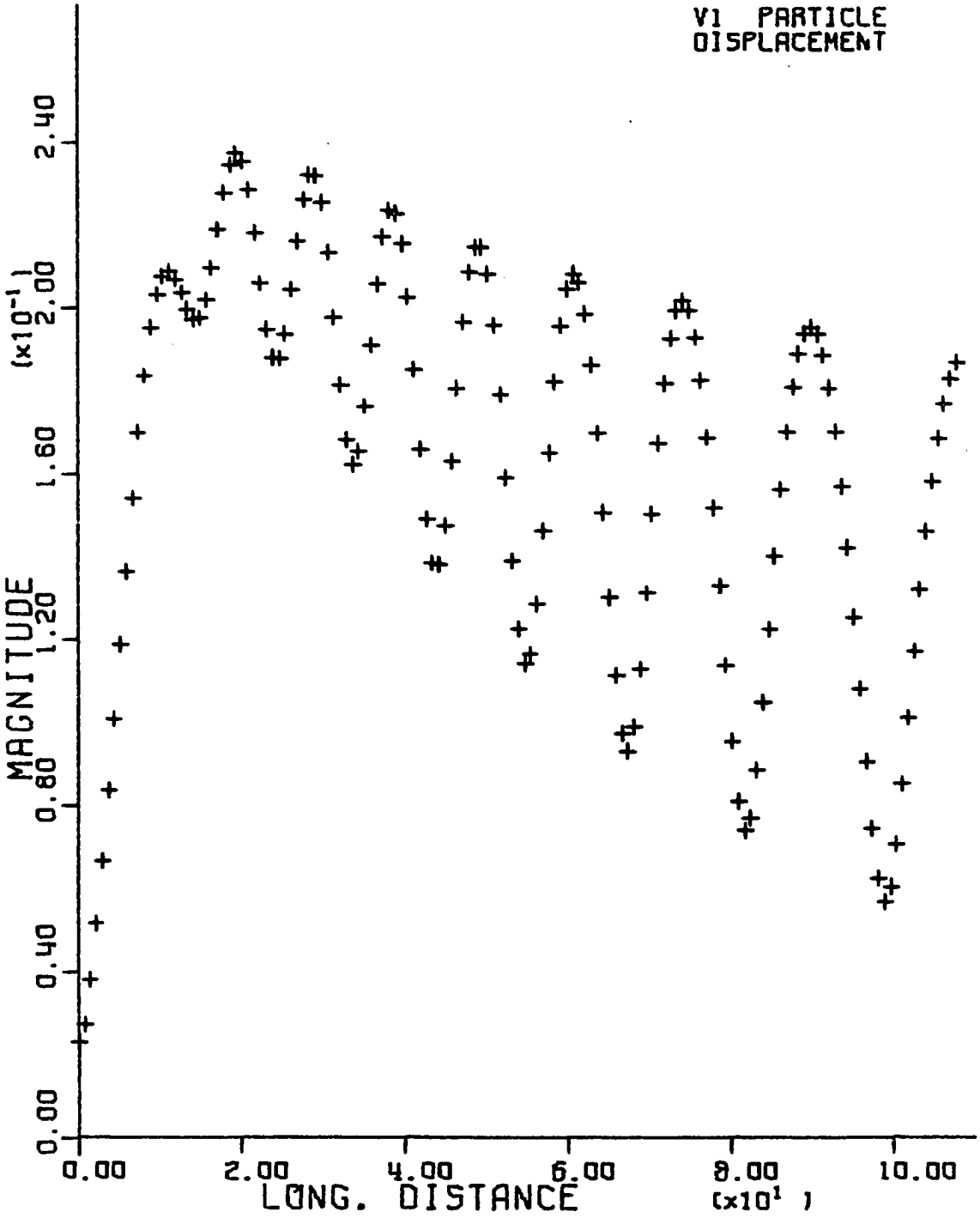

Figure 19. The magnitude of the U_1 particle displacement phasor vs. $k_o y$ at $k_o x = 50.0$

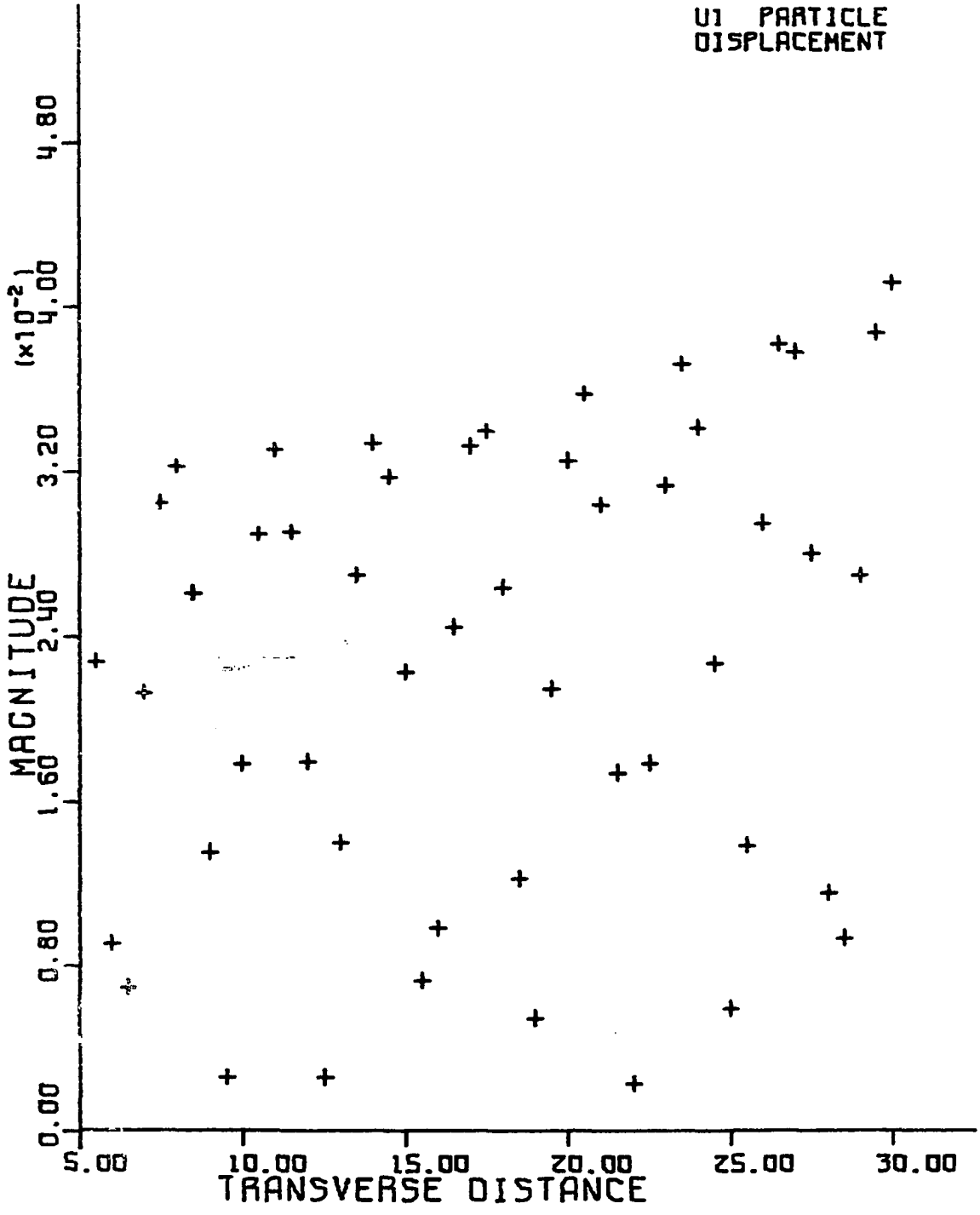

Figure 20. The magnitude of the U_1 particle displacement phasor vs. $k_o x$ at $k_o y = 1.0$

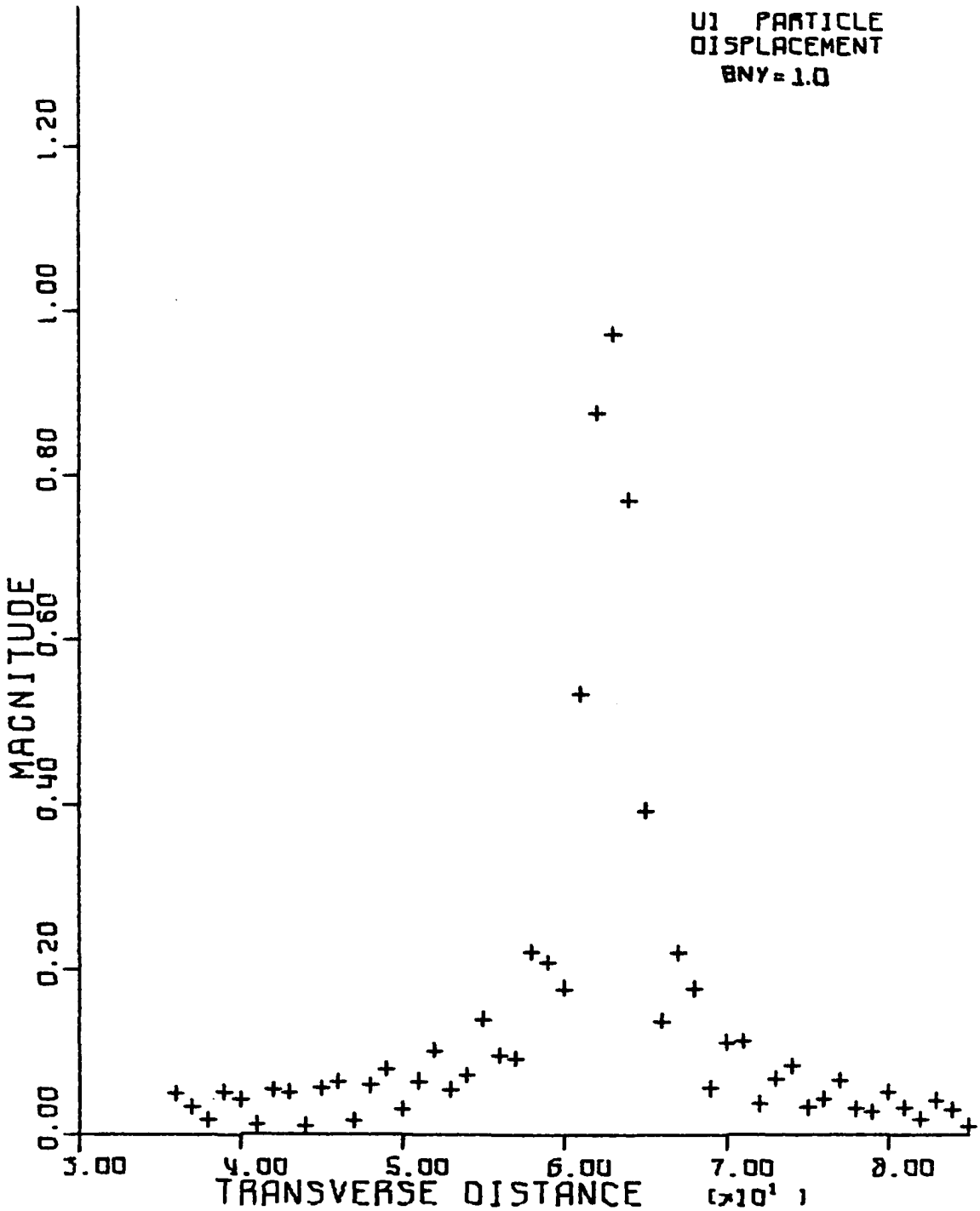

Figure 21. The magnitude of the U_1 particle displacement phasor vs. $k_o x$ at $k_o y = 1.0$

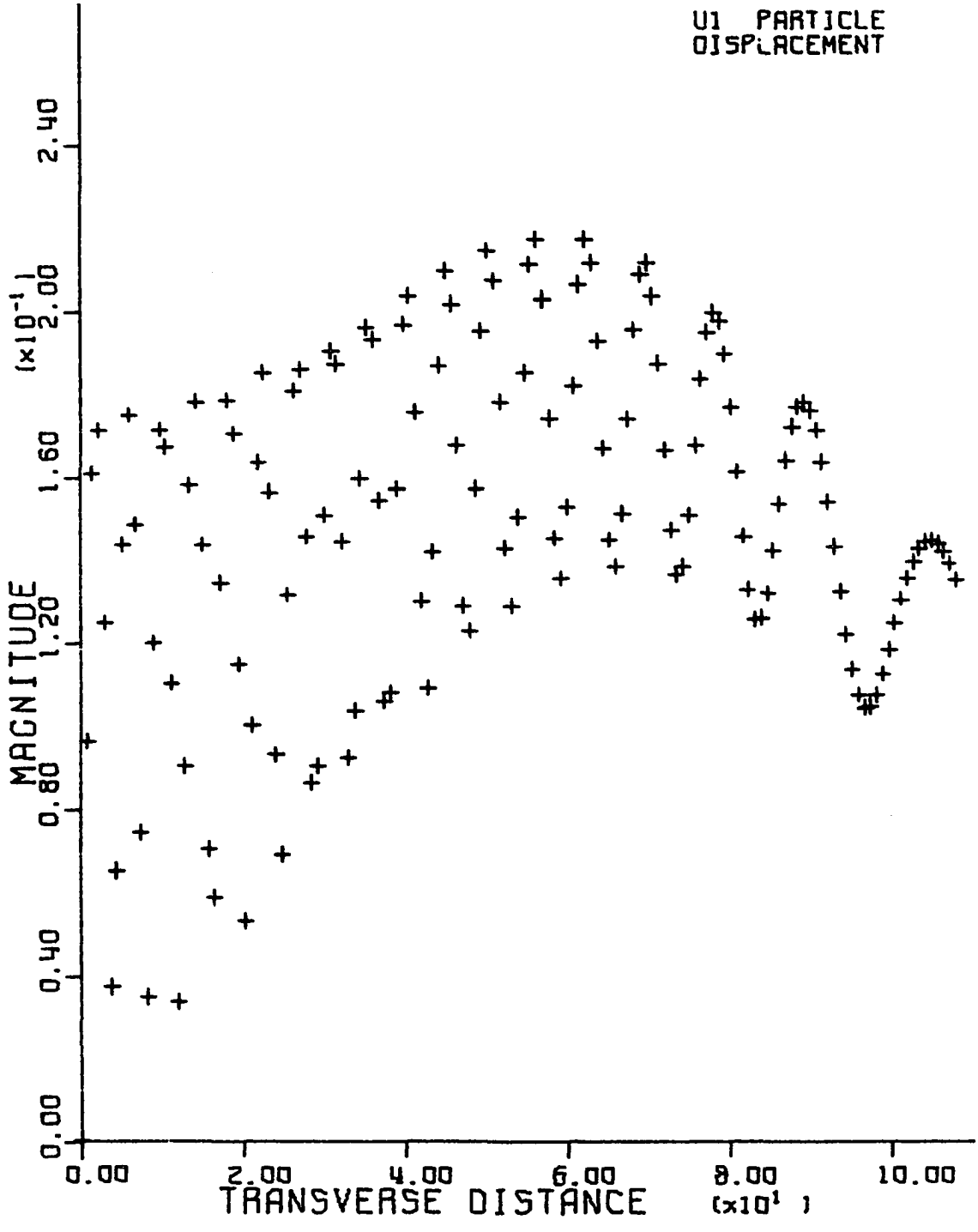

Figure 22. The magnitude of the U_1 particle displacement phasor vs. $k_o x$ at $k_o y = 50.0$

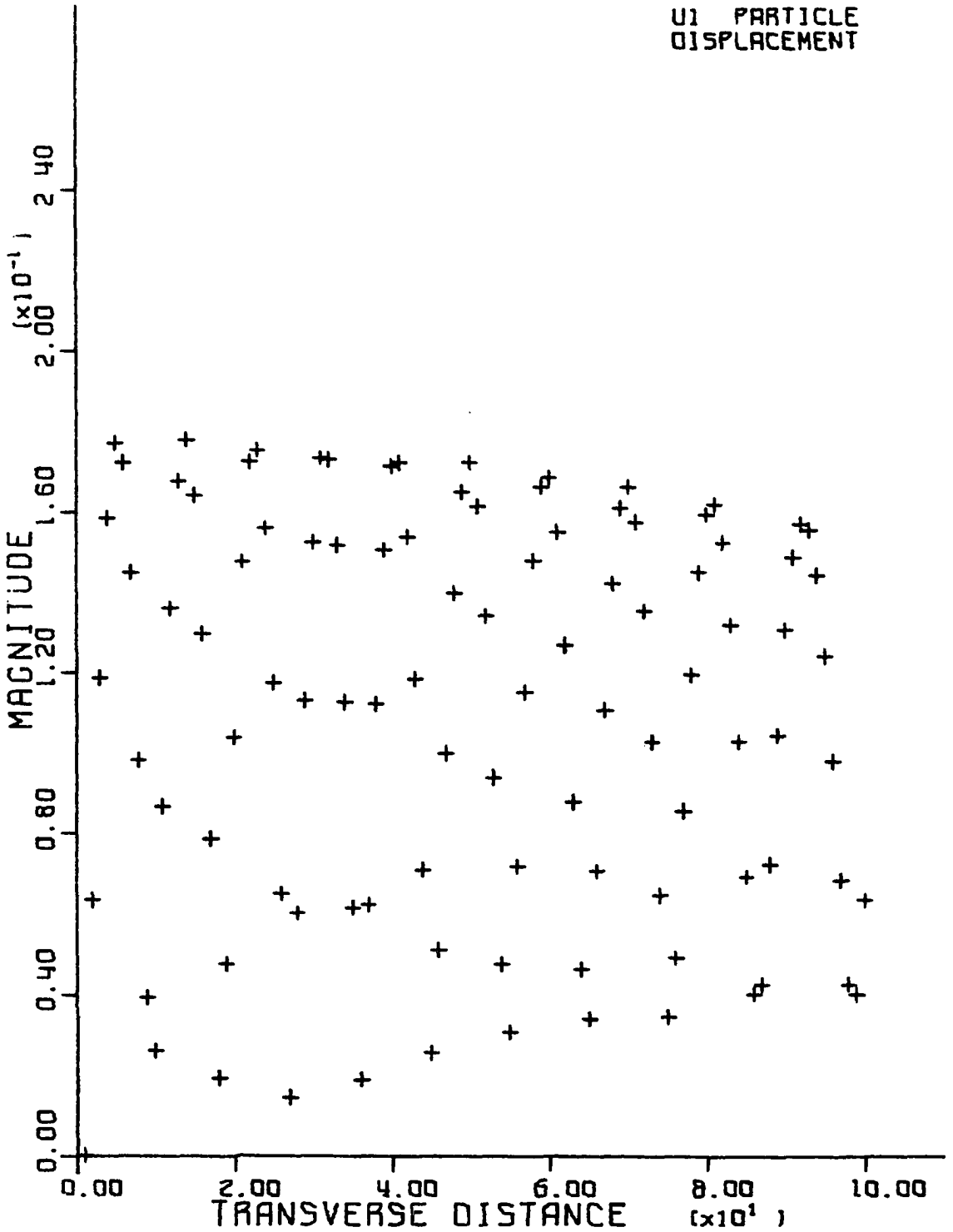

Figure 23. The magnitude of the U_1 particle displacement phasor vs. $k_o x$ at $k_o y = 160.0$

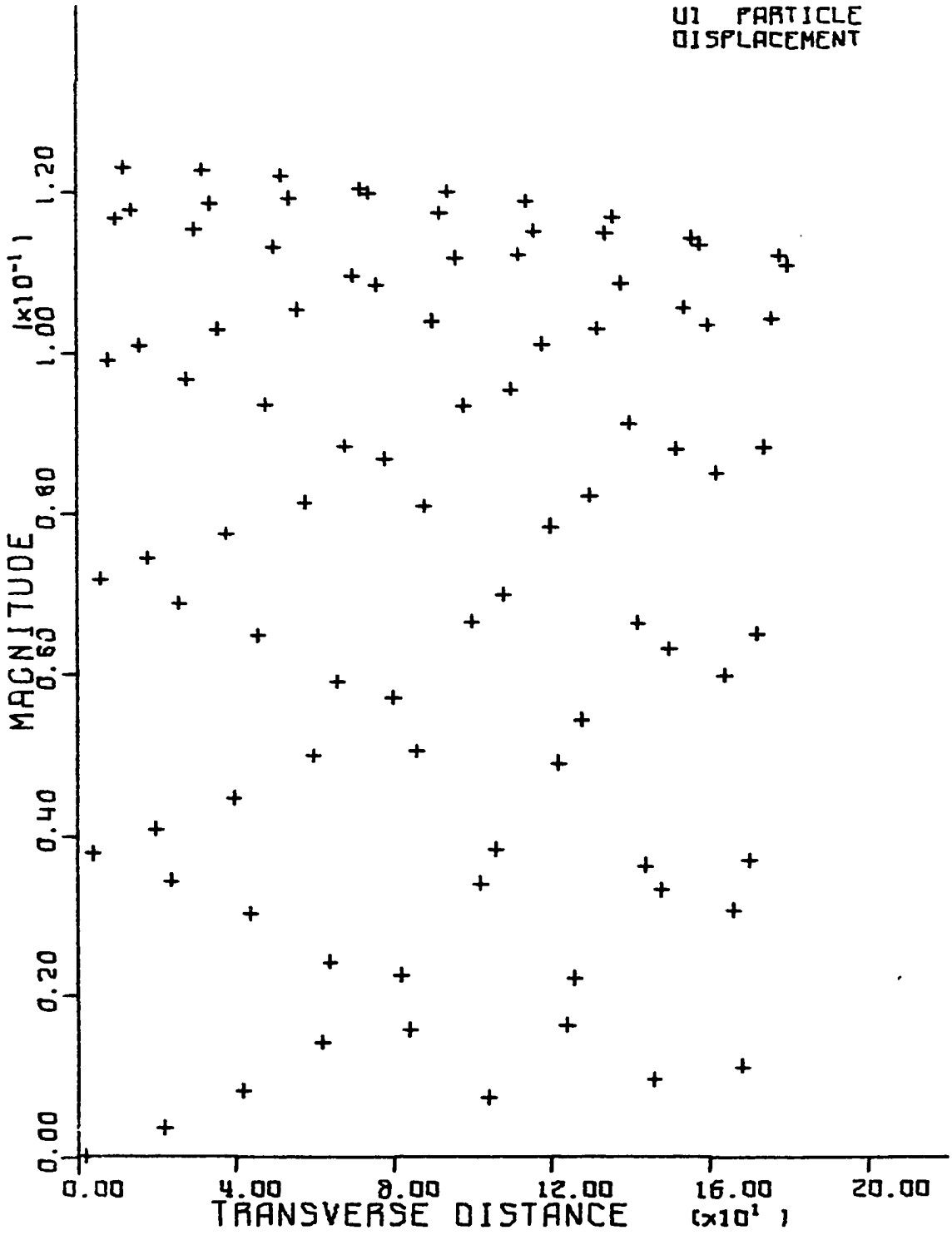

Figure 24. The magnitude of the U_1 particle displacement phasor vs. $k_o x_t$ at $k_o r = 400.0$

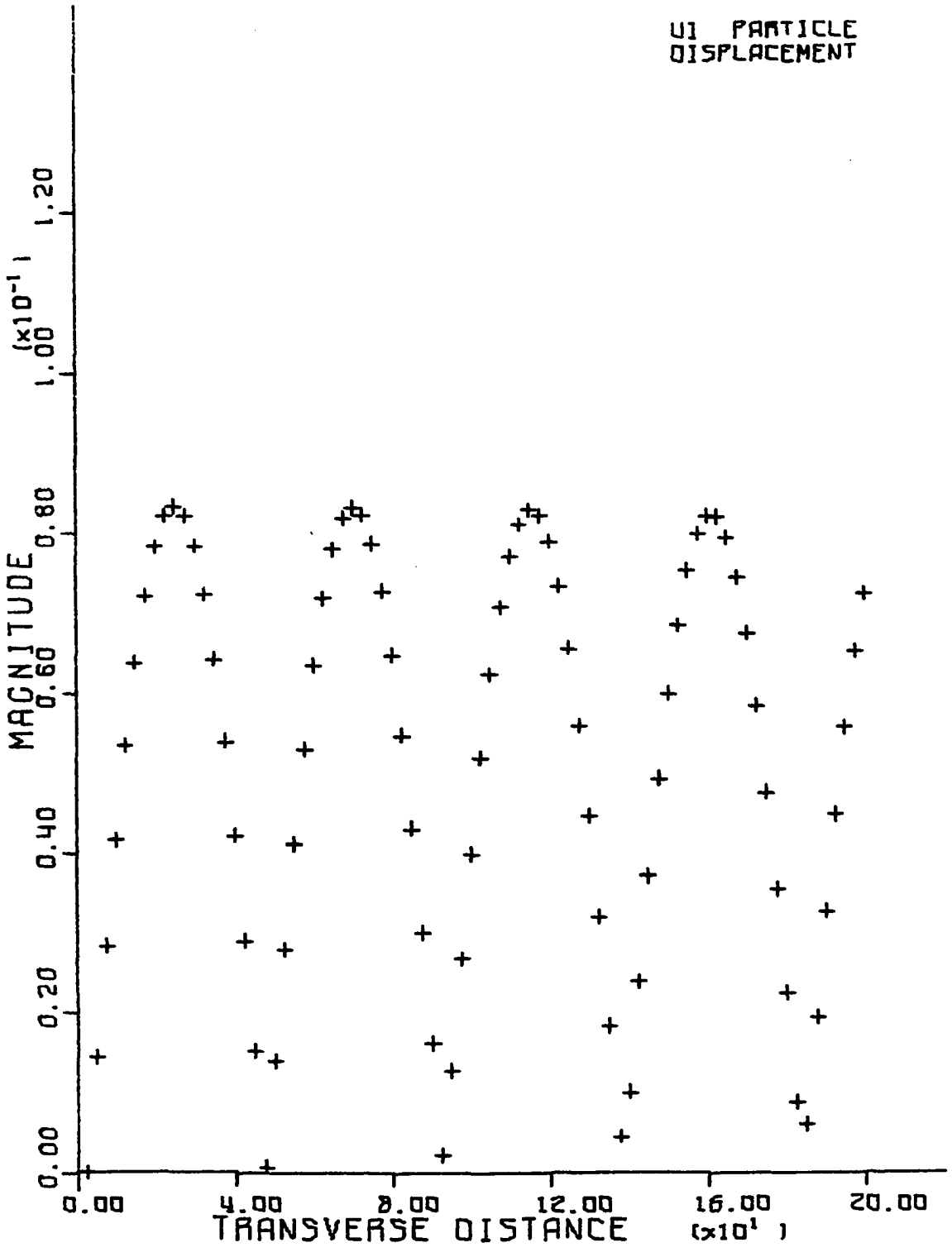

Figure 25. The magnitude of the U_1 particle displacement phasor vs. $k_o x_t$ at $k_o r = 900.0$

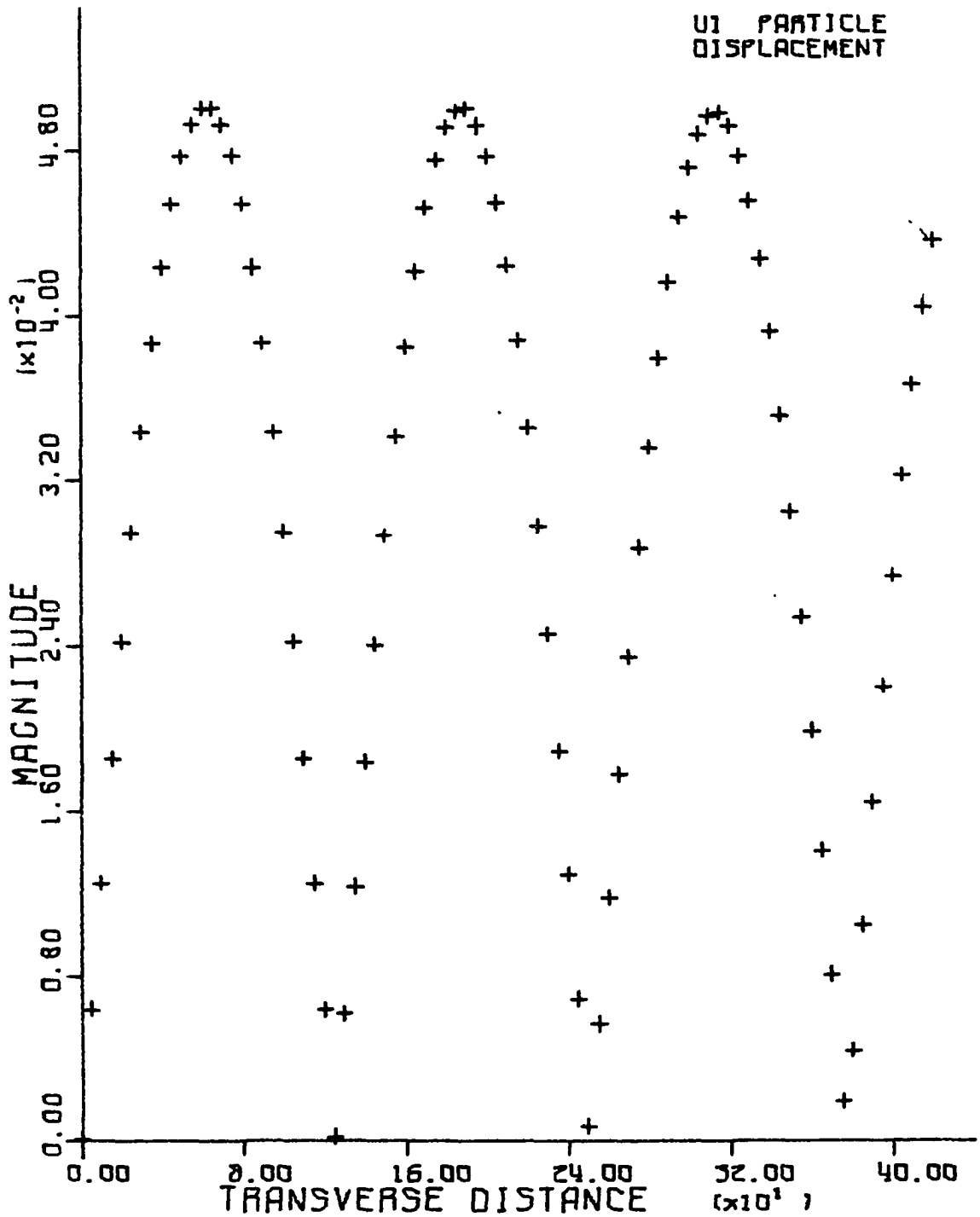

Figure 26. The magnitude of the U_1 particle displacement phasor vs. $k_o x_t$ at $k_o r = 2500.0$

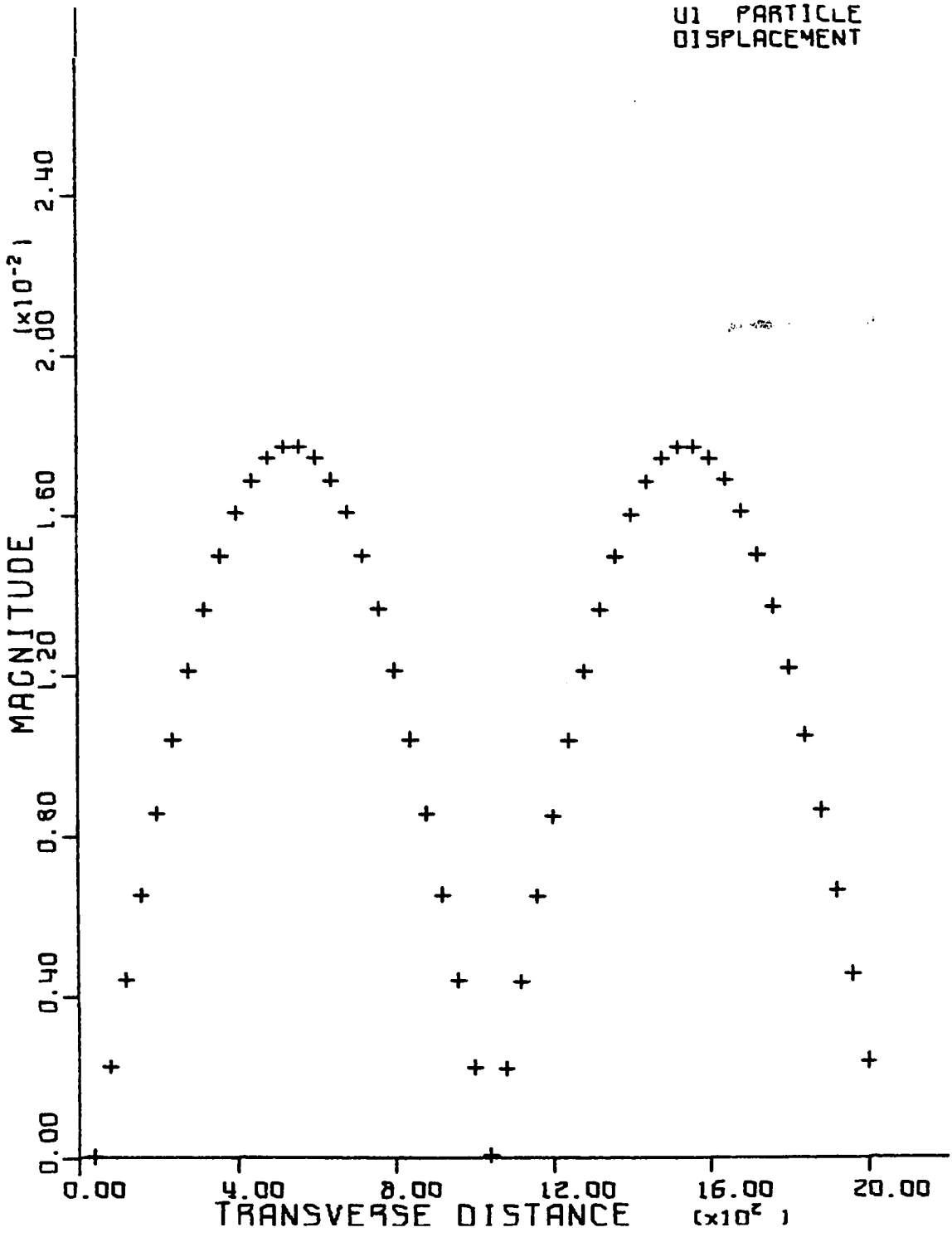

Figure 27. The magnitude of the U_1 particle displacement phasor vs. $k_o x_t$ at $k_o r = 20{,}000.0$

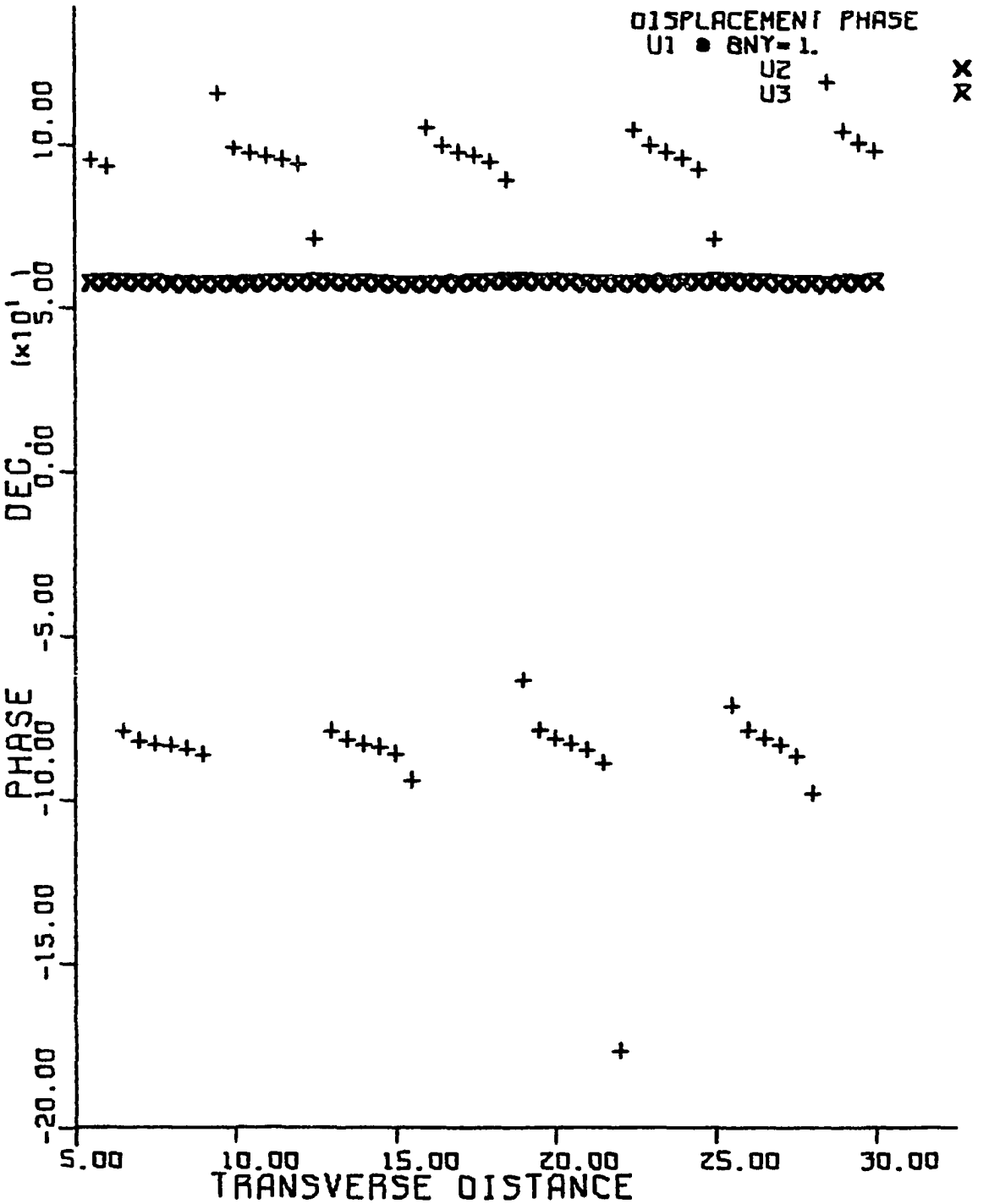

Figure 28. Phase of the U_1, U_2, and U_3 particle displacements vs. $k_o x$ at $k_o y = 1.0$

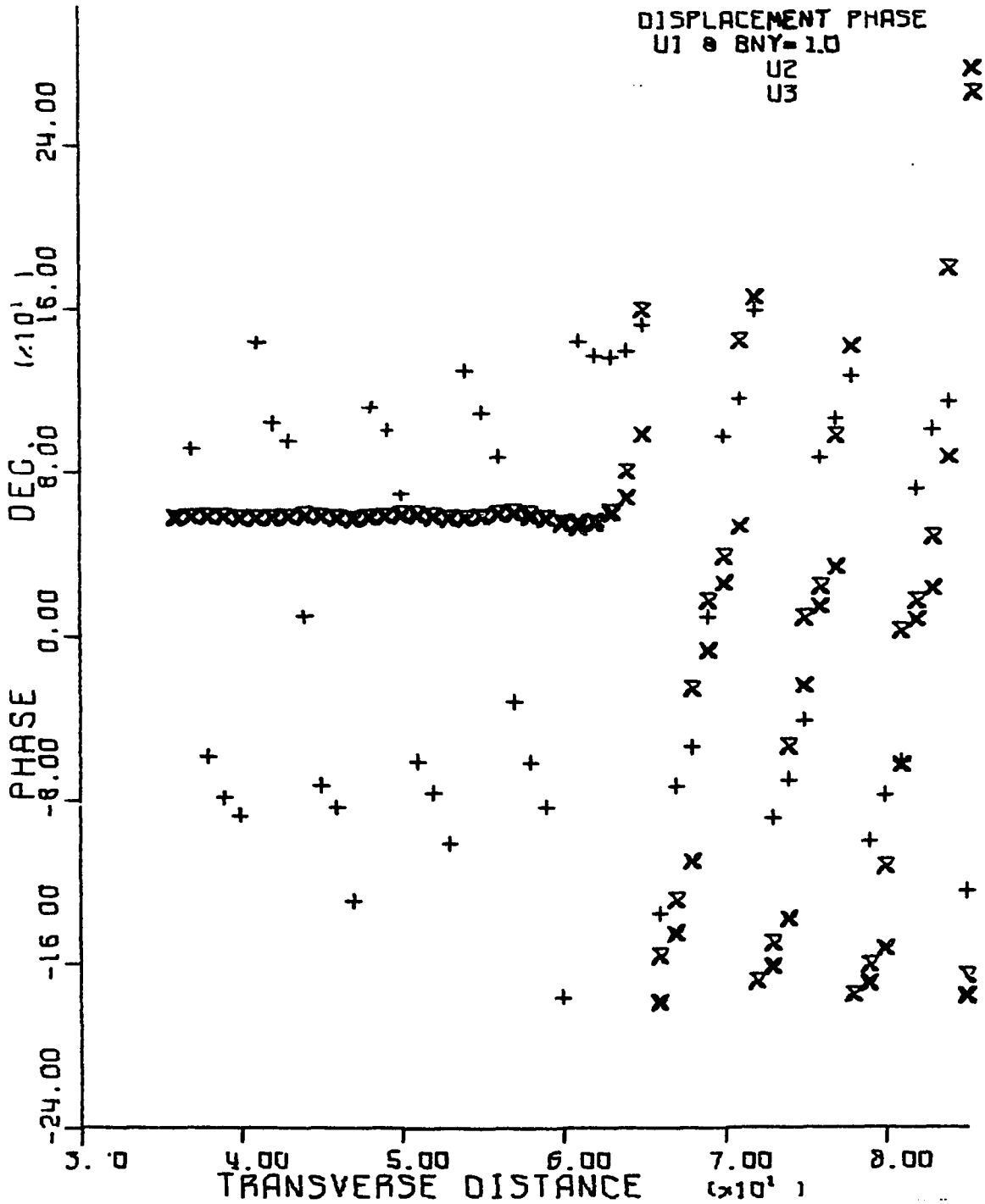

Figure 29. Phase of the U_1, U_2, and U_3 particle displacements vs. $k_o x$ at $k_o y = 1.0$

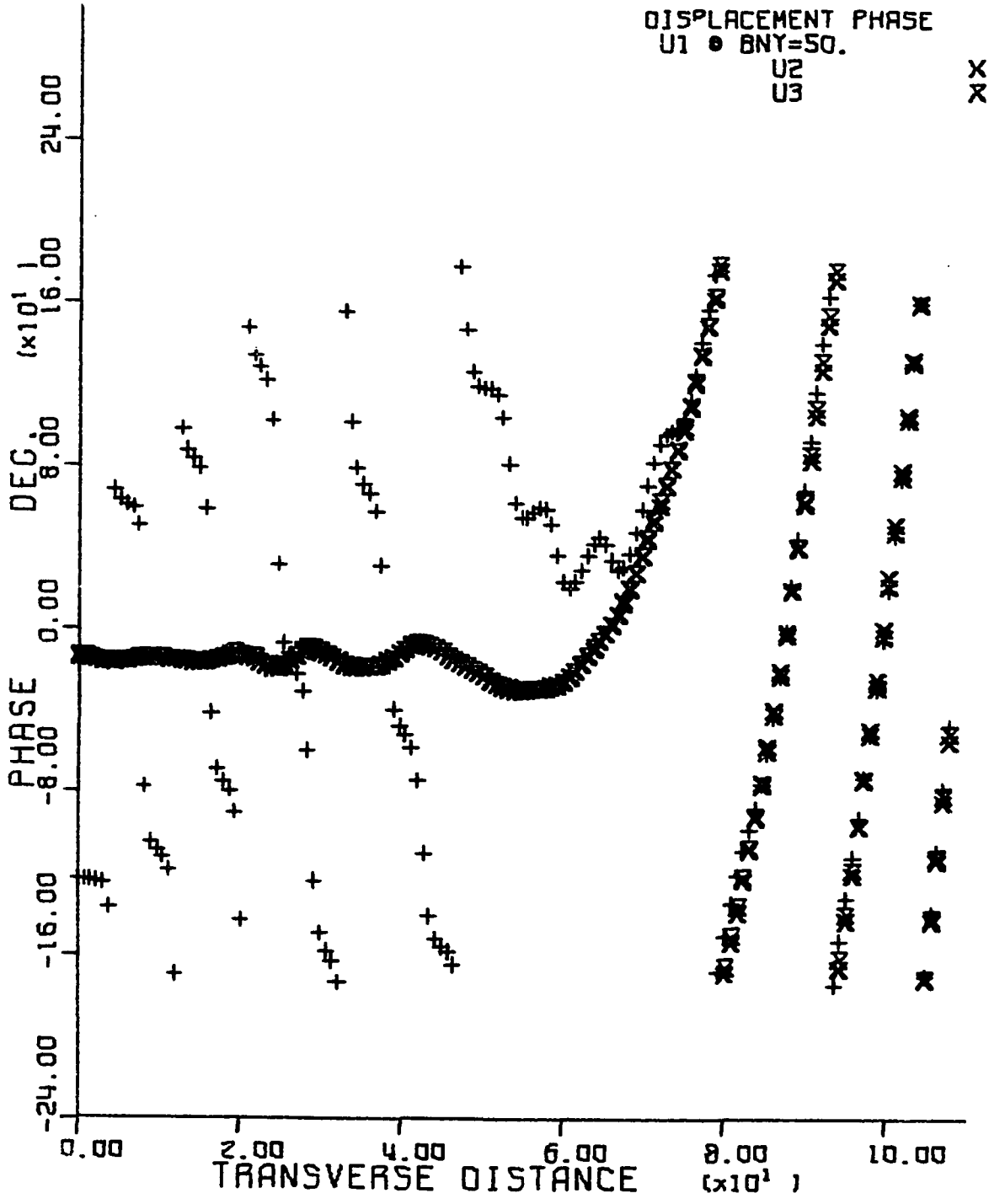

Figure 30. Phase of the U_1, U_2, and U_3 particle displacements vs. $k_o x$ at $k_o y = 50.0$

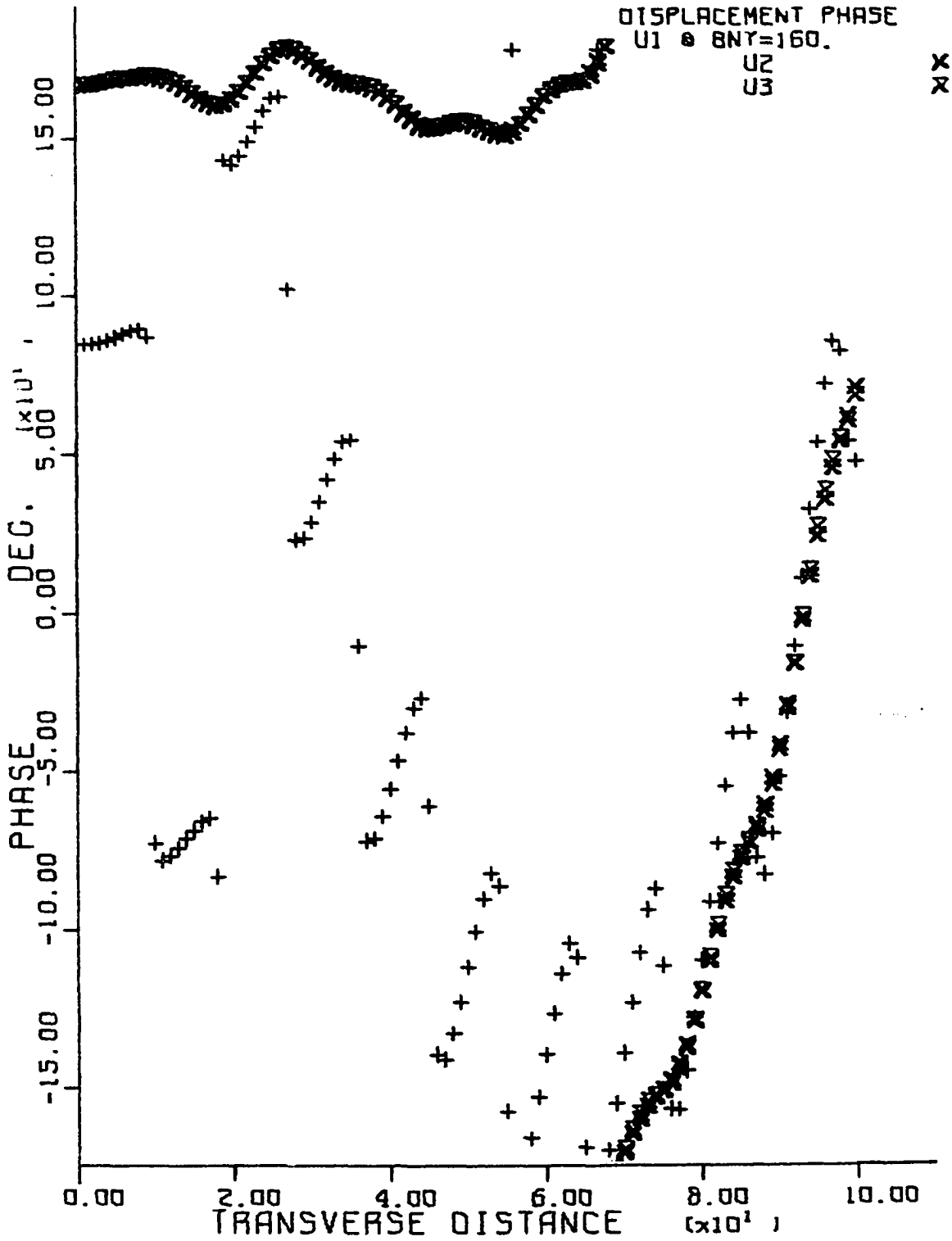

Figure 31. Phase of the U_1, U_2, and U_3 particle displacements vs. $k_o x$ at $k_o y = 160.0$

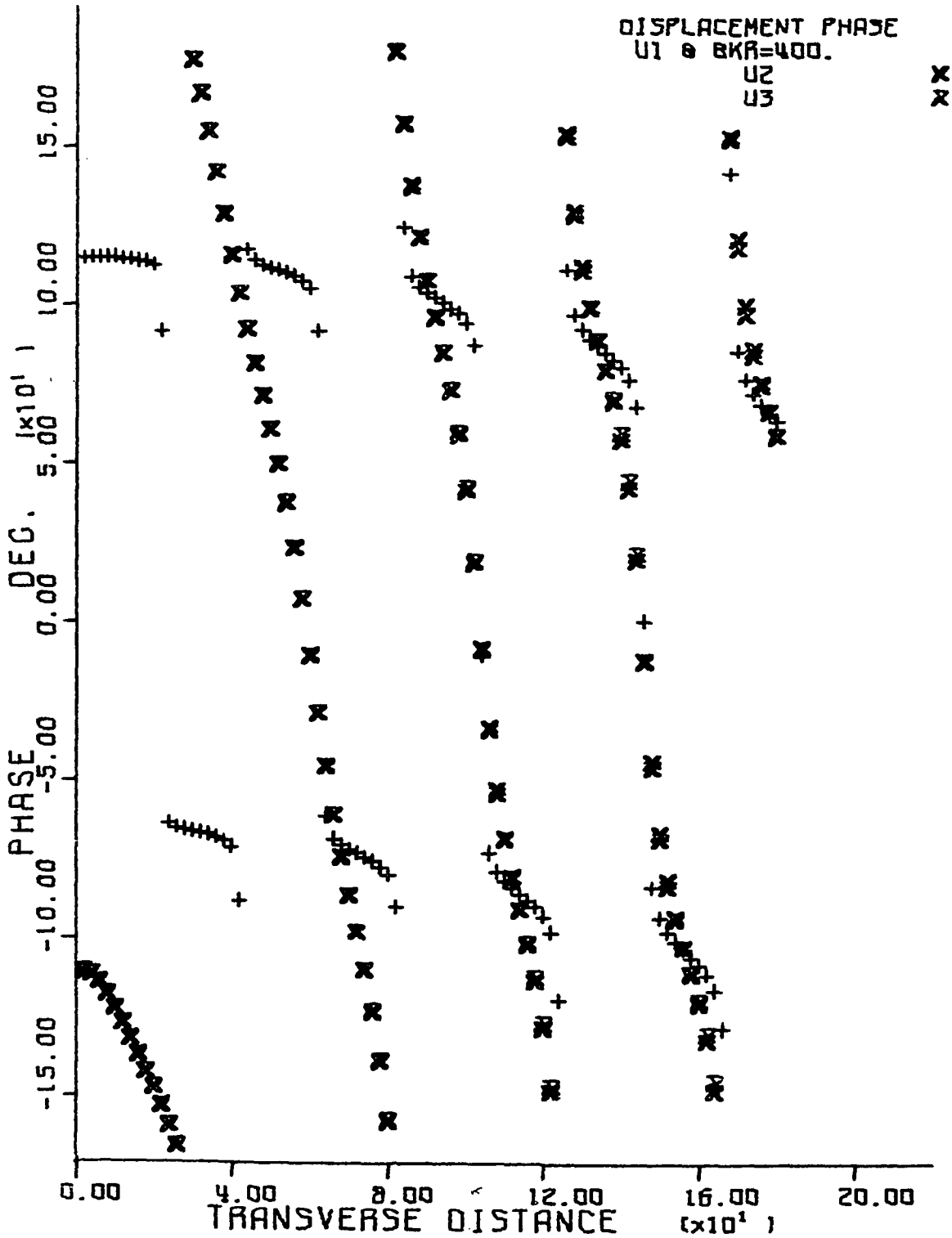

Figure 32. Phase of the U_1, U_2, and U_3 particle displacements vs. $k_o x_t$ at $k_o r = 400.0$

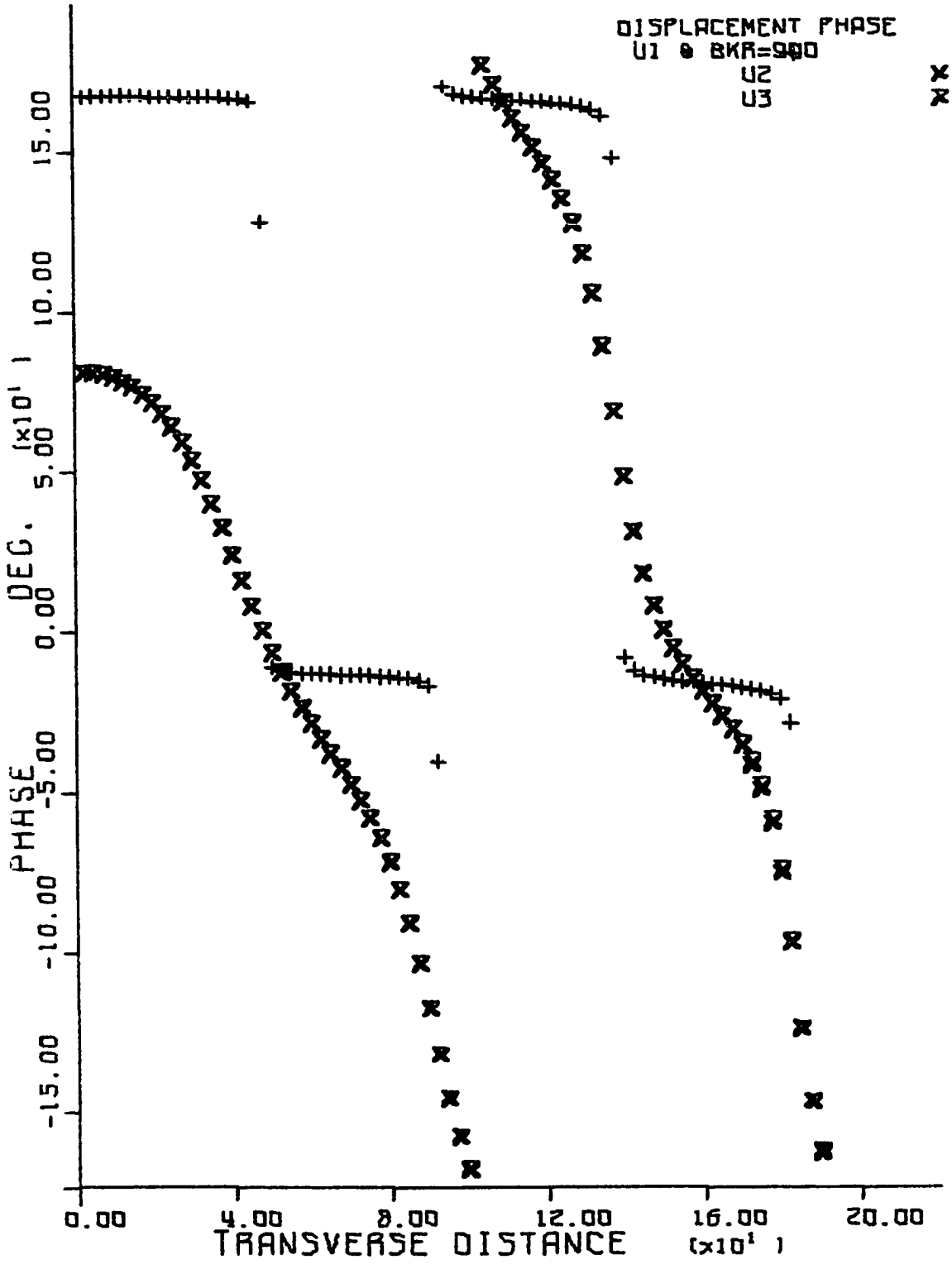

Figure 33. Phase of the U_1, U_2, and U_3 particle displacements vs. $k_o x_t$ at $k_o r = 900.0$

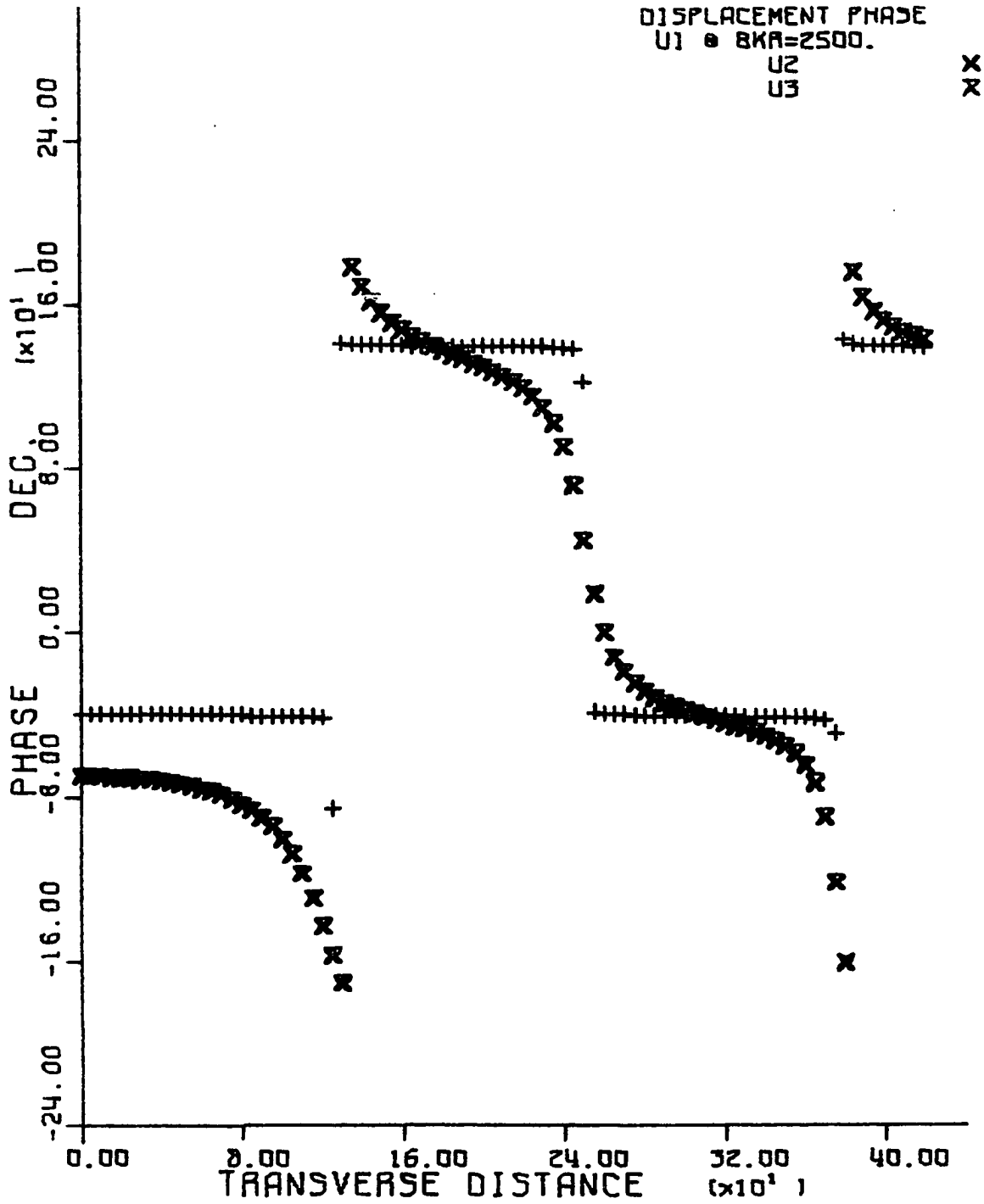

Figure 34. Phase of the U_1, U_2, and U_3 particle displacements vs. $k_o x_t$ at $k_o r$ = 2500.0

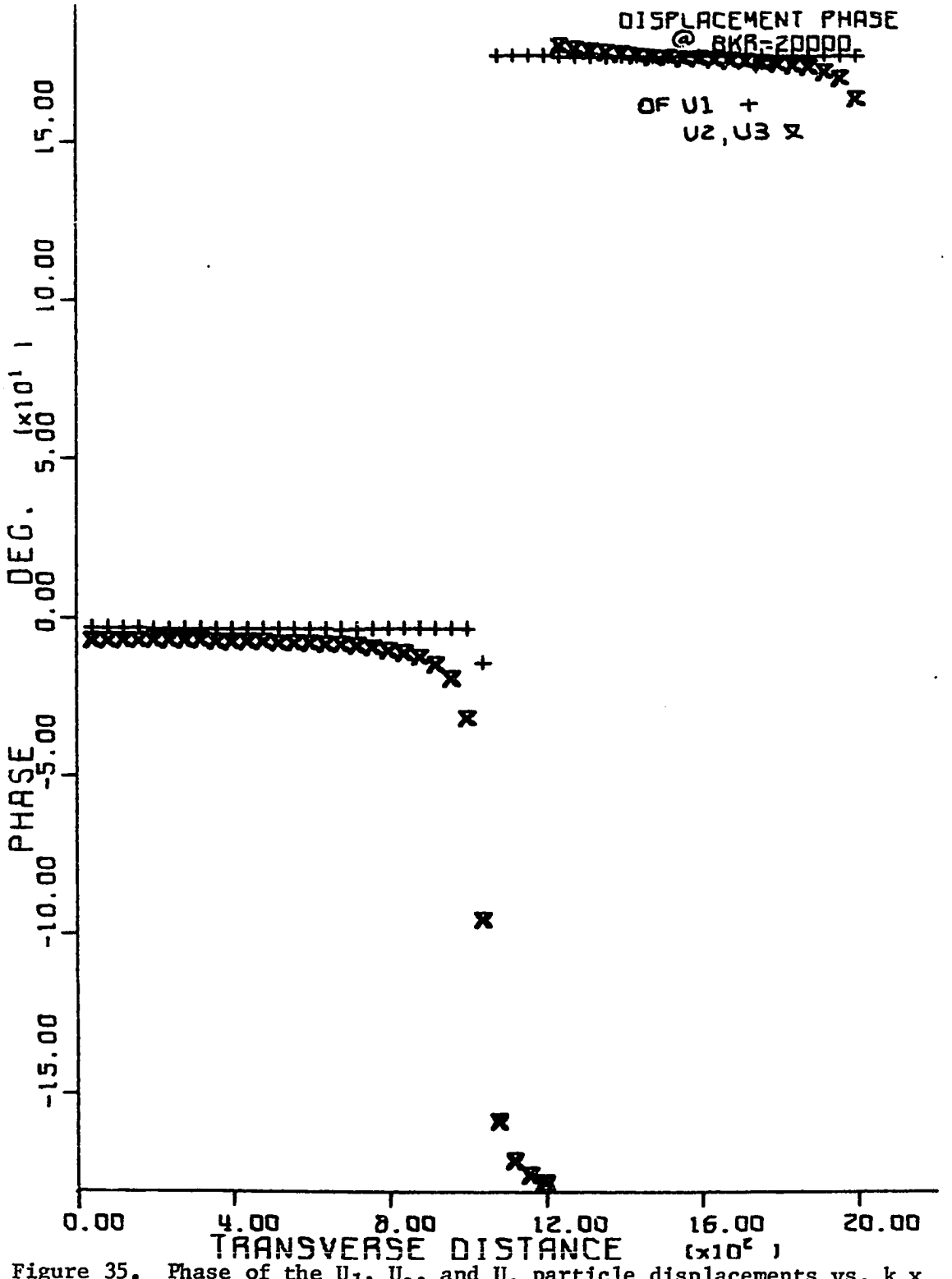

Figure 35. Phase of the U_1, U_2, and U_3 particle displacements vs. $k_o x_t$ at $k_o r = 200{,}000{,}0^2$

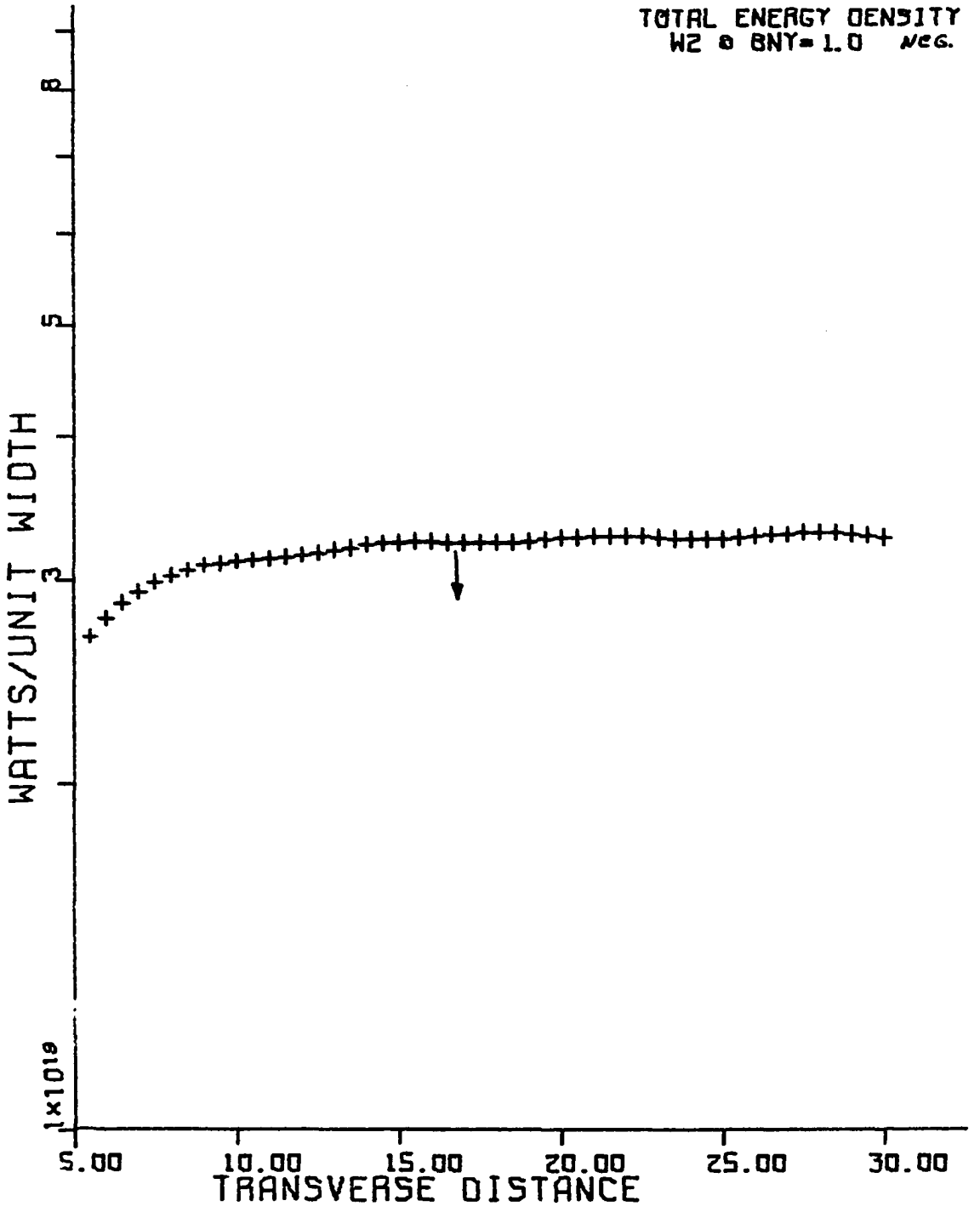

Figure 36. The y component of the integrated Poynting vector vs. $k_o x$ at $k_o y = 1.0$

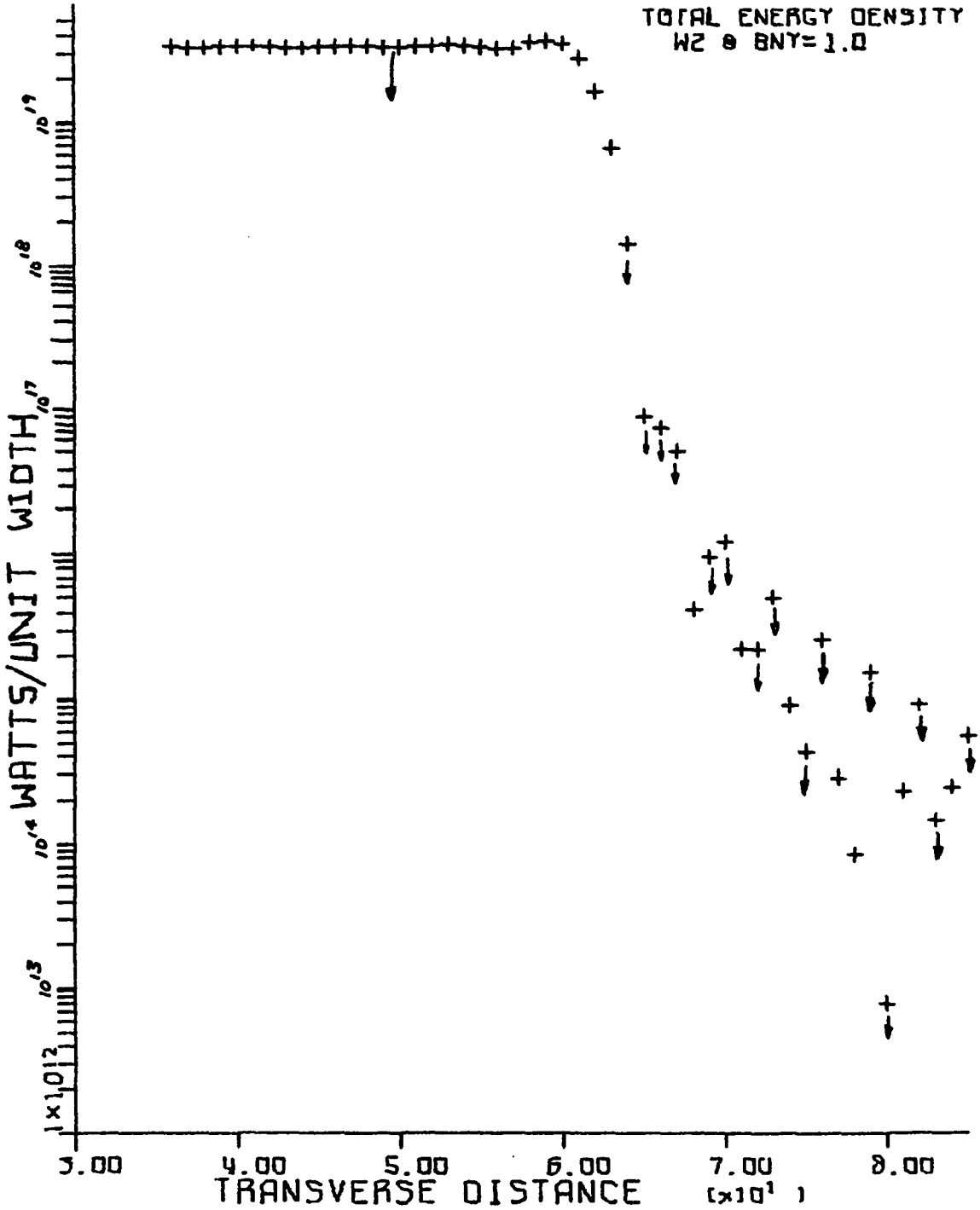

Figure 37. The y component of the integrated Poynting vector vs. $k_o x$ at $k_o y = 1.0$

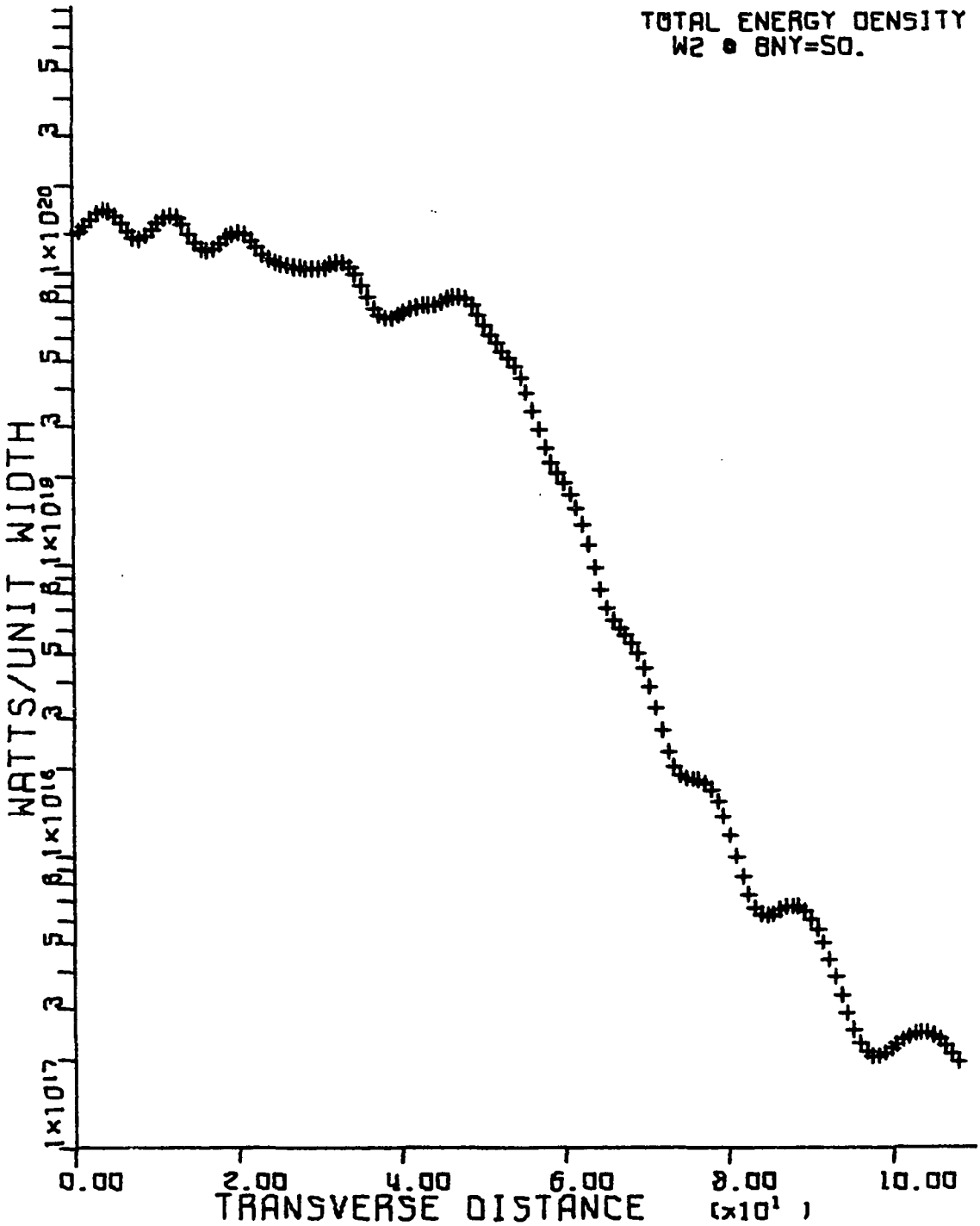

Figure 38. The y component of the integrated Poynting vector vs. $k_o x$ at $k_o y = 50.0$

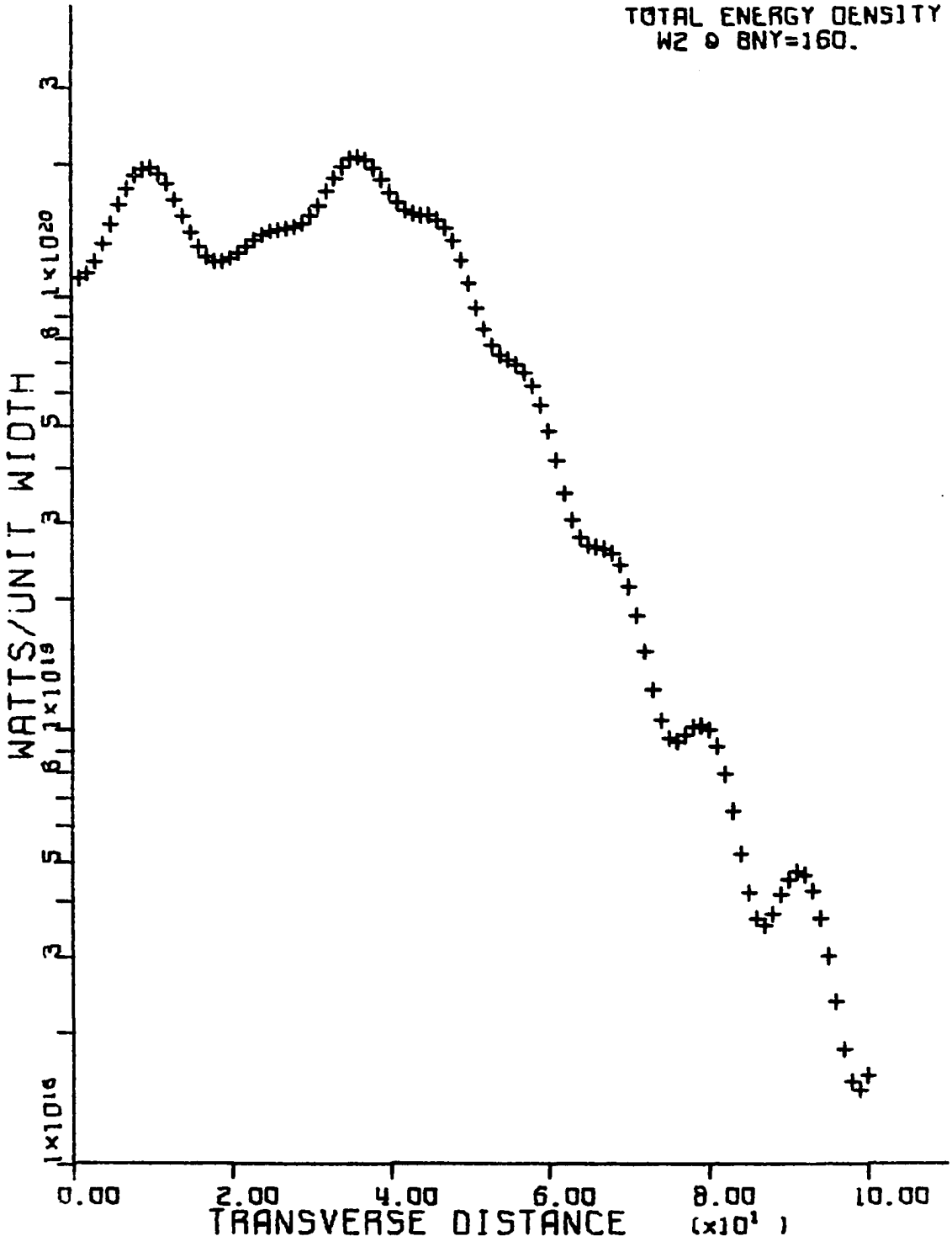

Figure 39. The y component of the integrated Poynting vector vs. $k_o x$ at $k_o y = 160.0$

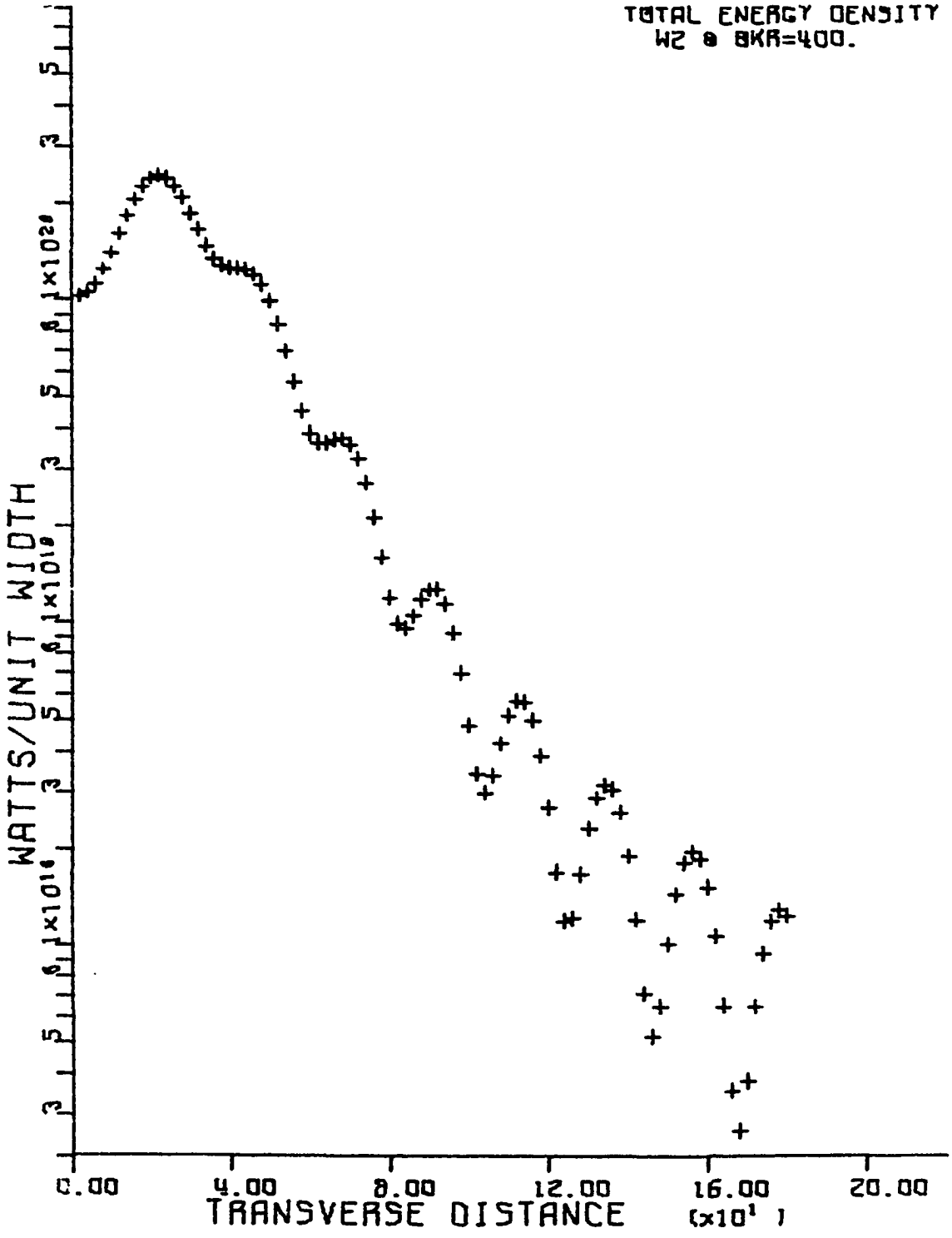

Figure 40. The y component of the integrated Poynting vector vs. $k_o x_t$ at $k_o r = 400.0$

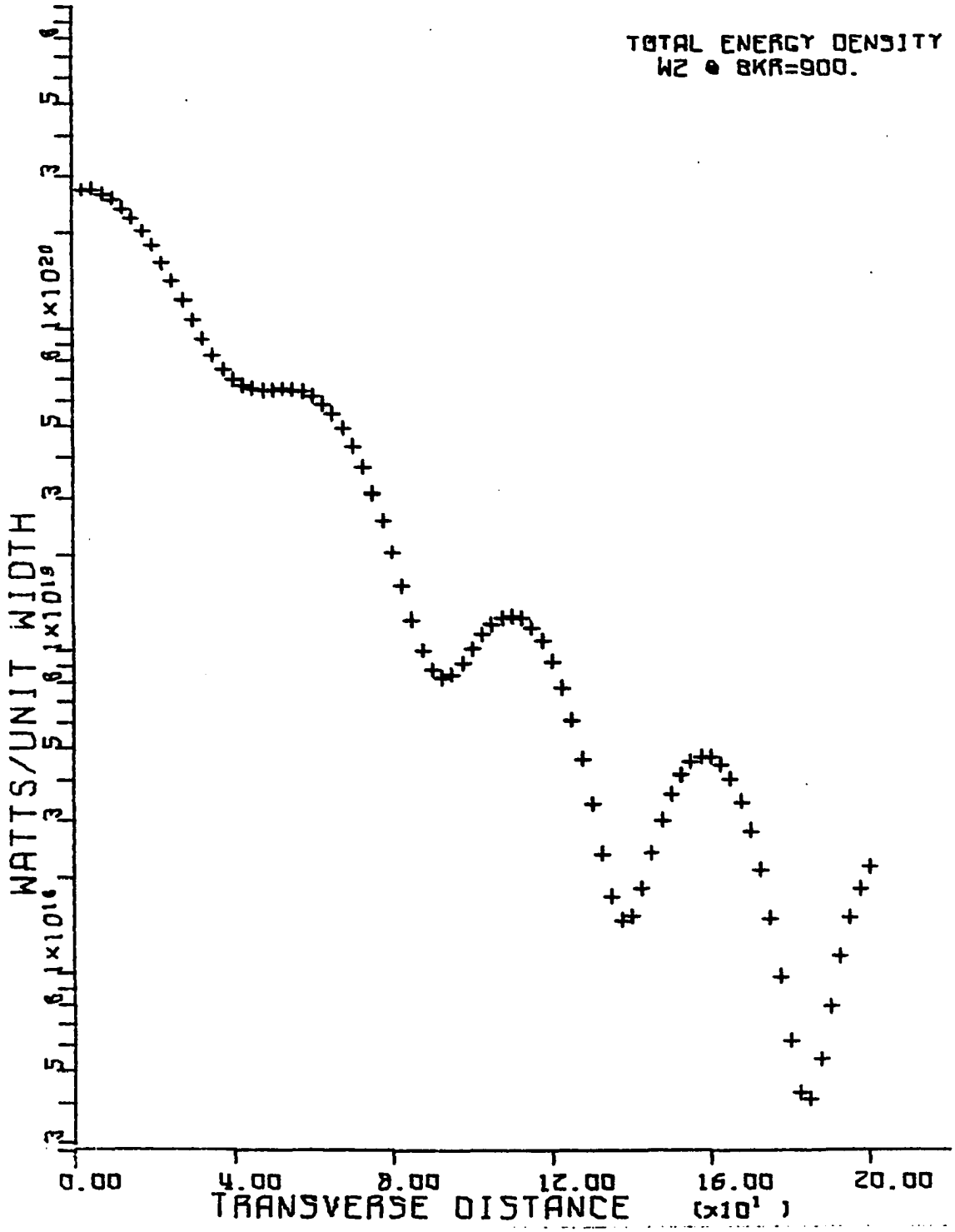

Figure 41. The y component of the integrated Poynting vector vs. $k_o x_t$ at $k_o r = 900.0$

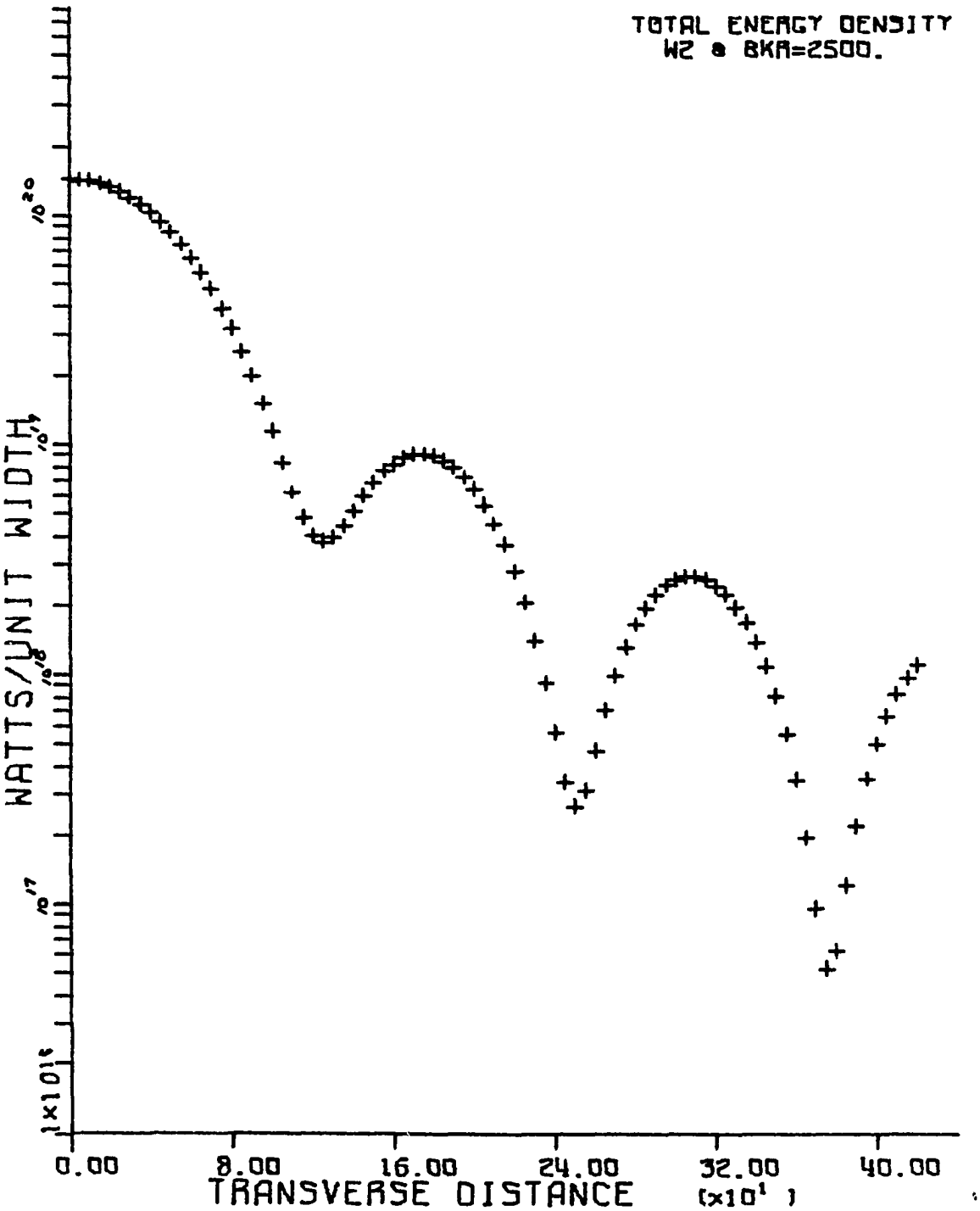

Figure 42. The y component of the integrated Poynting vector vs. $k_o x_t$ at $k_o r = 2500.0$

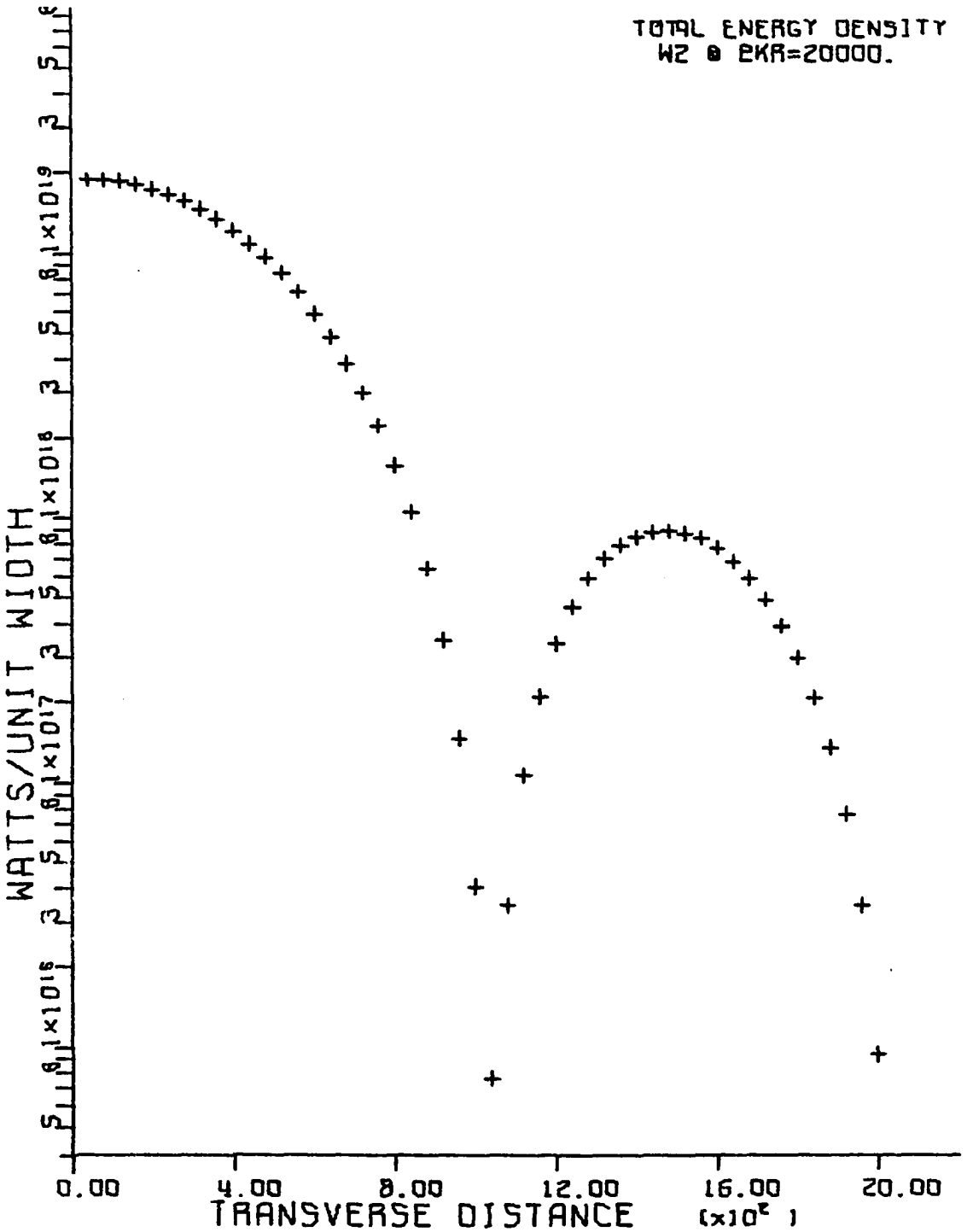

Figure 43. The y component of the integrated Poynting vector vs. $k_o x_t$ at $k_o r = 20{,}000.0$

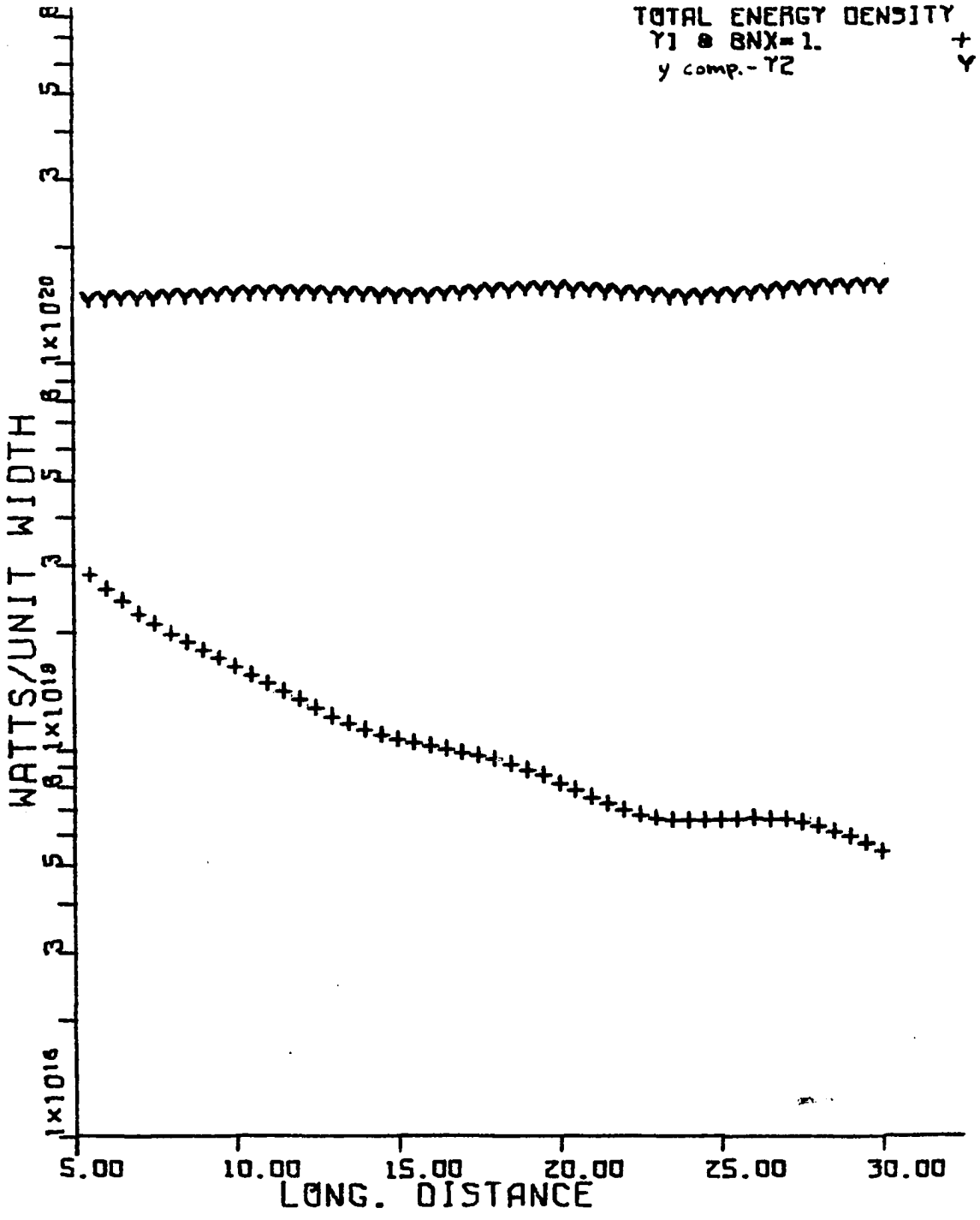

Figure 44. The x and y components of the integrated Poynting vector vs. $k_o y$ at $k_o x = 1.0$

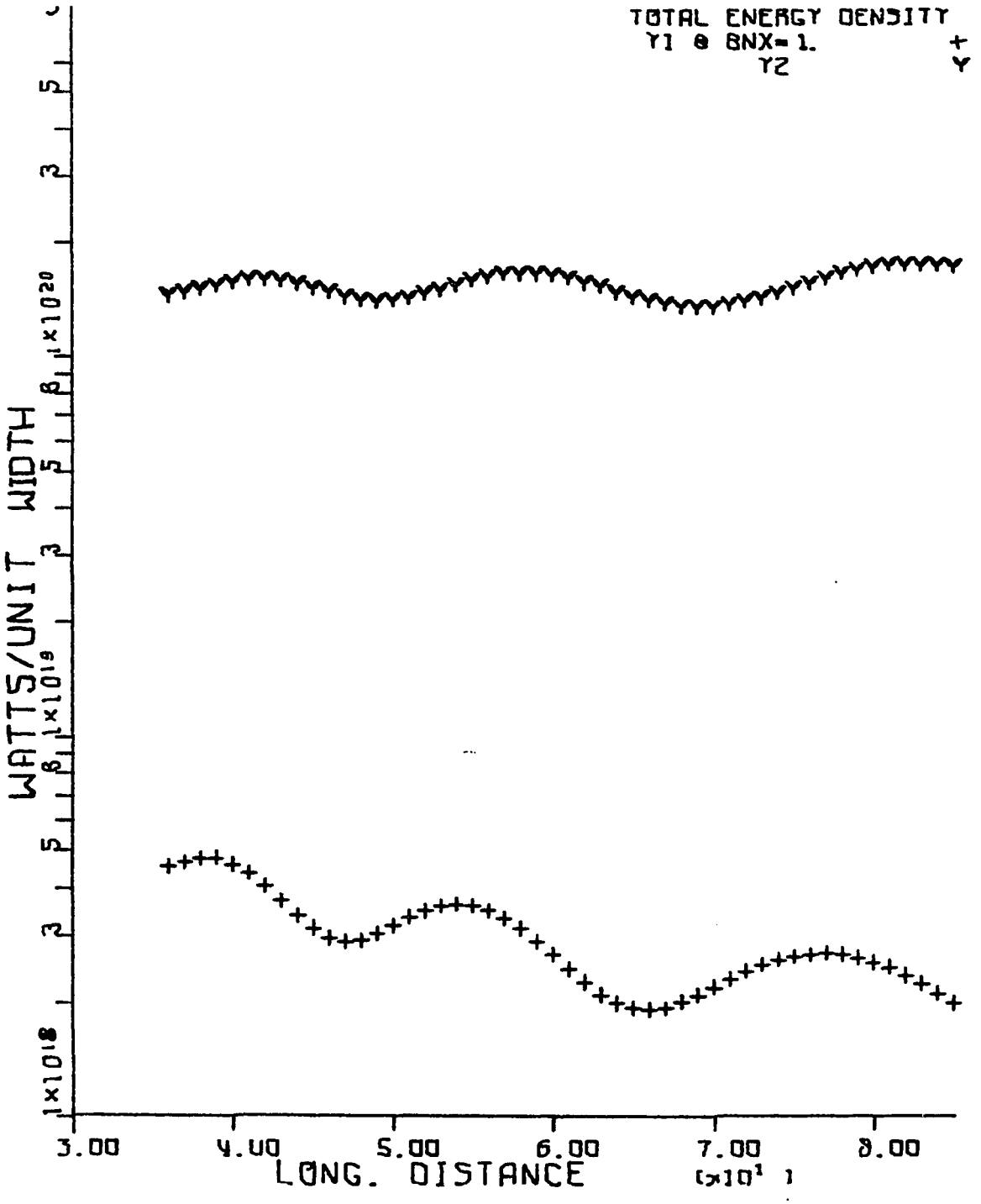

Figure 45. The x and y components of the integrated Poynting vector vs. $k_o y$ at $k_o x = 1.0$

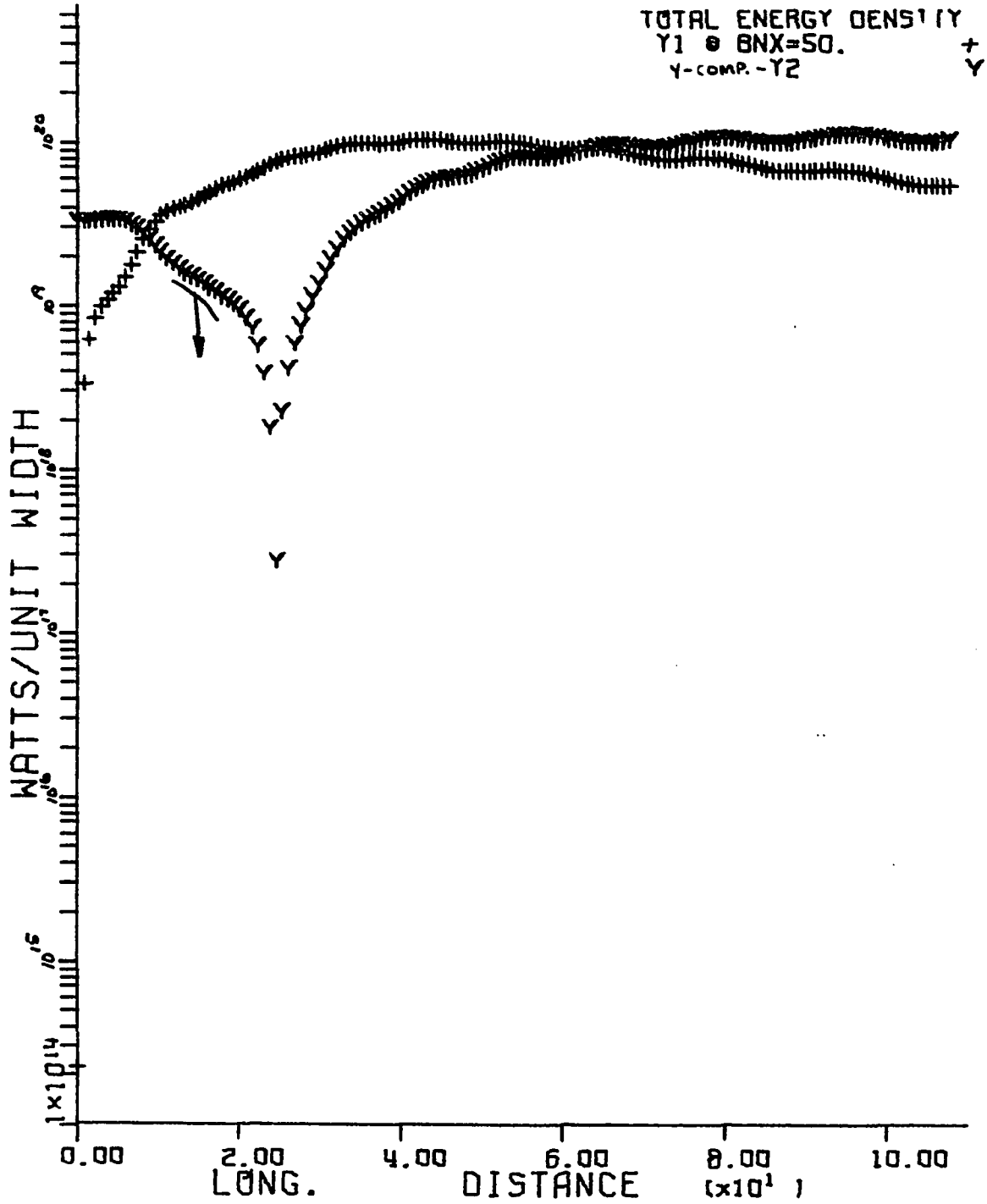

Figure 46. The x and y components of the integrated Poynting vector vs. $k_o y$ at $k_o x = 50.0$

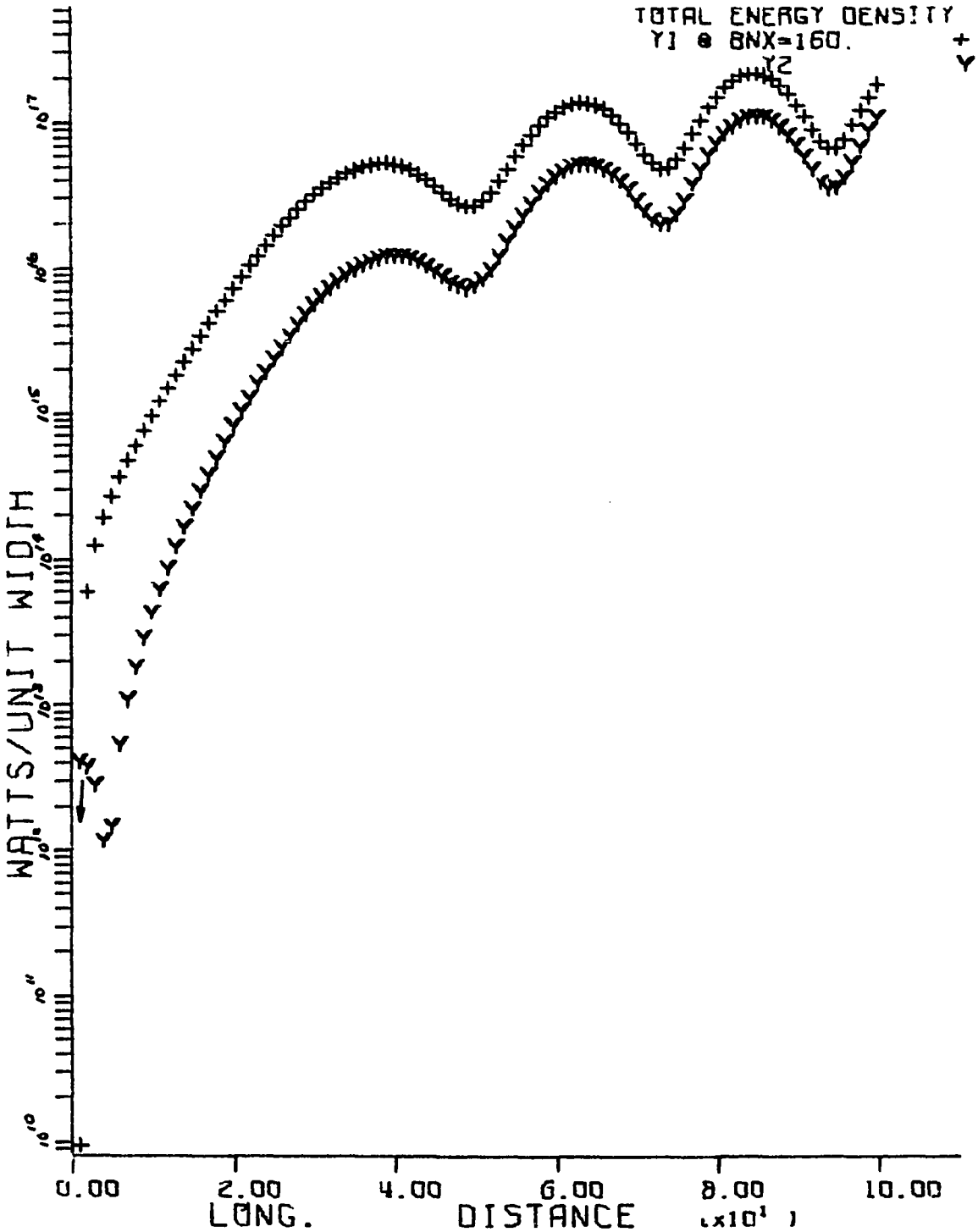

Figure 47. The x and y components of the integrated Poynting vector vs. $k_o y$ at $k_o x = 160.0$

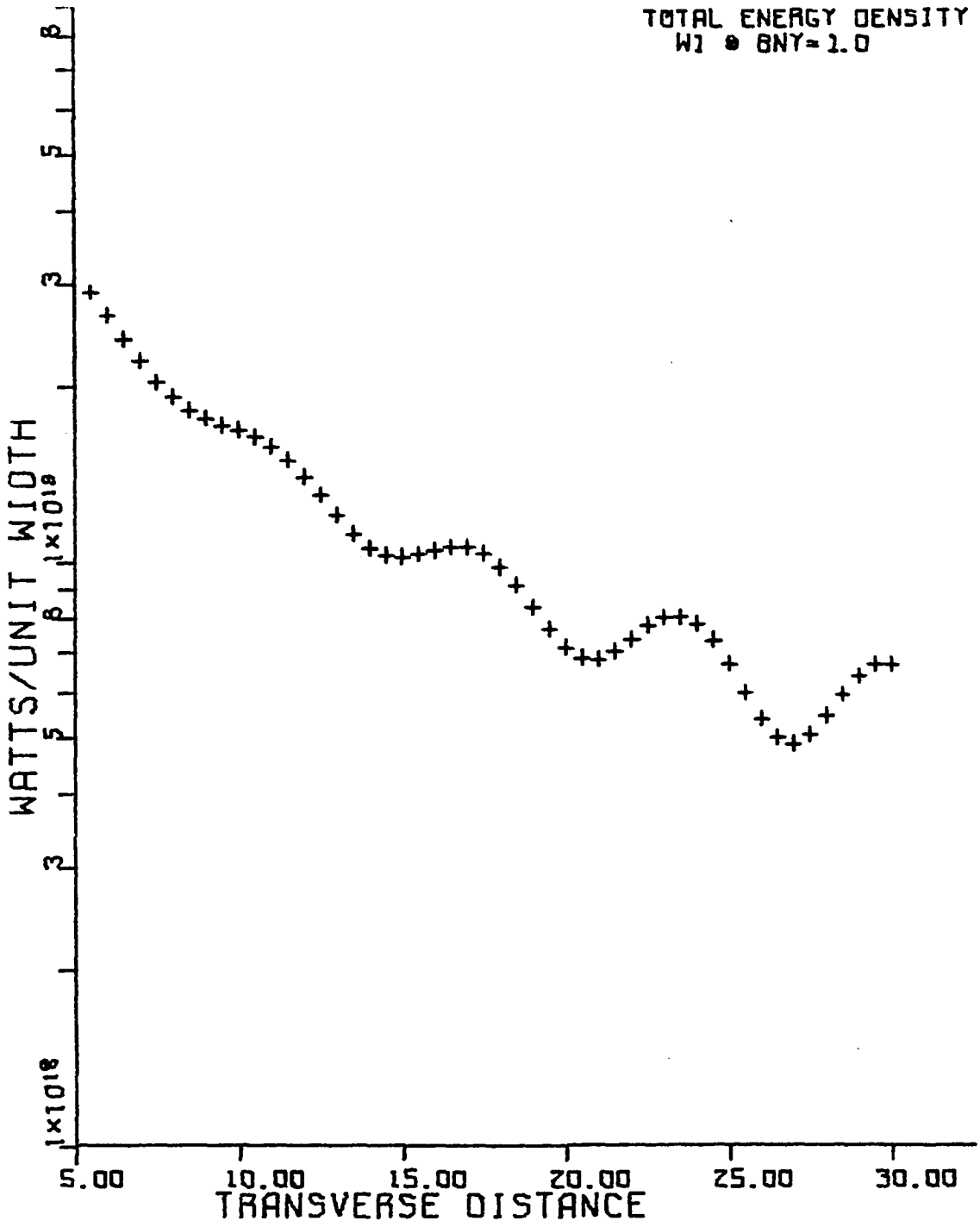

Figure 48. The x component of the integrated Poynting vector vs. $k_o x$ at $k_o y = 1.0$

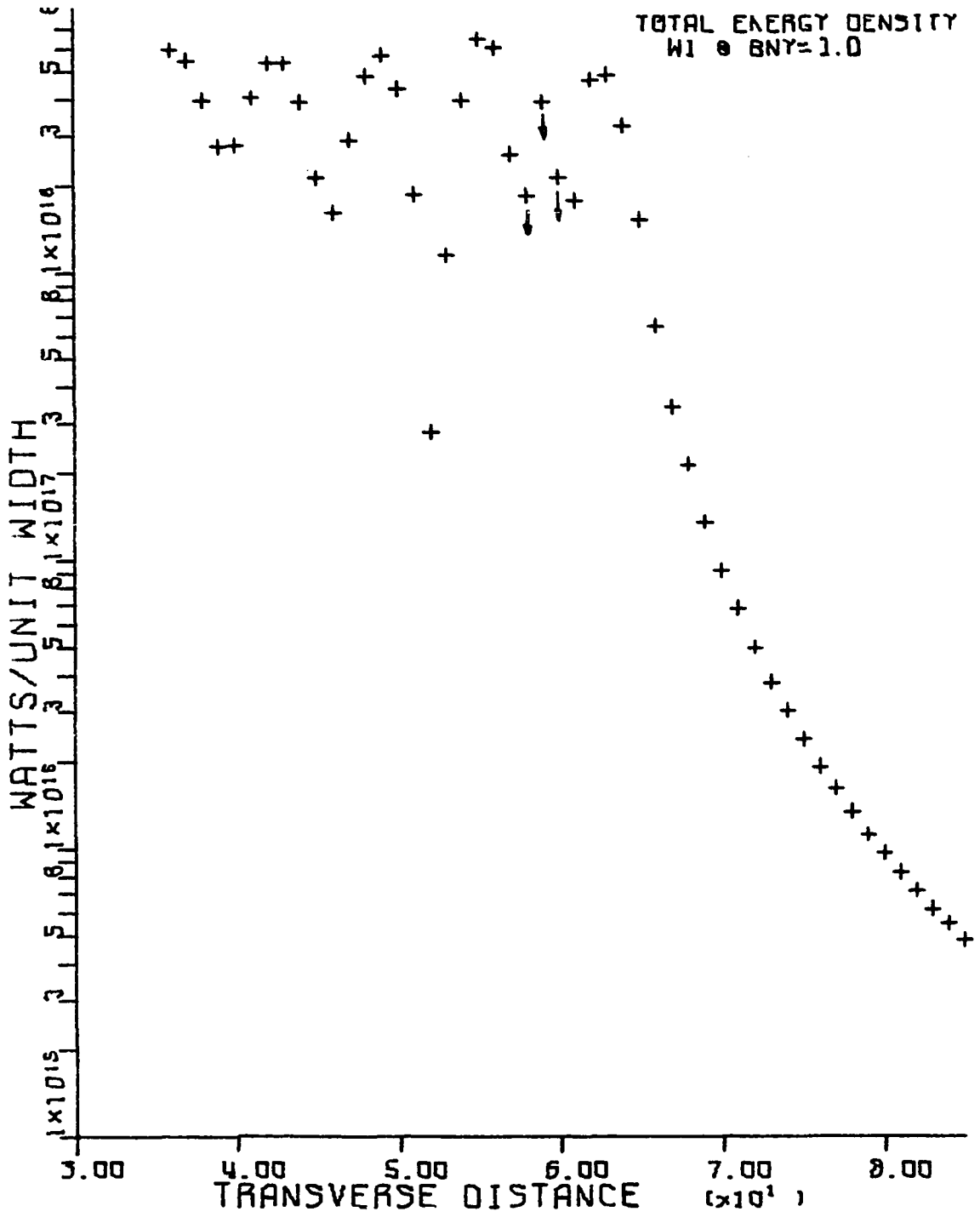

Figure 49. The x component of the integrated Poynting vector vs. $k_o x$ at $k_o y = 1.0$

Figure 50. The x component of the integrated Poyting vector vs. $k_o x$ at $k_o y = 50.0$

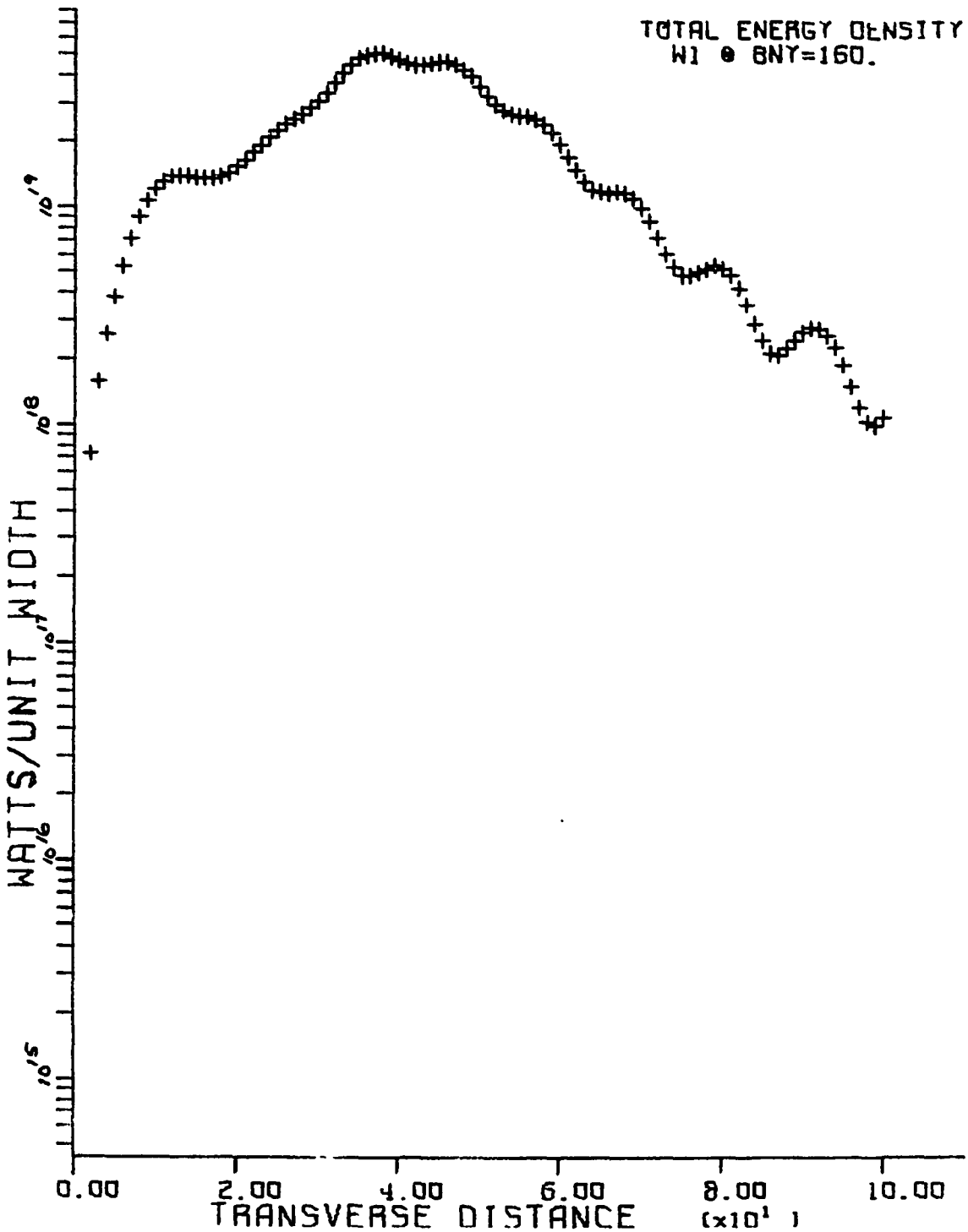

Figure 51. The x component of the integrated Poynting vector vs. $k_o x$ at $k_o y = 160.0$

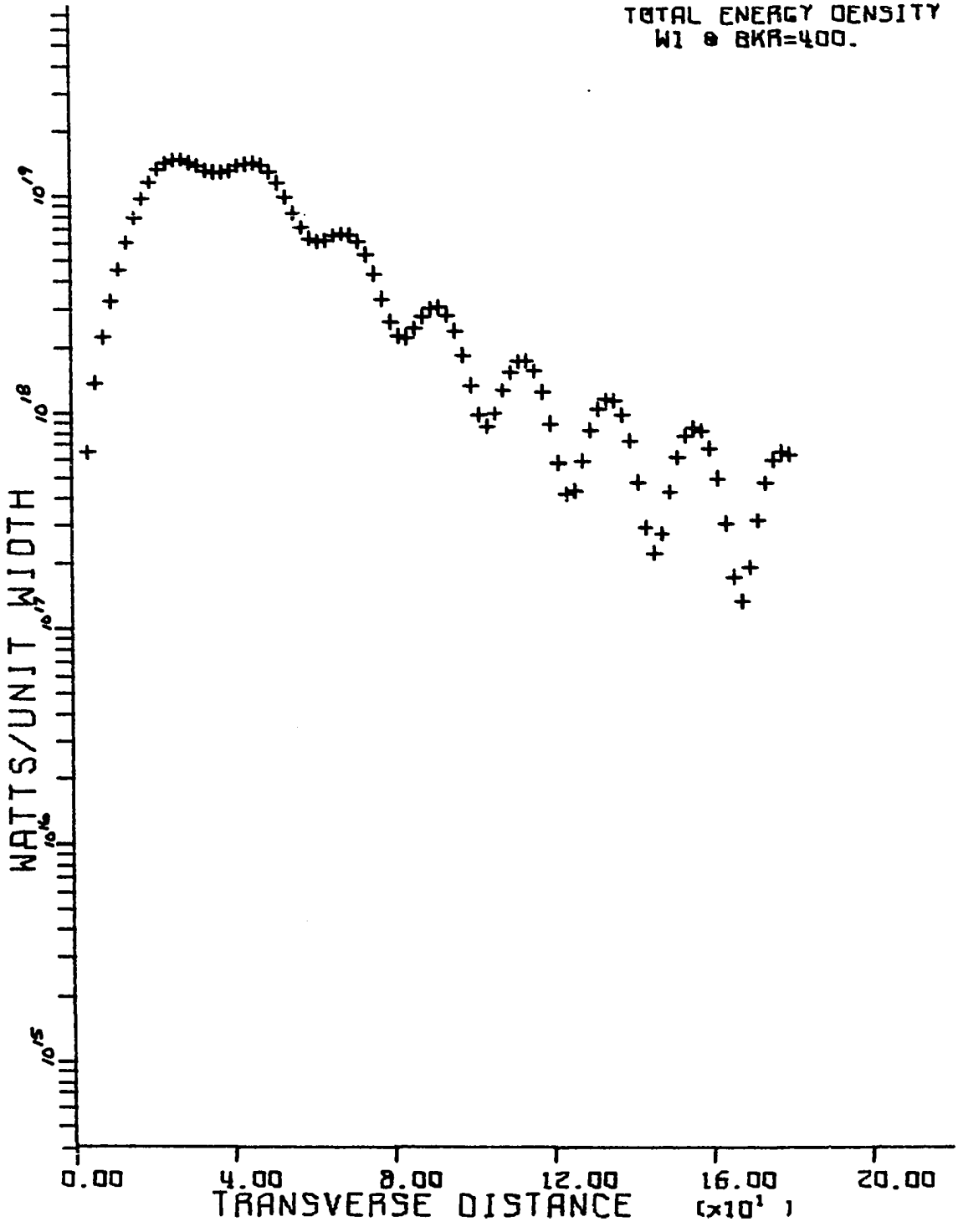

Figure 52. The x component of the integrated Poynting vector vs. $k_o x_t$ at $k_o r = 400.0$

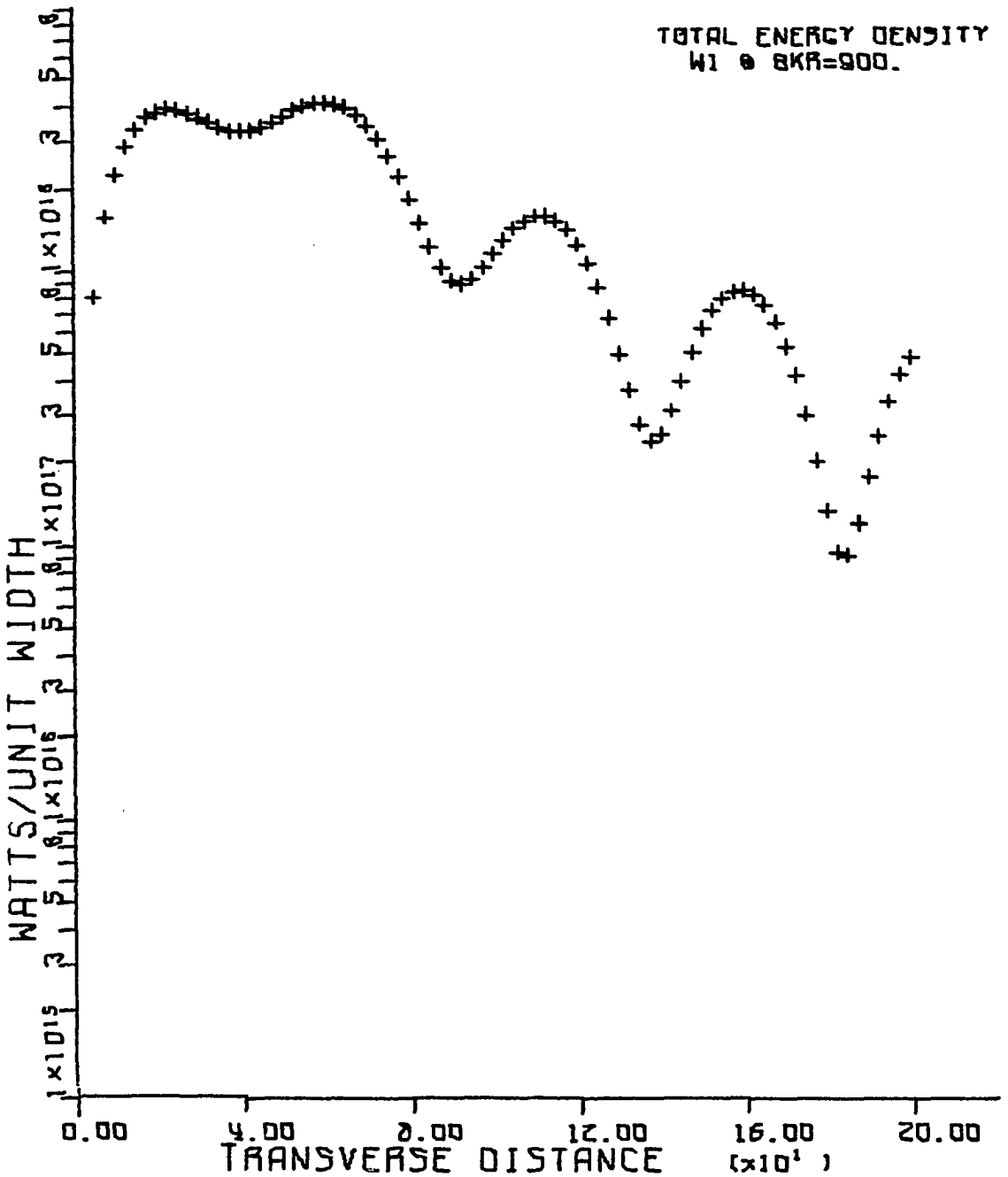

Figure 53. The x component of the integrated Poynting vector vs. $k_o x_t$ at $k_o r = 900.0$

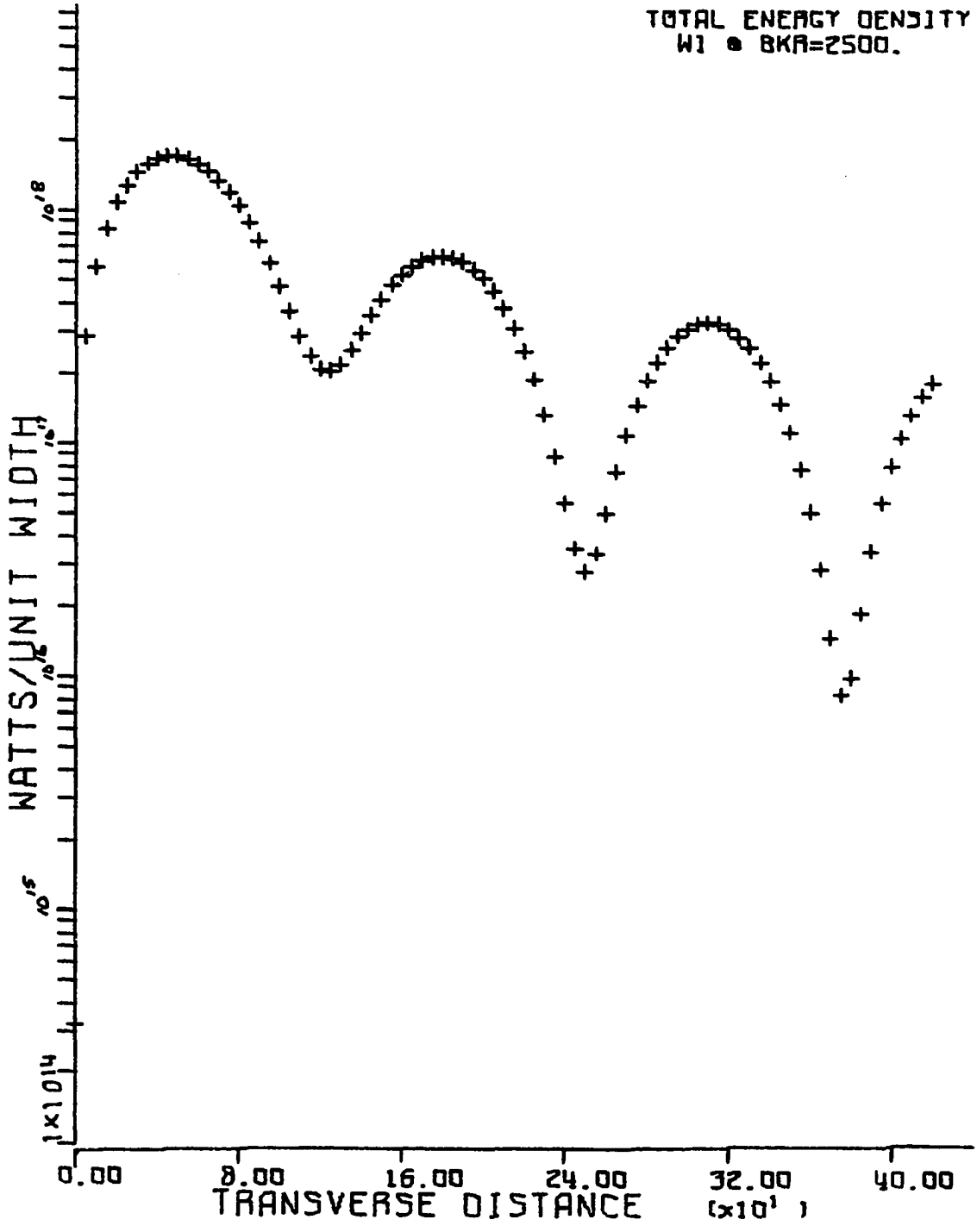

Figure 54. The x component of the integrated Poynting vector vs. $k_o x_t$ at $k_o r = 2500.0$

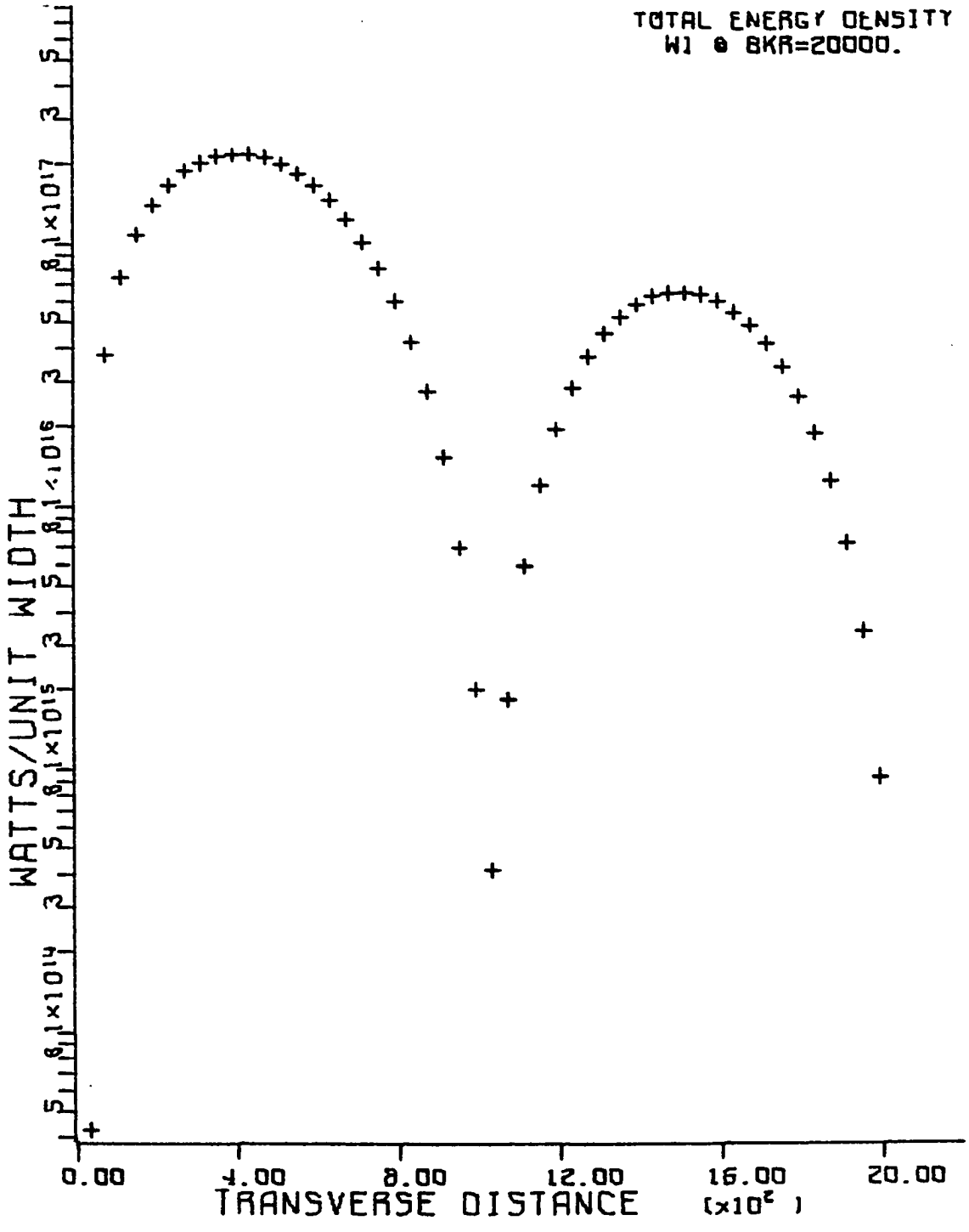

Figure 55. The x component of the integrated Poynting vector vs. $k_o x_t$ at $k_o r$ = 20,000.0

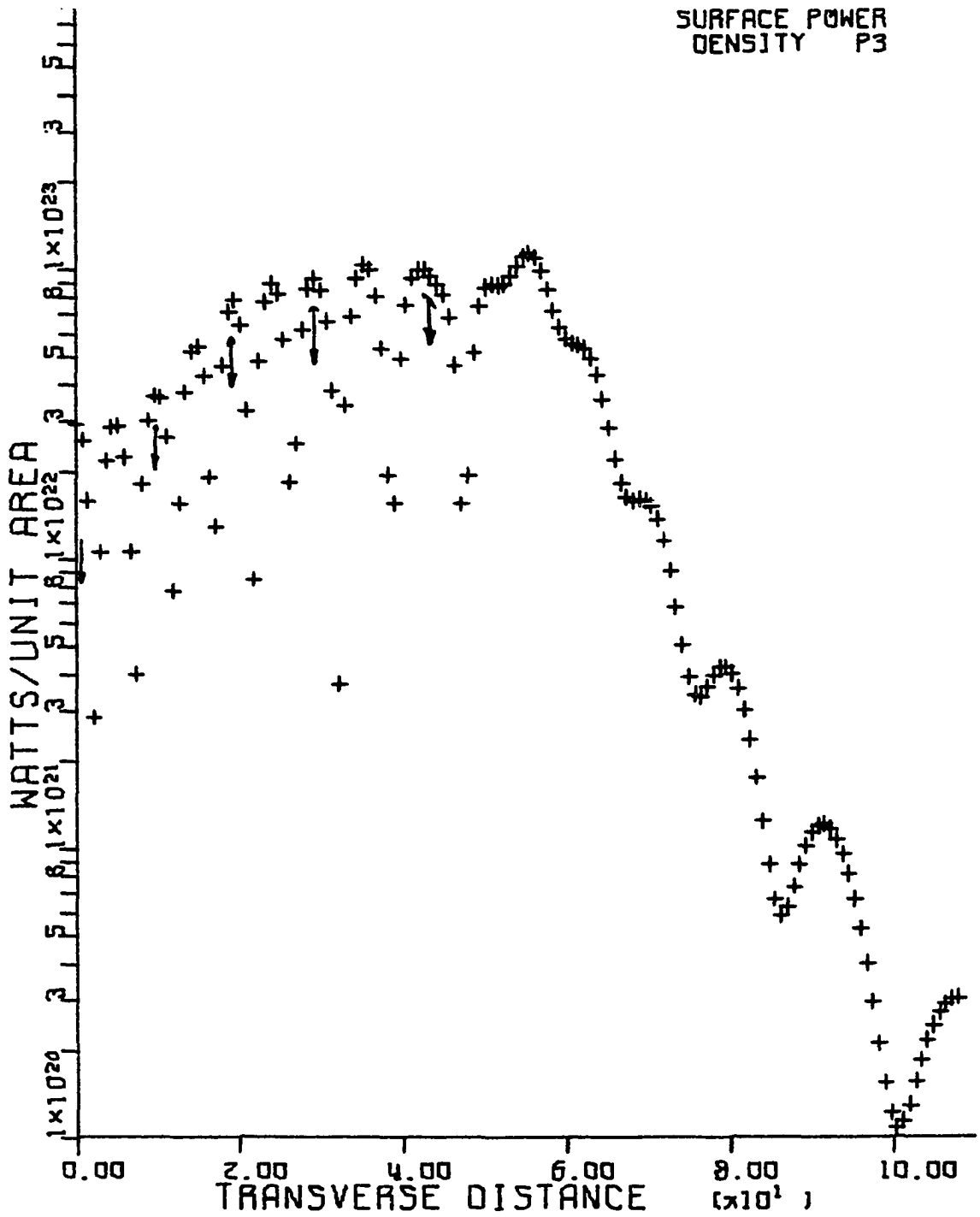

Figure 56. The x_3 component of the surface Poynting vector vs. $k_o x$ at $k_o y = 50.0$

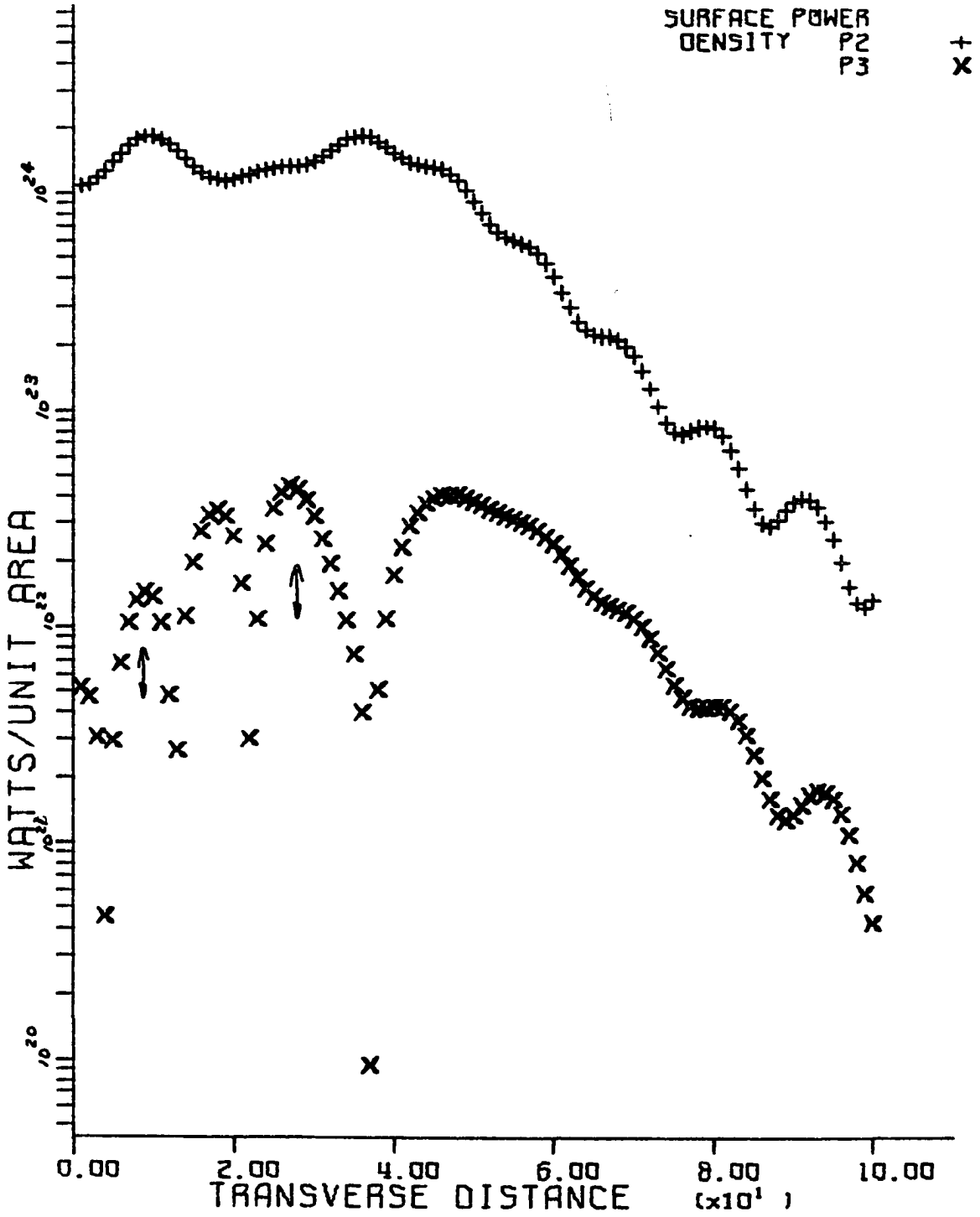

Figure 57. The y and x_3 component of the surface Poynting vector vs. $k_o x$ at $k_o y = 160.0$

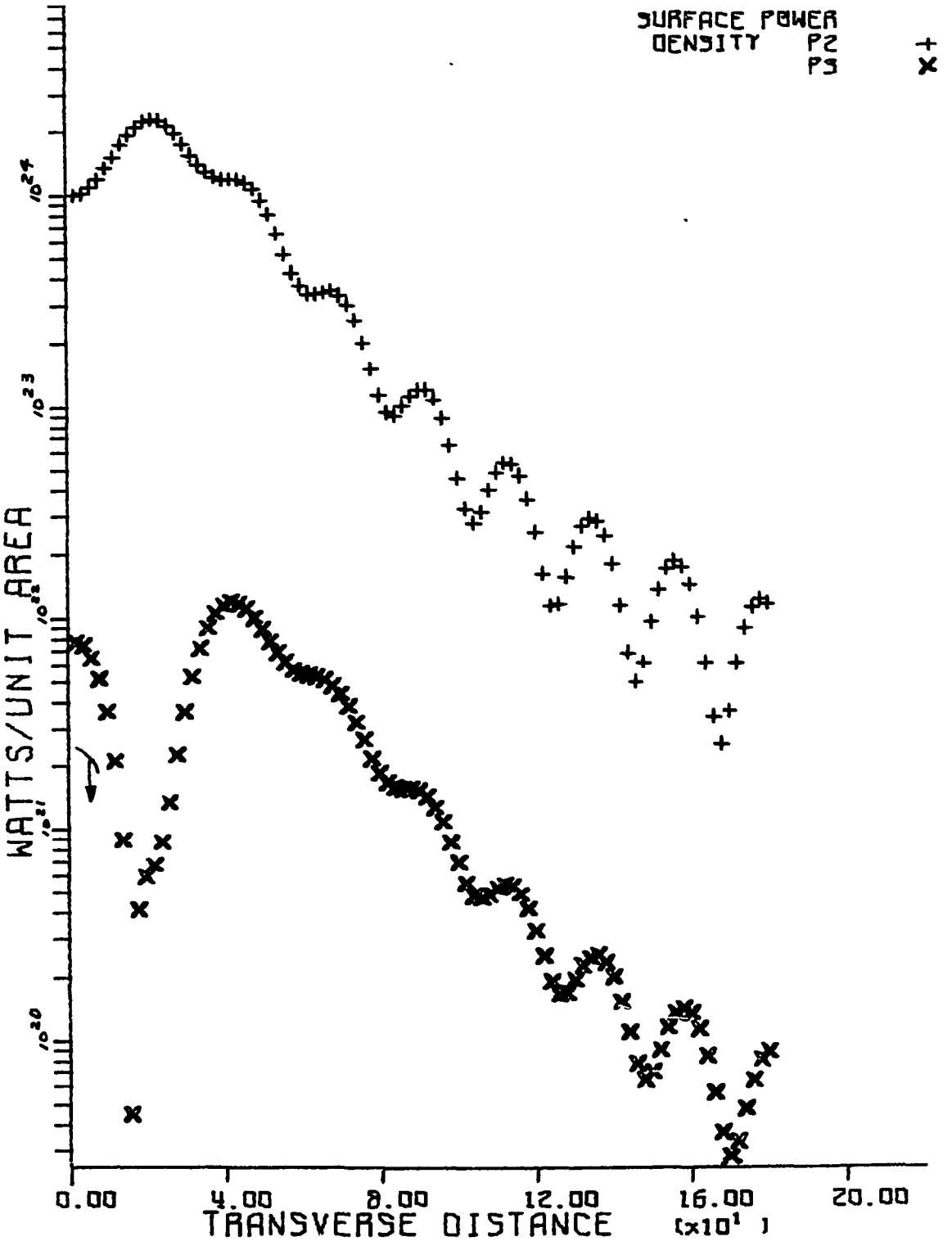

Figure 58. The y and x_3 components of the surface Poynting vector vs. $k_o x_t$ at $k_o r = 400.0$

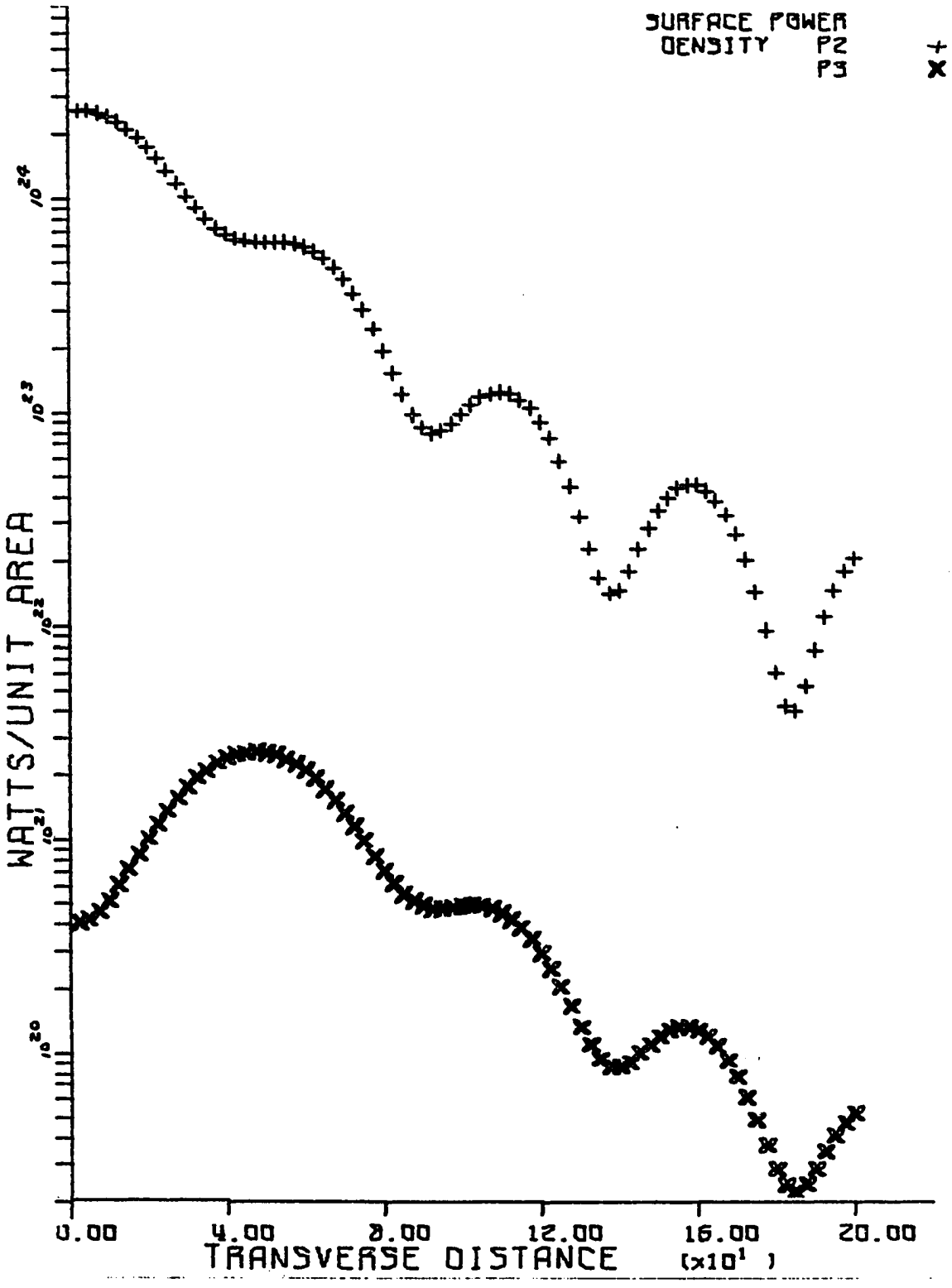

Figure 59. The y and x_3 components of the surface Poynting vector $k_o x_t$ at $k_o r = 900.0$

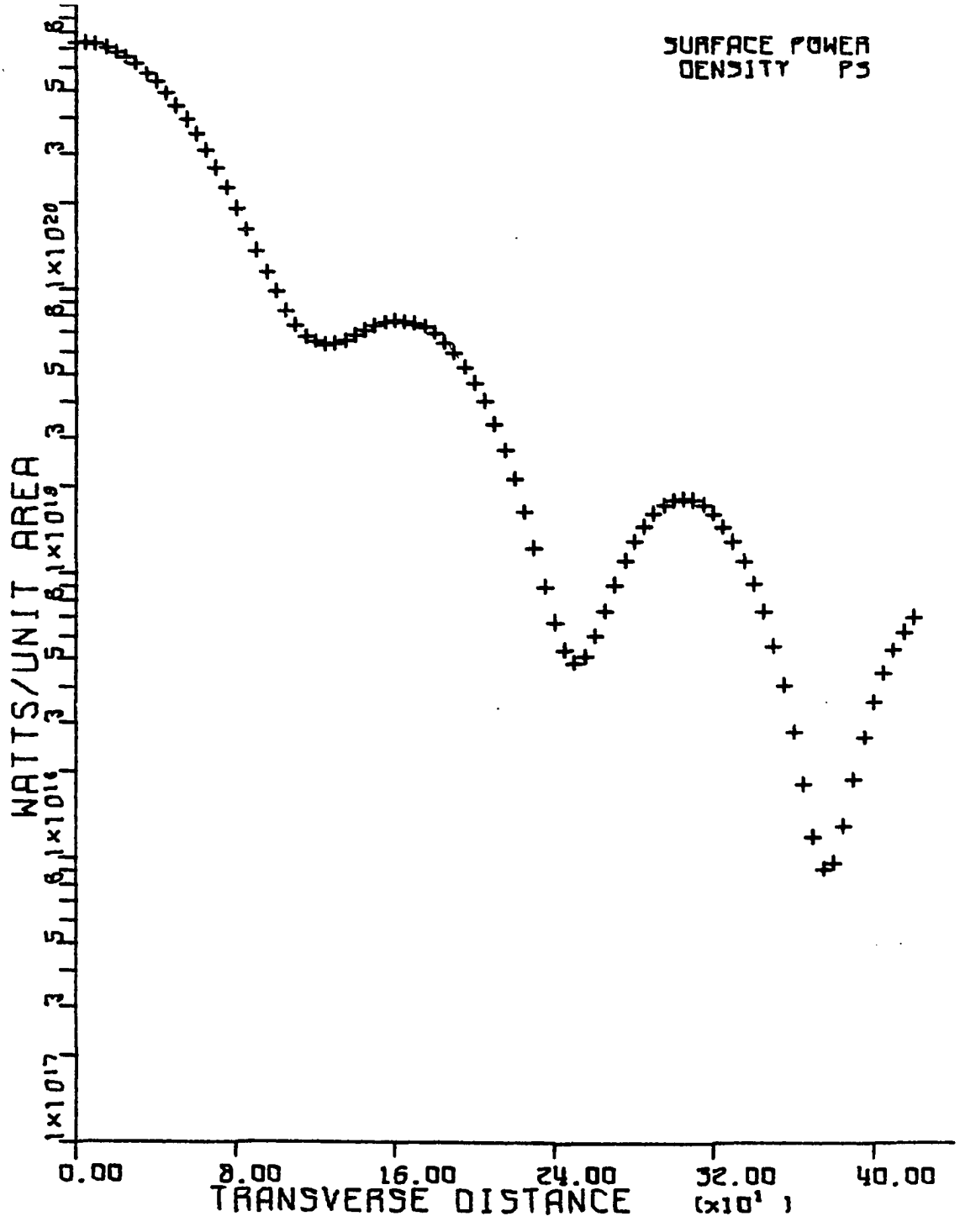

Figure 60. The x_3 component of the surface Poynting vector vs. $k_o x_t$ at $k_o r = 2500.0$

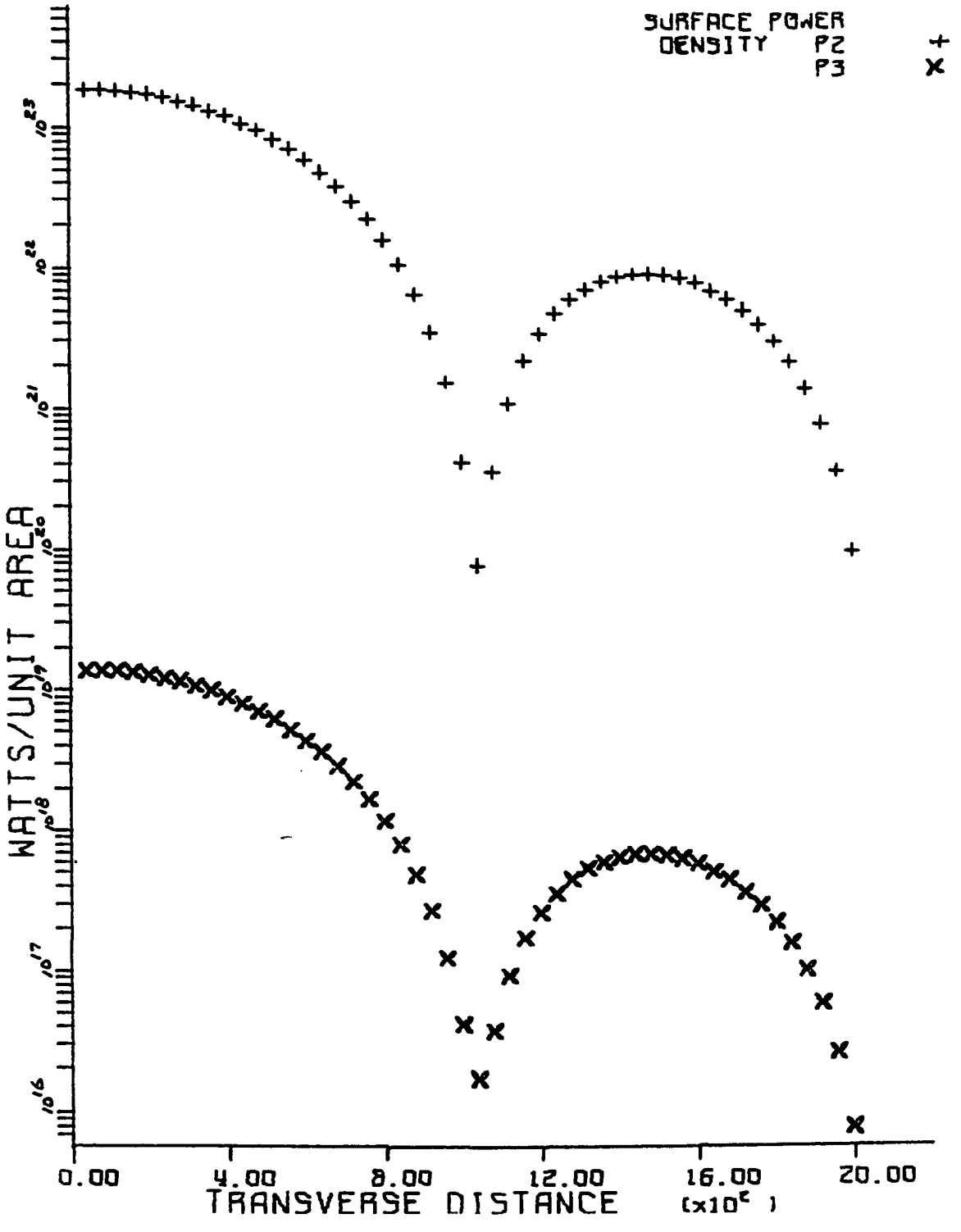

Figure 61. The y and x_3 components of the surface Poynting vector vs. $k_o x_t$ at $k_o r$ = 20,000.0

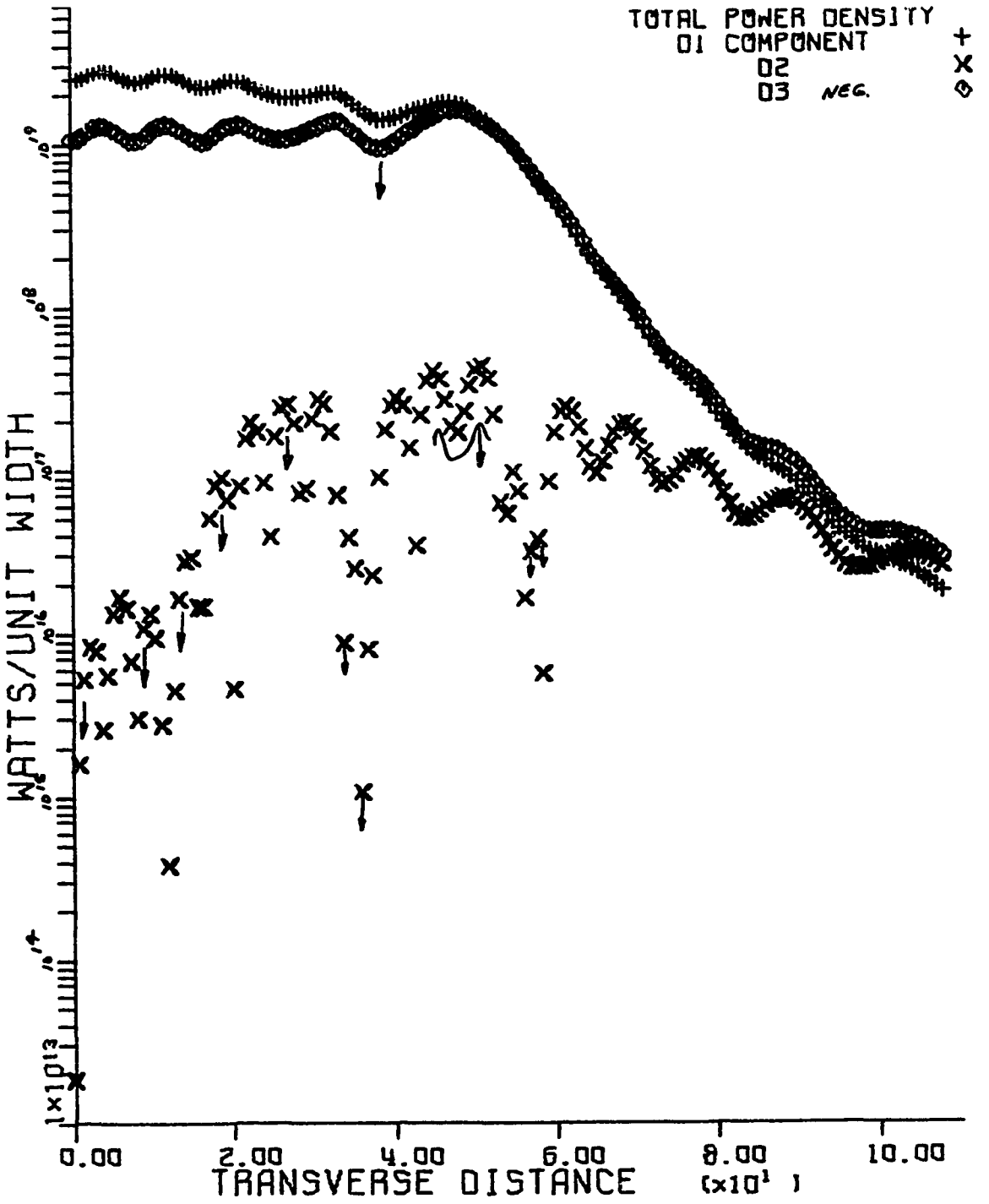

Figure 62. Terms of the total y component of the integrated Poynting vector due to C_{2222}, C_{2211}, and C_{2233} vs. $k_o x$ at $k_o y = 50.0$

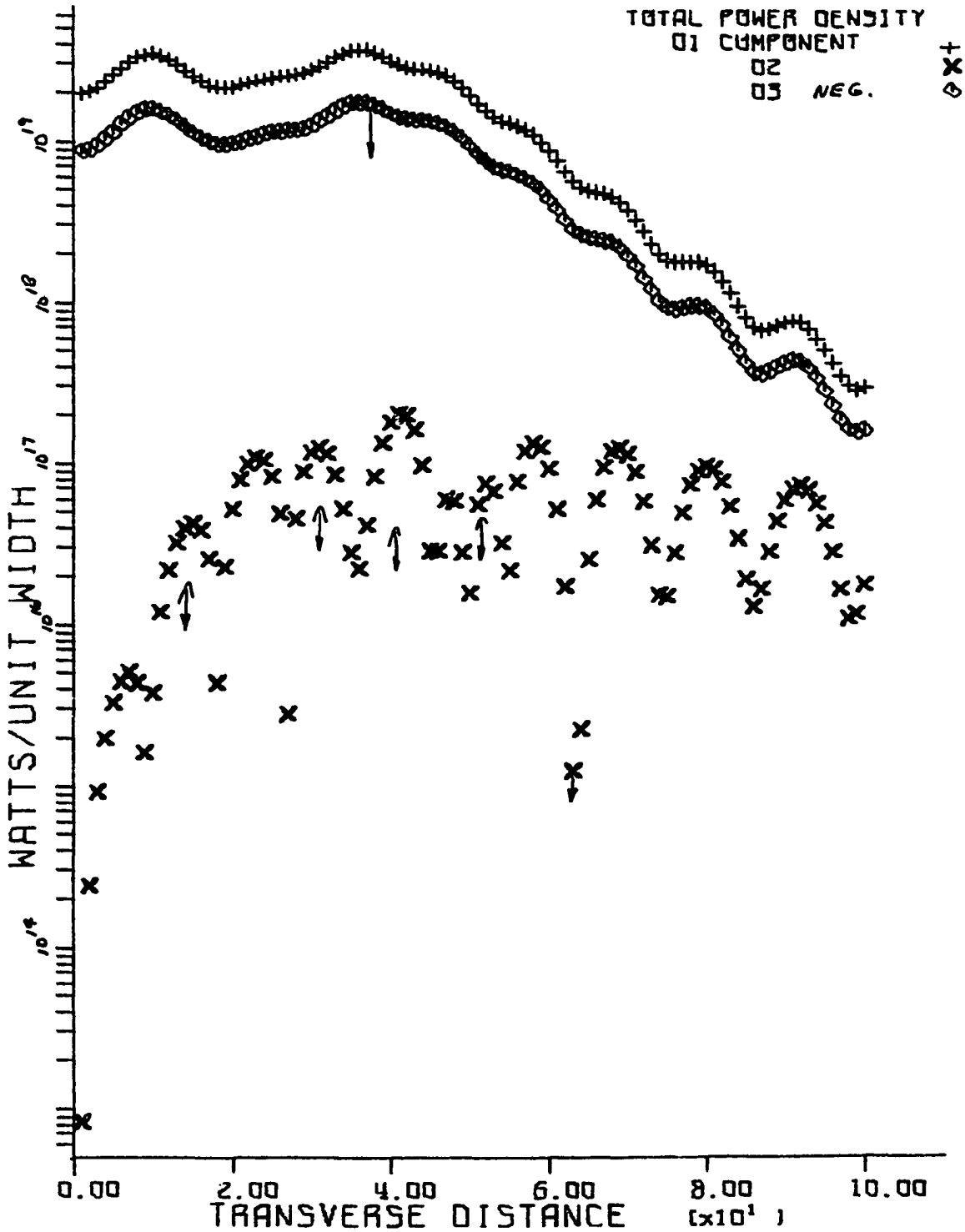

Figure 63. Terms of the total y component of the integrated Poynting vector due to C_{2222}, C_{2211}, and C_{2233} vs. $k_o x$ at $k_o r = 160.0$

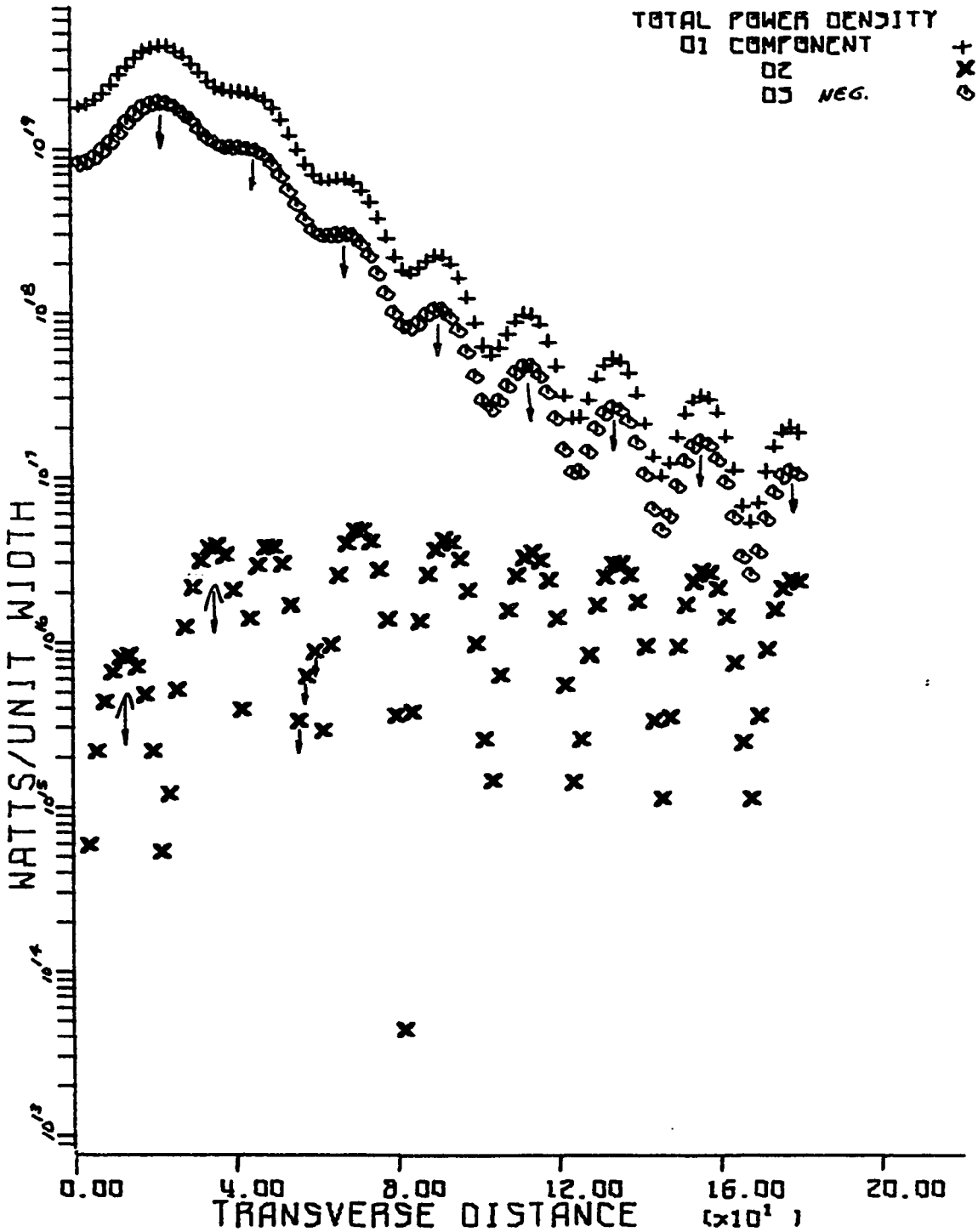

Figure 64. Terms of the total y component of the integrated Poynting vector due to C_{2222}, C_{2211}, and C_{2233} vs. $k_o x_t$ at $k_o r = 400.0$

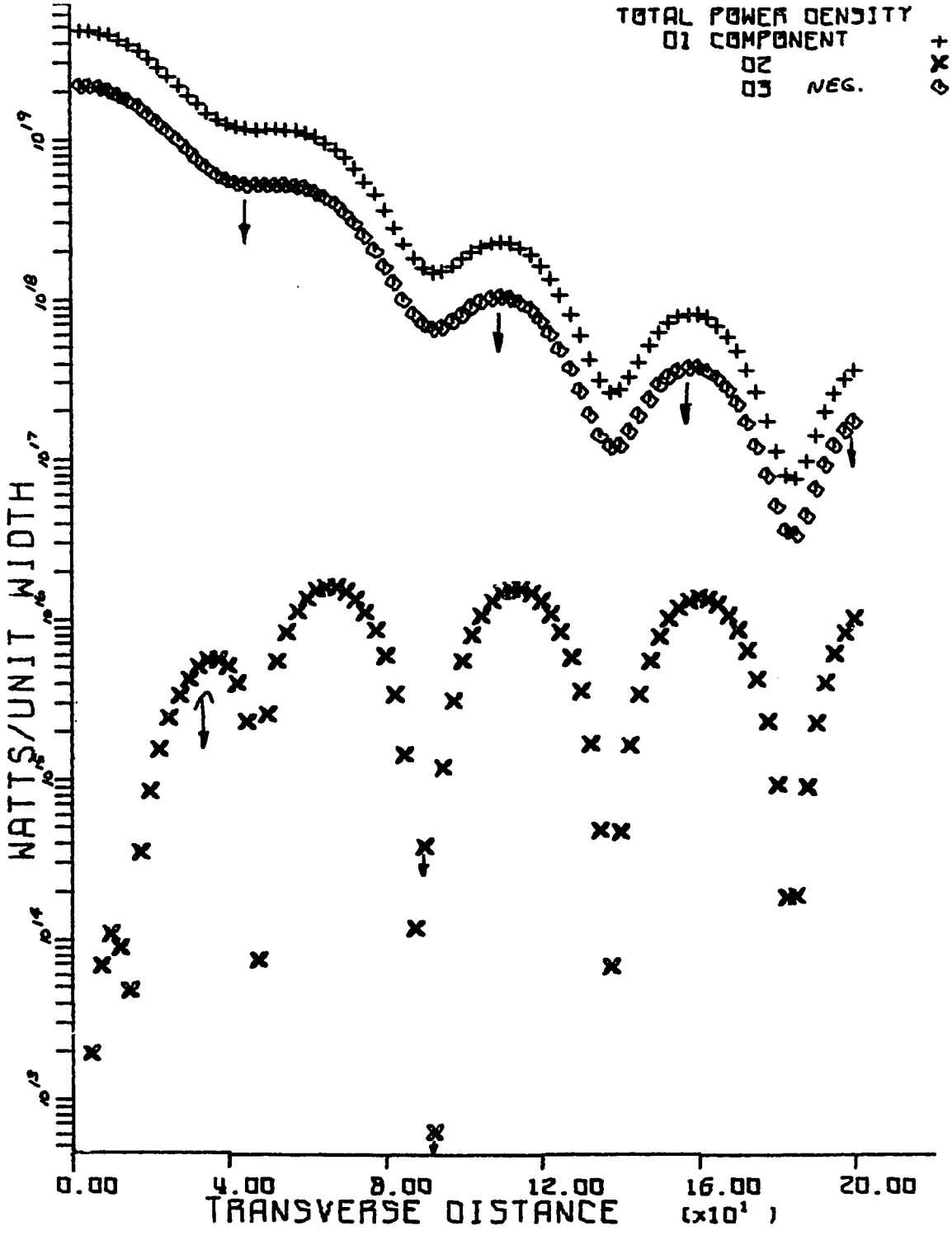

Figure 65. Terms of the total y component of the integrated Poynting vector due to C_{2222}, C_{2211}, and C_{2233} vs. $k_o x_t$ at $k_o r = 900.0$

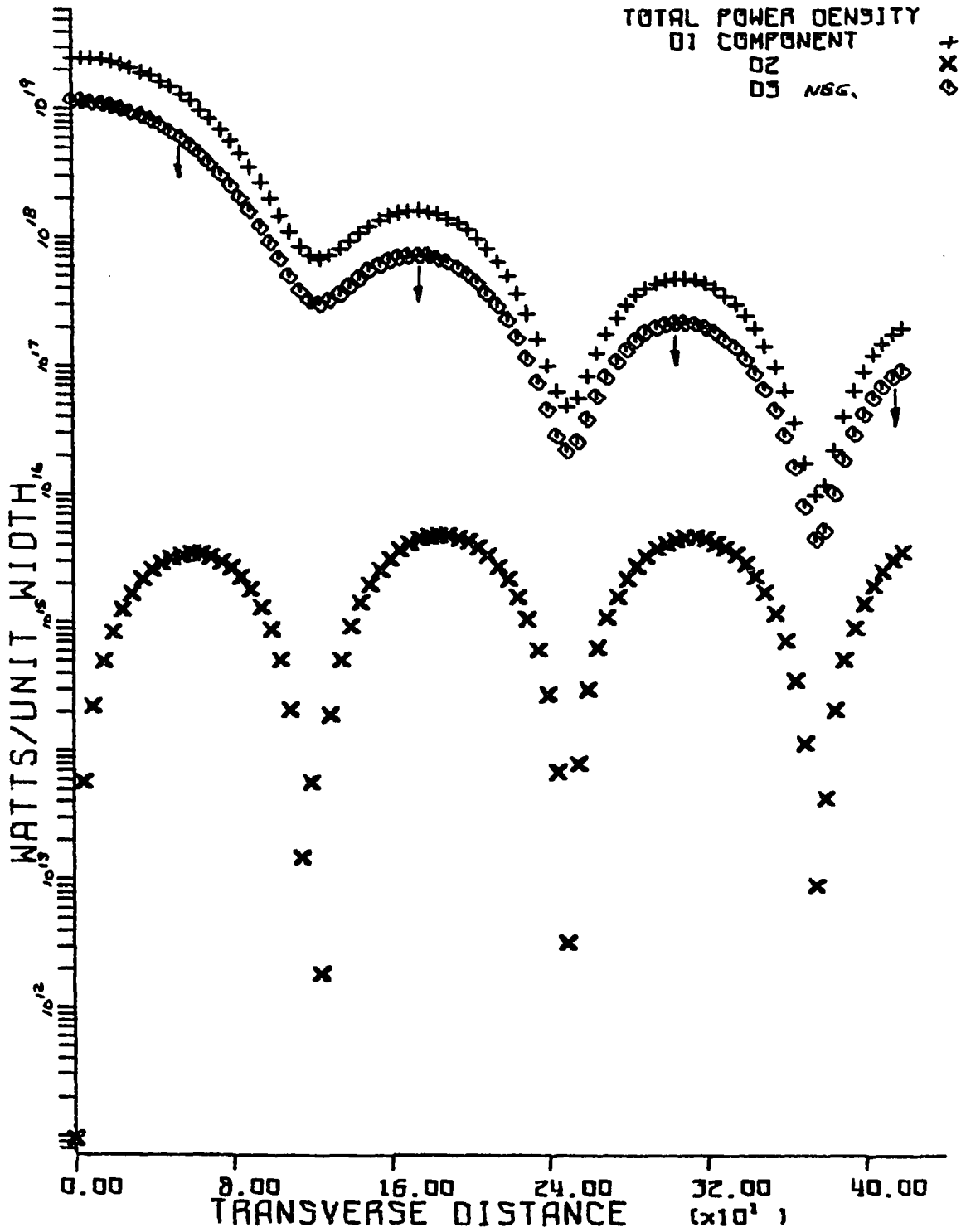

Figure 66. Terms of the total y component of the integrated Poynting vector due to C_{2222}, C_{2211}, and C_{2233} vs. $k_o x_t$ at $k_o r = 2500.0$

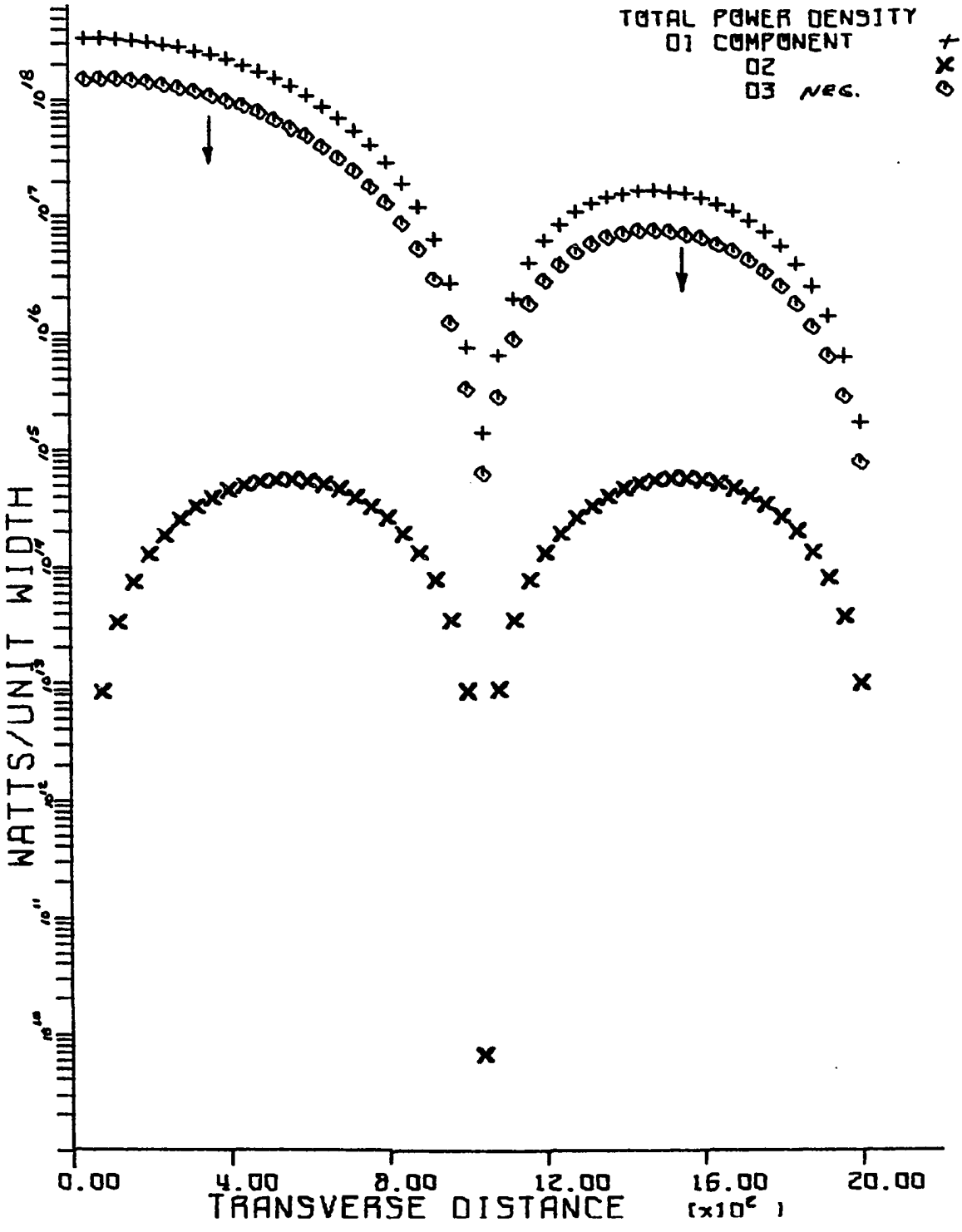

Figure 67. Terms of the total y component of the integrated Poynting vector due to C_{2222}, C_{2211}, and C_{2233} vs. $k_o x$ at $k_o y = 20{,}000.0$

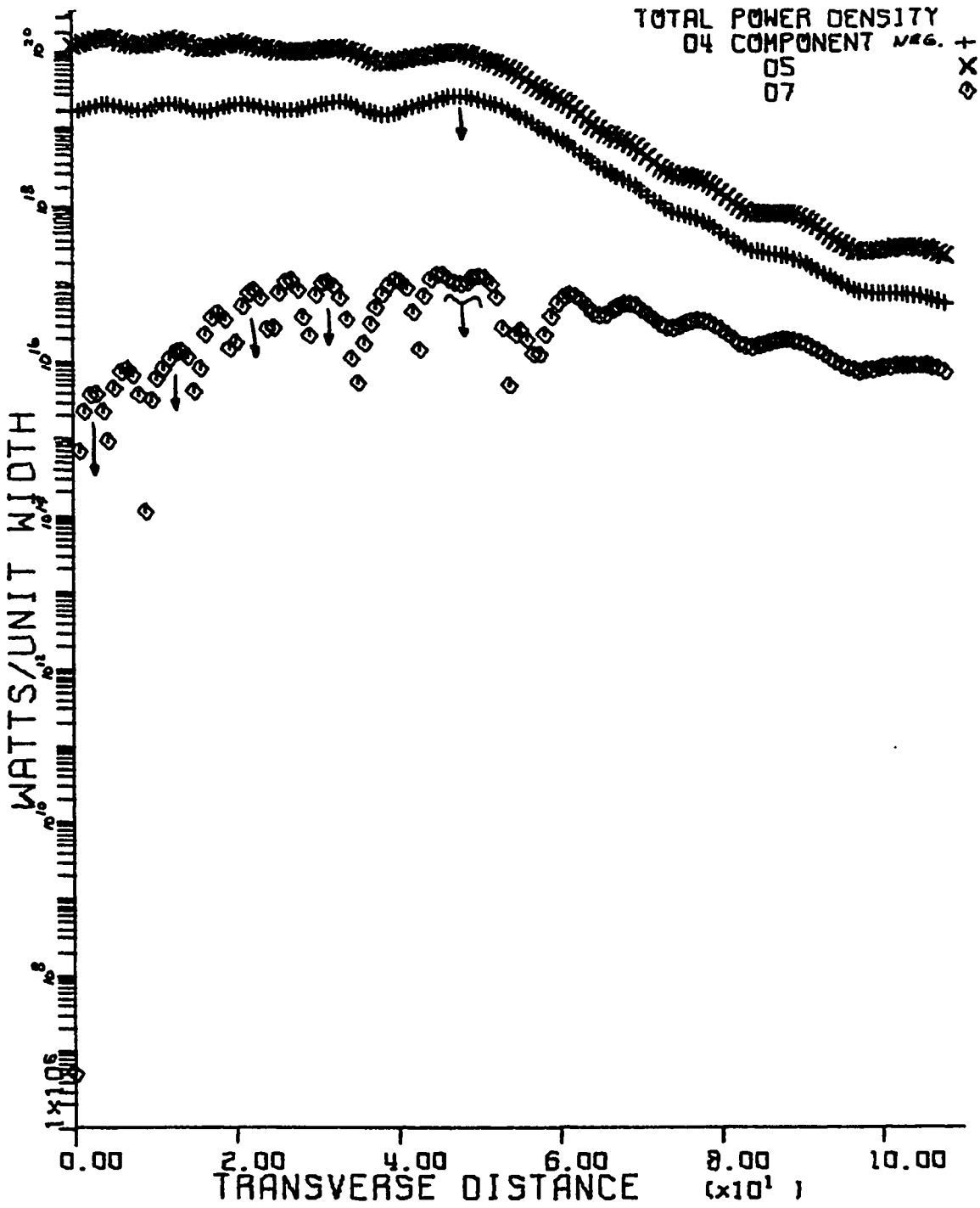

Figure 68. Terms of the total y component of the integrated Poynting vector due to C_{2323}, C_{2332}, and C_{2121} vs. $k_o x$ at $k_o y = 50.0$

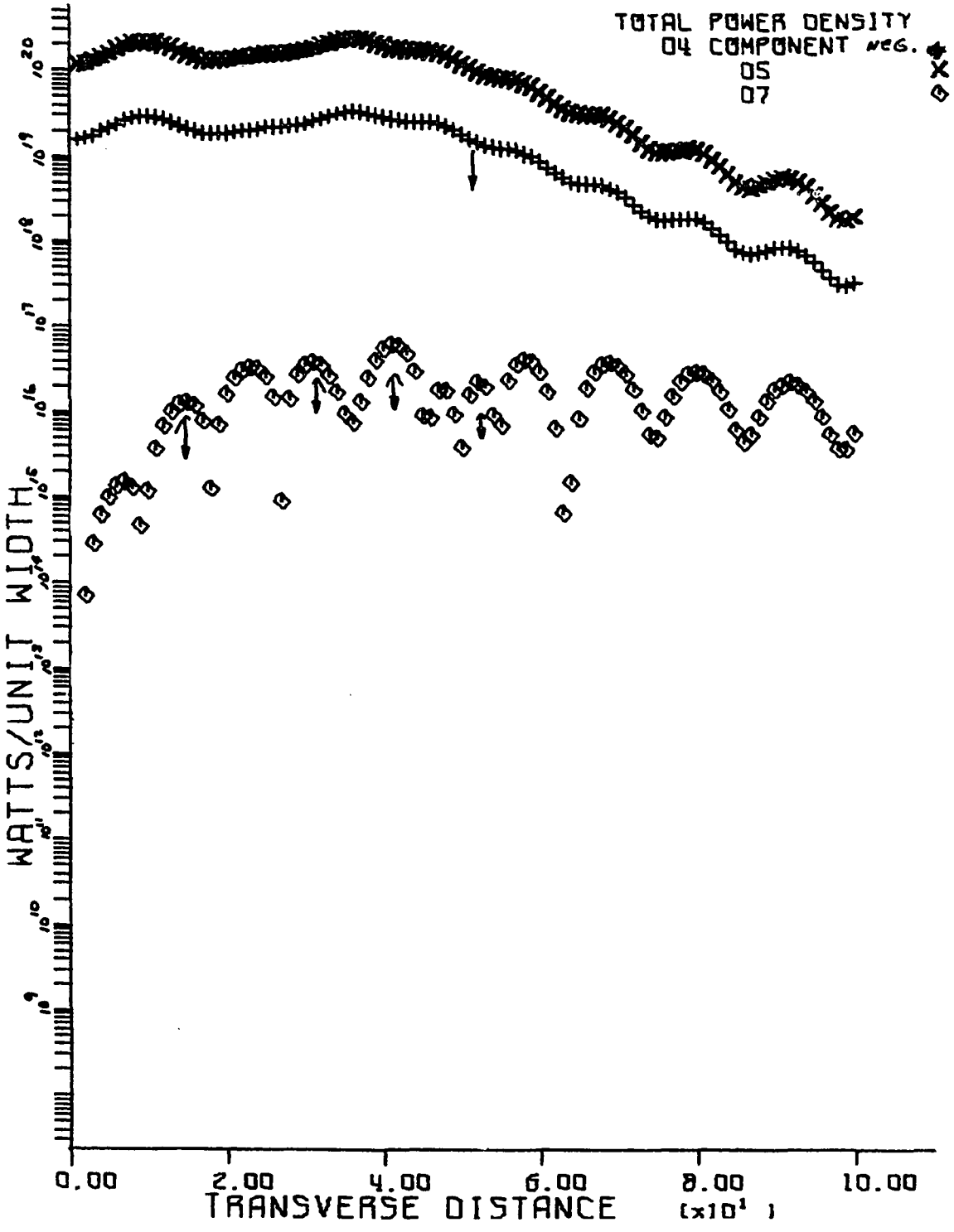

Figure 69. Terms of the total y component of the integrated Poynting vector due to C_{2323}, C_{2332}, and C_{2121} vs. $k_o x$ at $k_o y$ = 160.0

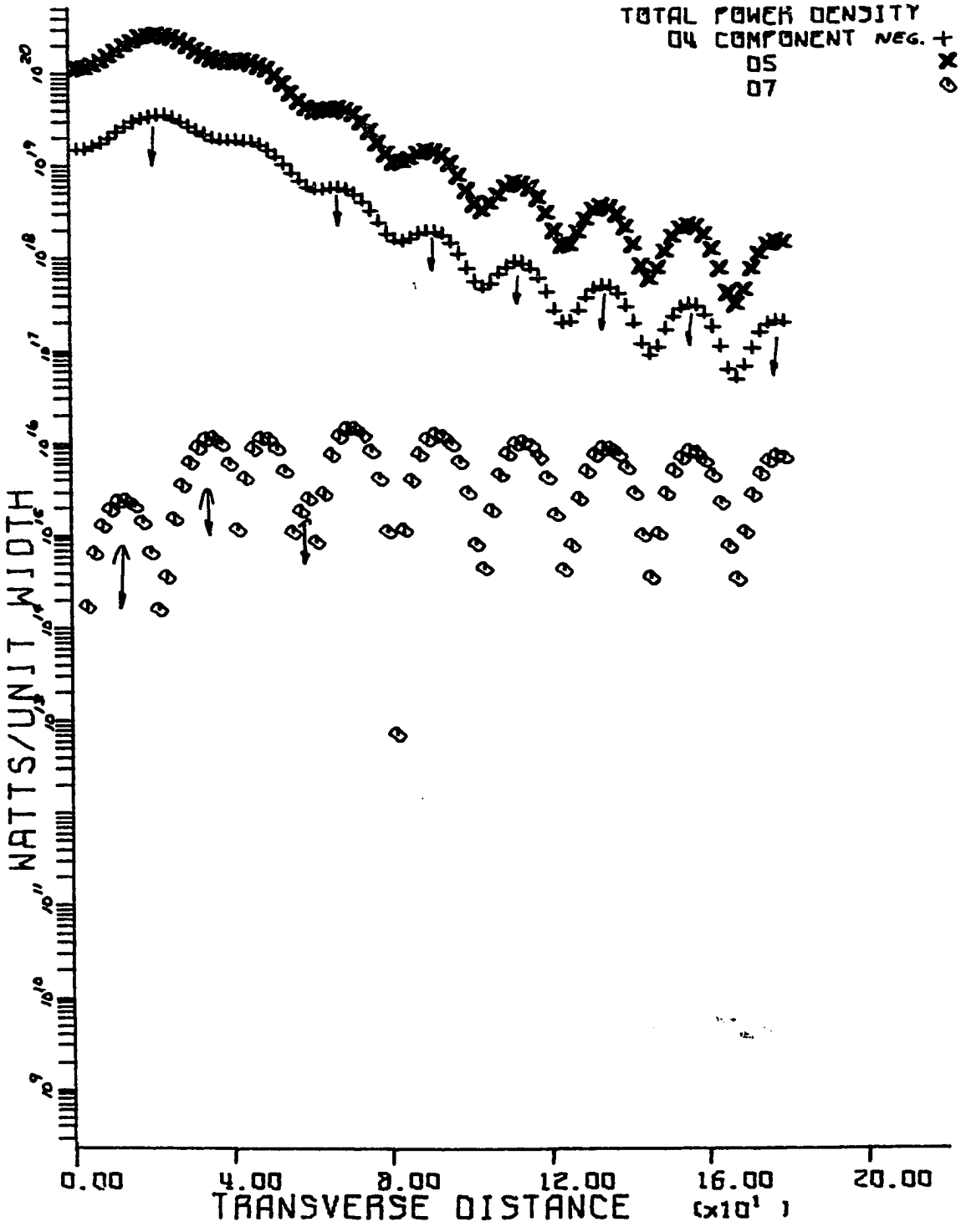

Figure 70. Terms of the total y component of the integrated Poynting vector due to C_{2323}, C_{2332}, and C_{2121} vs. $k_o x$ at $k_o y = 400.0$

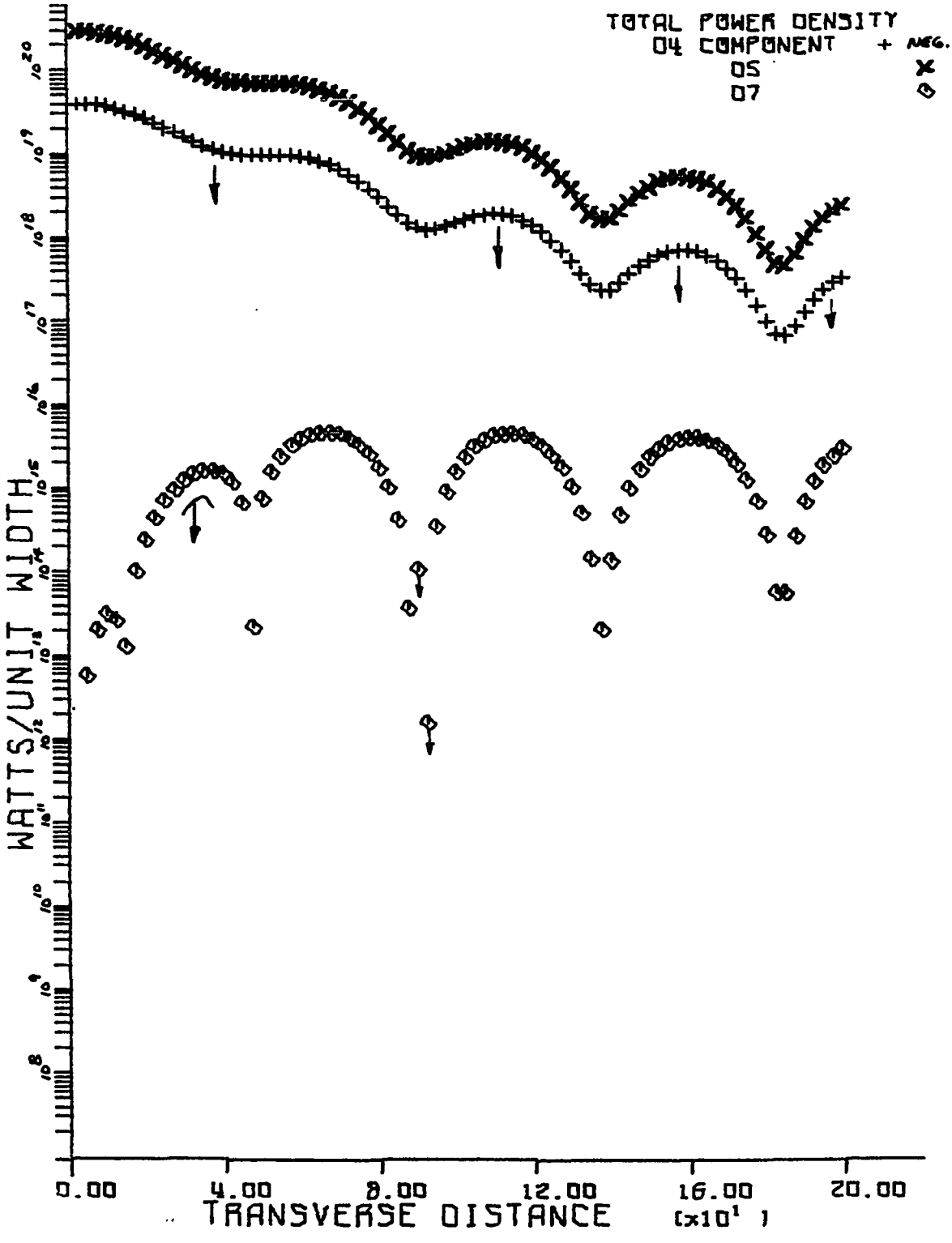

Figure 71. Terms of the total y component of the integrated Poynting vector due to C_{2323}, C_{2332}, and C_{2121} vs. $k_o x$ at $k_o y = 900.0$

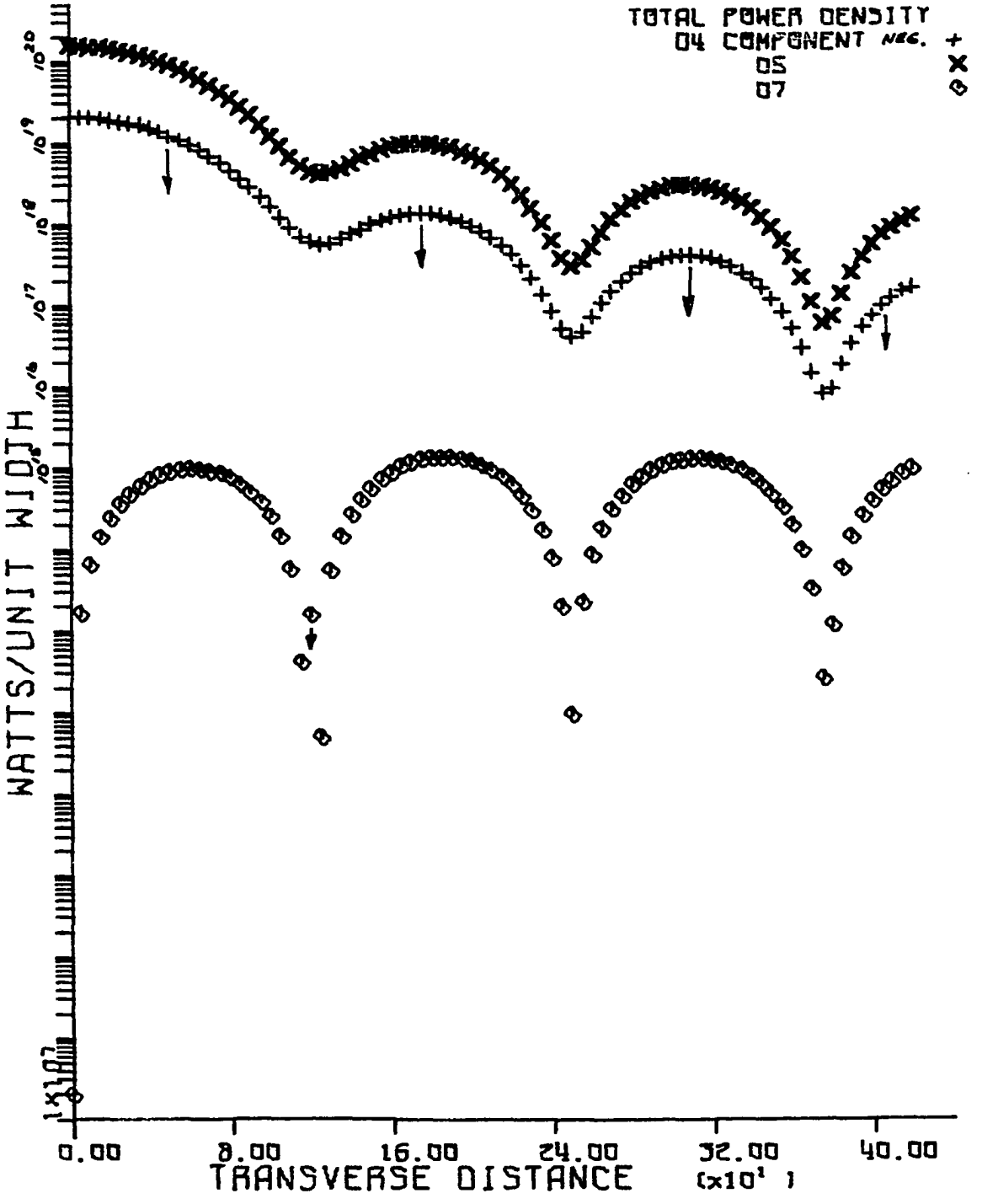

Figure 72. Terms of the total y component of the integrated Poynting vector due to C_{2323}, C_{2332}, and C_{2121} vs. $k_o x_t$ at $k_o r = 2500.0$

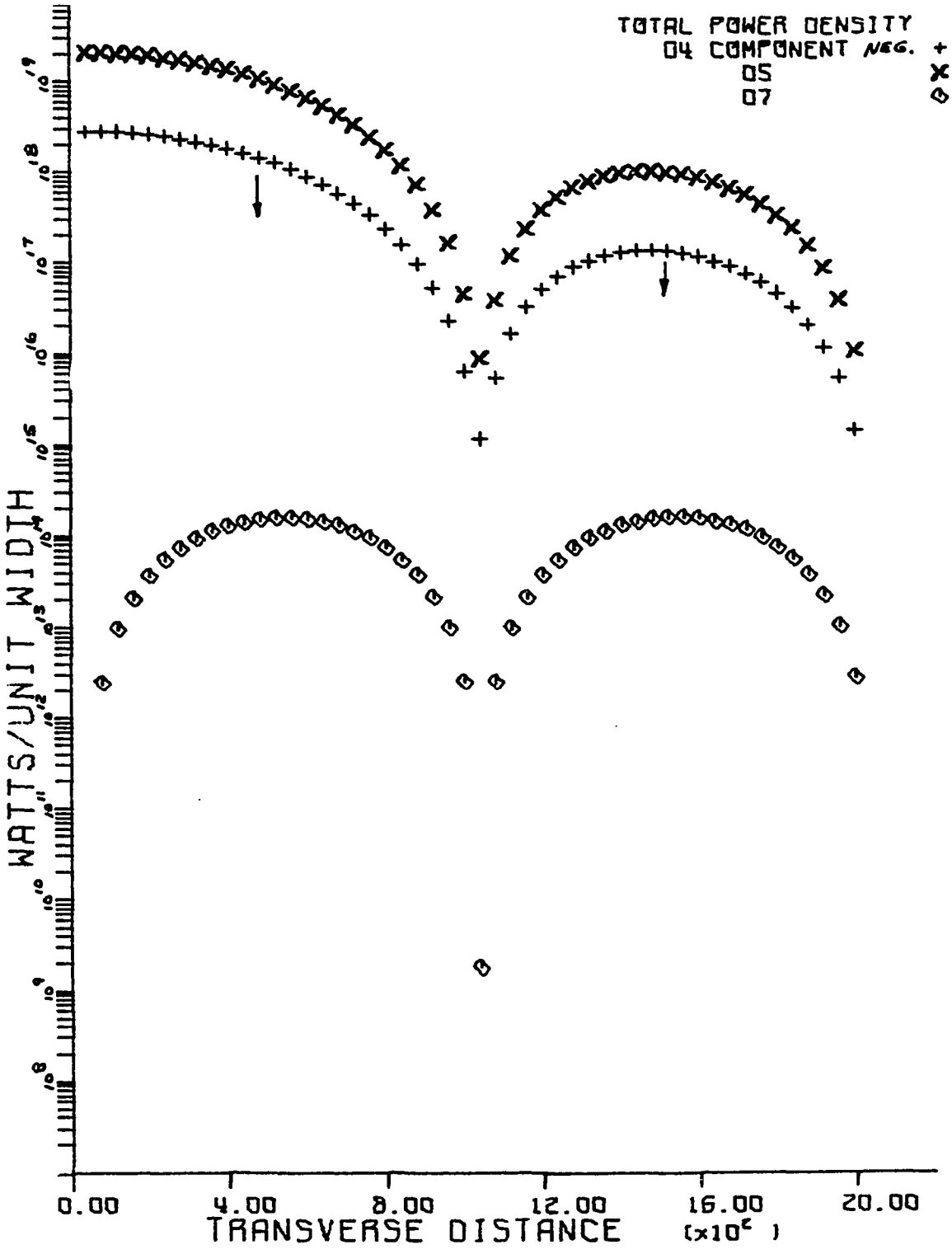

Figure 73. Terms of the total y component of the integrated Poynting vector due to C_{2323}, C_{2332}, and C_{2121} vs. $k_o x_t$ at $k_o r = 20{,}000.0$

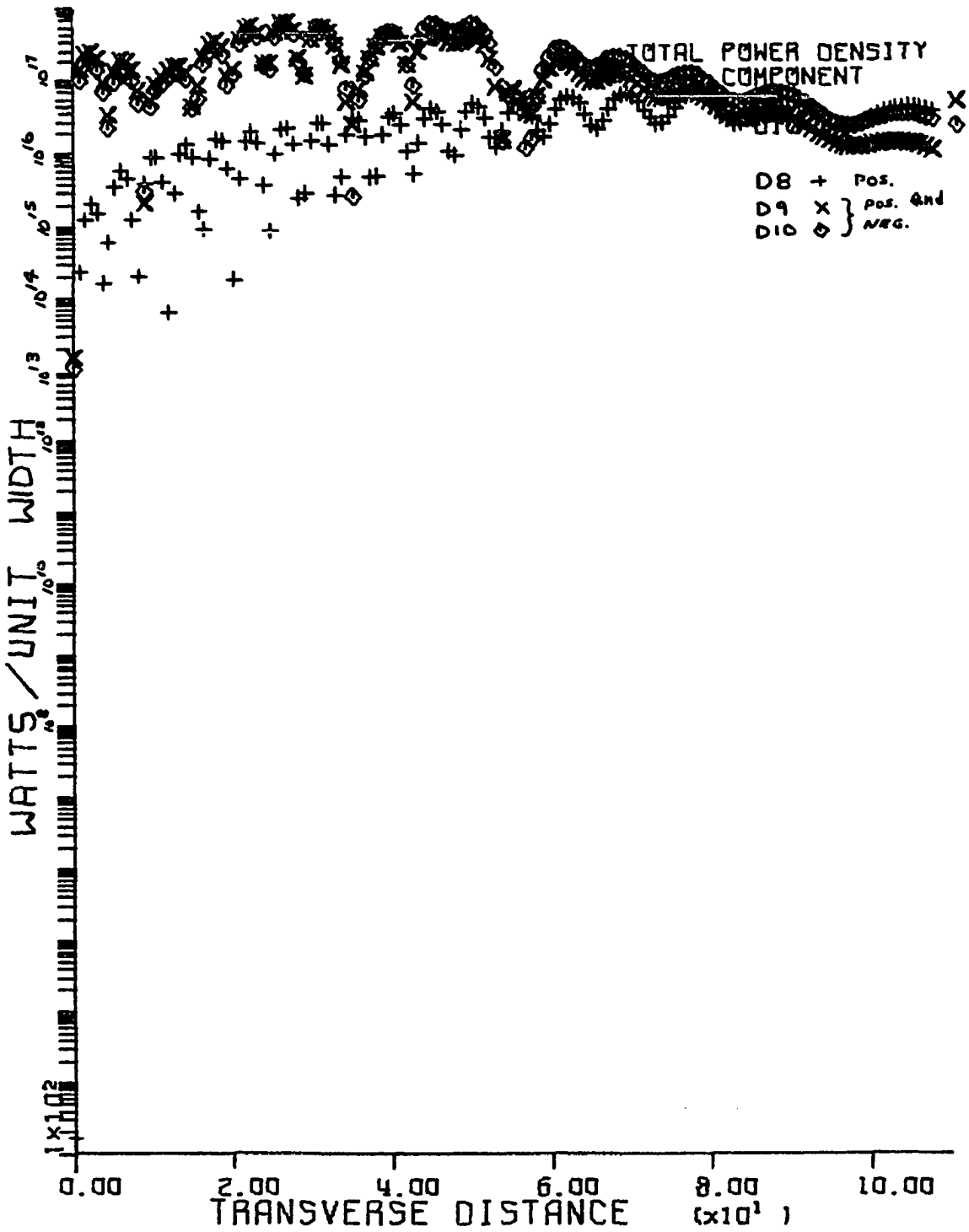

Figure 74. Terms of the total x component of the integrated Poynting vector due to C_{1111}, C_{1122}, and C_{1313} vs. $k_o x$ at $k_o y = 50.0$

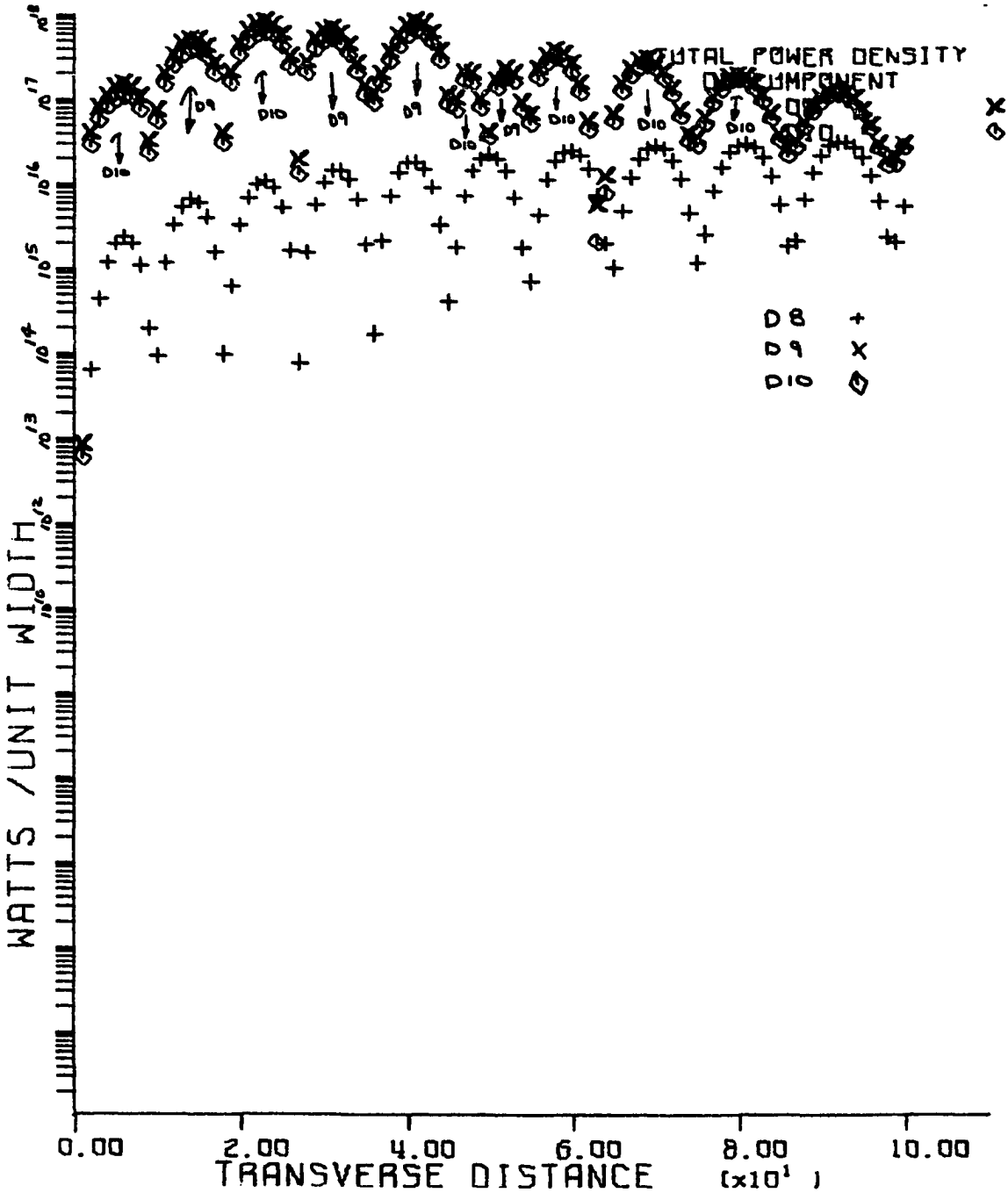

Figure 75. Terms of the total x component of the integrated Poynting vector due to C_{1111}, C_{1122}, and C_{1313} vs. $k_o x$ at $k_o y = 160.0$

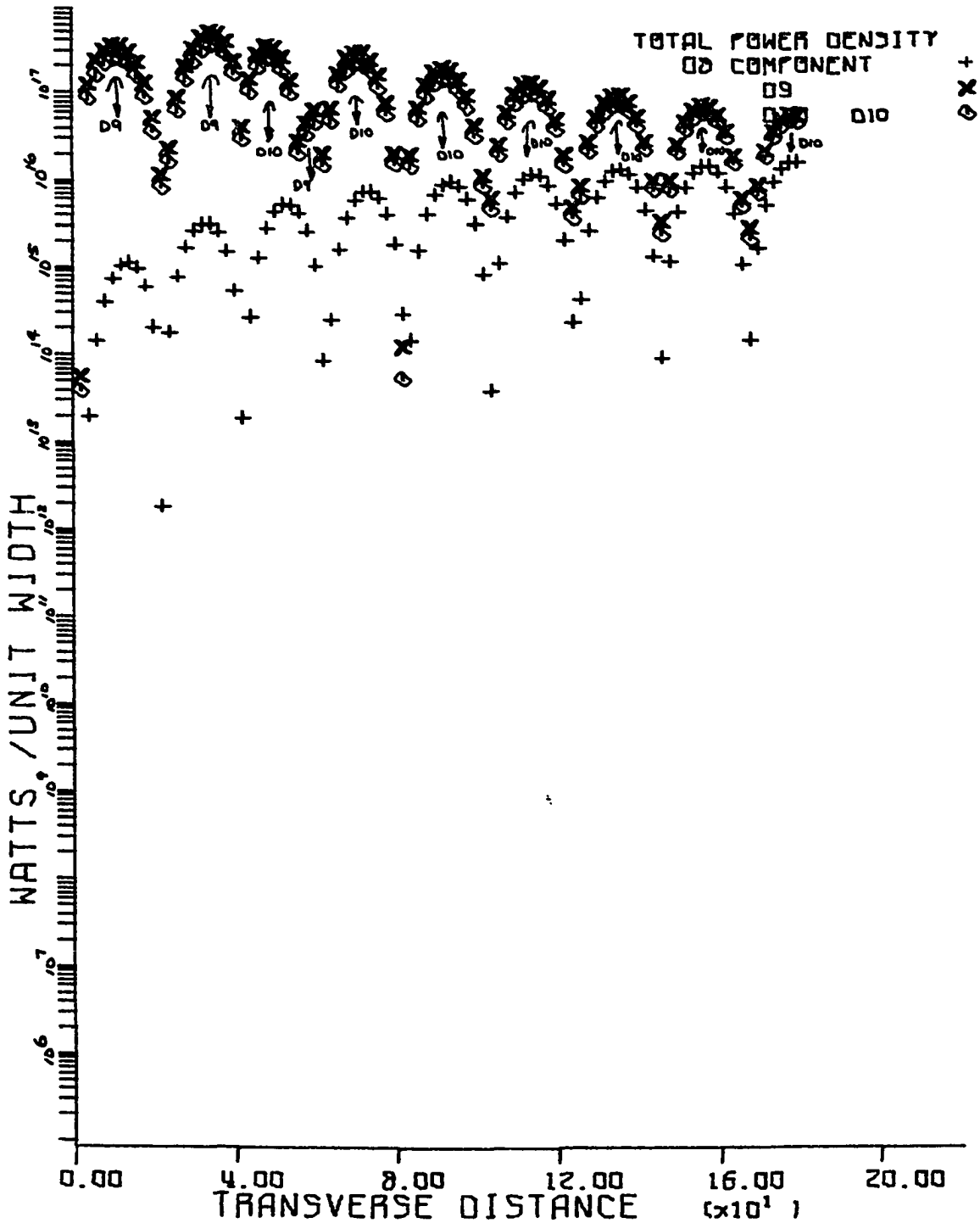

Figure 76. Terms of the total x component of the integrated Poynting vector due to C_{1111}, C_{1122}, and C_{1313} vs. $k_o x_t$ at $k_o r = 400.0$

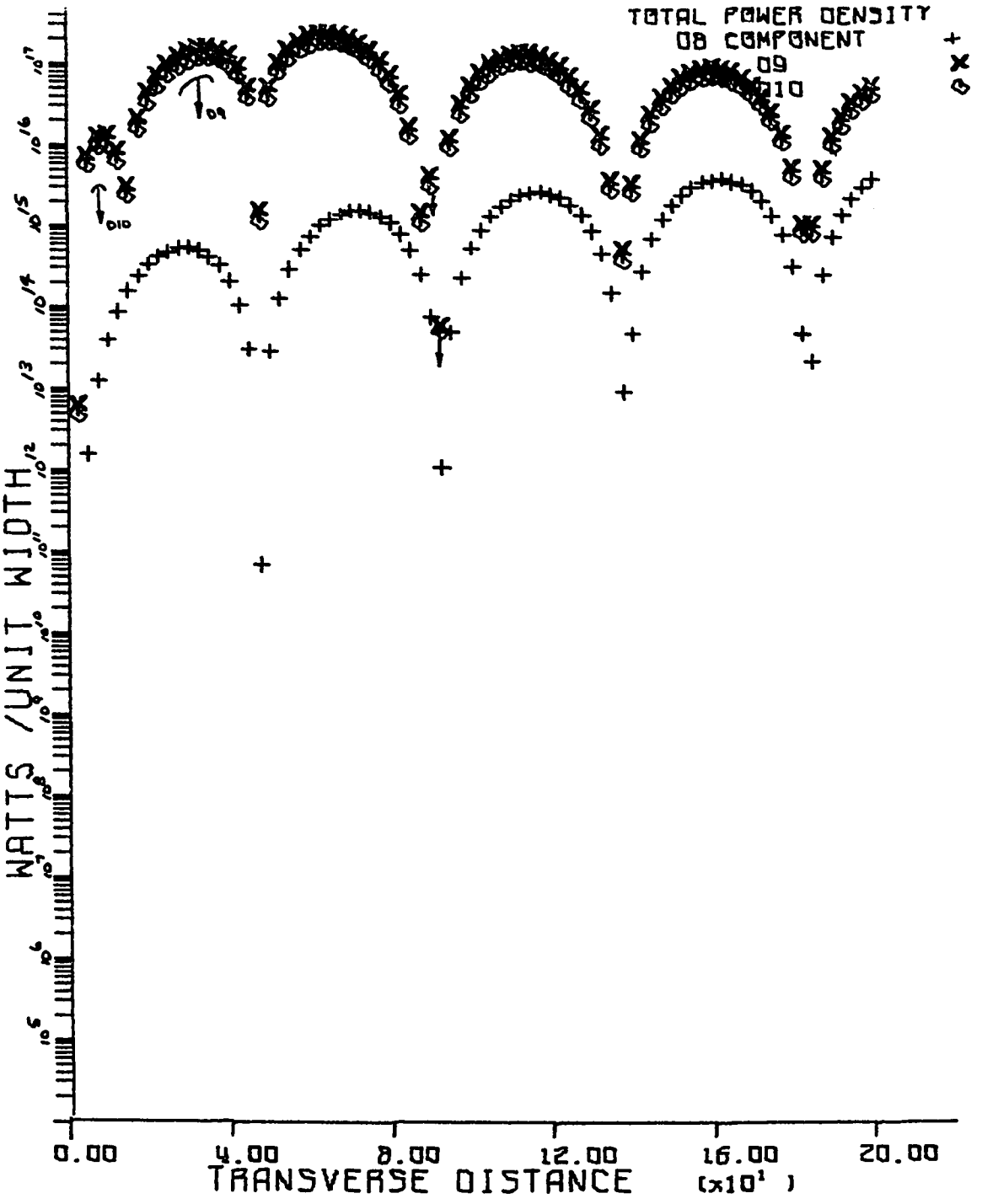

Figure 77. Terms of the total x component of the integrated Poynting vector due to C_{1111}, C_{1122}, and C_{1313} vs. $k_o x_t$ at $k_o r = 900.0$

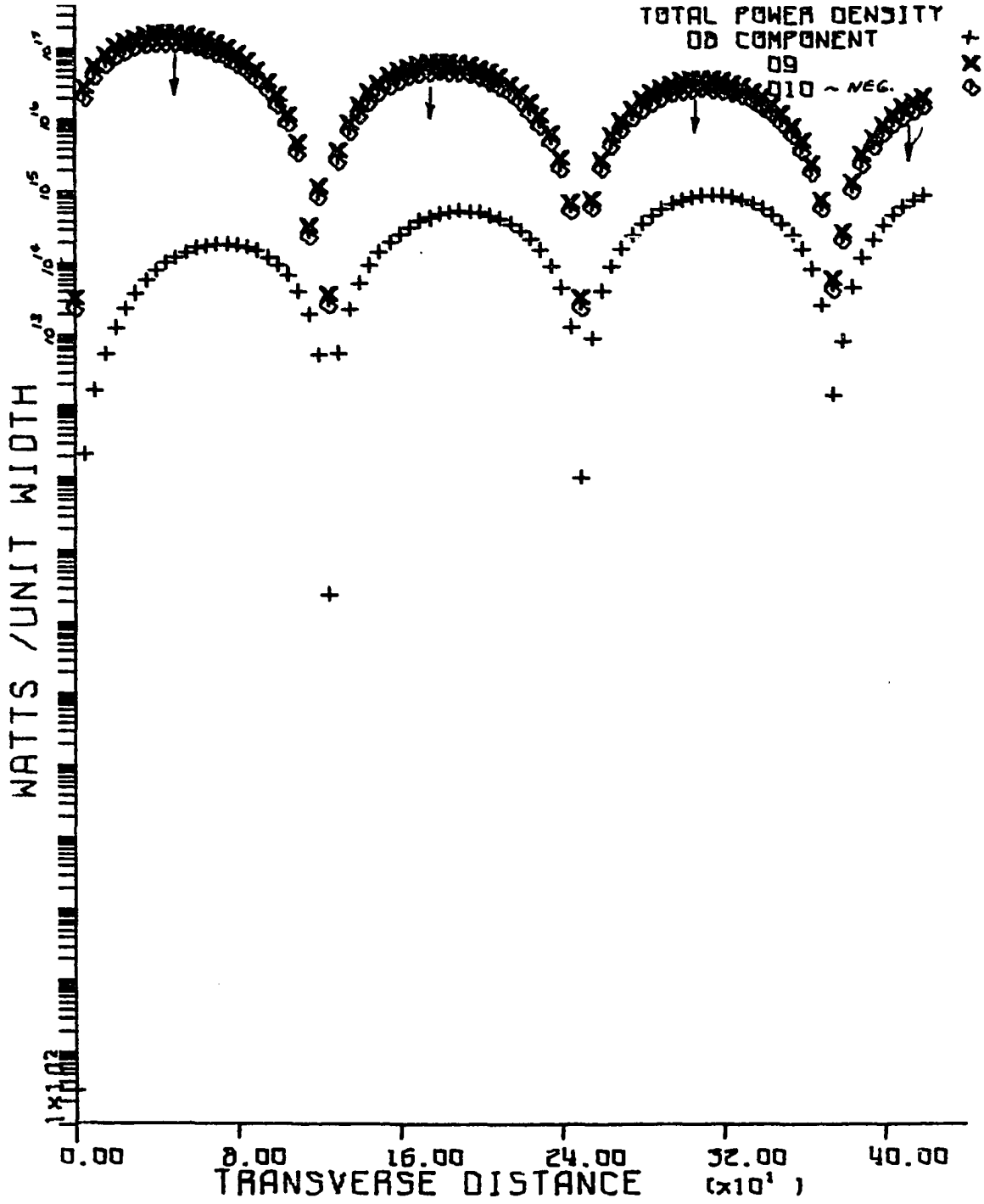

Figure 78. Terms of the total x component of the integrated Poynting vector due to C_{1111}, C_{1122}, and C_{1313} vs. $k_o x_t$ at $k_o r = 2500.0$

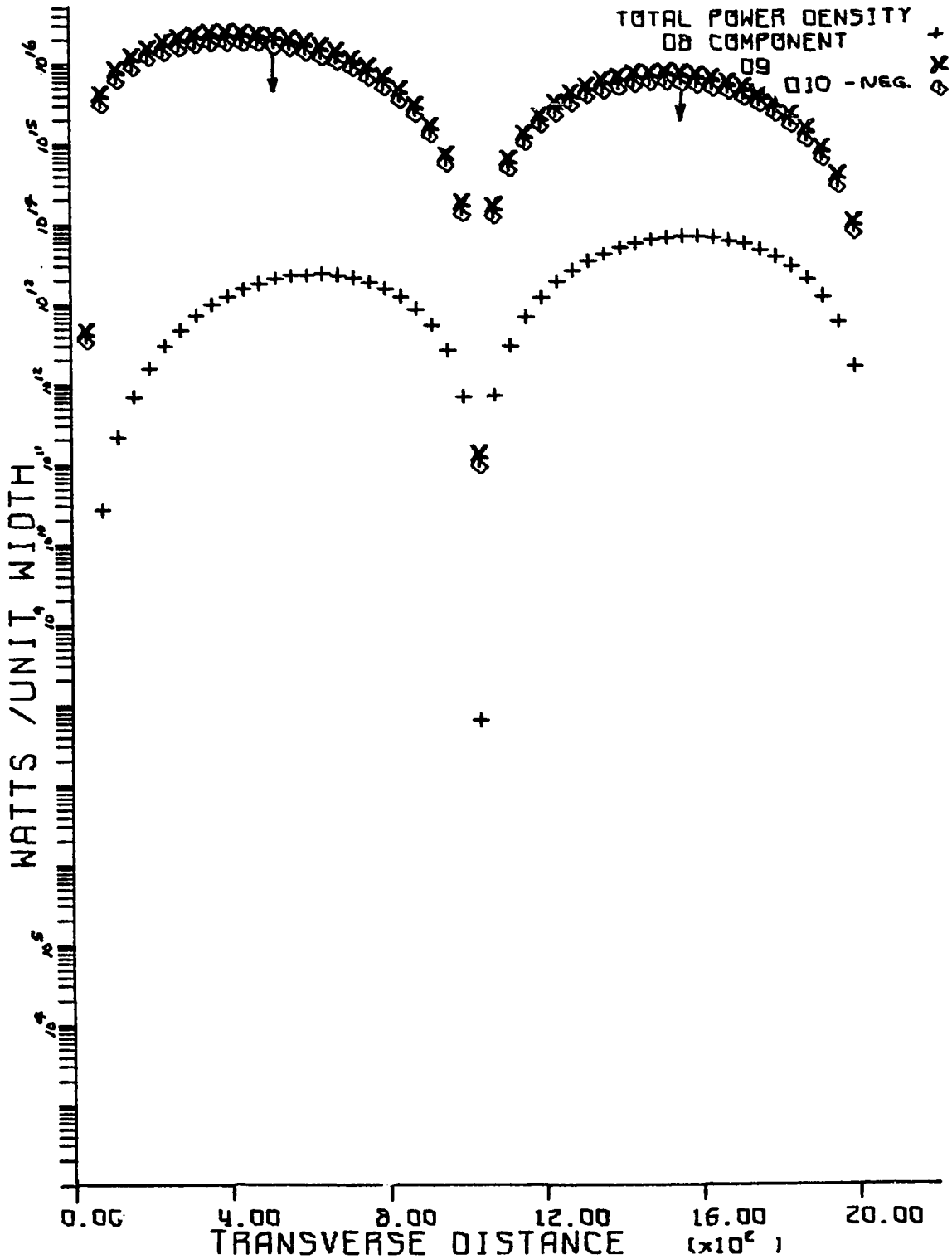

Figure 79. Terms of the total x component of the integrated Poynting vector due to C_{1111}, C_{1122}, and C_{1313} vs. $k_o x_t$ at $k_o r = 20{,}000.0$

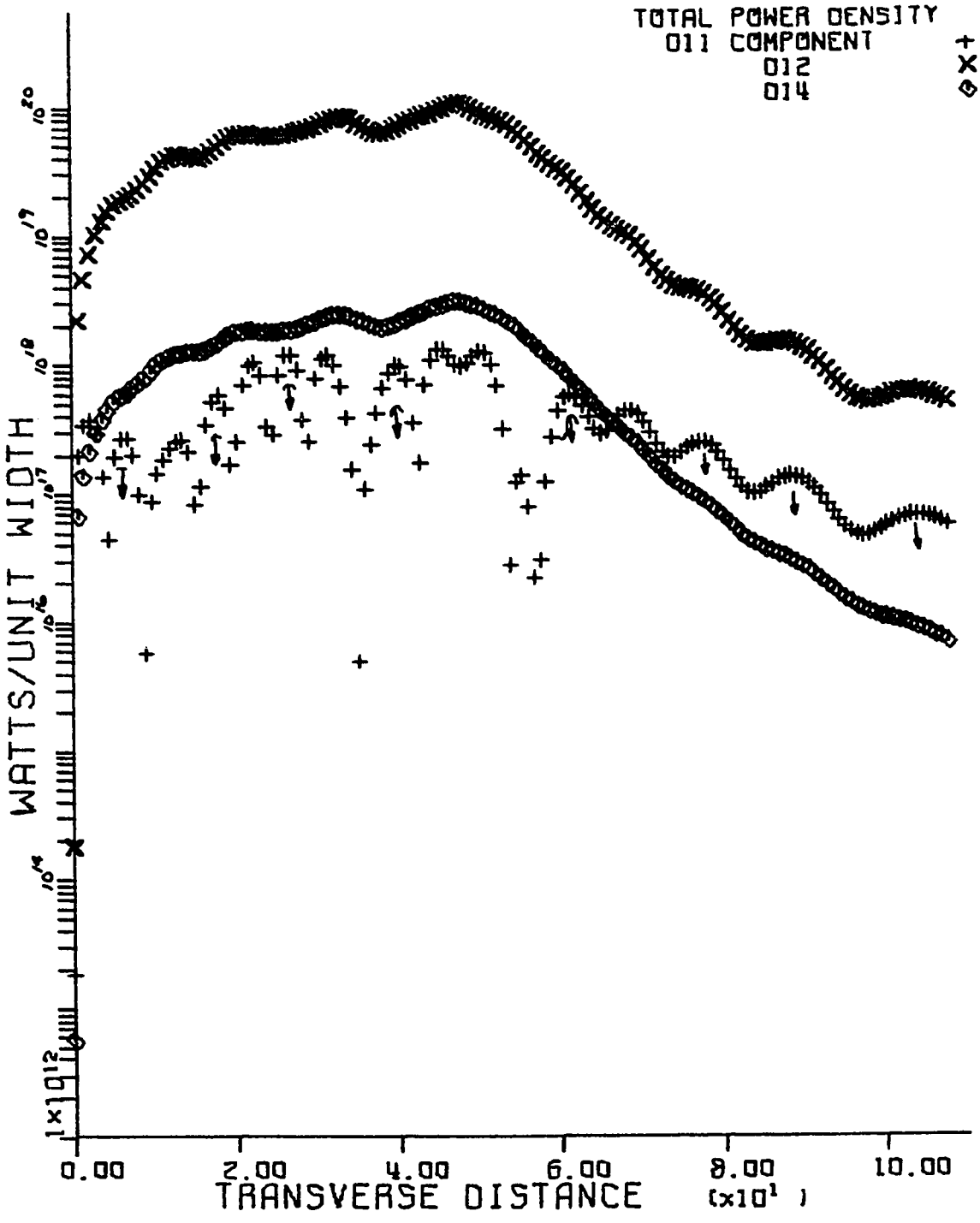

Figure 80. Terms of the total x component of the integrated Poynting vector due to C_{1133}, C_{1331}, and C_{1221} vs. $k_o x$ at $k_o y = 50.0$

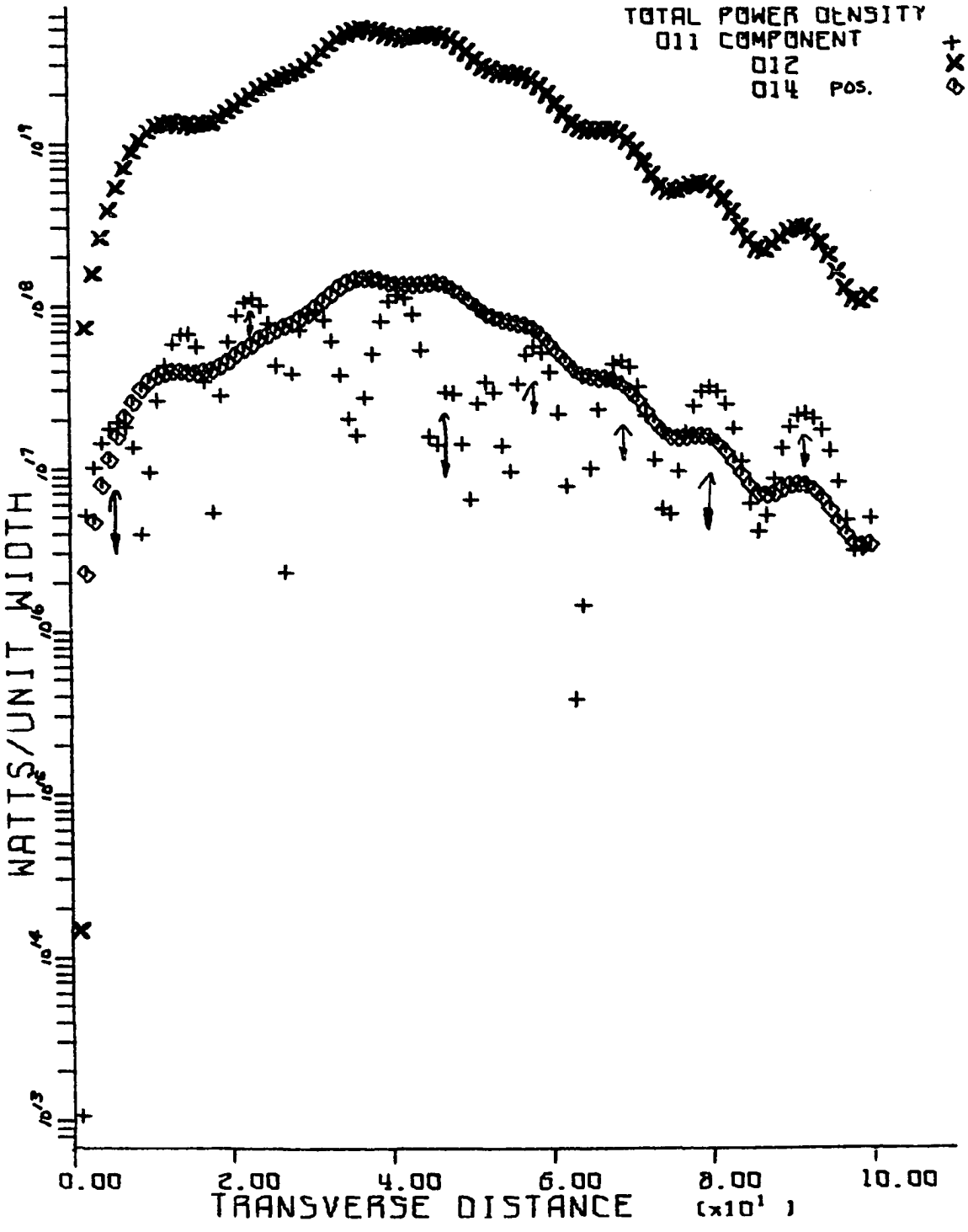

Figure 81. Terms of the total x component of the integrated Poynting vector due to C_{1133}, C_{1331}, and C_{1221} vs. $k_o x$ at $k_o y = 160.0$

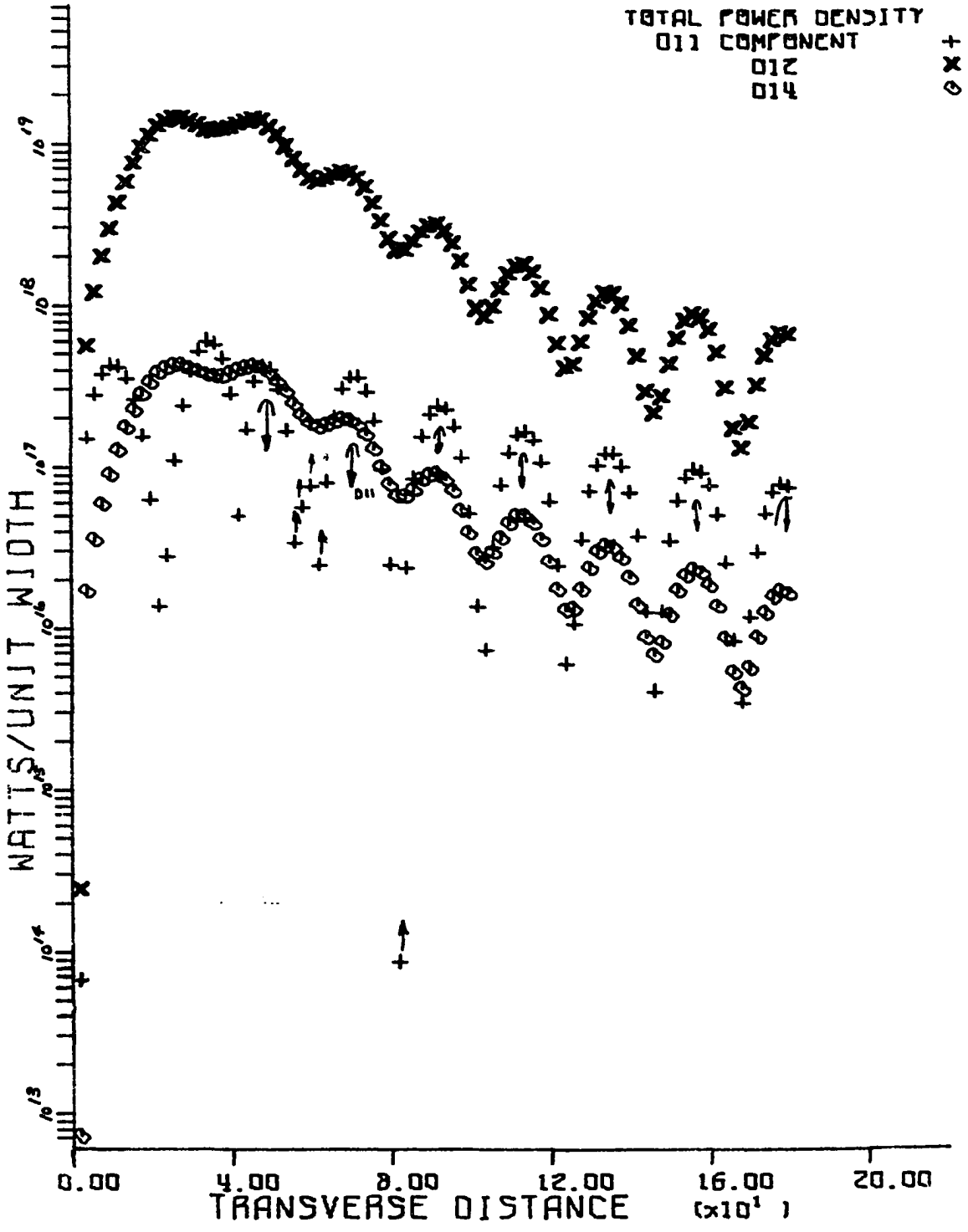

Figure 82. Terms of the total x component of the integrated Poynting vector due to C_{1133}, C_{1331}, and C_{1221} vs. $k_o x_t$ at $k_o r = 400.0$

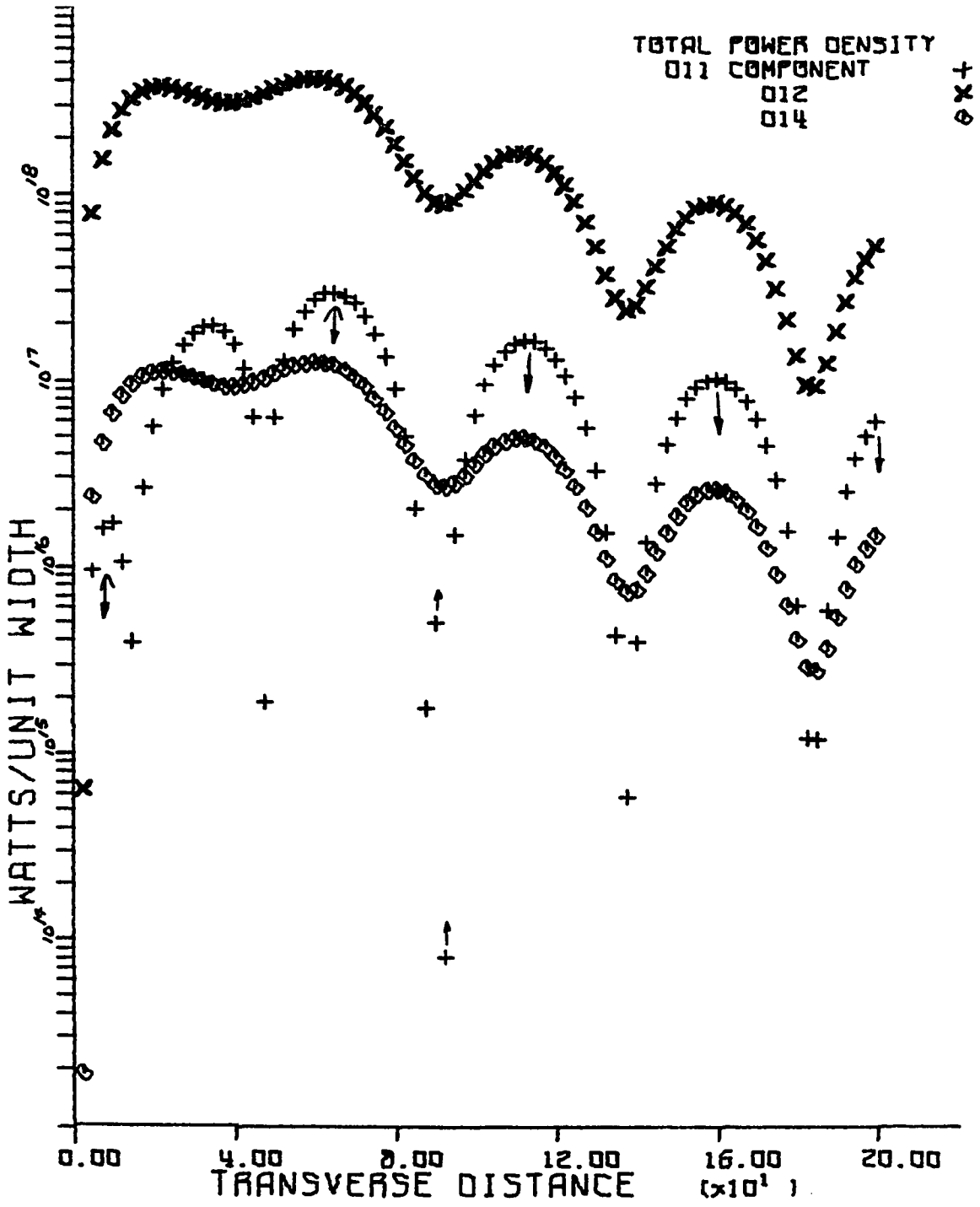

Figure 83. Terms of the total x component of the integrated Poynting vector due to C_{1133}, C_{1331}, and C_{1221} vs. $k_o x_t$ at $k_o r = 900.0$

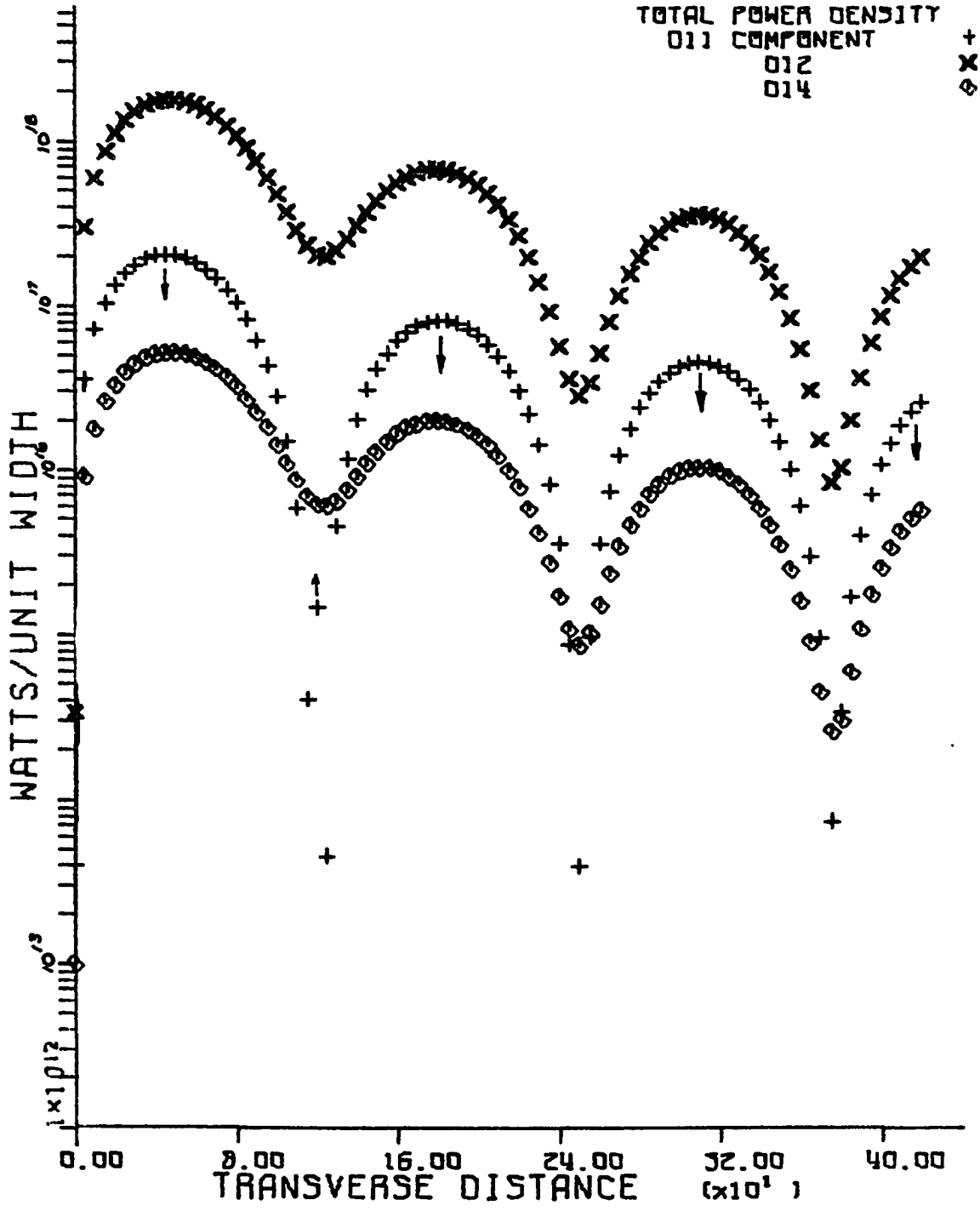

Figure 84. Terms of the total x component of the integrated Poynting vector due to C_{1133}, C_{1331}, and C_{1221} vs. $k_o x_t$ at $k_o r = 2500.0$

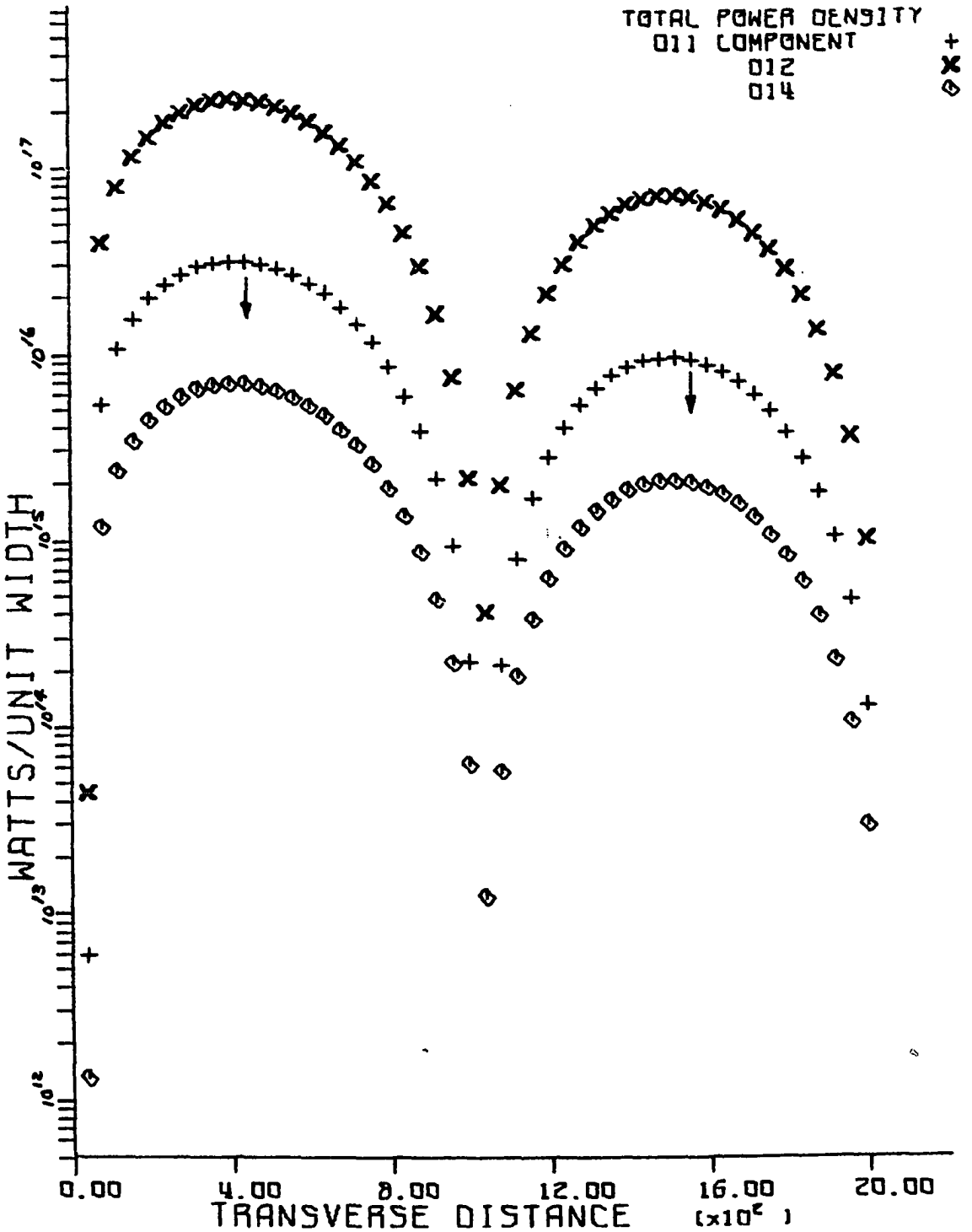

Figure 85. Terms of the total x component of the integrated Poynting vector due to C_{1133}, C_{1331}, and C_{1221} vs. $k_o x_t$ at $k_o r = 20{,}000.0$

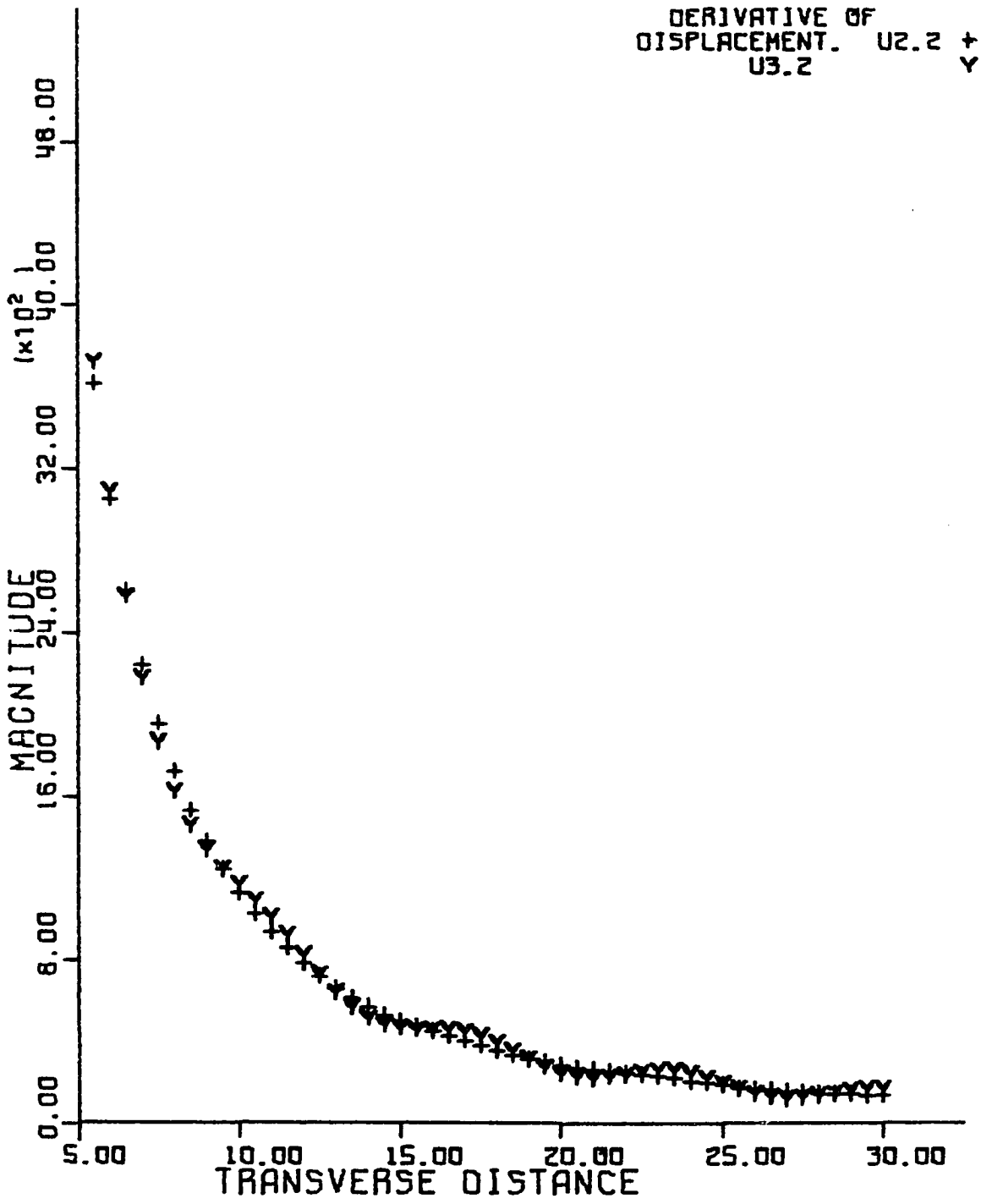

Figure 86. The magnitude of the derivative of U_2 and U_3 with respect to y vs. $k_o x$ at $k_o y = 1.0$

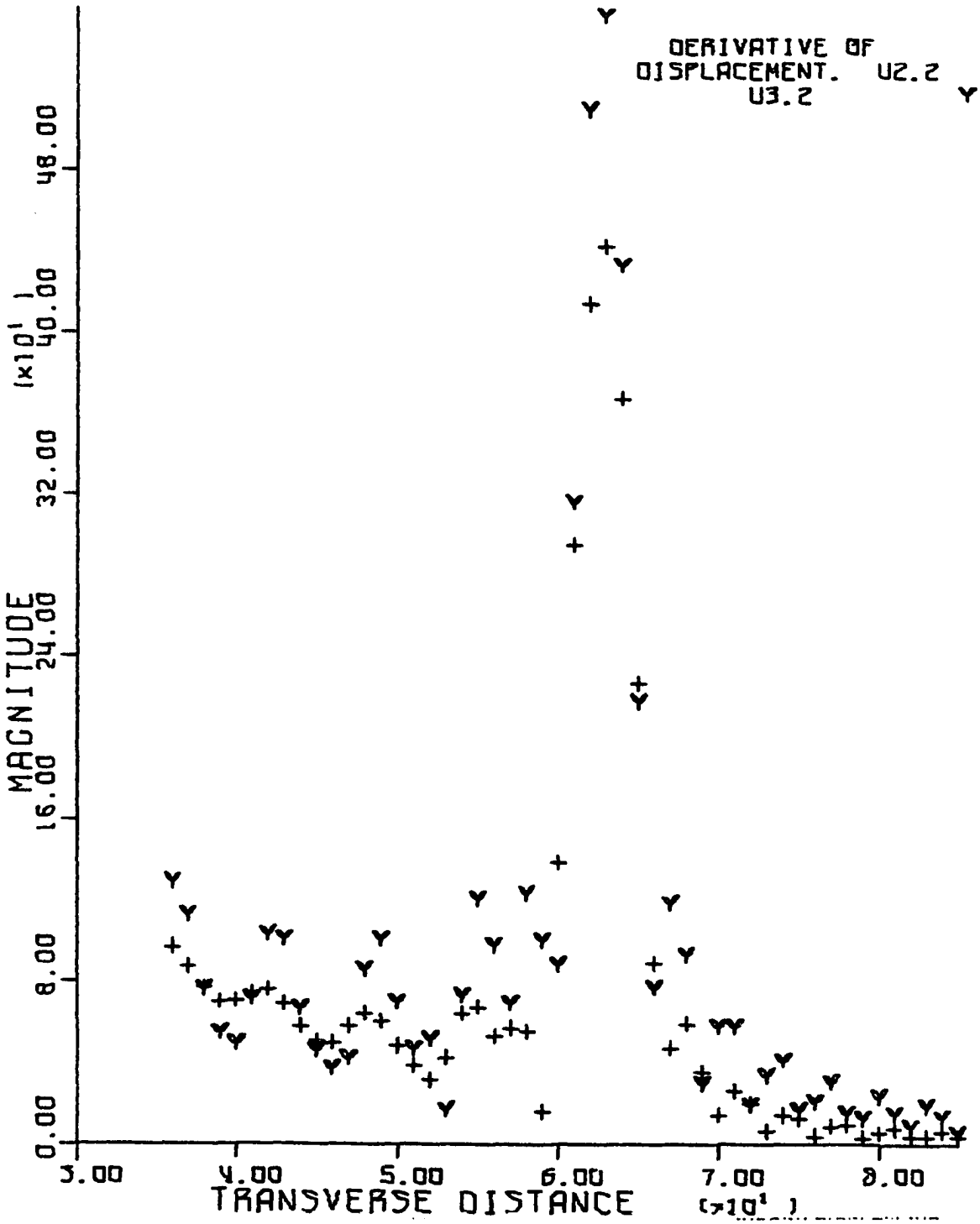

Figure 87. The magnitude of the derivative of U_2 and U_3 with respect to y vs. $k_o x$ at $k_o y = 1.0$

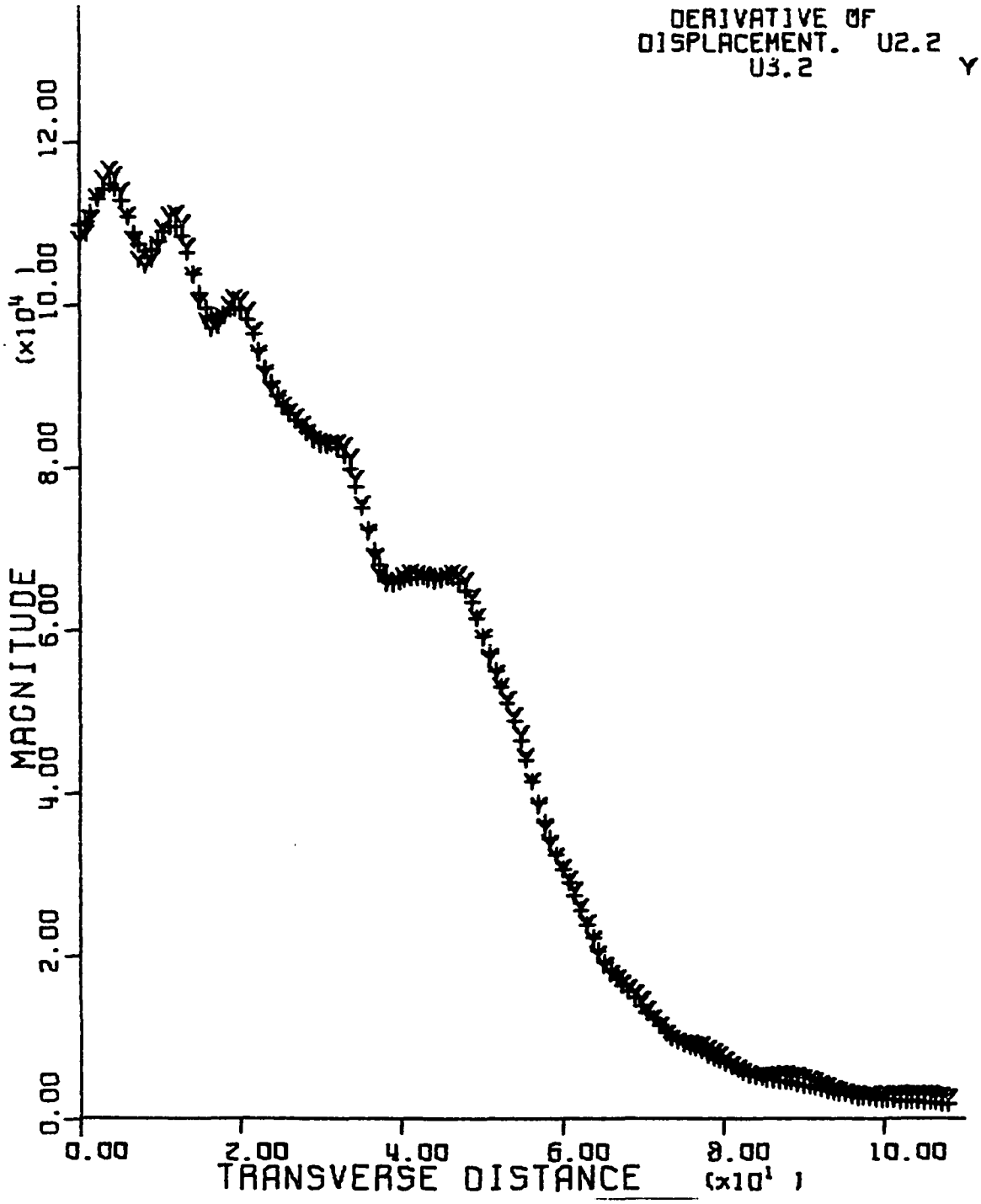

Figure 88. The magnitude of the derivative of U_2 and U_3 with respect to y vs. $k_o x$ at $k_o y = 50.0$

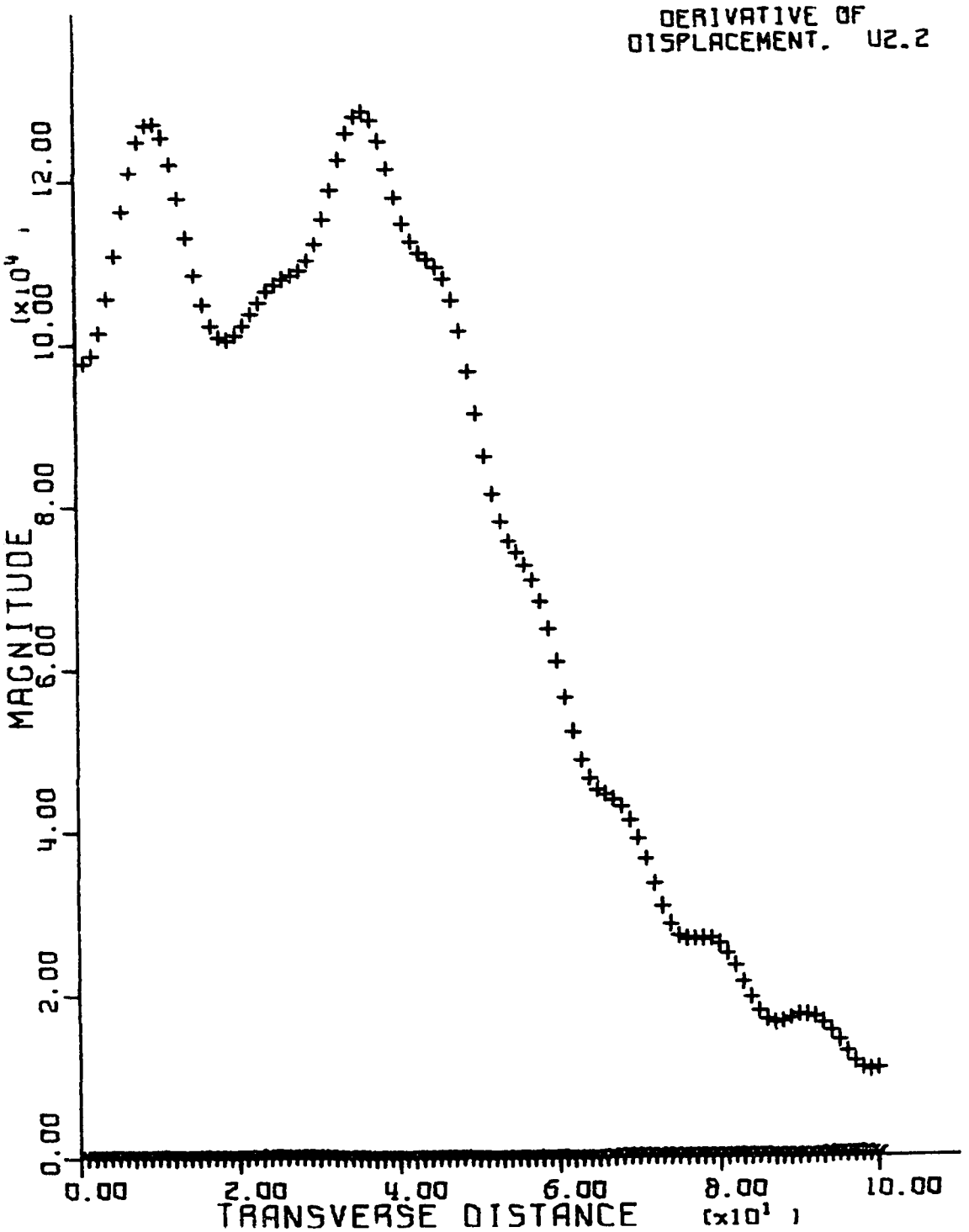

Figure 89. The magnitude of the derivative of U_2 with respect to y vs. $k_o x$ at $k_o y = 160.0$

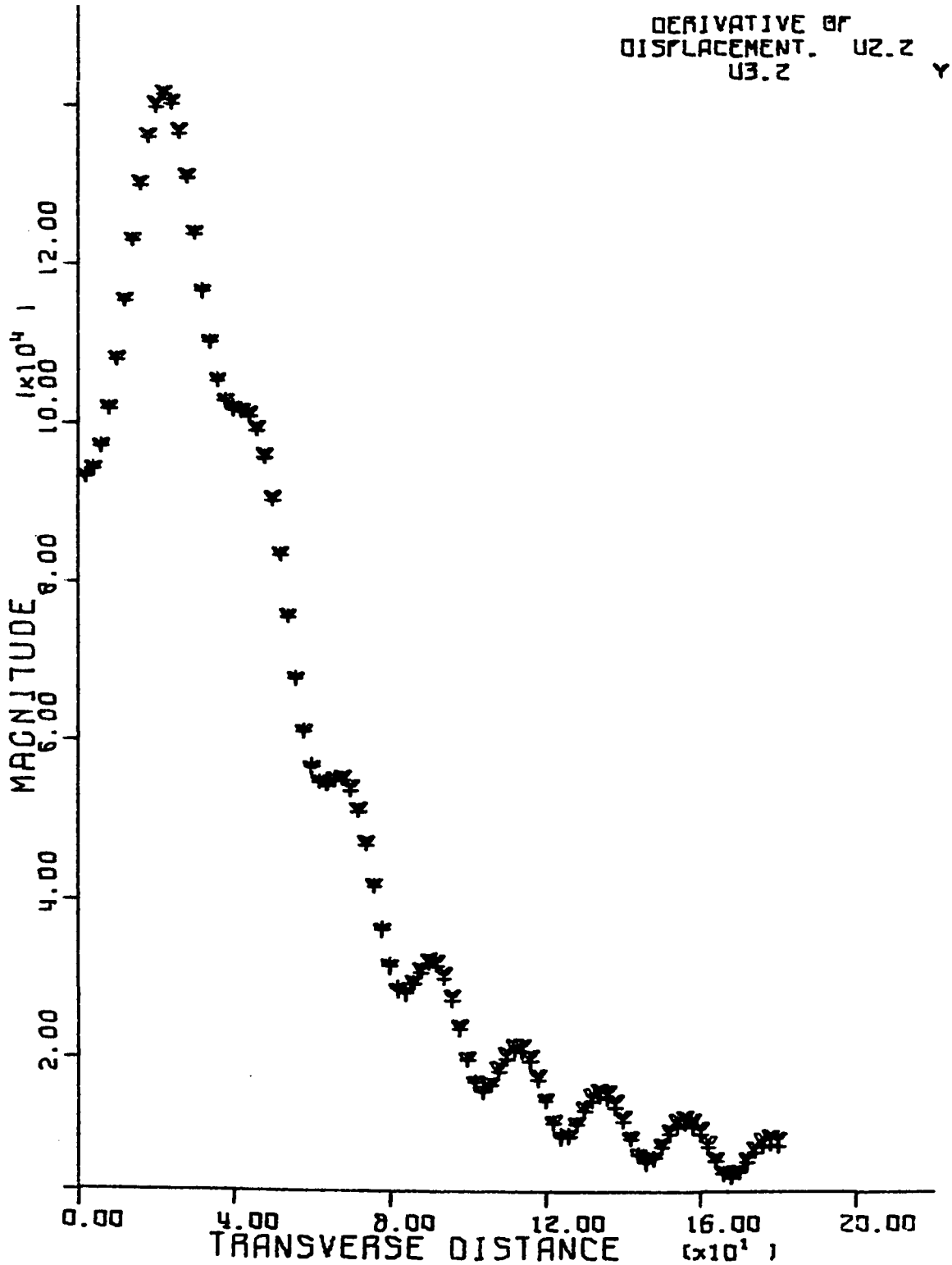

Figure 90. The magnitude of the derivative of U_2 and U_3 with respect to y vs. $k_o x_t$ at $k_o r = 400.0$

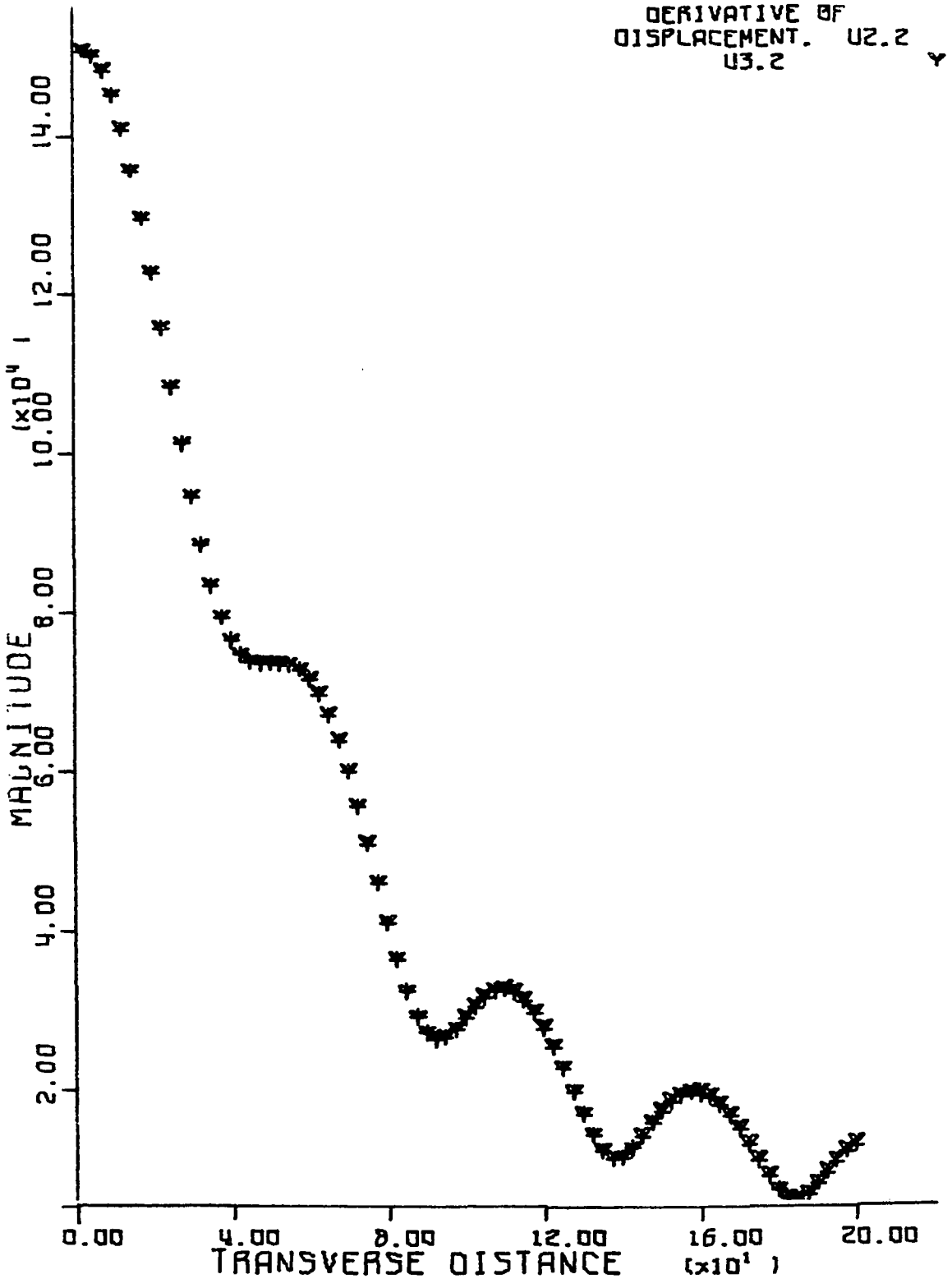

Figure 91. The magnitude of the derivative of U_2 and U_3 with respect to y vs. $k_o x_t$ at $k_o r = 900.0$

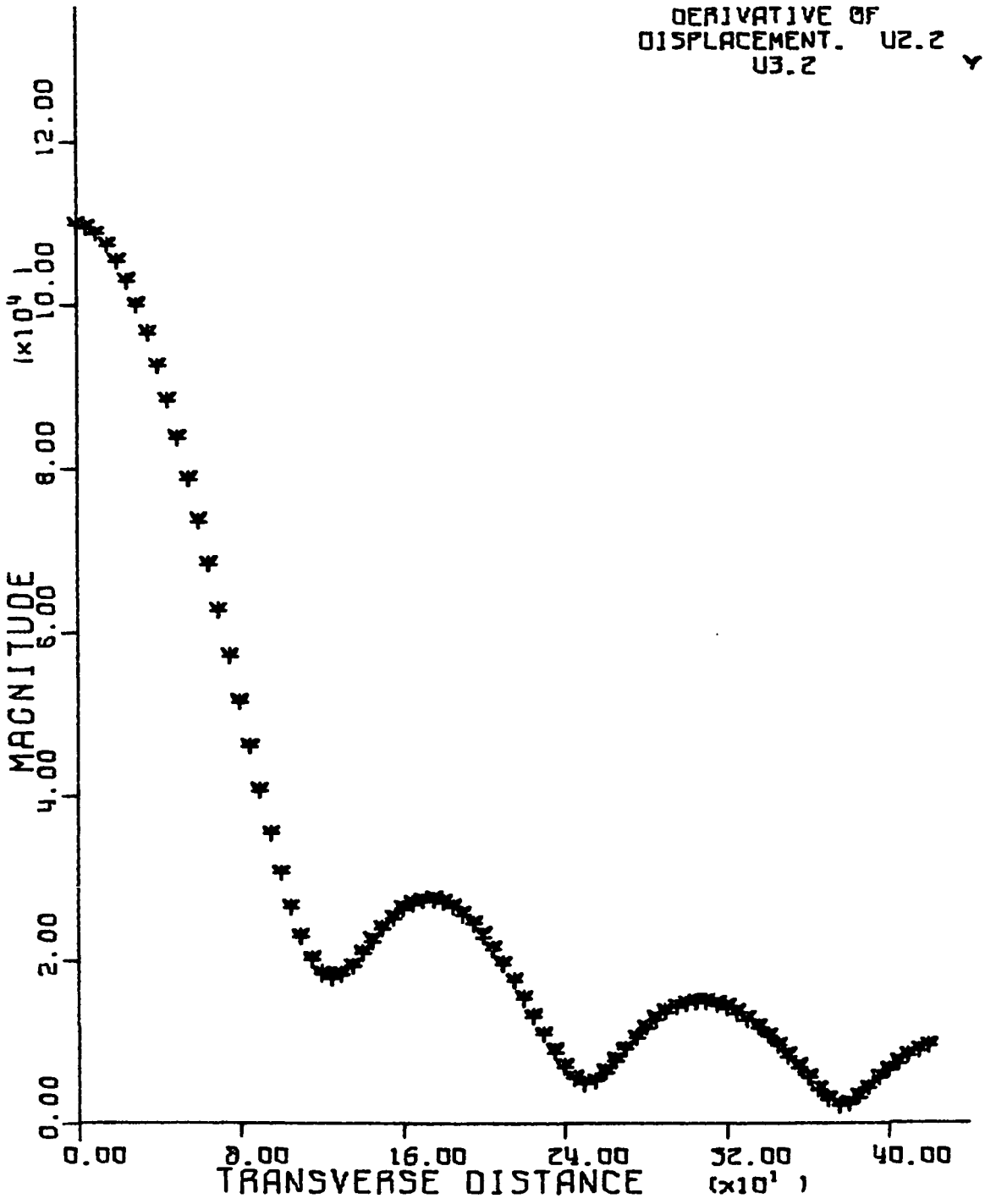

Figure 92. The magnitude of the derivative of U_2 and U_3 with respect to y vs. $k_o x_t$ at $k_o r = 2500.0$

Figure 93. The magnitude of the derivative of U_2 and U_3 with respect to y vs. $k_o x_t$ at $k_o r = 20{,}000.0$

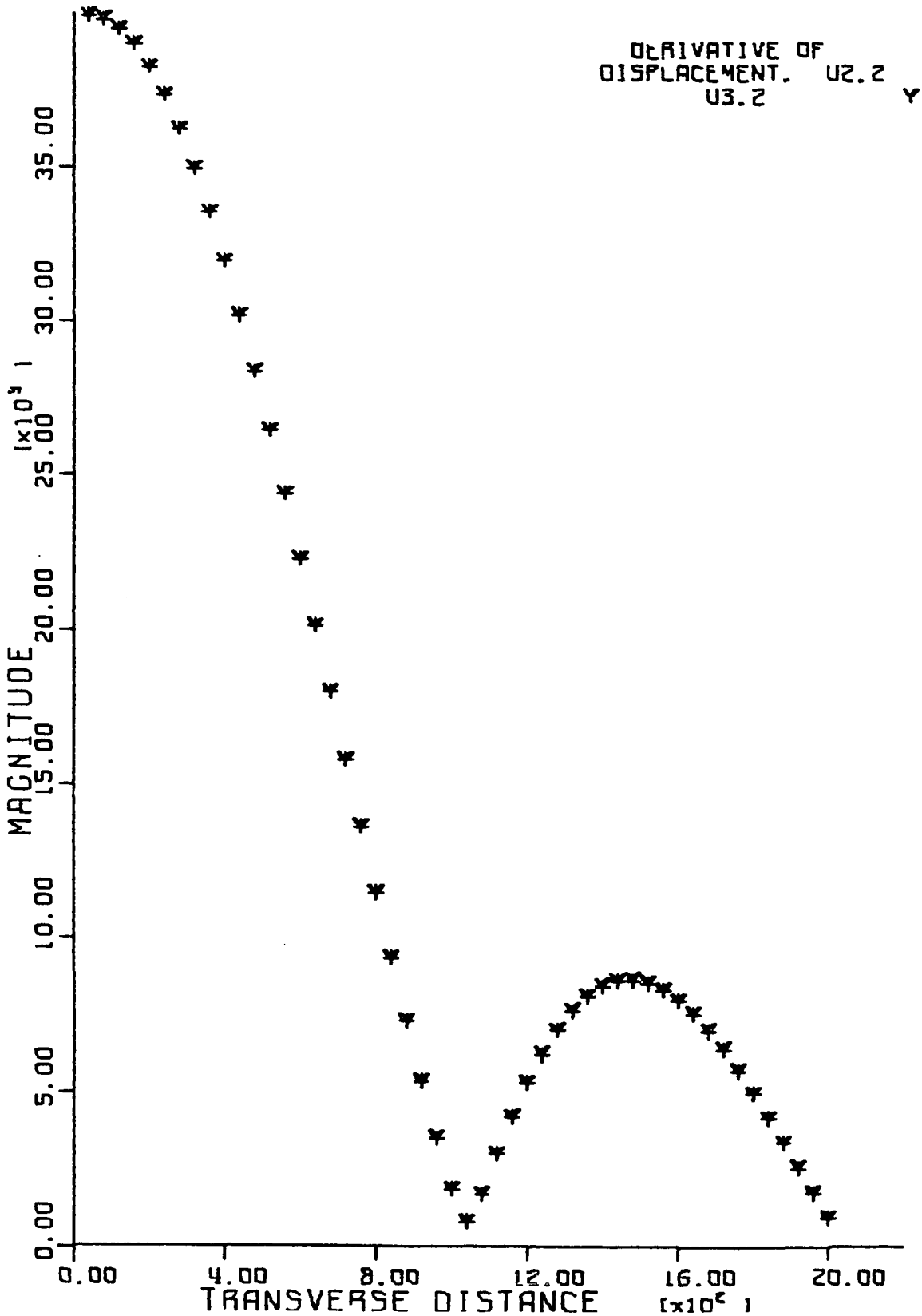
DERIVATIVE OF
DISPLACEMENT. U2.2
U3.2
Y
MAGNITUDE
[x10³]
0.00
5.00
10.00
15.00
20.00
25.00
30.00
35.00
0.00
4.00
8.00
12.00
16.00
20.00
TRANSVERSE DISTANCE
[x10²]

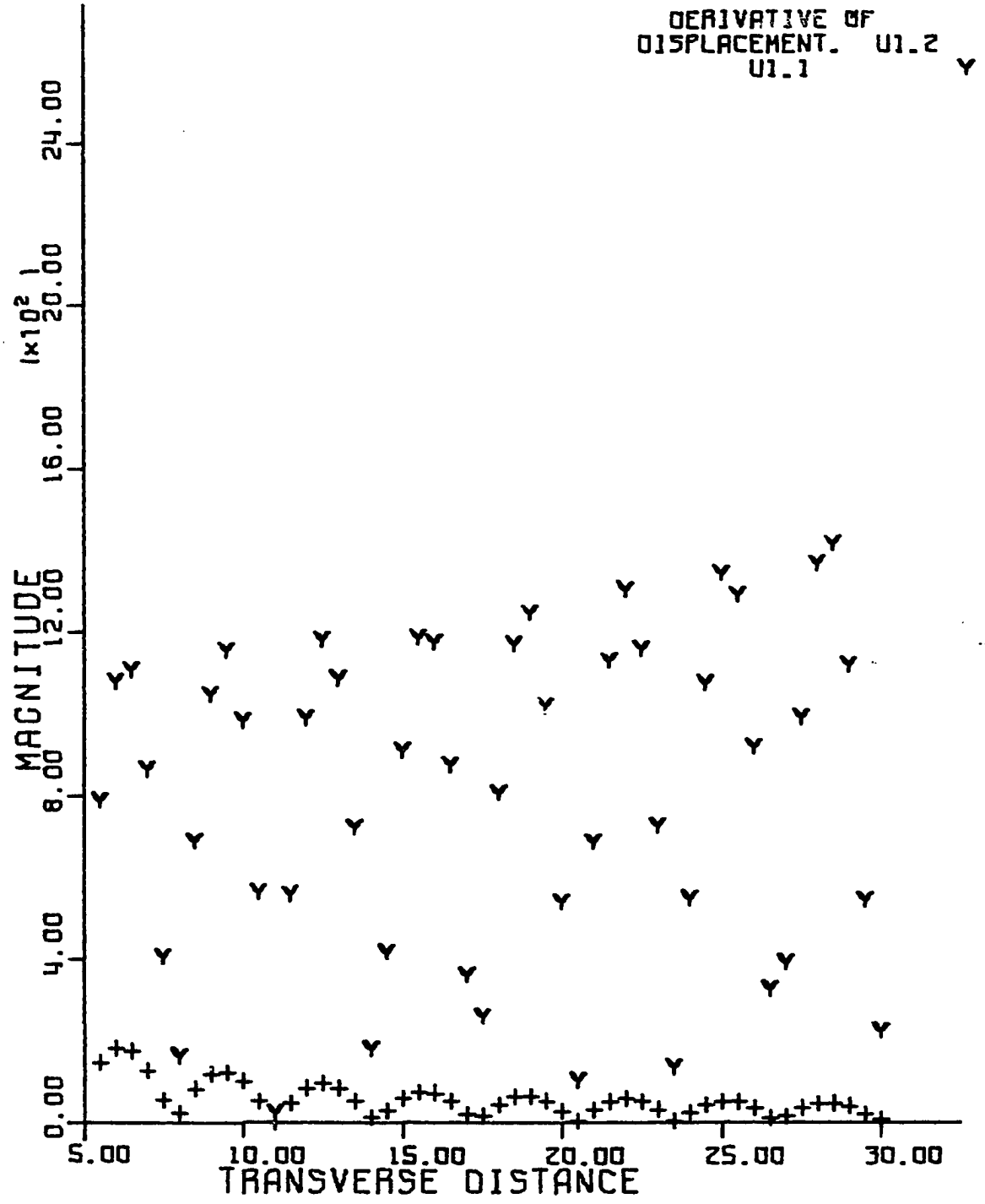

Figure 94. The magnitude of the derivatives of U_1 with respect to x and y vs. $k_o x$ at $k_o y = 1.0$

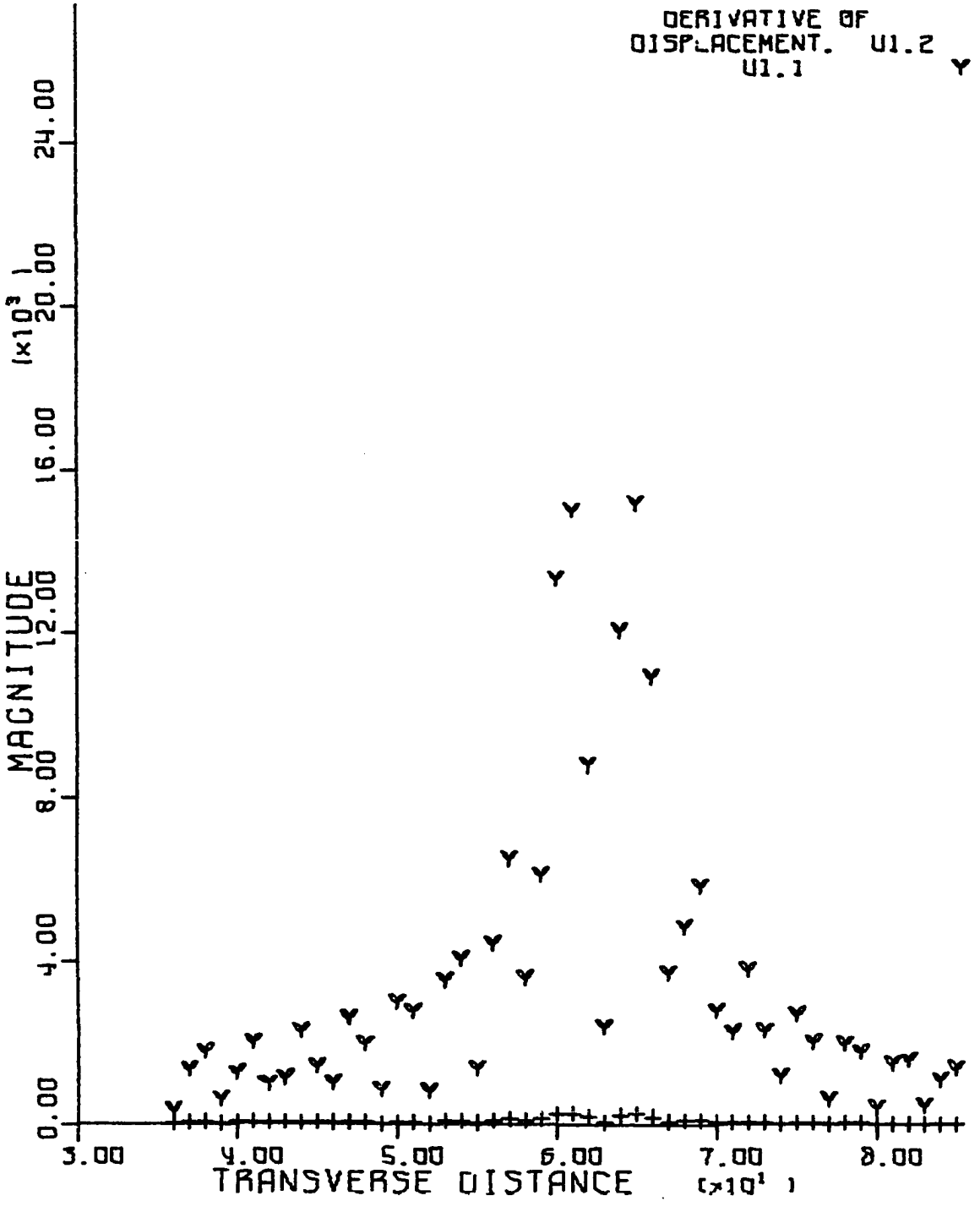

Figure 95. The magnitude of the derivatives of U_1 with respect to x and y vs. $k_o x$ at $k_o y = 1.0$

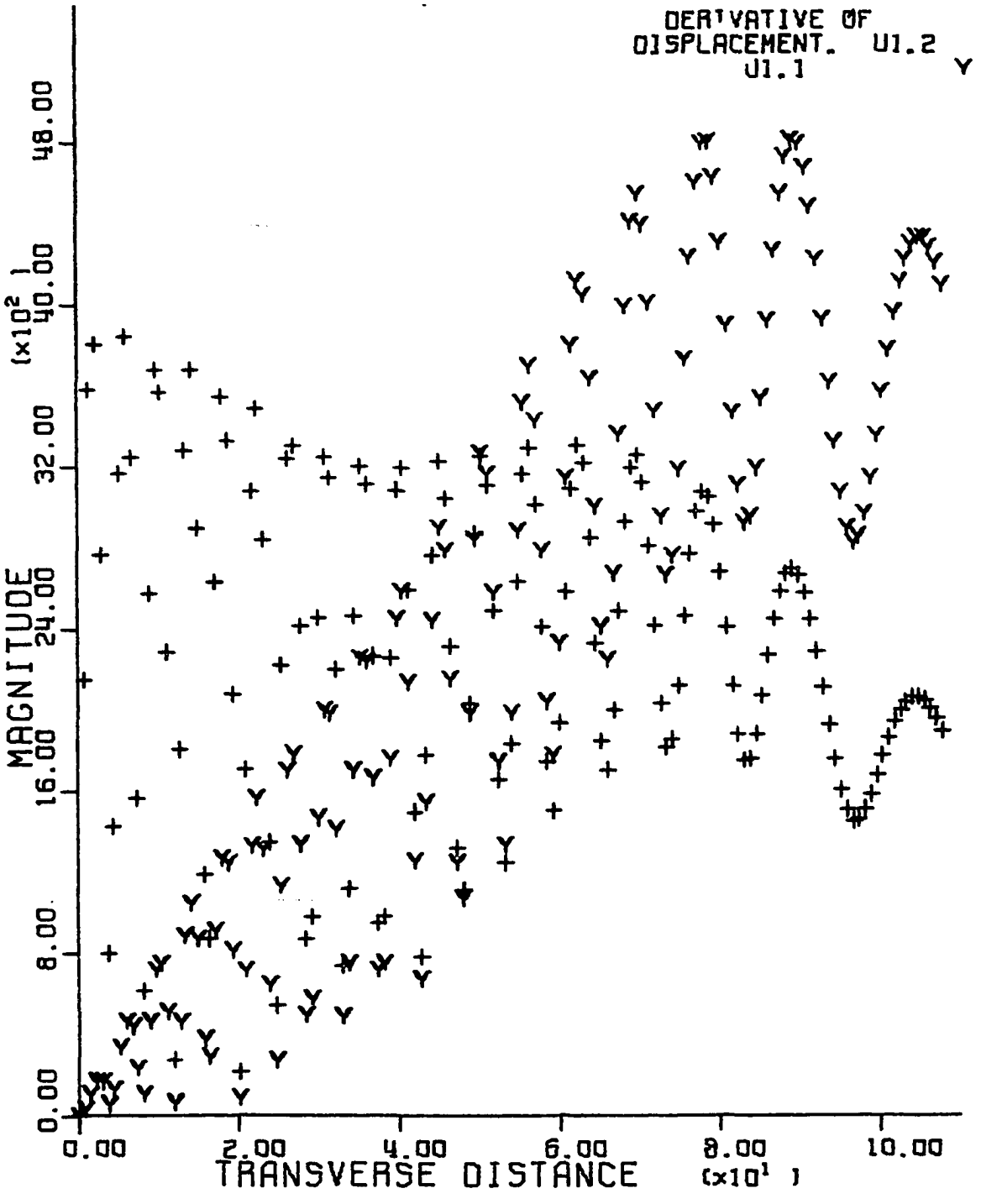

Figure 96. The magnitude of the derivatives of U_1 with respect to x and y vs. $k_o x$ at $k_o y = 50.0$

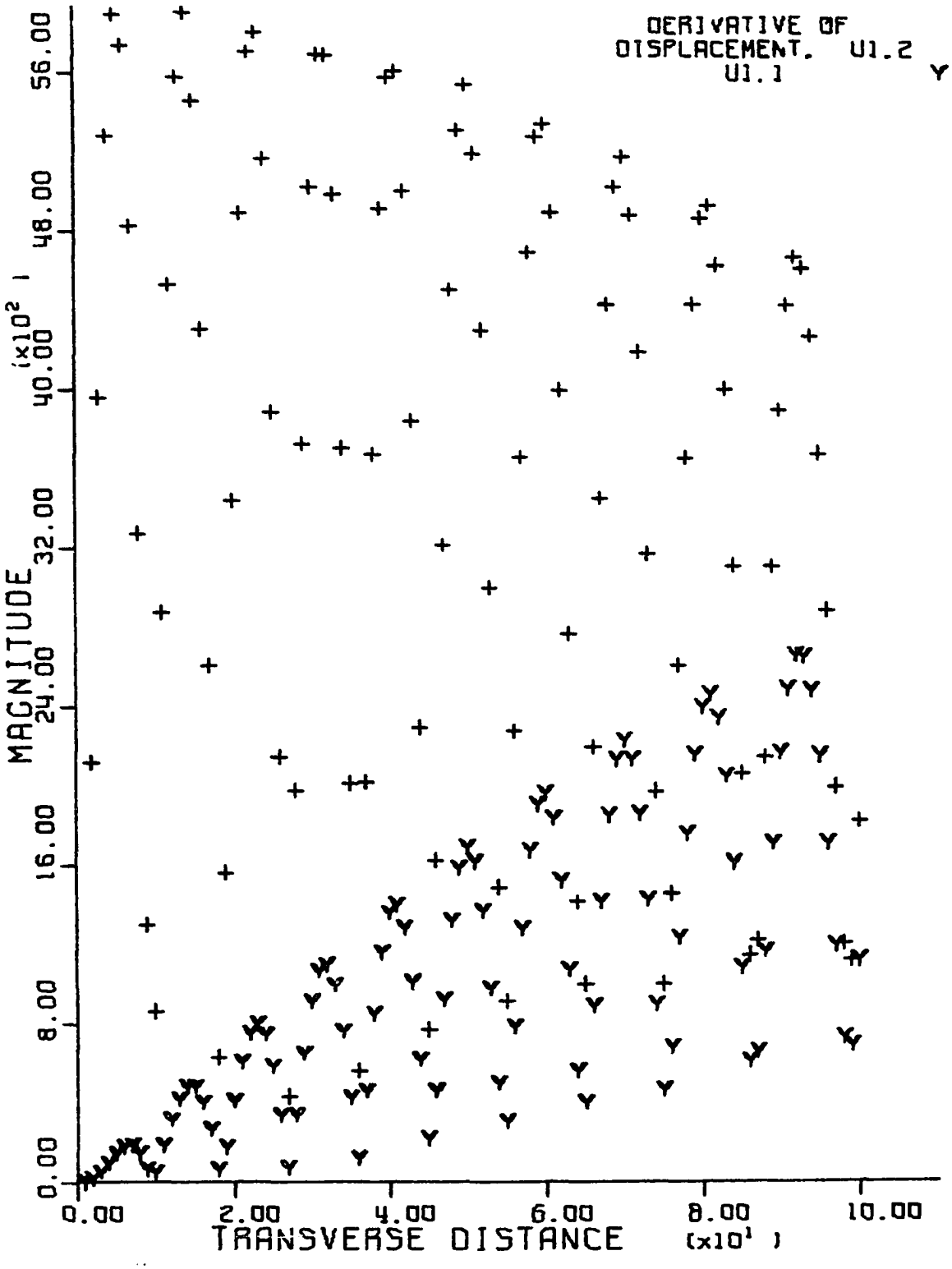

Figure 97. The magnitude of the derivatives of U_1 with respect to x and y vs. $k_o x$ at $k_o y = 160.0$

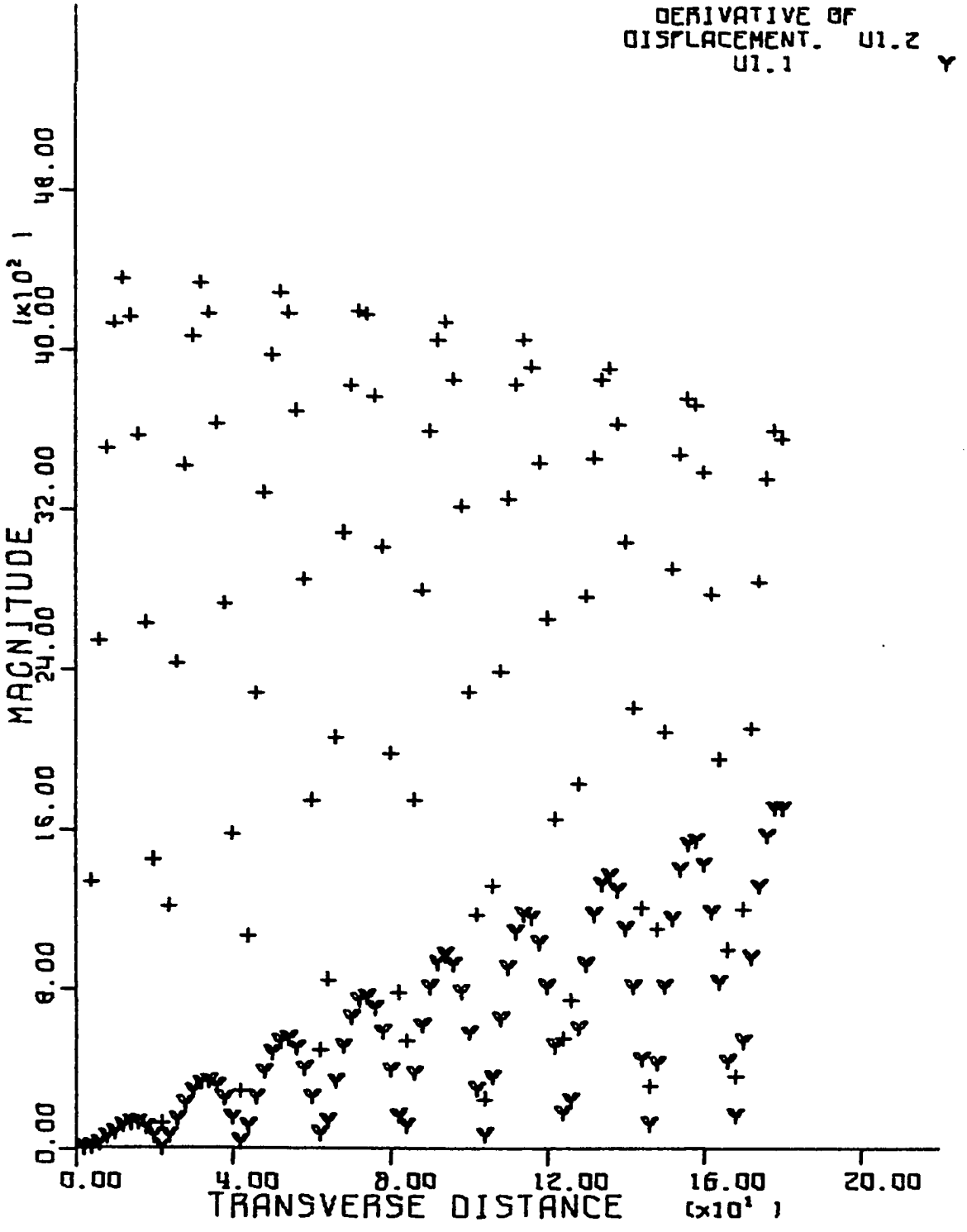

Figure 98. The magnitude of the derivatives of U_1 with respect to x and y vs. $k_o x_t$ at $k_o r = 400.0$

Figure 99. The magnitude of the derivatives of U_1 with respect to x and y vs. $k_o x_t$ at $k_o r = 900.0$

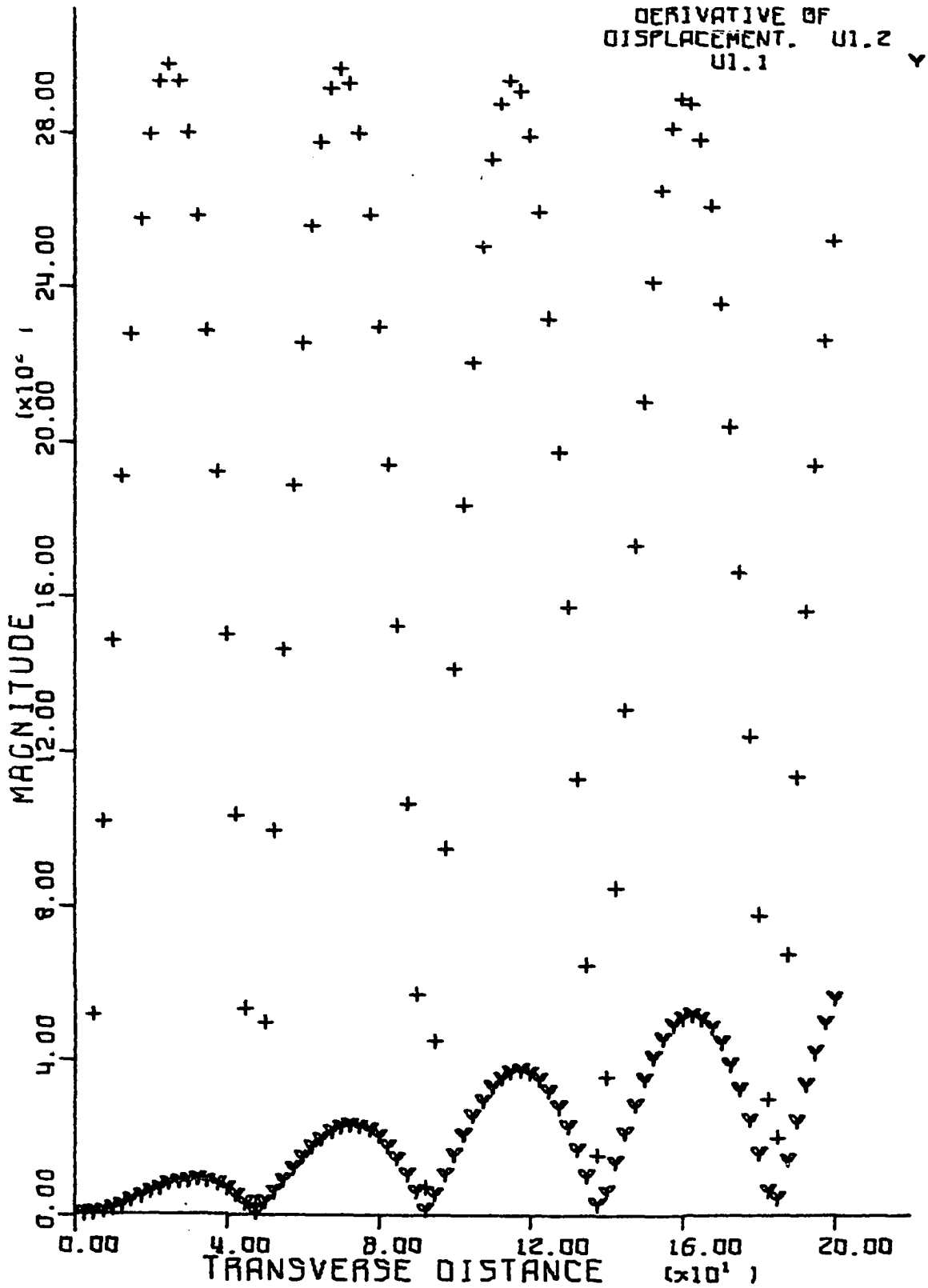
DERIVATIVE OF
DISPLACEMENT. U1.2
U1.1
MAGNITUDE (x10²)
0.00
4.00
8.00
12.00
16.00
20.00
24.00
28.00
0.00
4.00
8.00
12.00
16.00
20.00
TRANSVERSE DISTANCE (x10¹)

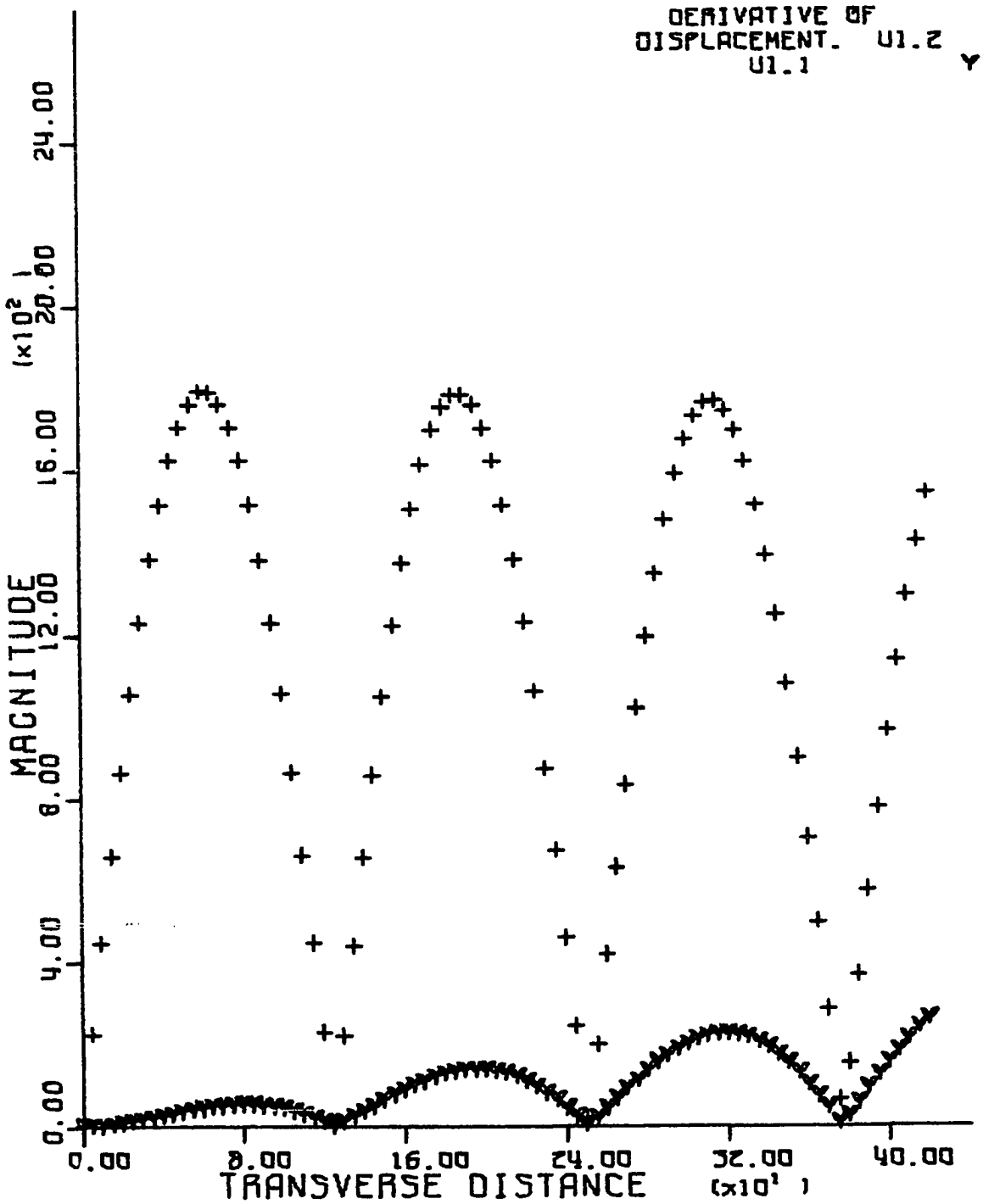

Figure 100. The magnitude of the derivatives of U_1 with respect to x and y vs. $k_o x_t$ at $k_o r = 2500.0$

Figure 101. The magnitude of the derivatives of U_1 with respect to x and y vs. $k_o x_t$ at $k_o r = 20{,}000.0$

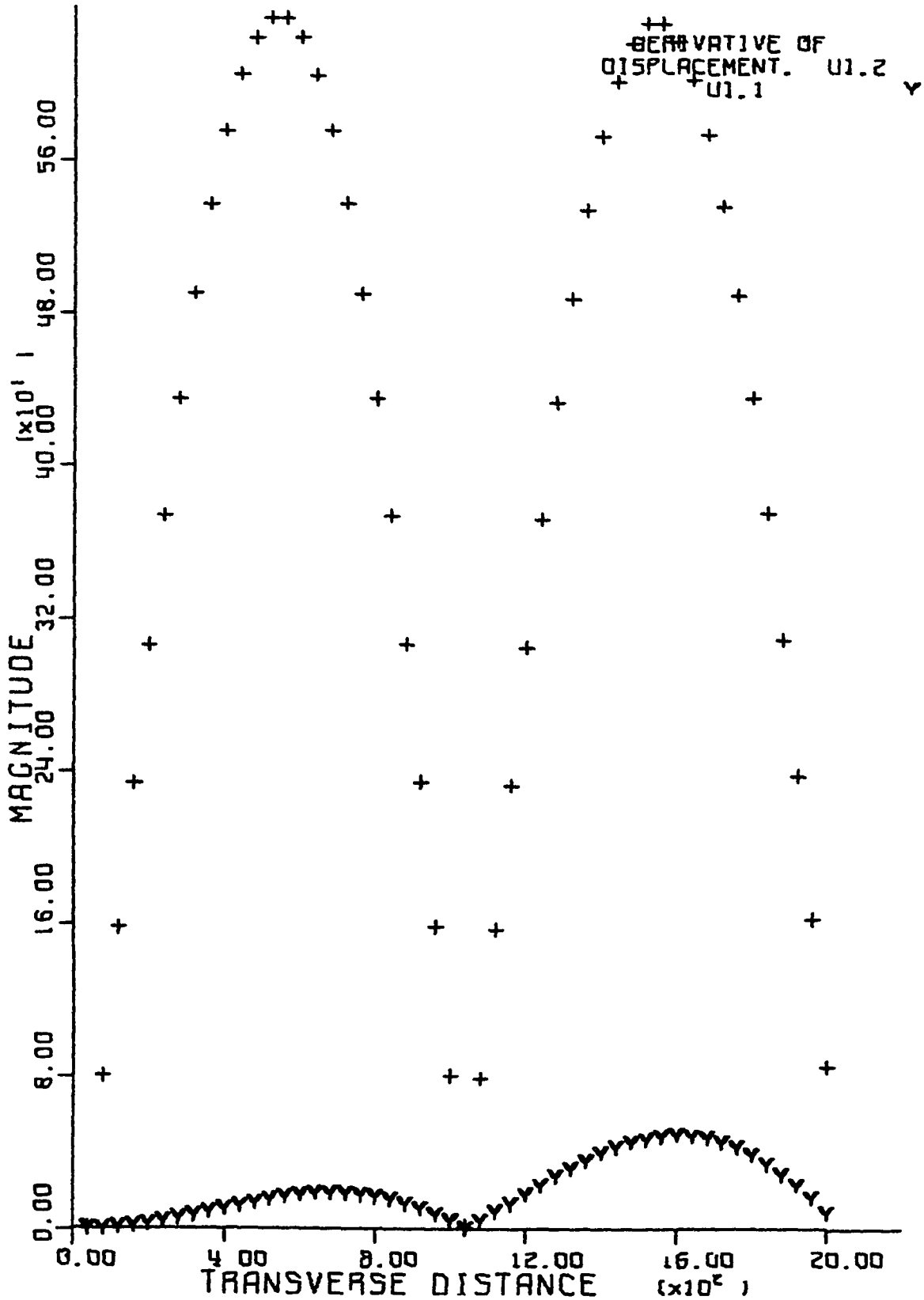
DERIVATIVE OF
DISPLACEMENT. U1.2
U1.1
MAGNITUDE (x10¹)
0.00
8.00
16.00
24.00
32.00
40.00
48.00
56.00
0.00
4.00
8.00
12.00
16.00
20.00
TRANSVERSE DISTANCE (x10²)

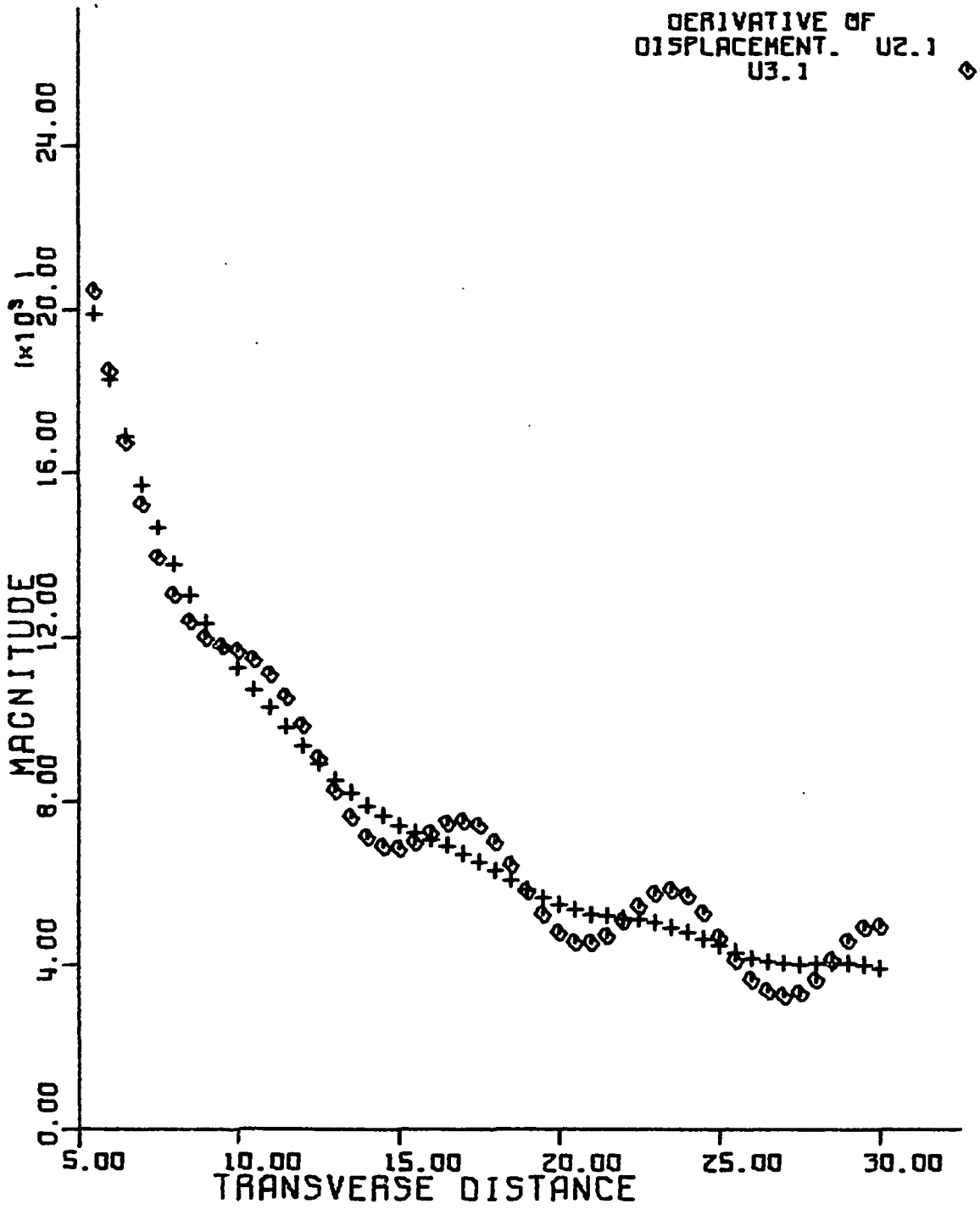

Figure 102. The magnitude of the derivatives of U_2 and U_3 with respect to x vs. $k_o x$ at $k_o y = 1.0$

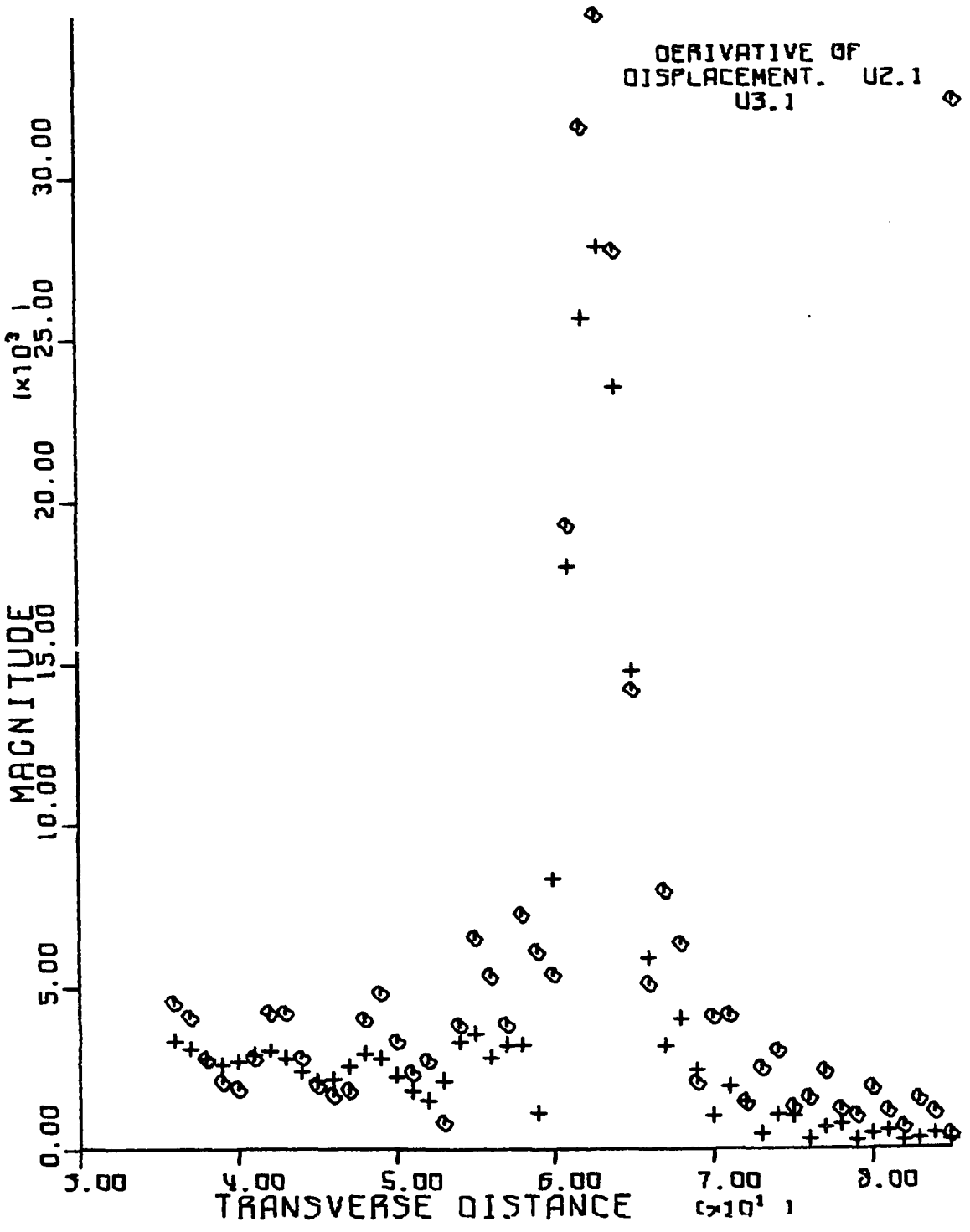

Figure 103. The magnitude of the derivatives of U_2 and U_3 with respect to x vs. $k_o x$ and $k_o y = 1.0$

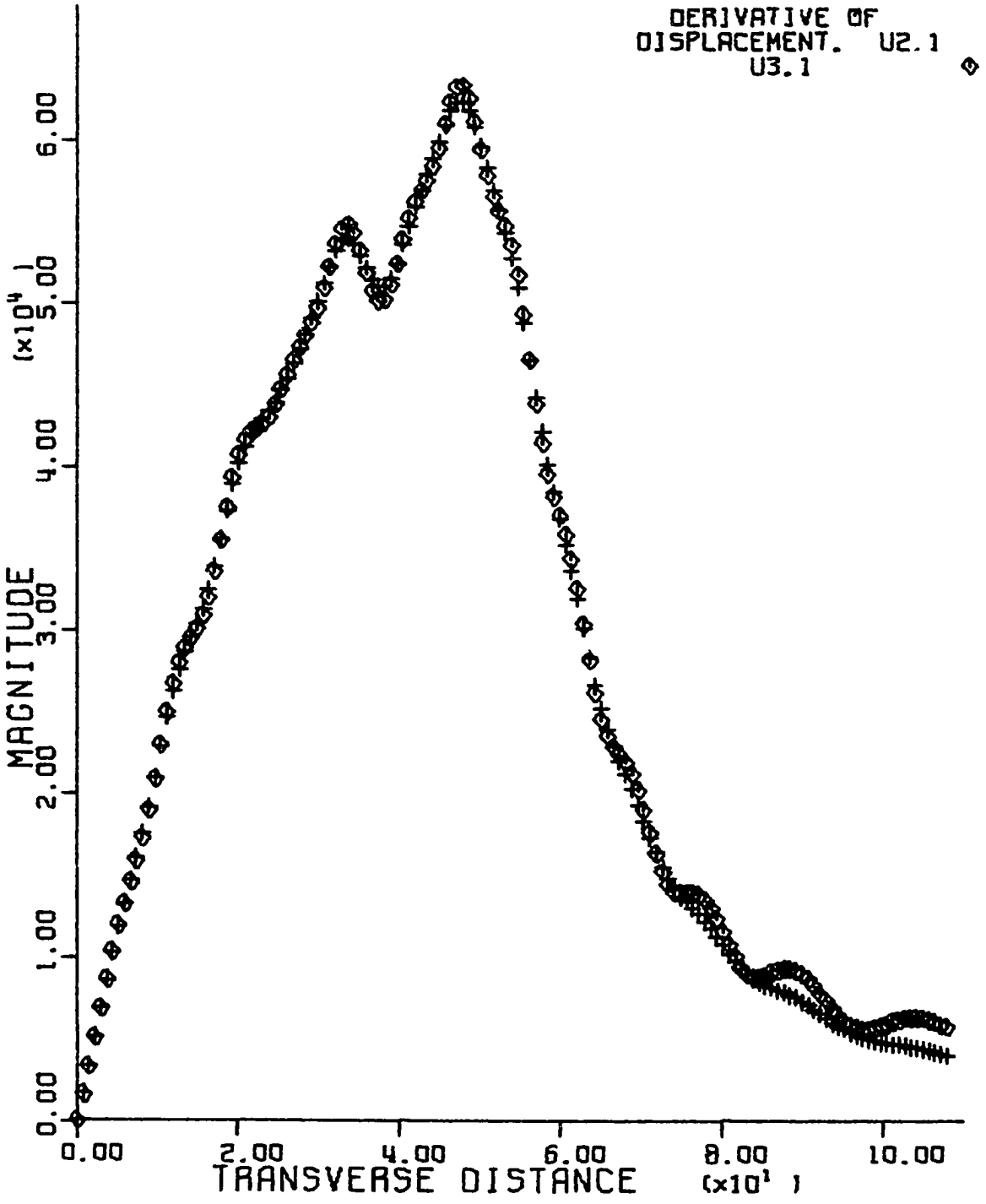

Figure 104. The magnitude of the derivatives of U_2 and U_3 with respect to x vs. $k_o x$ at $k_o y = 50.0$

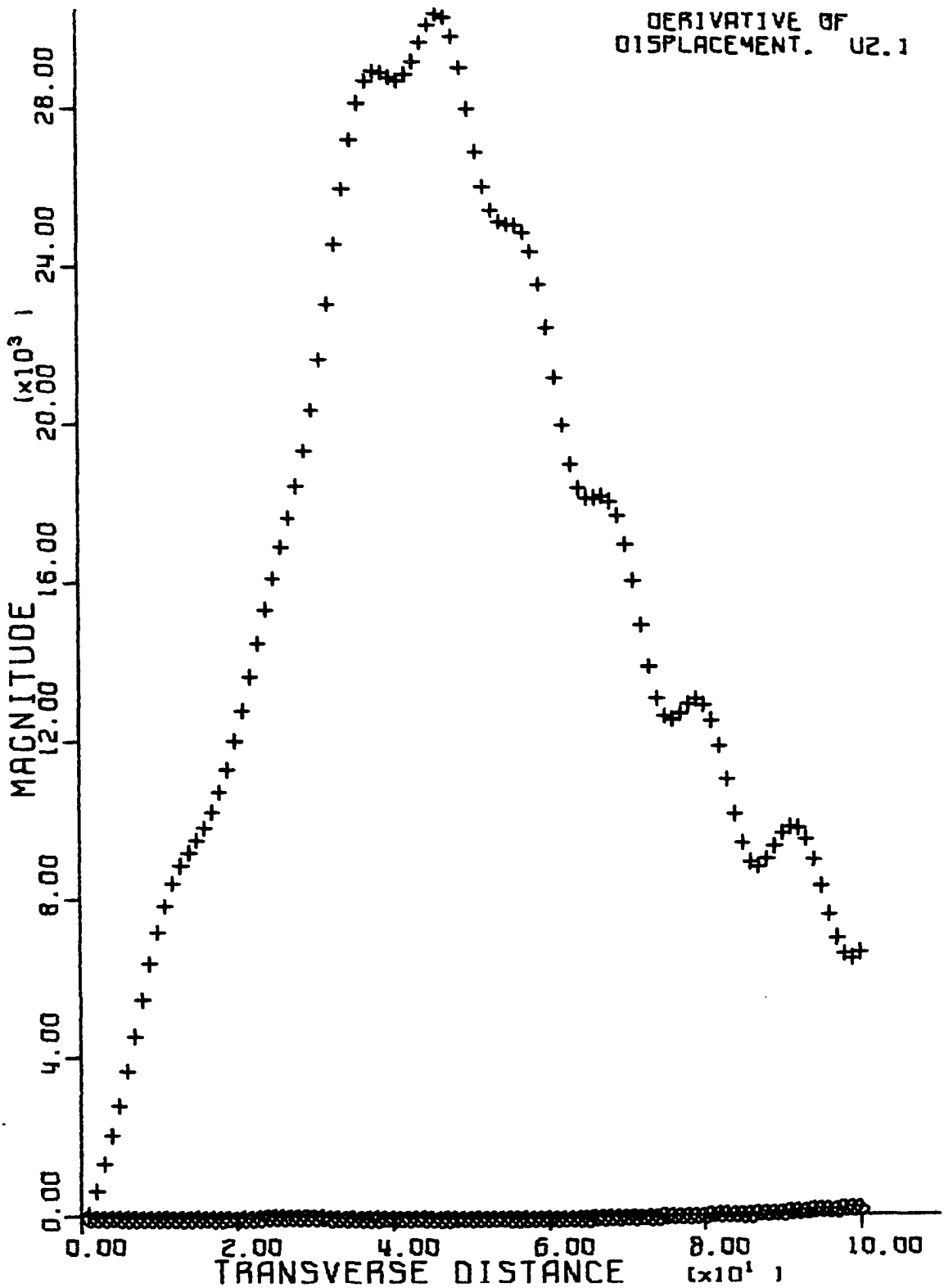

Figure 105. The magnitude of the derivative of U_2 with respect to x vs. $k_o x$ at $k_o y = 160.0$

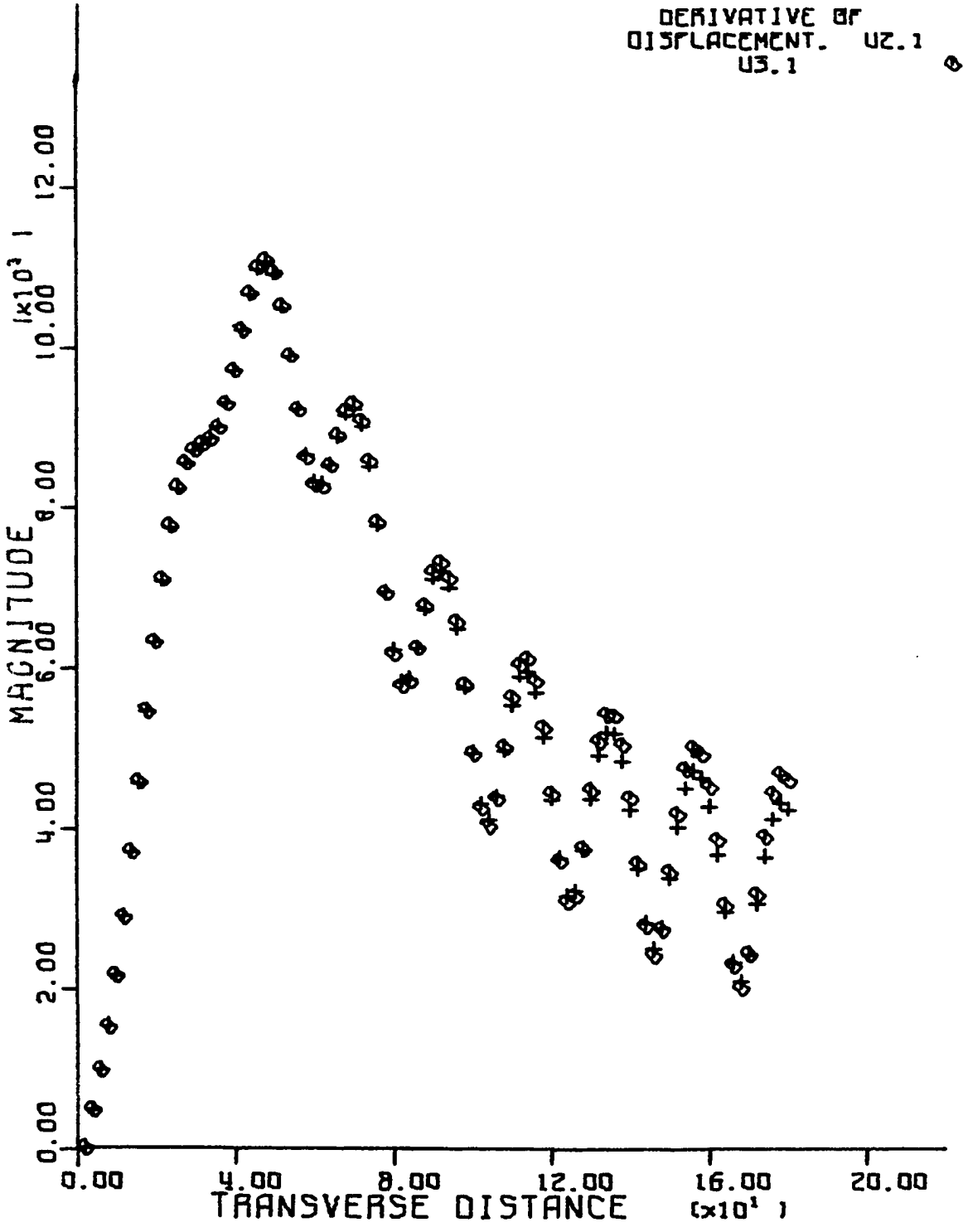

Figure 106. The magnitude of the derivatives of U_2 and U_3 with respect to x vs. $k_o x_t$ at $k_o r = 400.0$

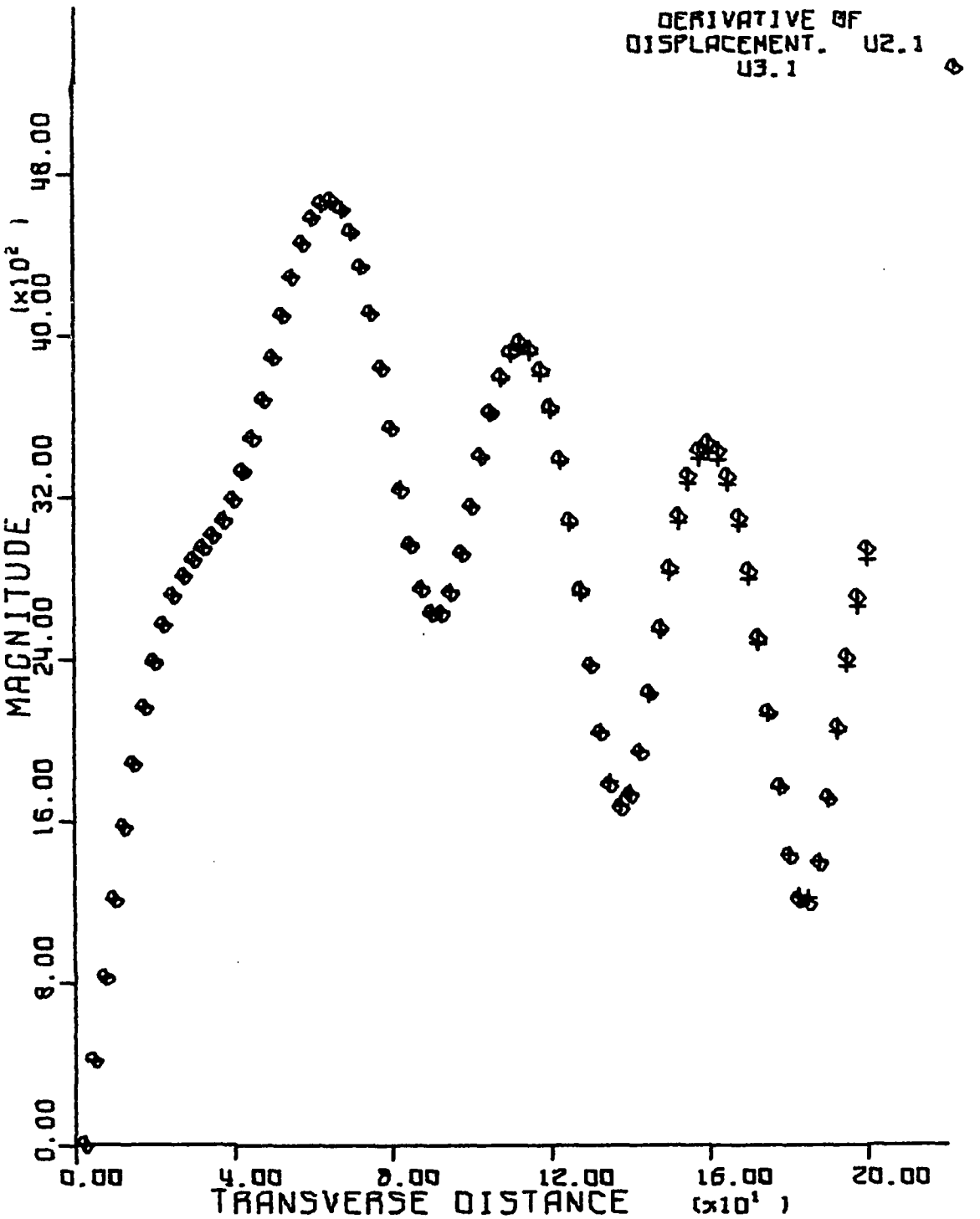

Figure 107. The magnitude of the derivatives of U_2 and U_3 with respect to x vs. $k_o x_t$ at $k_o r = 900.0$

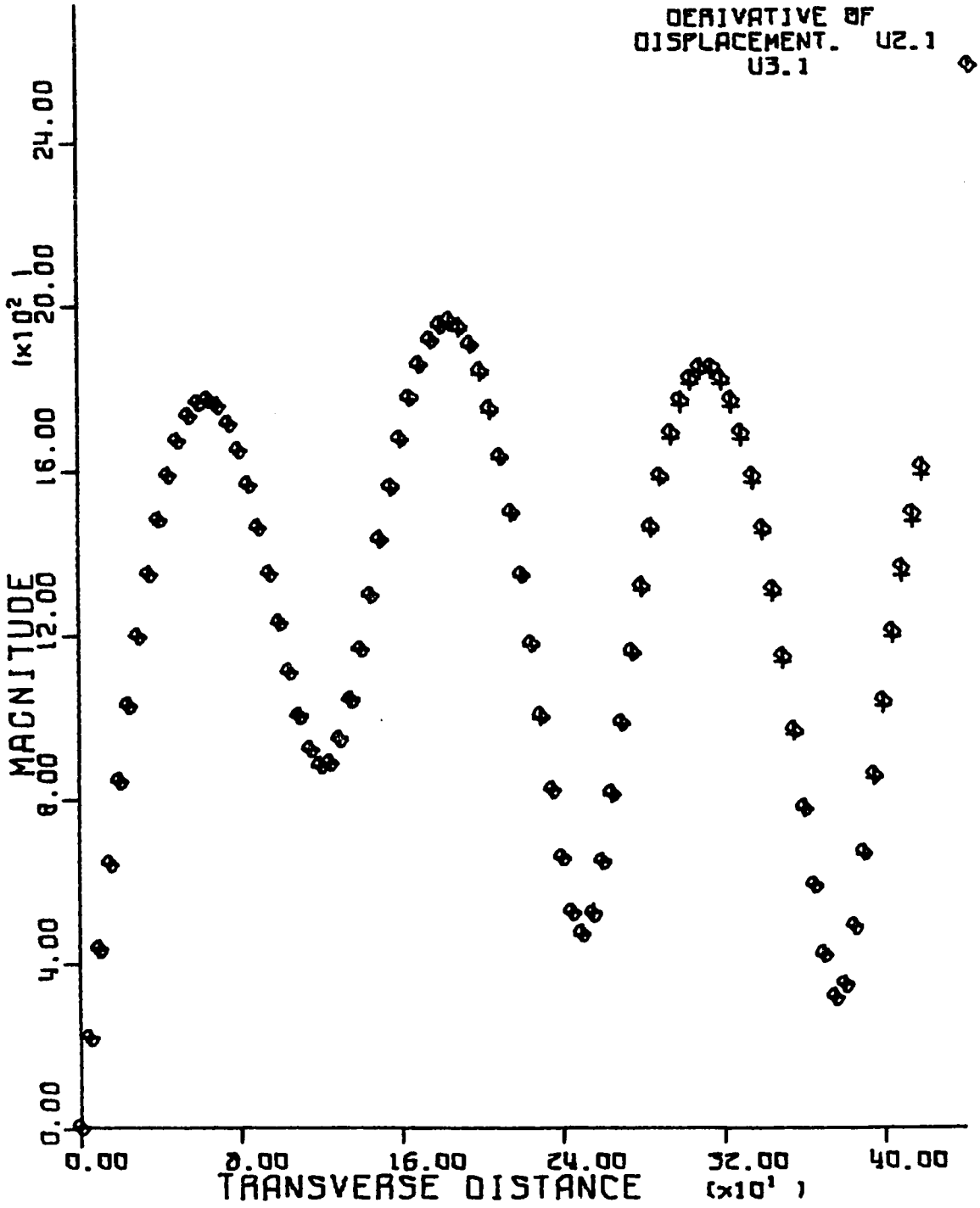

Figure 108. The magnitude of the derivatives of U_2 and U_3 with respect to x vs. $k_o x_t$ at $k_o r = 2500.0$

Figure 109. The magnitude of the derivatives of U_2 and U_3 with respect to x vs. $k_o x_t$ at $k_o r = 20{,}000.0$

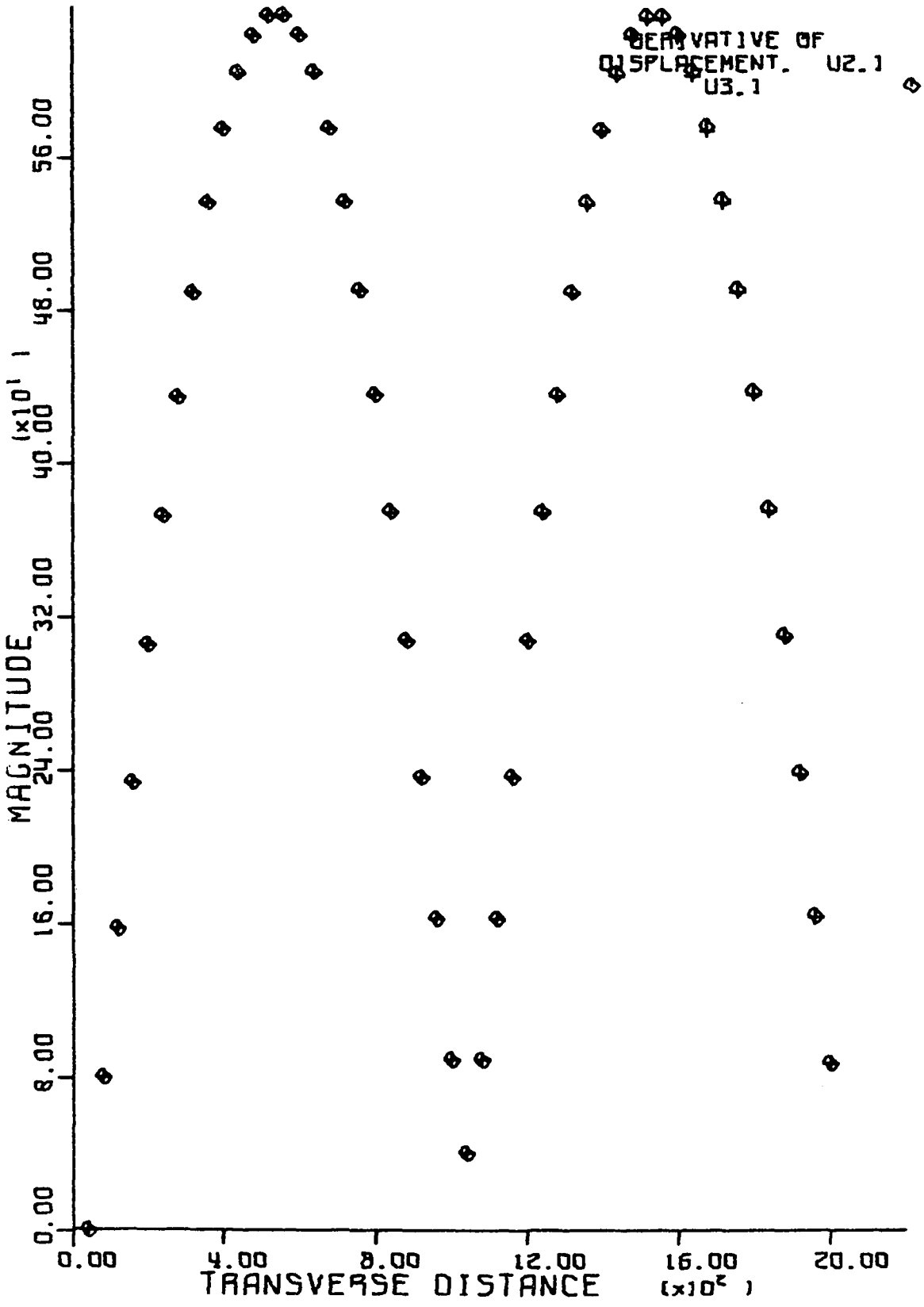
DERIVATIVE OF
DISPLACEMENT. U2.1
U3.1
MAGNITUDE
(x10¹)
0.00
8.00
16.00
24.00
32.00
40.00
48.00
56.00
0.00
4.00
8.00
12.00
16.00
20.00
TRANSVERSE DISTANCE
(x10²)

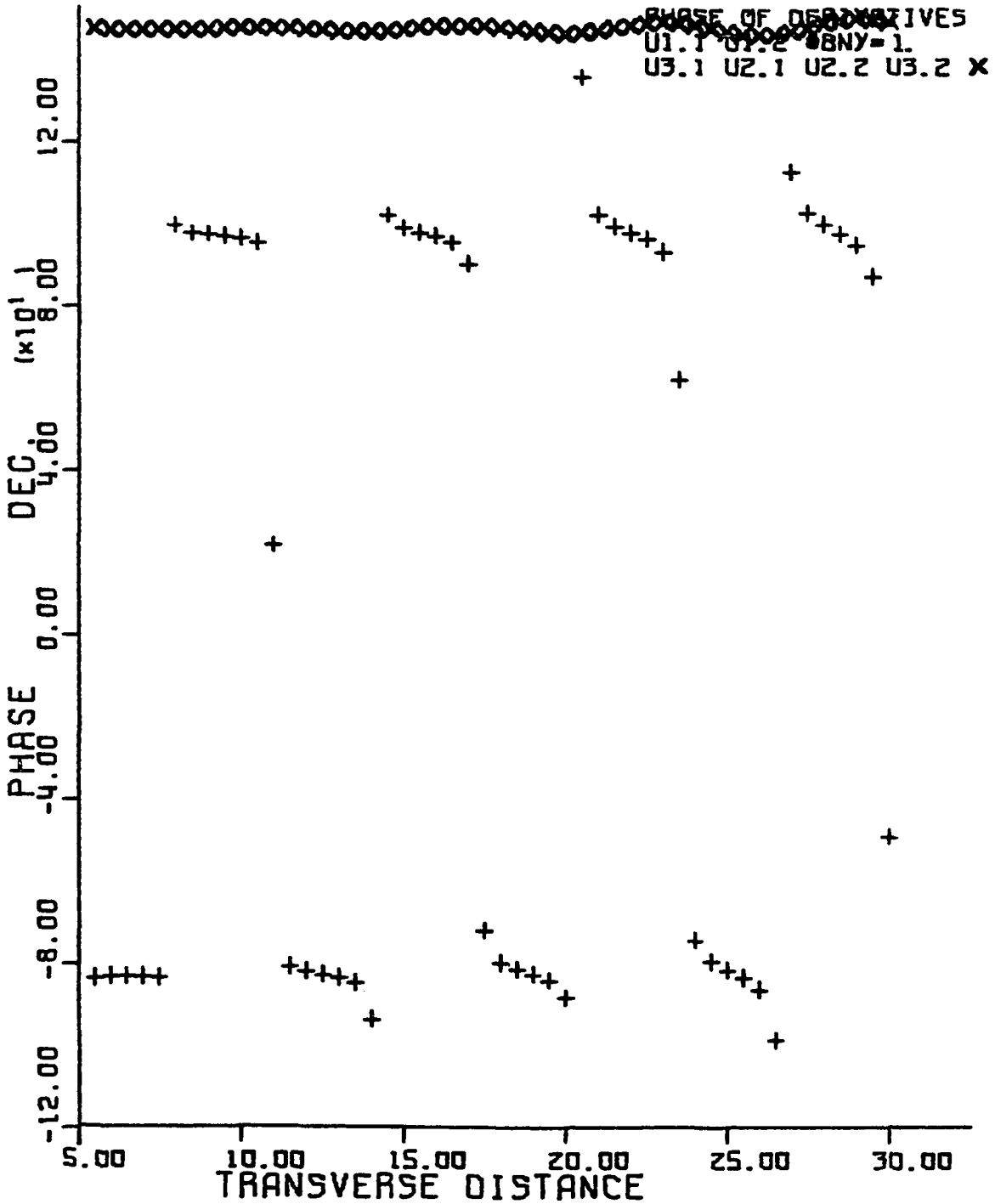

Figure 110. Phase of the derivatives of the particle displacements vs. $k_o x$ at $k_o y = 1.0$

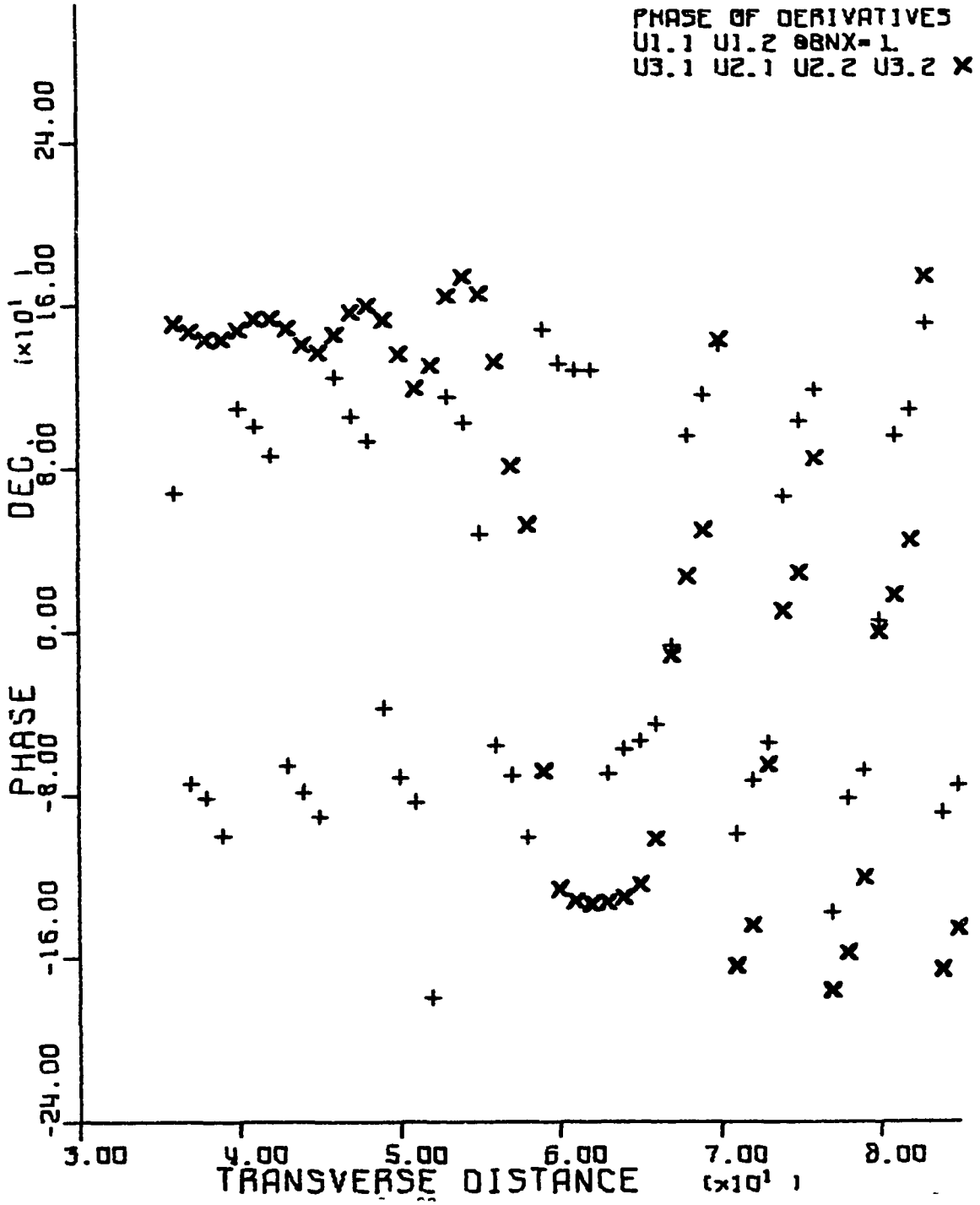

Figure 111. Phase of the derivatives of the particle displacements vs. $k_o x$ at $k_o y = 1.0$

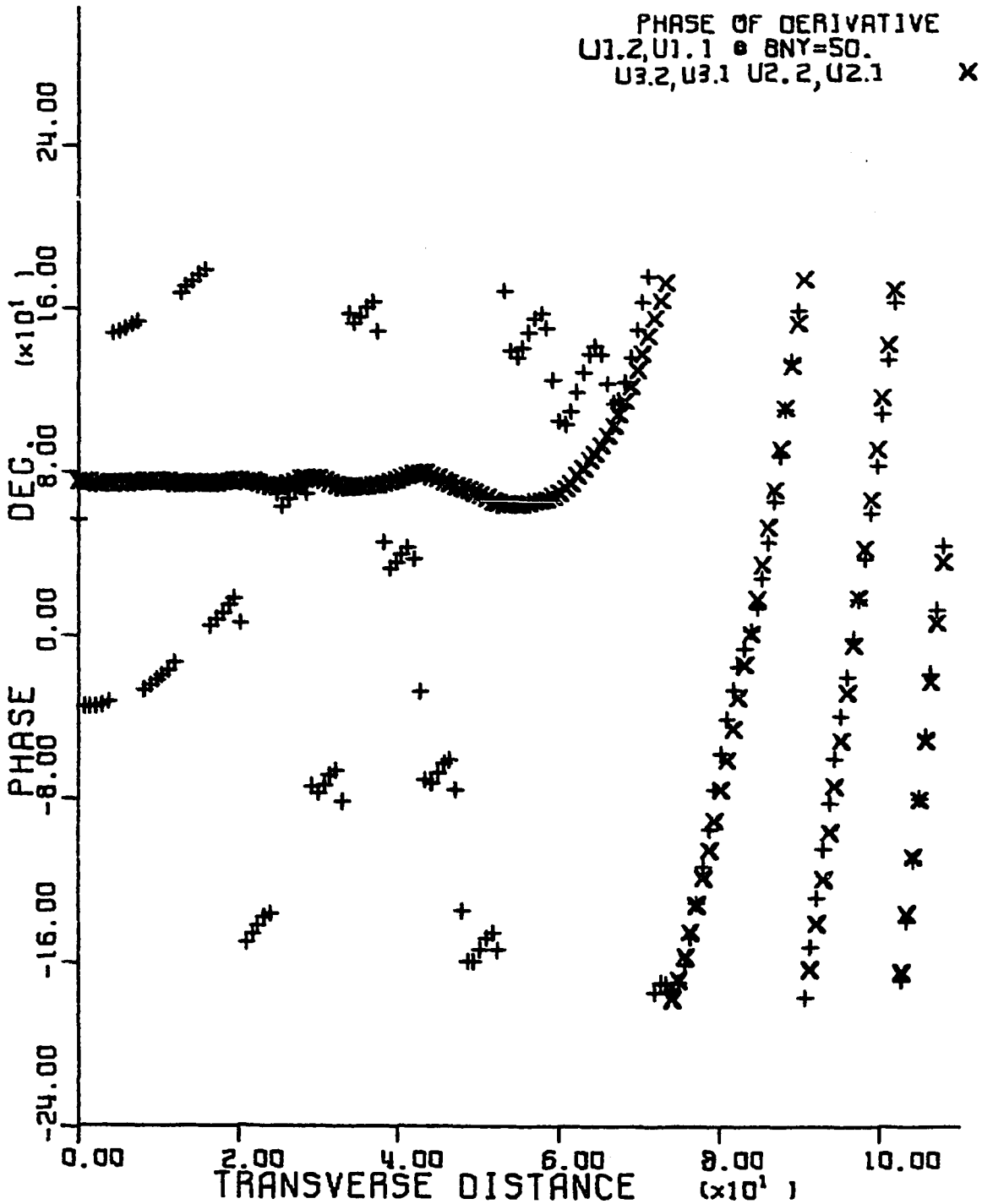

Figure 112. Phase of the derivatives of the particle displacements vs. $k_o x$ at $k_o y = 50.0$

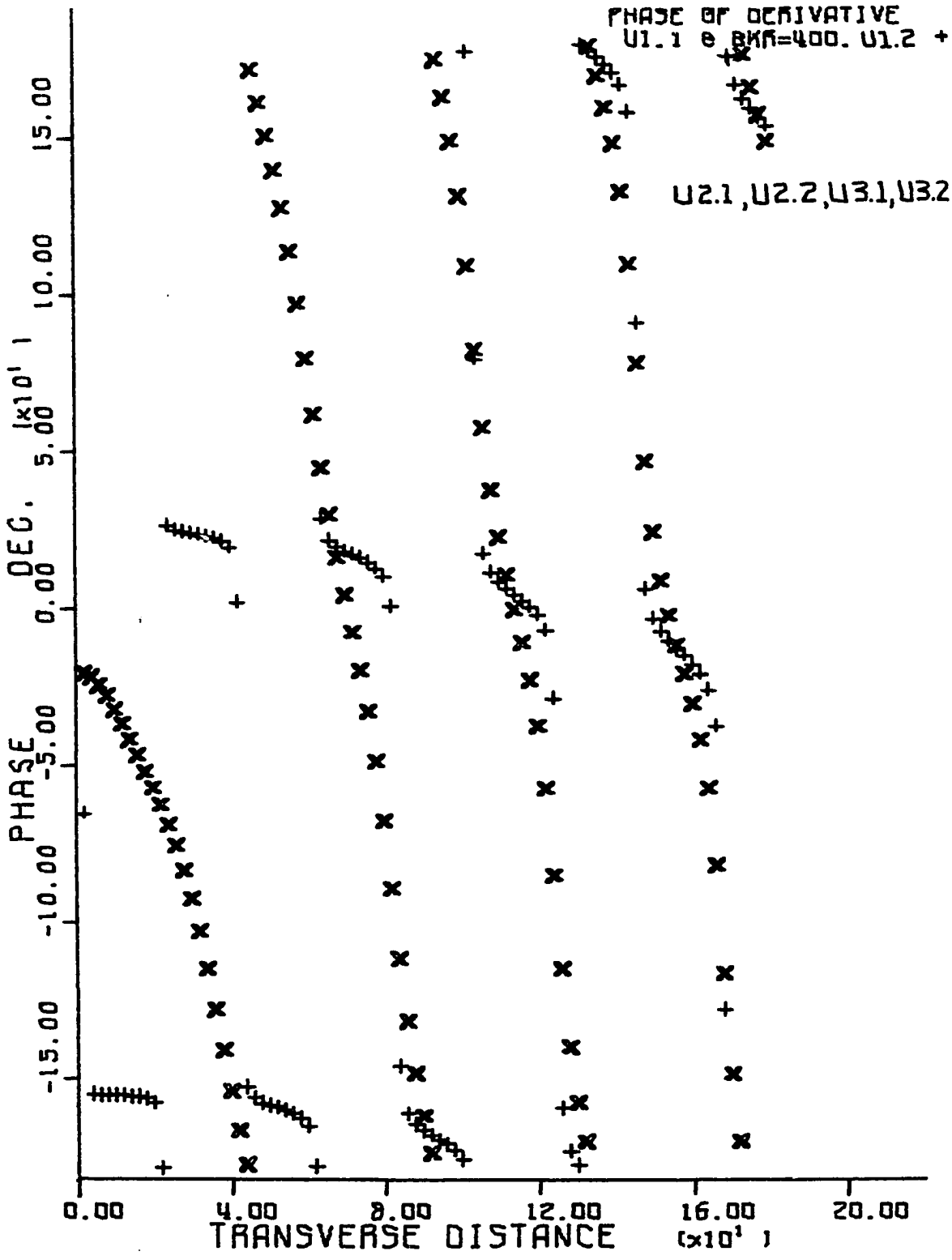

Figure 113. Phase of the derivatives of the particle displacements vs. $k_o x_t$ at $k_o r = 400.0$

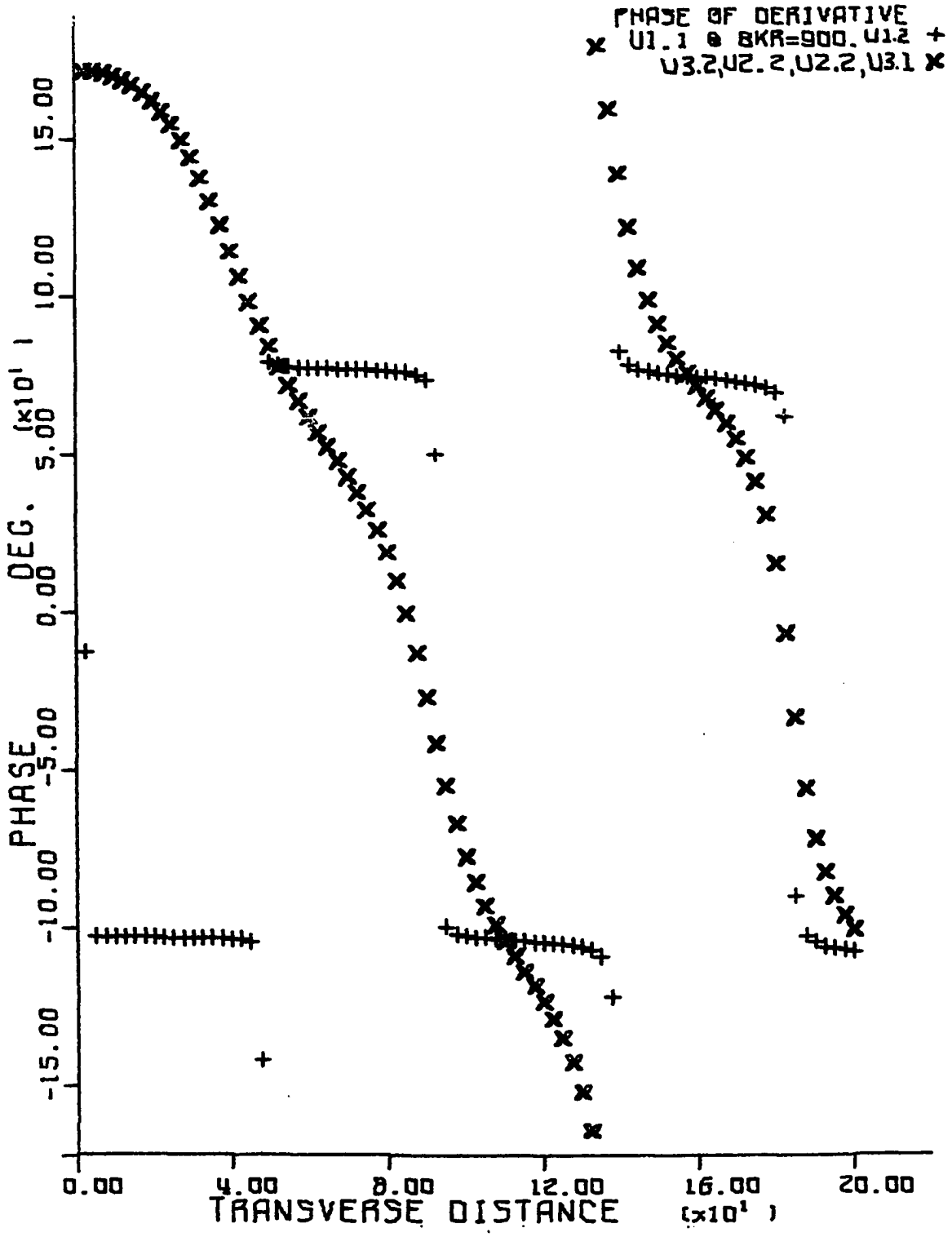

Figure 114. Phase of the derivatives of the particle displacements vs. $k_o x_t$ at $k_o r = 900.0$

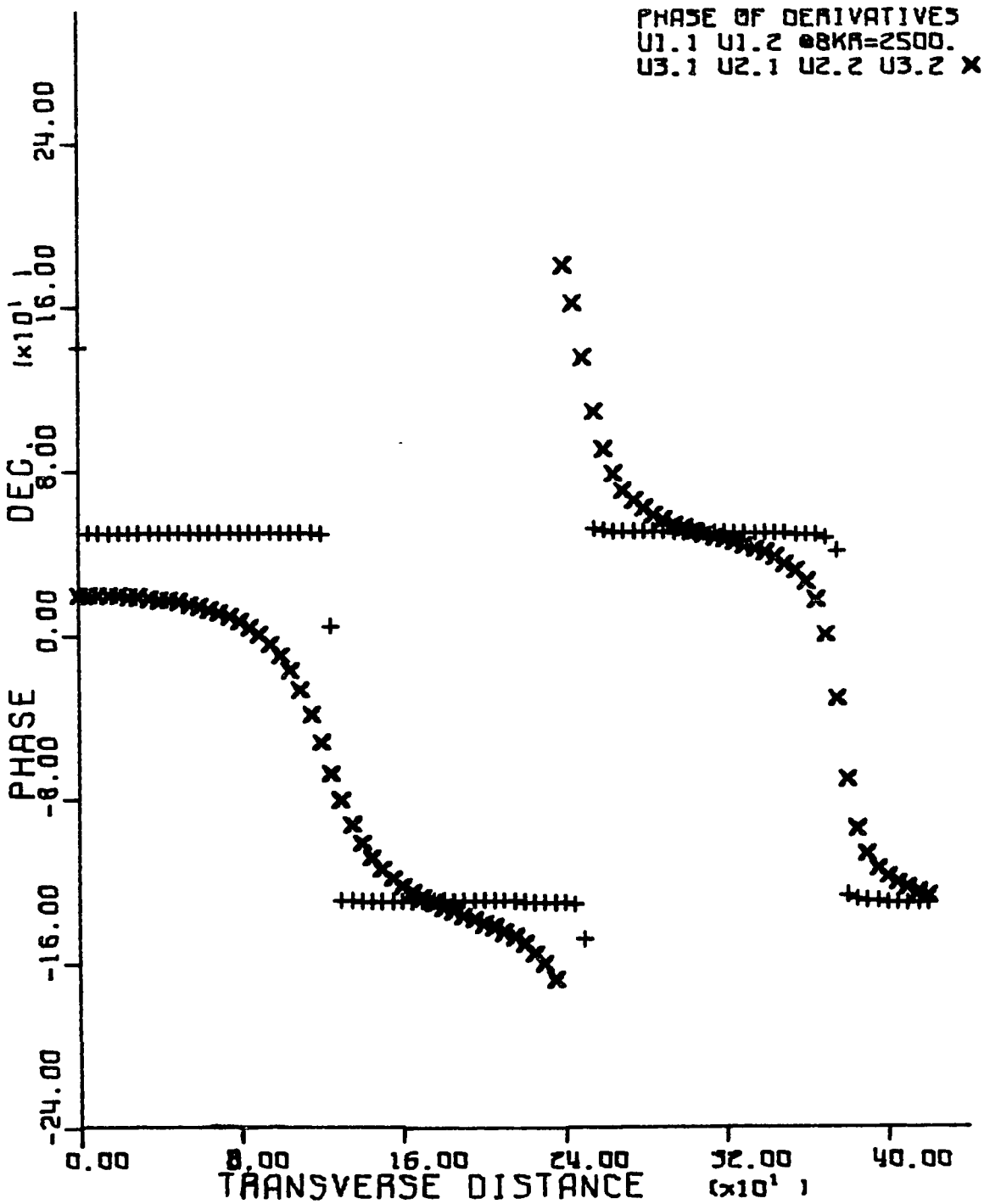

Figure 115. Phase of the derivatives of the particle displacements vs. $k_o x_t$ at $k_o r = 2500.0$

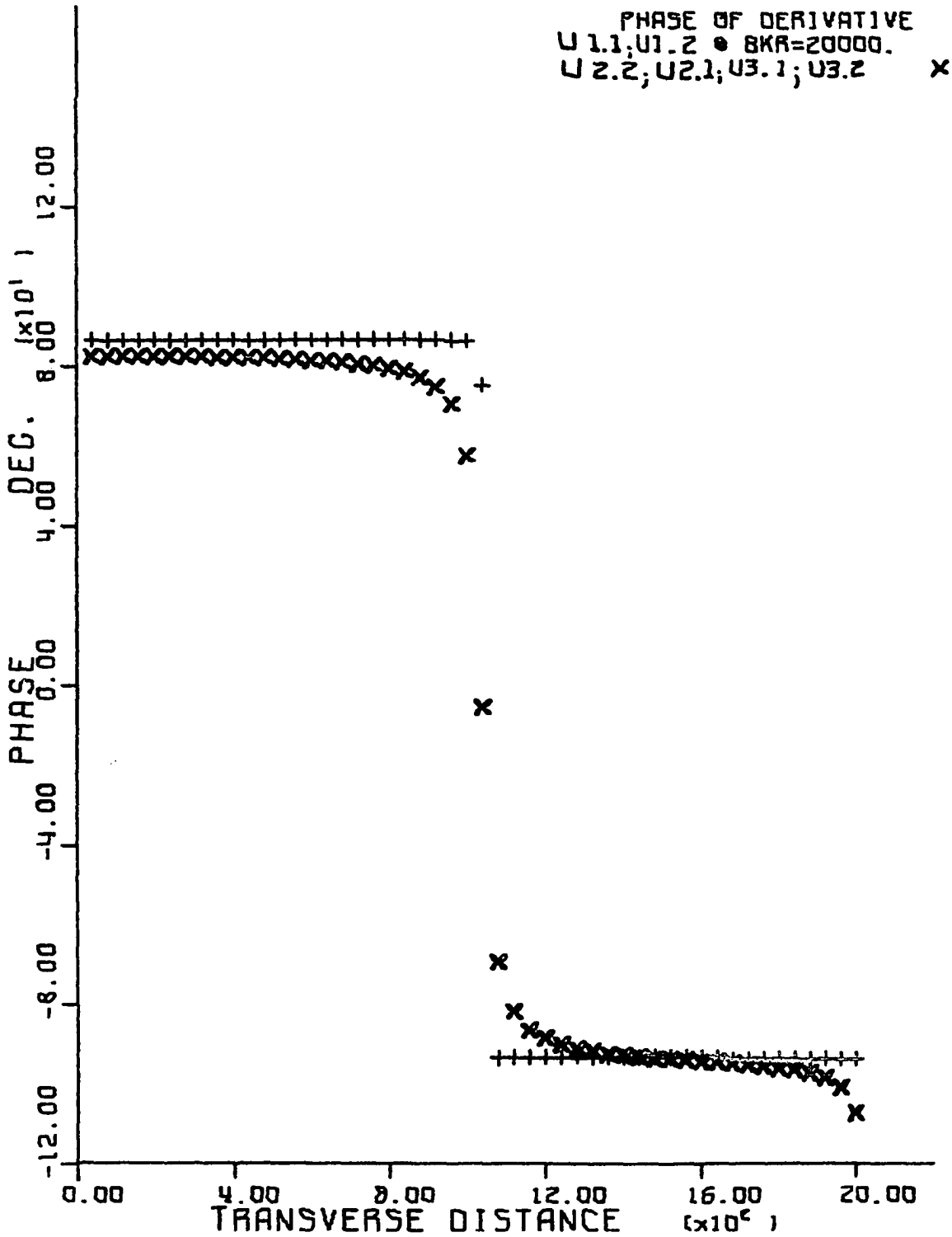

Figure 116. Phase of the derivatives of the particle displacements vs. $k_o x_t$ at $k_o r$ = 20,000.0

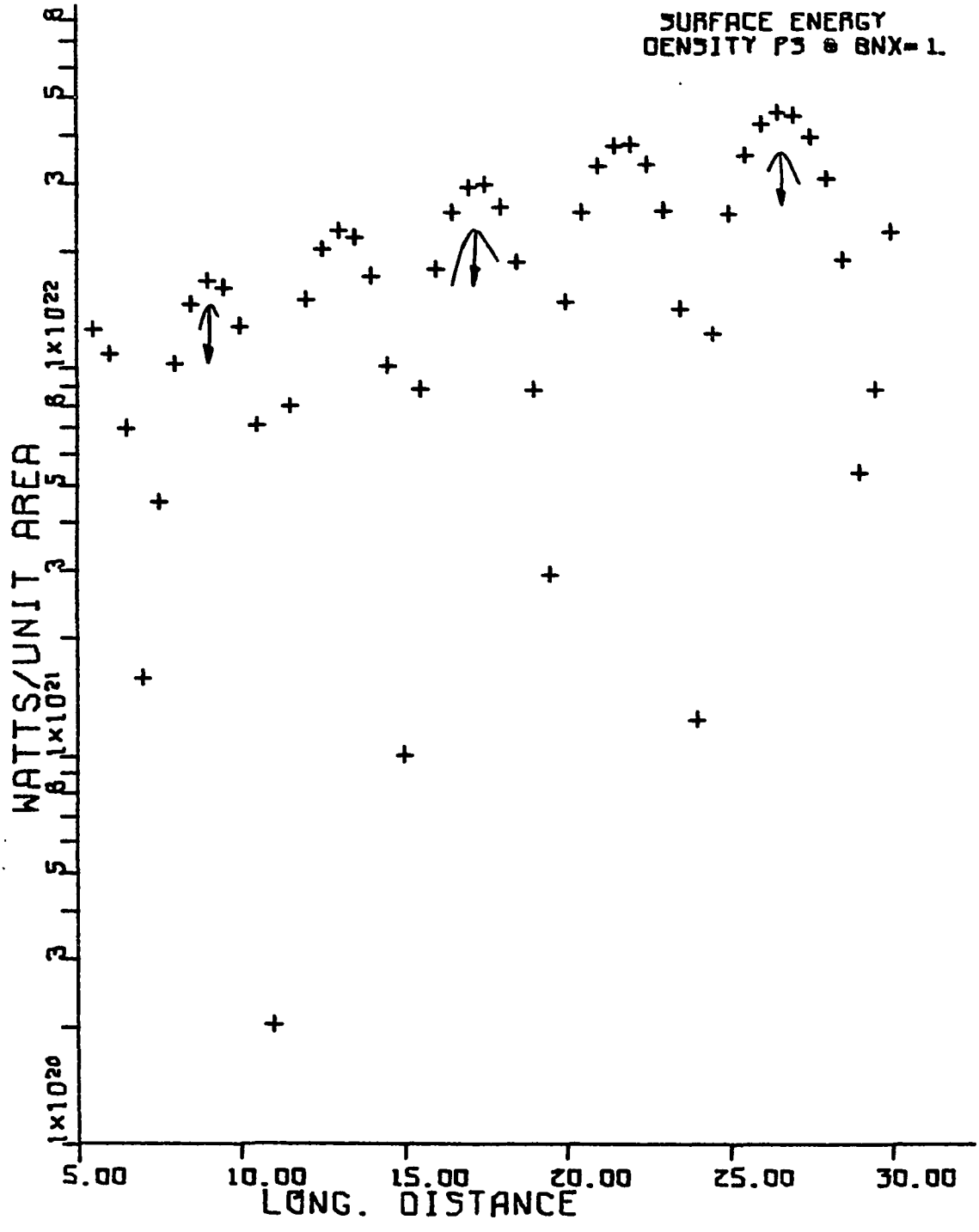

Figure 117. The x_3 component of the surface Poynting vector vs. $k_o y$ at $k_o x = 1.0$

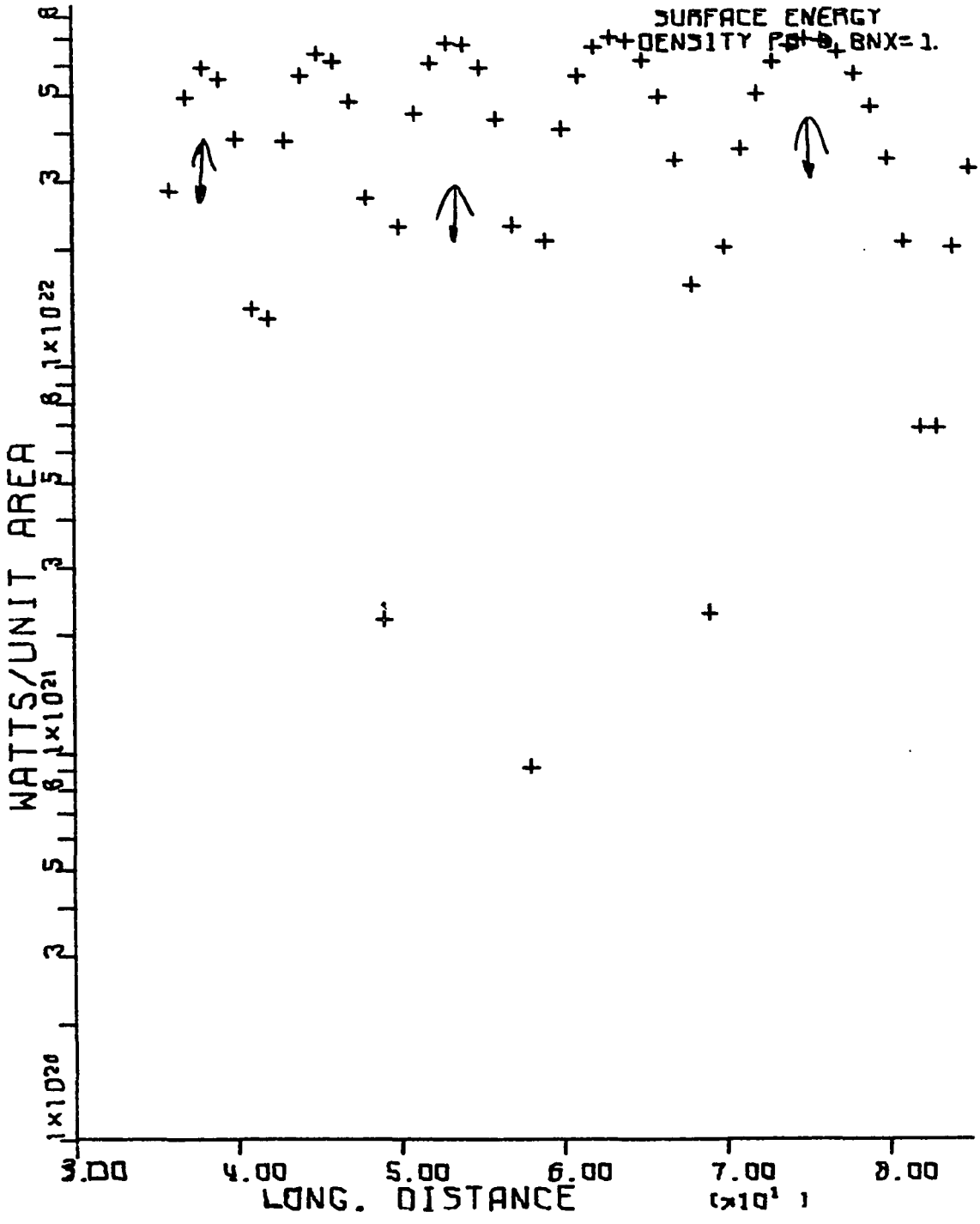

Figure 118. The x_3 component of the surface Poynting vector vs. $k_o y$ at $k_o x = 1.0$

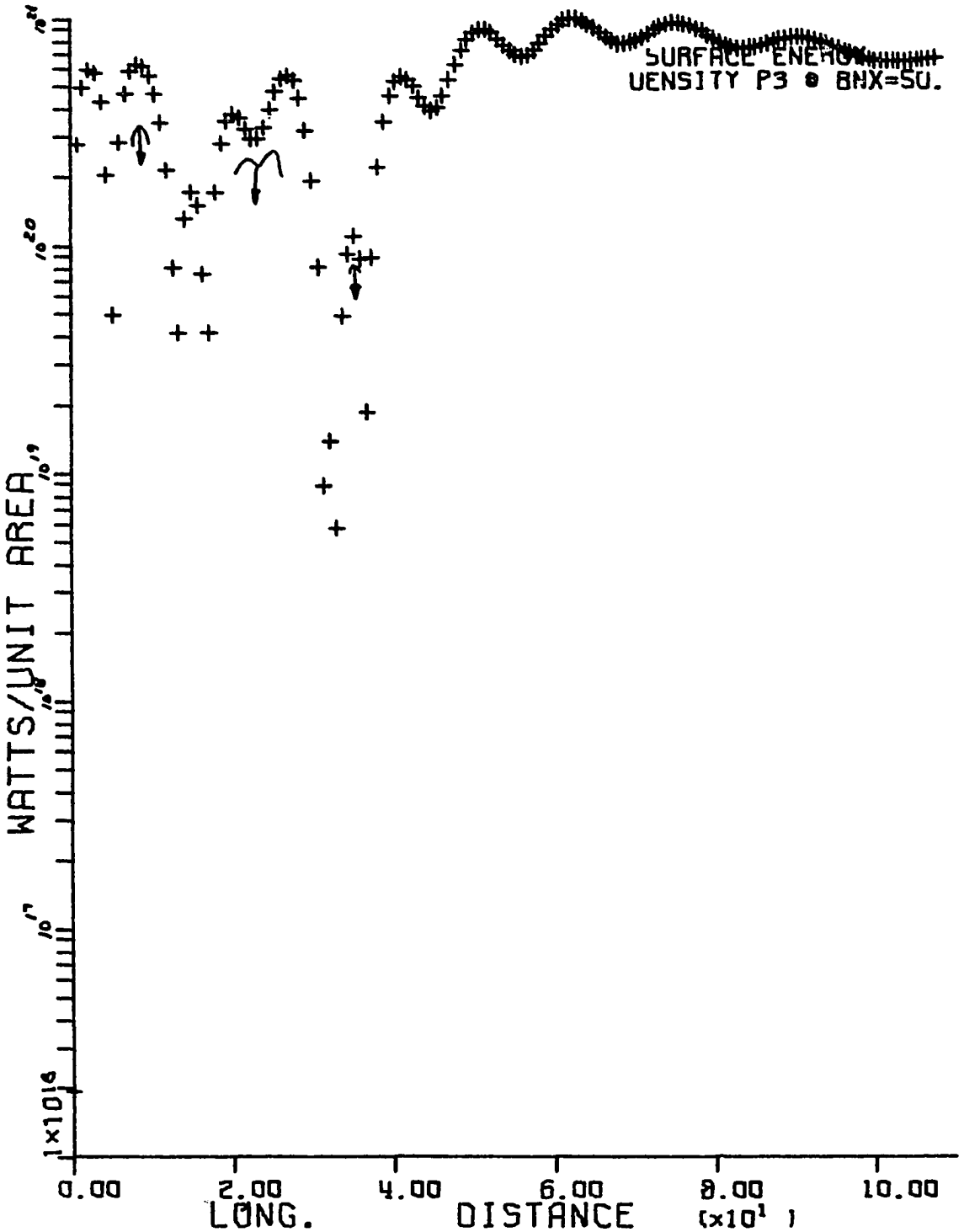

Figure 119. The x_3 component of the surface Poynting vector vs. $k_o y$ at $k_o x = 50.0$